UNIVERSITY OF Southampton

University of Southampton Research Repository
ePrints Soton

Copyright © and Moral Rights for this thesis are retained by the author and/or other copyright owners. A copy can be downloaded for personal non-commercial research or study, without prior permission or charge. This thesis cannot be reproduced or quoted extensively from without first obtaining permission in writing from the copyright holder/s. The content must not be changed in any way or sold commercially in any format or medium without the formal permission of the copyright holders.

When referring to this work, full bibliographic details including the author, title, awarding institution and date of the thesis must be given e.g.

AUTHOR (year of submission) "Full thesis title", University of Southampton, name of the University School or Department, PhD Thesis, pagination

http://eprints.soton.ac.uk

UNIVERSITY OF SOUTHAMPTON

FACULTY OF ENGINEERING, SCIENCE AND MATHEMATICS

Optoelectronics Research Centre

A Spectroscopic Investigation of Novel Doped Glasses for Active Infrared Devices

Jonathan Edward Aronson

Thesis submitted for the qualification of
Doctor of Philosophy

March 2006

UNIVERSITY OF SOUTHAMPTON

ABSTRACT

FACULTY OF ENGINEERING, SCIENCE & MATHEMATICS

OPTOELECTRONICS RESEARCH CENTRE

Doctor of Philosophy

A SPECTROSCOPIC INVESTIGATION OF NOVEL DOPED GLASSES FOR ACTIVE INFRARED DEVICES

By Jonathan Edward Aronson

A number of novel doped glasses have been studied for their potential as infrared amplifier materials. Optical amplifiers which operate outside of the C-band are likely to form part of future optical telecoms systems. This work is focused on transition metal and rare earth-doped materials which could provide gain in the telecoms S-band.

Nickel and Vanadium-doped gallium lanthanum sulphide (GLS) glasses were identified as possible new amplifier materials. Emission was observed at 1200 nm from Ni-doped GLS and at 1400 nm for V-doped GLS. The FWHM of the emission from V-doped GLS was 450 nm, making it particularly attractive for a broadband optical amplifier. Low temperature emission spectra from V-doped GLS suggest that it is not affected by nonradiative decay to the same extent as Cr-doped GLS.

Thulium and erbium-doped tin silicate glass-ceramics produced by the sol-gel method were studied for as potential amplifier materials. The addition of tin oxide to these glasses makes them photosensitive and is shown in this work to increase fluorescence lifetimes. However, the addition of >5% SnO_2 causes increased infrared absorption which would outweigh advantages gained by the increased lifetime. Thulium-doped tin silicate glass-ceramics were investigated for the first time, and show a broad fluorescence band at 1470 nm with a FWHM of ~120 nm. The maximum lifetime of the $^3F_4$ level was 37 μs, which is higher than in Tm-doped silica.

Y_2O_3-Al_2O_3-SiO_2 (YAS) glass was investigated as a low phonon silicate host for a thulium-doped fibre amplifier. Raman and FTIR measurements showed that the maximum phonon energy can be reduced by increasing the yttria:alumina ratio and decreasing the silica content. This was confirmed by emission lifetime measurements of the $^3F_4$ level, which showed an increase in lifetime of 20% over the range studied. A Tm-doped YAS fibre was successfully drawn from a glass of the composition 17.4% Y_2O_3, 22.5% Al_2O_3 and 60% SiO_2. 7.5 m of continuous unclad fibre was fabricated with a diameter of 150-350 μm at a temperature of 1150°C. The minimum loss in the fibre was measured to be 3.6 dB/m at 1360 nm. This material is shown to have good potential for use in S-band fibre amplification.

Contents

List of Figures

List of Tables

Acknowledgments

I would like first to thank the ORC and EPSRC for giving me the opportunity and resources to carry out the research presented in this thesis.

I also thank my supervisor Dr Bill Brocklesby for his help and encouragement, and for telling it to me straight when things were going wrong!

I am grateful to many people who have helped me over the last few years, in particular:

Peter Jander for spending countless hours and days showing me the ropes when I started and offering invaluable advice throughout my PhD

Mark Hughes and Richard Curry for working with me on the chalcogenide glasses

Beth Taylor, Heike and Angelique for useful discussions on glass-melting

Gilberto Brambilla for his advice on fibre-drawing

Andy Webb for his patience and persistence in helping to produce the YAS preform

Roger Moore for his unparalleled expertise in fibre-drawing

I must also mention the friends I have made over the last few years: Tim, Jeff, Gates, Chris H, Steve, Iain, Mark, Chris F, Mike, Matt and everyone else who made my exhausting and stressful time at the ORC such good fun! Finally, thanks to Claire for her patience, understanding and support.

Chapter 1

Introduction

1.1 Motivation for the research

Current optical telecommunications systems utilise wavelength division multiplexing (WDM) to increase transmission capacity through individual optical fibres. This technique involves transmitting a number of closely-spaced signal wavelengths through each fibre. A key component of a long haul WDM system is the optical amplifier, which is required to compensate for the loss in signal as it travels through the fibre.

The erbium-doped fibre amplifier (EDFA) is currently the most widely used optical amplifier. EDFAs can operate over the telecoms C-band (1530-1565 nm) and L-band (1565-1625 nm), though this is a fraction of the available transmission window of silica fibre (1400-1700 nm). The ranges covered by the EDFA and other optical amplifiers which operate within the telecoms window are shown in Fig. 1.1. The figure shows that a number of doped fibre amplifiers (DFAs) cover a good portion of the window. Semiconductor optical amplifiers (SOAs) and Raman amplifiers can cover the entire window, though only through the use of multiple devices. A major aim of this thesis is to find new optical materials which will extend the wavelength ranges amplified by DFAs.

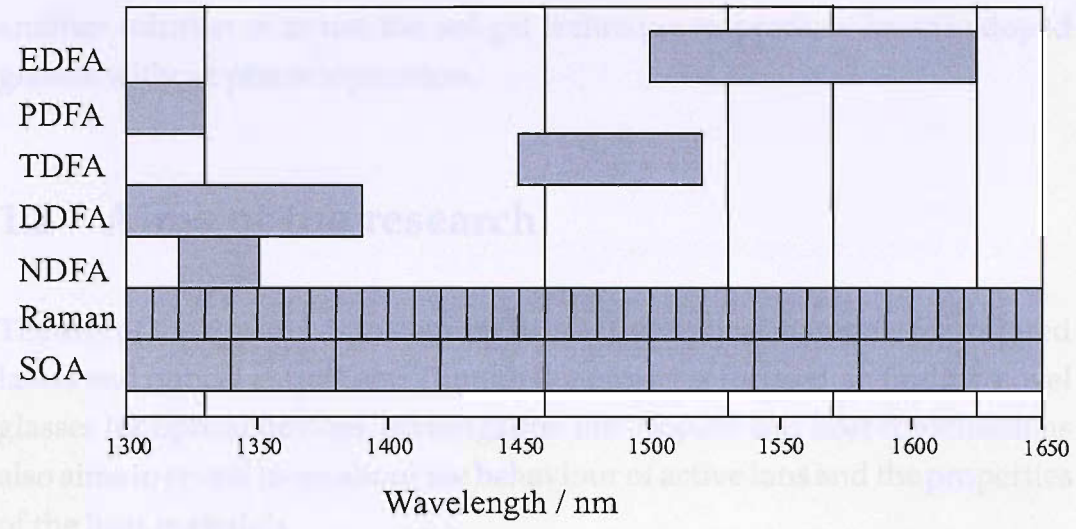

Figure 1.1: Overview of amplified wavelengths within the telecoms window. The vertical lines on the Raman band show typical spacings of pump sources required and those in the SOA band show typical operating ranges of single devices.

Recently there has been interest in both thulium-doped silicate and thulium-doped bismuth glass fibres for S-band (1460-1530 nm) amplification. These fibres are attractive for telecoms applications because they generally have good mechanical strength and high melting temperatures, which allows the potential of fusion-splicing to standard silica telecoms fibre. In order to develop rare earth-doped amplifiers for other regions of the telecoms window, alternative glass hosts are required. Research in this area has traditionally involved praseodymium or thulium-doped fluoride, tellurite or chalcogenide glasses.

Transition metal-doped crystals are well known as broadband laser materials. A transition metal-doped glass could have the potential to amplify wavelengths across the entire low loss region of silica.

In addition to extending the wavelength range used by WDM systems, there is also a desire towards miniaturisation in optical amplifiers. The length of the EDFA is limited by the low solubility of erbium in alumina-doped silica, so new materials with increased rare earth solubility are desirable in order to reduce the size of devices. Current research in this area is focused on erbium-doped bismuth glass which has improved erbium solubility, though

another solution is to use the sol-gel technique to produce heavily doped glasses without phase separation.

1.2 Aims of the research

The aim of the research is to develop new active optical materials for infrared lasers and optical amplifiers. Though the project is focused on finding novel glasses for optical devices, investigation into dopant and host combinations also aims to reveal more about the behaviour of active ions and the properties of the host materials.

1.3 Outline of the thesis

A overview of the theoretical background required to interpret the results presented in this thesis is given in chapter 2. The mechanisms causing the splitting of energy levels when a dopant ion is incorporated into a solid are outlined, then optical spectroscopy is introduced as the observation of transitions between these levels. The operation of optical amplifiers and lasers is then described. The chapter concludes with a review of current amplifier technology and a discussion of possible solutions for future amplifiers.

Chapter 3 provides details of the experimental techniques used to obtain spectroscopic data in this thesis. The chapter also contains an explanation of the stretched exponential function used to analyse fluorescence lifetime data in this work.

An investigation into transition metal-doped chalcogenide glasses is presented in chapter 4. The first half describes a study of a range of chromium-doped chalcogenide glasses. A fluorescence excitation spectrum provides evidence that chromium is hosted as Cr^{4+} and fluorescence spectra are measured and compared at 300 K, 77 K and 4 K. The second half of the chapter contains a survey of a range of transition metal-doped gallium lanthanum sulphide (GLS) glasses. Absorption spectra are reported and analysed with a detailed comparison with transition metal-doped glasses

and crystals reported in the literature. Fluorescence is reported for the first time in both nickel and vanadium-doped GLS. The emission from V-doped GLS has a FWHM of 450 nm and is centred at 1420 nm, making it very interesting as a potential amplifier material.

Erbium and thulium-doped tin silicate glass-ceramics are investigated in chapter 5. Raman spectra and ultraviolet absorption measurements confirm that the samples contain tin oxide nanocrystals. Samples containing higher tin oxide concentrations are shown to have increased fluorescence lifetimes. Hydroxyl concentrations in the samples were estimated to be ~2000 ppm wt. A second batch of samples with reduced hydroxyl concentrations showed no improvement in fluorescence lifetimes. A broad emission peak was observed in the thulium-doped samples at 1470 nm. The results suggest that tin silicate glass-ceramics host rare earth ions at the interfaces between the nanocrystals and the glass.

Chapter 6 presents a study of thulium-doped yttrium aluminosilicate (YAS) glasses for S-band amplification. In the first part, the glass composition is optimised in order to maximise the fluorescence lifetime. Raman and infrared spectra show that altering the yttria:alumina ratio and the silica content changes the maximum phonon energy of the glass. The relative effects of this change in maximum phonon energy and changes in refractive index are assessed and supported by fluorescence lifetime measurements. The second part describes the fabrication of a thulium-doped YAS fibre. An unclad fibre with diameter of ~200 μm was drawn from a solid YAS preform rod. Loss measurements were conducted using the cutback method and show a minimum loss of 3.6 dB/m at 1360 nm. The characteristic broad emission at 1470 nm was retained in the fibre and fluorescence resulting from upconversion processes was identified at 470 nm.

The results obtained in this thesis are summarised in chapter 7 and future directions of study are proposed as a result of findings in this work.

Chapter 2

Theoretical background

2.1 Introduction

This chapter provides the theoretical basis for the work contained in the thesis. It begins with an overview of the quantum mechanics which causes the splitting of energy levels when dopant ions are incorporated into a solid host. Optical spectroscopy is then introduced as the observation of transitions between these electronic energy levels. The principles behind the optical amplifier and laser are then outlined and the chapter concludes with a review of current optical amplifier technology.

2.2 Optically active centres

When a pure glass or crystal is doped with certain ions, optical absorption and emission bands are introduced which are not observed in the pure host material. The combination of the dopant ion and its local environment is termed an optically active centre. It is both the nature of the dopant ion and that of its site in the host material which determine the position, shape and strength of the absorption and emission bands of the centre.

This section contains an outline of the mechanisms which cause the splitting of energy levels when a free ion is incorporated into a solid host.

2.2.1 Energy levels of a static ion

Considering first an isolated static ion, the electronic energy levels are given by the solution to the time-independent Schrödinger equation:

$$H\psi = E_n\psi, \tag{2.1}$$

where H is the Hamiltonian operator, ψ is the wavefunction of the ion and E_n are the eigenvalues of the equation and are the values of the energy levels. The energy levels of a free ion can be described by the Hamiltonian H_{FI}:

$$H_{FI} = H_o + H_e + H_{SO}, \tag{2.2}$$

where:

H_o is the orbital Hamiltonian for electrons in the field of a nucleus. This term arises from the Coulomb interaction between the ion's outer electrons and both the filled electron shells and the nucleus. This is the central field approximation, which assumes that the interaction with filled shells and the nucleus can be averaged to a spherically symmetric term.

H_e is the Hamiltonian for the Coulomb interaction of outer electrons. This energy term comes from the non-central force experienced by electrons in a partly filled shell.

H_{SO} results from the spin-orbit coupling. This is due to the interaction between the electron spin magnetic moment and the orbital angular momentum of the electron.

When the free ion is incorporated into a host, the energy levels are split and shifted by the interaction with the electrons of the ligands. The electric field of the ligands is termed the crystal field, and is accounted for by an additional term in the Hamiltonian H_{CF}. The effect of the crystal field is treated differently for rare earth and transition metal ions. Another consequence of introducing an ion into a solid host is that the coulomb interaction term is changed. This occurs because the electrons are delocalised onto the ligands. This is called the nephelauxetic effect and reduces the energy levels compared to the free ion.

The rare earths or lanthanides are the group of elements between lanthanum and lutetium on the periodic table. Triply ionised rare earths have the electronic structure of xenon with a partially filled $4f$ shell which is shielded by the larger $5s^2$ and $5p^6$ shells. This shielding effect makes the energy levels of the rare earths relatively insensitive to their local environment, and so $H_{CF} \ll H_e, H_{SO}$. This system is in the weak crystal field regime and so H_{CF} is treated as a perturbation to the free ion energy levels. In rare earths, the effect of the crystal field is to split the free ion energy levels into Stark levels. A group of Stark levels originating from the same free ion energy level is termed a Stark manifold. In 1968, Dieke published a diagram showing the energy levels of all rare earth ions doped into $LaCl_3$ [1]. The energy level diagram for Er^{3+} is reconstructed in Fig. 2.1. The width of the energy levels shows the strength of the crystal field splitting and the semicircles identify levels from which luminescence occurs.

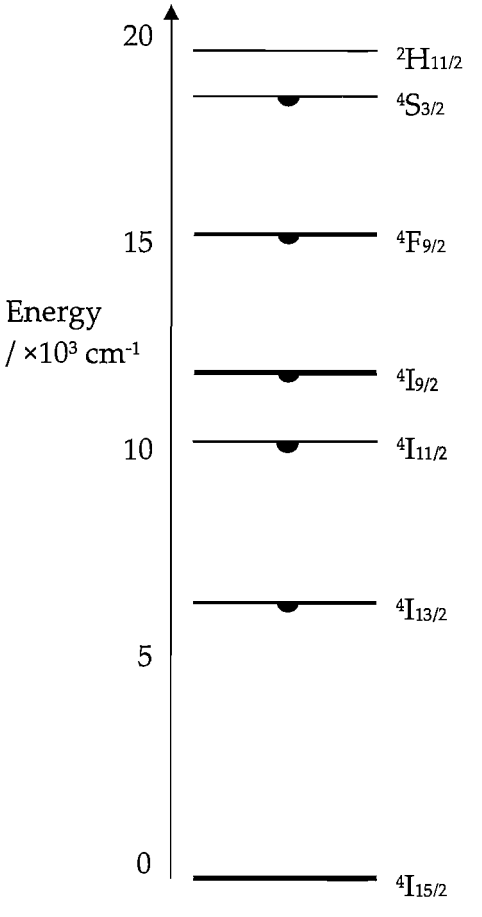

Figure 2.1: Partial energy level diagram for the trivalent rare earth ion Er^{3+}. The data was obtained for Er-doped $LaCl_3$ by Dieke [1]

The first row transition metal ions are the group of elements from titanium to copper on the fourth row of the periodic table. They are characterised by a partially filled $3d$ electron shell. Unlike the case for rare earths, this unfilled shell is not shielded from the crystal field in a transition metal-doped solid. Consequently, the energy levels of transition metal ions are strongly affected by the crystal field and the system can be in either an intermediate crystal field regime ($H_{SO} < H_{CF} < H_e$), or in a strong crystal field regime ($H_{SO} < H_e < H_{CF}$). In either case the spin-orbit coupling term is treated as a perturbation on the crystal field split levels.

The Coulomb interaction between the $3d$ electrons can be described by the three Racah parameters. The Racah A parameter can be approximated to a constant offset energy, and so is neglected in the discussion of transitions between energy levels. The ratio of the C and B parameters, C/B is approximately constant for all the first row transition metals and lies between 4 and 5. The system can now be described by the B parameter alone, which is a measure of the interelectronic repulsion. Tanabe and Sugano represented the energy levels of the $3d$ transition metals as a function of the crystal field strength and the Racah B parameter in a diagram such as the one shown in Fig. 2.2 [2]. Dq represents the crystal field strength and the energy level labels correspond to representations for the symmetry group. Each Tanabe-Sugano diagram is specific to the number of $3d$ electrons, the site symmetry and the exact value of C/B.

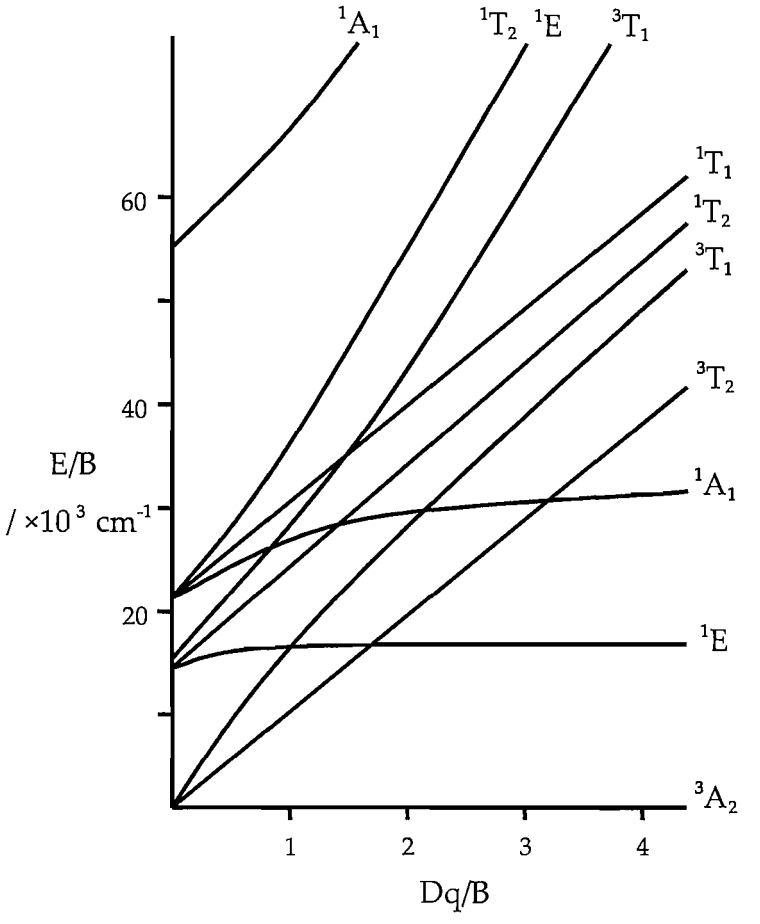

Figure 2.2: The Tanabe-Sugano diagram for $3d^2$ ions in a tetrahedral field (e.g. Cr^{4+}) [2]. The energies are plotted relative to the lowest level.

2.2.2 The effect of the vibrating host material

In this section the coupling of the dopant ion with the vibrating host is considered. The consequences of this coupling are that the vibrations in the host affect the electronic energy levels of the dopant ion and that changes in the electronic state of the dopant ion can induce vibrations in the ion's environment.

This complex electron-phonon interaction can be illustrated through the single configurational coordinate model (SCCM). In this model, the movement of the ligands is considered as a single symmetrical 'breathing' mode, so the position of the all the ligands is described by a single parameter: the ion-ligand separation Q. The ion is considered to sit in a harmonic

potential, which is a good approximation to the Morse potential near the minimum. The SCCM also uses the Born-Oppenheimer approximation which states that the motion of electrons and nuclei can be separated. This allows the motion of the electrons to be considered around a stationary nucleus and ligand arrangement. This is a reasonable approximation because nuclei are much more massive than electrons and so move on a longer timescale.

Figure 2.3 shows the single configurational coordinate diagram for electronic states *a* and *b*. For each electronic state, the interionic potential is considered as harmonic and is therefore represented by a parabola in the diagram. The horizontal lines within the parabolas represent the allowed vibrational levels of the harmonic oscillator. Optical transitions between electronic states are shown as vertical lines. This is due to the Franck-Condon principle which states that electronic transitions occur on such a short timescale that the nuclei can be considered stationary.

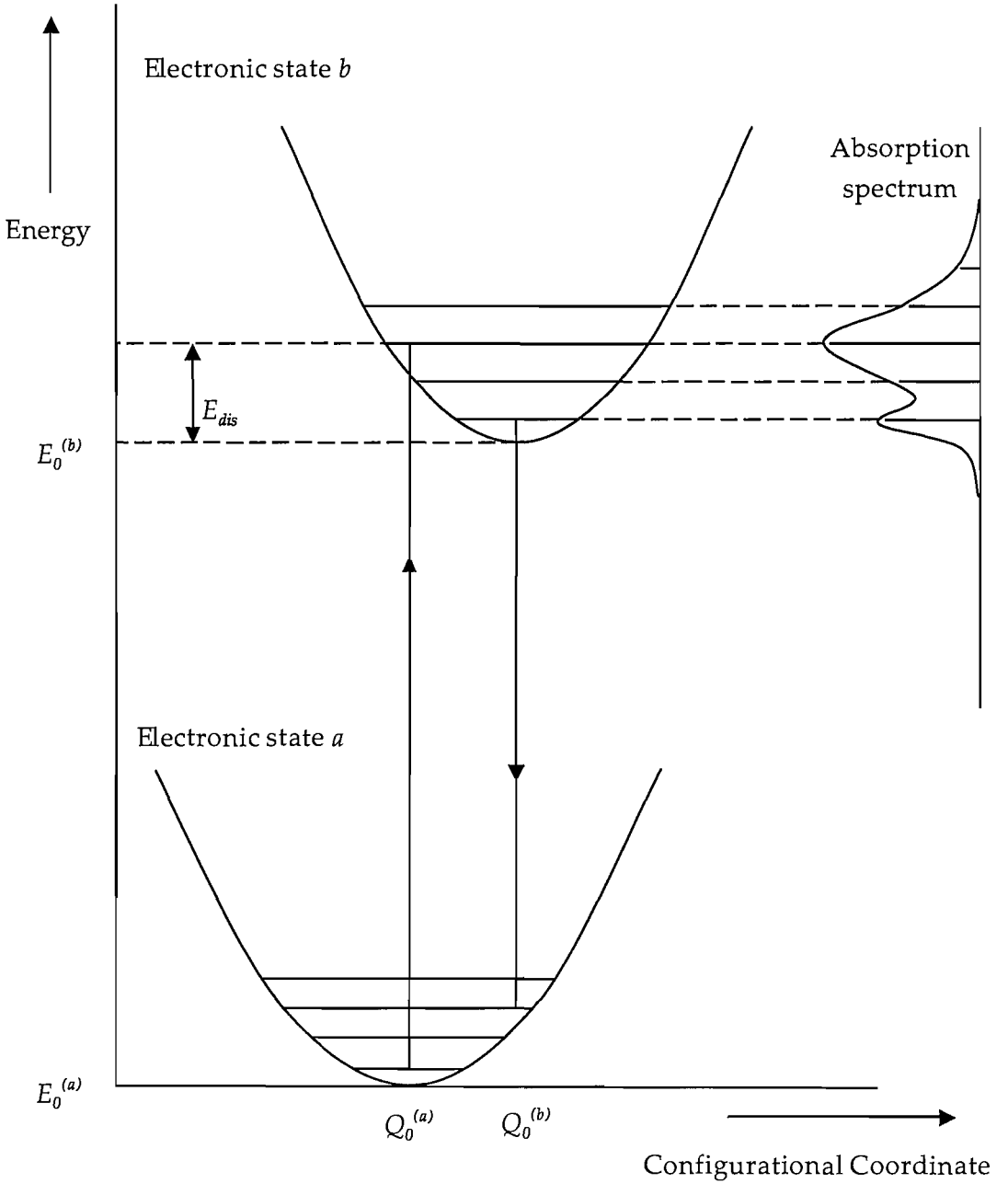

Figure 2.3: The single configurational coordinate model [3], showing how phonon-assisted absorption gives rise to absorption lineshapes.

An absorption and emission process can be described using the SCCM as follows:

1. An incoming photon excites the system from the ground vibrational state in electronic state a to an excited vibrational state in electronic state b.

2. The system then quickly relaxes into the ground vibrational state of electronic state b by producing phonons in the host material.

3. Assuming a fully radiative transition, the system remains electronically excited until spontaneous or stimulated emission causes the system to return to electronic state a through the emission of a photon.

4. Again, the system relaxes into the ground vibrational state of electronic state a by the emission of phonons.

The difference in equilibrium position coordinates $Q_0^{(a)}$ and $Q_0^{(b)}$ reflects the difference in electron-phonon coupling between two states. This difference in electron-lattice coupling is characterised by the Huang-Rhys factor:

$$S = \frac{E_{dis}}{\hbar\omega}, \tag{2.3}$$

where $\hbar\omega$ is the energy of the breathing mode vibration and, for absorption and emission peaks E_a and E_e, E_{dis} is:

$$E_{dis} = \frac{1}{2}(\hbar\omega + E_a - E_e). \tag{2.4}$$

This factor is closely related to the Stokes shift which is defined as the energy difference between the absorption and emission peaks. From the diagram:

$$E_a - E_e = (2S - 1)\,\hbar\omega \tag{2.5}$$

For transitions between $4f$ states in rare earth ions $S \simeq 0$ because the $4f$ electrons are shielded by complete outer electron shells. From equation 2.5 the Stokes shift is therefore $\simeq 0$ and so phonon-assisted transitions are rarely observed. In transition metal ions, $3d$ electrons are more strongly coupled to the ligands and so vibrational sidebands may be seen on spectra. The spectral peak arising from the transition between ground vibrational states of the lower and upper electronic states is termed the zero phonon line (ZPL).

Since each of vibrational states is described by a harmonic oscillator function, for the lowest energy state the most probable position of the system is the equilibrium position Q_0. For higher energy states, the system is most

likely to be in the position where the vibrational energy level crosses the parabola. The intensity of the transition depends upon the square of the overlap integral of these wavefunctions and so this affects the shape of the absorption and emission bands. It can be seen from Fig. 2.3 that for sufficient S no ZPL will be observed.

The SCCM is also successful in accounting for the temperature dependence of absorption and emission lineshapes. At 0 K all absorption and emission transitions will occur from the vibrational ground state. As the temperature is increased, transitions from higher vibrational states will occur, adding vibrational sidebands to the absorption and emission spectra.

Nonradiative decay can also be illustrated using the SCCM, Fig. 2.4 shows such a diagram for electronic states with a large Huang-Rhys parameter. For sufficiently large S, excitation of the system from the ground vibrational state results in the population of a vibrational level of the upper electronic state which coincides with the crossing point of the parabolas. In this case the system may relax through the vibrational levels of the lower electronic state without the emission of a photon. If the system is excited to a state just below the crossing point, then the same process may occur by tunneling. Sufficiently high vibrational states may also be thermally populated; this leads to thermal quenching of fluorescence at higher temperatures.

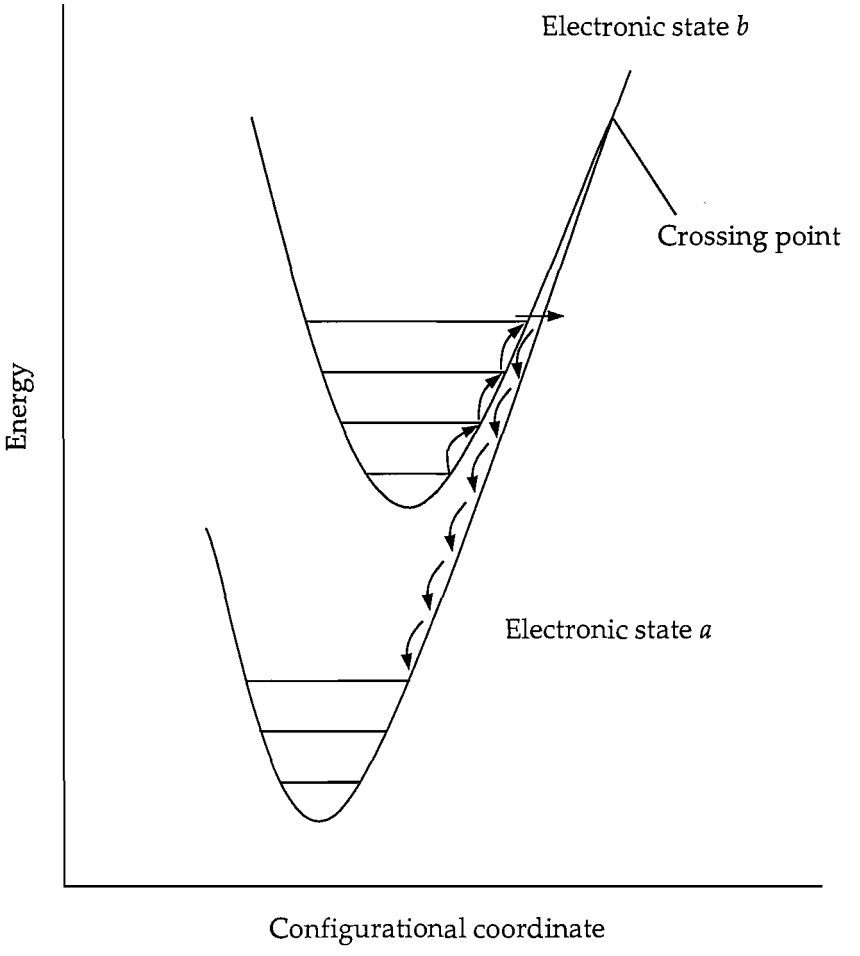

Figure 2.4: The single configurational coordinate model, showing mechanisms of phonon assisted nonradiative decay.

2.2.3 Broadening mechanisms

The SCCM shows how the electron-phonon system gives rise to a number of absorption and emission lines in optical spectra. However, in measured spectra these lines are broadened and can sometimes appear as single broad peaks. The mechanisms responsible for this broadening can be categorised as either homogeneous or inhomogeneous.

2.2.3.1 Homogenous broadening mechanisms

Homogenous broadening mechanisms affect equally all dopant ions in a material. The largest contribution to the homogeneous linewidth is often due

to dephasing processes. As phonons travel through a material, they will be elastically scattered by optical centres. These collisions cause small changes in the emission frequency of the ion through the crystal field interaction. Consequently, temporal coherence is reduced and the emission linewidth is broadened. This process is temperature dependent, as it relies on the presence of phonons in the host material.

Other homogenous broadening mechanisms increase spectral linewidths by decreasing the lifetime of excited states. Nonradiative multiphonon decay (discussed in section 2.2.5.1) decreases the lifetime of the excited state by providing an alternative path for de-excitation. There are other phonon processes which can occur which reduce the lifetime of more closely-spaced Stark levels. These processes are shown in Fig. 2.5.

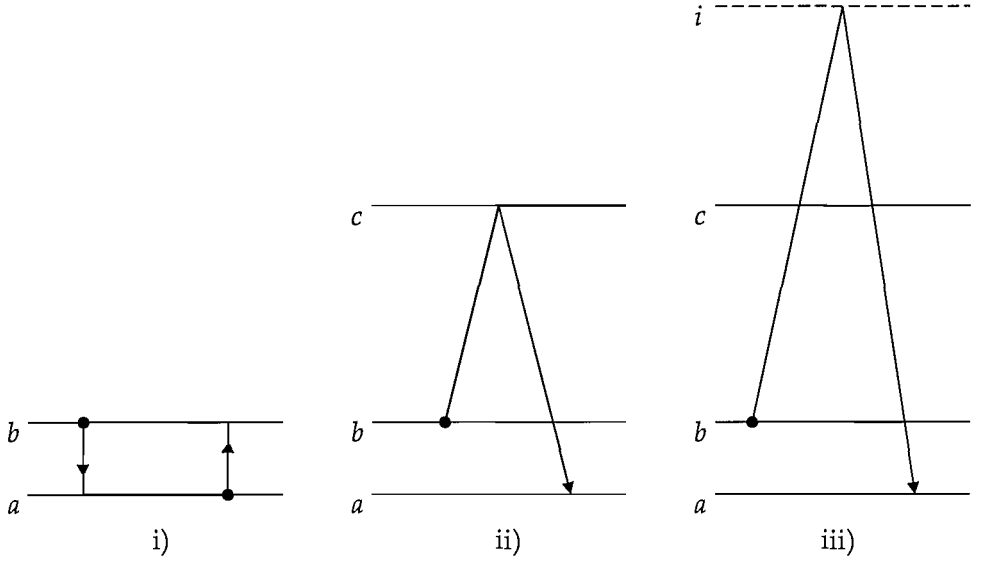

Figure 2.5: Phonon processes which lead to homogeneous broadening i) direct processes ii) Orbach relaxation and iii) Raman process.

The single phonon transition shown in Fig. 2.5 i) occurs between adjacent energy levels and, because of the small energy difference, are supported by single phonons in the host. This process leads to rapid thermalisation of the Stark levels, with levels being occupied according to the Boltzmann distribution. Therefore as the temperature of the host tends towards 0 K, all the ions will occupy the lowest Stark level in the manifold.

Orbach relaxation is the two-phonon process shown in Fig. 2.5 ii). Here the relaxation proceeds from b through an intermediate state c to a, though

this process can also act to excite an ion from state a to b. The energy gap between b and c, and the difference between c and a are assumed to be less than the maximum vibrational energy supported by the host material. As for the direct one-phonon process described above, Orbach processes are dependent on the availability of phonons in the host.

Another contribution to lifetime broadening is through Raman processes, shown in Fig. 2.5 iii). These processes are similar to the Orbach process, except that they involve exciting the ion into a virtual intermediate state i.

Homogeneous broadening also arises from the finite lifetime of excited electronic states τ. According to the Heisenberg uncertainty principle, the energy level must have a width of $\Delta E \geq \hbar/\tau$. The contribution to the broadening of the radiative lifetime is referred to as the natural linewidth and it determines the ultimate limit of spectral resolution.

2.2.3.2 Inhomogenous broadening mechanisms

Inhomogeneous broadening arises from the range of local environments experienced by different ions in a doped material. Altered site symmetries and ion-ligand separations cause shifts in the energy levels of individual ions throughout the solid. Emission and absorption transitions involving these levels therefore occur over a range of energies, producing broadened spectral bands.

Inhomogeneous broadening is much larger in glasses than in crystals. In crystals, site to site variations arise from defects and strains in the crystal lattice, and inhomogeneous broadening is small enough so that for rare earth ions, homogeneous lines corresponding to individual Stark levels can be resolved in absorption and emission spectra. In glasses, the dopant ions enter the host as network modifiers and the broadening is many times stronger. The superposition of the range of homogeneous lines creates a broad inhomogeneous profile in absorption and emission spectra.

2.2.4 Radiative transitions

2.2.4.1 Transition strengths

Transitions between energy levels occurs from an additional term in the Hamiltonian which arises from the interaction of electric and magnetic dipoles with the electric field of the radiation. Since electric dipole processes dominate over magnetic dipole transition strengths, magnetic dipole transitions are neglected in this discussion. The transition strength is dependent upon the square of the matrix element of the electric dipole operator:

$$S(a,b) = \sum_{a,b} |\langle a|\boldsymbol{p}|b\rangle|^2, \tag{2.6}$$

where $\boldsymbol{p}$ is the electric dipole operator.

Experimentally, transition strengths are determined by measuring absorption cross sections, which can be obtained from transmittance measurements:

$$\sigma_{ab}(\nu) = \frac{1}{\rho d} \ln \frac{I_{in}(\nu)}{I_{out}(\nu)} \tag{2.7}$$

where ρ is the number density of active centres, d is the path length, I_{in} is the incident intensity and I_{out} in the transmitted intensity. The integrated absorption cross section is related to the transition strength by [3]:

$$\int \sigma(\nu) d\nu = \frac{1}{4\pi\epsilon_0} \frac{8\pi^3 \nu n}{3hc} \chi_{ED} \frac{1}{g_a} S_{ED}(ab) \tag{2.8}$$

where ϵ_0 is the electric permittivity of free space, n is the refractive index of the material, c is the speed of light in a vacuum $\chi_{ED}=(\frac{n^2+2}{3})^2$ is the local field correction and g_a is the statistical weight of state a. This relationship is important in Judd-Ofelt analysis, which can be used to calculate radiative transition rates between energy levels in rare earth-doped materials. Judd-Ofelt analysis is discussed further in section 6.6.1.

2.2.4.2 Selection rules

Since the transition strength depends on the matrix element of the electric dipole operator, if the matrix element is zero no electric dipole transition will be observed. Consideration of when this matrix element is non-zero leads to a number of selection rules for allowed transitions [4]:

- Transitions are only allowed between states of opposite parity
- For ^{2S+1}L terms, $\Delta S = 0$ and $\Delta L \neq 0$
- For $^{2S+1}L_J$ terms, $\Delta J = 0, \pm 1$ but not $J = 0 \rightarrow J = 0$

So both $4f$-$4f$ and $3d$-$3d$ transitions in octahedral symmetry are forbidden, which is the reason that these transitions exhibit relatively long lifetimes. However these transitions are still allowed by the magnetic dipole process, and deviations from perfect symmetry in the active centre cause $5d$ states of opposite parity to be mixed into the $4f$ configuration. The strength of this mixing can be calculated using Judd-Ofelt analysis, as described in section 6.6.1.

2.2.4.3 Transition rates

The spontaneous emission rate between electronic states a and b is [3]:

$$A_{ED}(\nu) = \frac{1}{4\pi\epsilon_0}\frac{64\pi^4\nu^3 n}{3hc^3}\chi_{ED}\frac{1}{g_a}S_{ED}(ab) \tag{2.9}$$

In the absence of other processes, the rate of decay of the upper state population is proportional to the population of that level:

$$\frac{dN_2}{dt} = -A_{ED}N_2 \tag{2.10}$$

where N_2 is the population of ions in the upper level. This leads to the emission having a spontaneous lifetime of $\tau_{sp} = 1/A_{ED}$. Rearranging equation 2.10 to obtain N_2 as a function of t gives:

$$N_2 = N_{2(0)}e^{-A_{ED}t} \tag{2.11}$$

where $N_{2(0)}$ is the initial population of level 2. This shows that as the excitation light is removed from an active material, the fluorescence intensity will decrease exponentially. In fact fluorescence decay is often non-exponential and the deviation from exponential behaviour can give information about processes occurring in the solid.

2.2.5 Nonradiative decay

2.2.5.1 Multiphonon decay

In rare earth-doped solids where $S \simeq 0$, nonradiative relaxation cannot occur by level-crossing, but can occur by multiphonon emission. Where the energy gap between the excited and lower electronic states is larger than the energy of single phonons supported by the host, multiphonon decay occurs through the simultaneous emission of a number of phonons into the solid host.

The multiphonon decay rate W_{nr} is [5]:

$$W_{nr} = C[(n(T) + 1) \cdot \gamma]^p, \tag{2.12}$$

where $n(T)$ is the Bose-Einstein occupation number, p is the number of phonons required to bridge the energy gap ($p = \Delta E/\hbar\omega$), γ is the electron-phonon coupling constant and C is a constant of the host. An important feature of this relationship is that the multiphonon decay rate depends exponentially on the number of phonons. This means that multiphonon decay rate is determined largely by the highest energy phonons supported by the host. The maximum phonon energy of a material can be determined through Raman spectroscopy. Multiphonon decay is expected to be a significant contribution to the total decay rate when five phonons or fewer can span the energy gap between levels.

2.2.5.2 Interionic interactions

When a solid is doped with a sufficiently high concentration of active ions, the interionic distance will be decreased so that the effect of interionic

interactions will be observed. The three basic types of energy transfer between ions are shown in Fig. 2.6.

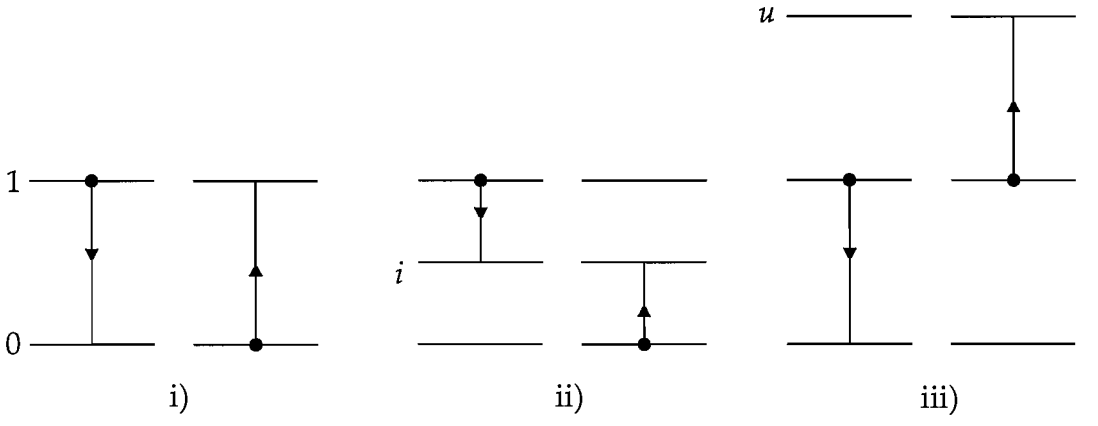

Figure 2.6: Energy transfer mechanisms: i) energy migration ii) cross relaxation iii) upconversion.

Energy migration as shown in Fig. 2.6 i) is the transfer of energy from one excited ion to a nearby ion in the ground state. Though this process does not affect the decay rate of excited states, the energy may migrate to a trap site where the ion relaxes nonradiatively. Another process which reduces the excited state population is cross relaxation, shown in Fig. 2.6 ii). This mechanism involves the partial transfer of the excitation energy to a neighbouring ion in the ground state. The third method of energy transfer is upconversion, shown in Fig. 2.6 iii). Upconversion involves the transfer of energy from one excited ion to another excited ion.

Förster [6] and Dexter [7] first considered multipolar energy transfer between ions. The largest contribution is from electric dipole interactions and the strength of dipole-dipole interactions depends on the inverse sixth power of the interionic distance. Since the interionic distance depends on the inverse third root of the ion concentration, the interaction strength depends on the square of the concentration. Since both energy migration and cross relaxation are concentration dependent and cause a decrease in population of the excited state in a doped solid, these processes contribute to a decrease in fluorescence intensity known as concentration quenching.

Since both energy migration and cross relaxation require an ion in the excited state, they depend on the excitation intensity. Because upconversion requires

two ions in the excited state, upconversion processes depend on the square of the excitation intensity below saturation.

Though energy transfer processes can be useful in certain laser systems, it is often desirable to avoid these effects in the development of new active materials. For this reason, the samples made and studied in this work are doped at concentrations below 1% and fluorescence measurements are made using low excitation intensities.

2.3 Lasers

Over the last forty years, the use of lasers has become increasingly widespread, with lasers having applications in science, communications, materials processing, medical therapies, data storage and environmental sensing. There are several types of lasers and they are generally classified as solid-state, liquid, gas or semiconductor. The operation of solid-state lasers is based on the behaviour of optically active centres.

A laser consists primarily of three components: a gain medium, an energy source and mirrors which form a resonant cavity. The pump energy is used to excite electrons in the gain medium, which relax by emitting photons. The mirrors of the cavity then feed back the radiation into the gain medium, causing stimulated emission of photons with the same energy and momentum. This process causes a buildup of photons in the cavity, which leave to form the laser beam.

In a laser, the probability of stimulated emission from the excited level must exceed that of absorption from the lower level at the laser wavelength. This requires the population of the metastable state to be greater than that of the ground state. In an optically pumped system, this population inversion is most efficiently achieved if there are more than two levels. Figures 2.7 i) and ii) show the 3-level and 4-level pumping schemes commonly used in laser systems. In the 3-level laser scheme, electrons are pumped into a higher-lying energy level, from which they rapidly decay to a lower excited metastable state. Emission of photons from this state feeds back to the system through stimulated emission which causes a buildup of photons of

a particular energy. Laser action occurs when light oscillating in the cavity experiences a net gain for each round trip.

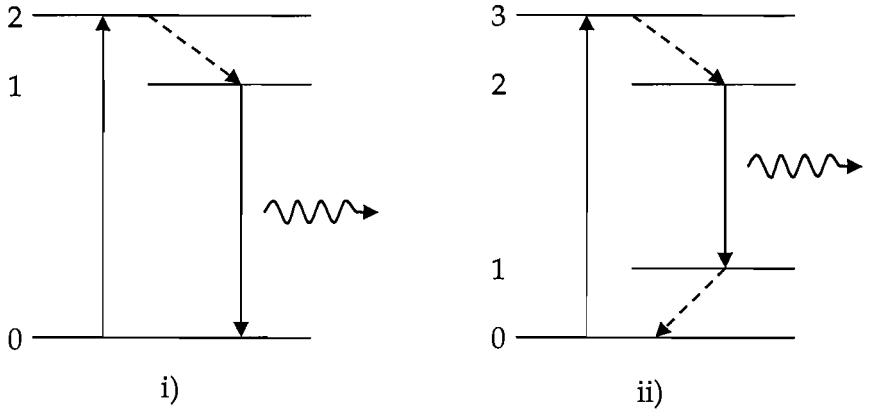

Figure 2.7: Laser pumping schemes i) a 3-level pumping scheme ii) a 4-level pumping scheme, dashed arrows represent fast nonradiative transitions.

In the 4-level scheme, fast nonradiative processes help to depopulate the lower laser level, making it easier to achieve population inversion. This can result in laser operation at lower threshold pump powers. The threshold of a laser is inversely proportional to the product of upper state lifetime and emission cross section [8]. The efficiency of a laser can be characterised by the increase in output power gained per unit increase in pump power; this is termed the slope efficiency. The slope efficiency of a laser is limited by the quantum defect and the quantum efficiency. The quantum defect is the ratio of laser photon to pump photon energy. Quantum efficiency is defined as the number of emitted photons for each absorbed photon, or QE = τ/τ_{rad} where τ is the total lifetime and τ_{rad} is the radiative lifetime.

2.4 Optical telecommunications

Over the last 20 years, rare earth-doped glass amplifiers have become an integral part of long-haul telecommunications systems. This section contains a brief introduction to optical telecommunications systems, which leads into a discussion of current optical amplifier solutions and how current systems can be improved through the development of novel doped materials.

A typical modern point-to-point optical telecommunications system comprises a laser source, modulation device, transmission fibres, optical amplifiers and a detector.

Light travels from the source to the detector through glass optical fibres. The transmission fibre is typically made of silica by modified chemical vapour deposition (MCVD) [9]. Progress in fibre fabrication techniques over the last 25 years has resulted in the production of silica fibres with a minimum loss of ~0.2 dB/km, close to the theoretical minimum of 0.1 dB/km at 1550 nm.

In order to transmit data over long distances, the optical signal must be amplified periodically to compensate for the intrinsic absorption and scattering losses associated with the fibre. During the 1980s, electrical regenerators were widely used for this purpose. In these devices, the optical signal was detected and converted into an electrical signal. It was then amplified and reshaped before being converted back to an optical signal using a semiconductor laser. Though this system was sufficient for transmission rates up to 10 Gb/s, the electrical regenerator became the bottleneck in higher capacity systems [10]. Also, networks using these amplifiers were limited to a single bitrate, which strongly restricts the scalability of the system. Further expansion of such networks is limited because if different transmission wavelengths were used, a separate device would be required to amplify each wavelength.

The development of the erbium-doped fibre amplifier (EDFA) in the late 1980s opened up new possibilities for high bandwidth optical telecommunications. This all-optical amplifier not only allows many channels to be amplified simultaneously in a single device, but they are also insensitive to bitrate and modulation format. All-optical amplification is now by far the most cost effective method of achieving high capacity long-haul networks.

Detectors in optical telecoms systems usually utilise a low noise pre-amplifier which amplifies the optical signal before it is detected. The most common detector used in optical telecommunications is the InGaAs PIN photodiode.

One of the long term aims of current research in optoelectronics is to develop integrated optical devices. These devices would comprise a number of functions on a single optical chip. The first challenge of this development is

to incorporate switching, attenuating and filtering capabilities onto a planar device. It will then become important to amplify light within the same structure. This poses an interesting problem, when considering that the length of the EDFA is ~10 m. A possible solution to this may be to use sol-gel-produced silica glasses, which are known to host significantly more erbium ions than MCVD-produced silica without clustering effects. This area is the subject of chapter 5 of this thesis.

2.5 Optical amplifiers

In order to meet the increasing demand for bandwidth, the technique of wavelength division multiplexing (WDM) was introduced. This allows a number of data streams, spread across multiple wavelengths, to be transmitted simultaneously along a single fibre. Dense WDM (DWDM) systems use channels separated by less than 1 nm to maximise transmission capacity. WDM has now been widely adopted in long-haul optical telecommunications systems. This technology requires the amplification of multiple signal wavelengths; there are currently three main ways of achieving this.

2.5.1 Existing amplifier technology

2.5.1.1 Rare earth-doped fibre amplifiers

Erbium-doped fibre amplifier

The most commonly used optical amplifier in long-haul telecoms is the EDFA. An EDFA essentially consists of a length of silica fibre with Er^{3+} doped into the core.

The pump light required for amplification in an EDFA is provided by a laser diode and is coupled into the erbium-doped fibre with the signal. The pump beam excites the erbium ions into the metastable state. The signal photons stimulate emission from these excited ions and the resulting emitted photons have the same wavelength as the incoming photons and travel in the same

direction, and so increase the signal strength. This amplification process operates over the range 1530-1560 nm in an EDFA. The gain profile over this region is not uniform, so the gain may be equalised by using a fibre Bragg grating or another type of filter.

The 1550 nm transition relies on the decay from the $^4I_{13/2}$ level to the $^4I_{15/2}$ level as shown in Fig. 2.8 i). The energy gap between these levels is approximately 6500 cm^{-1}, while the maximum phonon energy of silica is around 1100 cm^{-1}. This means that quenching due to multiphonon decay in the EDFA is negligible and this transition is very efficient. It is a remarkable coincidence that this near-infrared emission from erbium coincides with the low loss wavelength region of silica fibre (C-band). Because silica is a high phonon energy glass, the EDFA is the only silica-based rare earth-doped amplifier developed to operate in the 1200-1700 nm region.

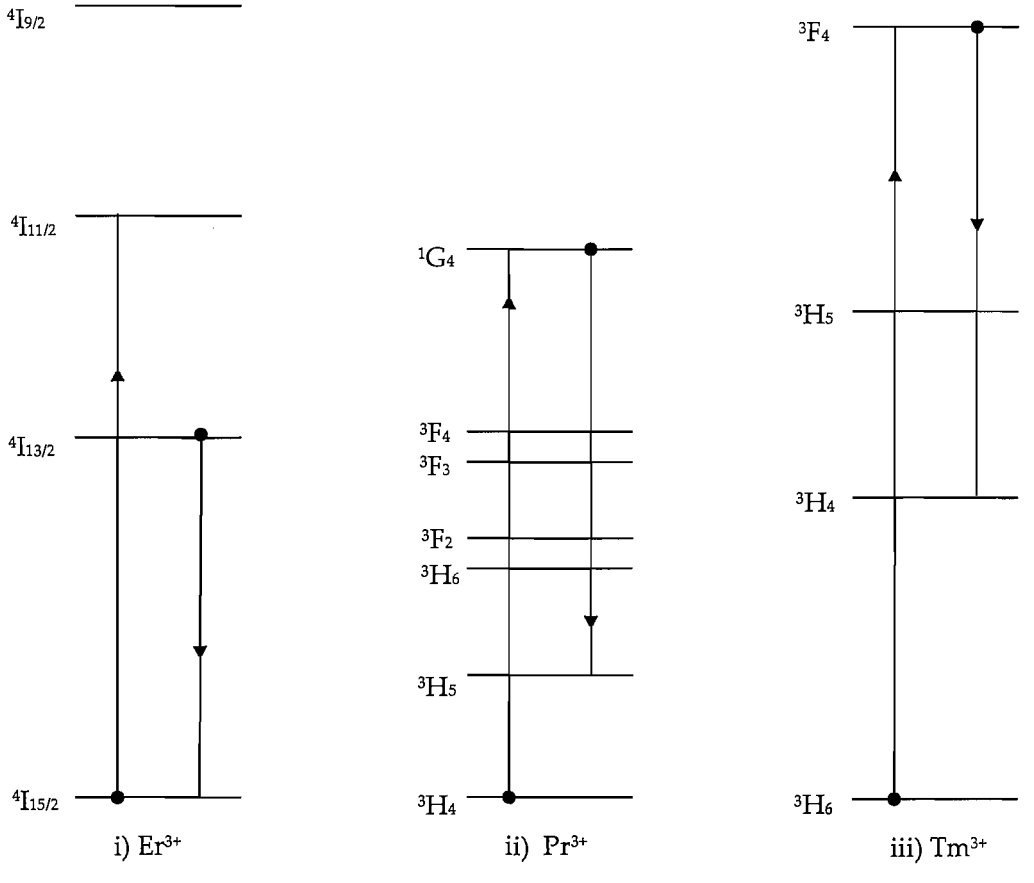

Figure 2.8: Partial energy level diagrams for i) Er^{3+} ii) Pr^{3+} iii) Tm^{3+} [4]

The EDFA can be pumped either resonantly at 1480 nm from $^4I_{15/2}$ to $^4I_{13/2}$ or indirectly at 980 nm from $^4I_{15/2}$ to $^4I_{11/2}$ which relies on multiphonon relaxation to $^4I_{13/2}$ to populate the metastable state. The performance of these amplifiers has been maximised by incorporating several stages into a single device. These multistage EDFAs typically comprise a low noise pre-amplifier and a high gain booster amplifier. The first stage uses a 980 nm AlGaInAs diode pump, which provides a better signal to noise ratio. The second stage uses a 1480 nm InGaAsP diode pump for more efficient pumping and a more uniform gain.

Because silica glass is used as the host in EDFAs, they can be connected to standard telecoms transmission fibre by fusion splicing. Erbium-doped fibres can be made by MCVD using solution doping to incorporate the erbium ions. Silica has a limited solubility of erbium ions, and by adding small amounts of alumina, the erbium solubility is improved [11]. However, the performance of erbium-doped fibres is limited by energy transfer effects at a concentration of around 1% atomic. This requires that fibre lengths of ~10 m are used in EDFAs.

Praseodymium-doped fibre amplifier

The praseodymium doped fibre amplifier (PDFA) operates on the same principle as the EDFA. It relies on emission from $^1G_4$ to $^3H_5$ levels of trivalent praseodymium shown in Fig. 2.8 ii), which is centred at 1310 nm and covers the wavelength range 1290-1315 nm [12]. The PDFA can be pumped by an InGaAs diode laser at 1017 nm (<50 mW output) from the $^3H_4$ level to the $^1G_4$ level [13].

Because there is a relatively small energy gap between the $^3F_4$ and $^1G_4$ levels, silica is not an appropriate host for the PDFA and a low phonon energy host such as ZrF_4-BaF_2-LaF_3-AlF_3-NaF (ZBLAN) is required to reduce multiphonon decay and therefore increase the quantum efficiency of this transition. The quantum efficiency of praseodymium-doped ZBLAN is ~4% [14].

The fact that the PDFA is based on a glass with much lower melting temperature than silica means that it cannot be fusion spliced to existing fibre networks. The fibres are glued instead, resulting in a much higher coupling loss than for a fusion splice (0.3 dB compared to 0.1 dB). Further

signal loss results from the large refractive index difference between the transmission fibre and amplifier, which causes increased back-reflection.

It is notable that PDFAs did achieve commercial production despite their low quantum efficiency, though they have not achieved widespread use in optical telecommunications.

Thulium-doped fibre amplifier

Fluoride-based thulium-doped fibre amplifiers (TDFA) have also been produced commercially in the last few years, though like the PDFA they have not been widely adopted. TDFAs, which operate at telecoms wavelengths, also require a low phonon energy host to reduce multiphonon decay and increase efficiency. The transition involved is shown in Fig. 2.8 iii) and is from the $^3F_4$ level to the $^3H_4$ level. This system has the added complication that the lower level lifetime is longer than that of the upper level. There are several pumping schemes which can be used to achieve gain in a TDFA and these are described in chapter 6. Current TDFAs exhibit gain from 1460-1490 nm.

2.5.1.2 Raman amplification

Although Raman amplification in silica fibres was first demonstrated in the early 1970s, the unavailability of cheap high power diode pump sources precluded the possibility for commercial devices until the late 1990s. Raman amplifiers are now widely deployed in long-haul and ultra long-haul optical telecommunications networks [15].

Raman amplification uses the intrinsic properties of silica to achieve amplification. The process which produces the amplification is stimulated Raman scattering, shown in Fig. 2.9, and requires high pump intensities. The incoming pump photon releases some energy by the emission of one or more phonons in the solid, resulting in a scattered photon with a higher wavelength that that of the pump. The peak of Raman scattering in silica is shifted by about 450 cm^{-1} from the pump beam, this corresponds to a shift of about 100 nm at 1500 nm.

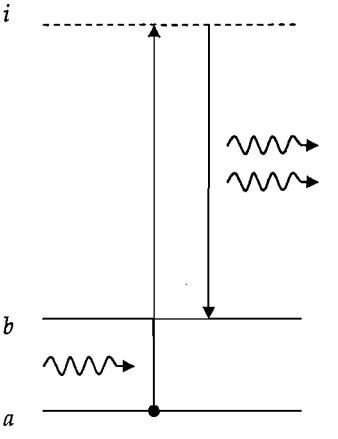

Figure 2.9: Stimulated Raman scattering from energy level *a* to *b* through the virtual state *i*.

Raman amplifiers require high power pump sources, typically 0.5 W continuous wave (CW) diode lasers are used. Because the Raman gain coefficient of silica fibre is small, many kilometers are required to produce a significant signal gain. In these systems the amplification occurs throughout the transmission fibre, and so Raman amplifiers are described as distributed amplifiers, whereas the EDFA and PDFA are termed lumped amplifiers. The high pump power required for Raman amplification can cause unwanted non-linear effects, including four-wave mixing (FWM) which decreases the signal strength [16].

In order for a Raman amplifier to operate over a large spectral range, several pump wavelengths are needed to maintain a broad flat gain [17]. The fact that these pump sources may degrade at different rates could cause problems with the durability of the device.

The very short virtual upper level lifetimes make Raman amplifiers susceptible to pump noise and crosstalk by cross gain saturation. This noise can be reduced by adopting a counter pumping scheme with a long interaction length [18]. At high pump powers, a significant amount of light will be Rayleigh scattered and then scattered again. This double Rayleigh scattered light is then amplified and can constitute a major source of noise in the system [19].

2.5.1.3 Semiconductor optical amplifier

The structure of a semiconductor optical amplifier (SOA) is essentially the same as that of a semiconductor laser. The light is guided in a planar sandwich-type waveguide, where the central layer is of higher refractive index than those either side. The major difference between SOAs and semiconductor lasers is that the facets of an SOA are designed to have low reflectivity.

Each device will operate over a bandwidth of about 40 nm, but by controlling the materials used in the amplifier, devices can be made which operate over different wavelength ranges throughout the telecoms windows [20].

SOAs also suffer from FWM, which can be reduced by splitting the input signal to several amplifiers and recombining it, however this lowers the signal to noise ratio. Also, crosstalk is excessive even at widest standard telecoms wavelength spacing (1.6 nm) because of the short excited state lifetime of the electrons. Pulse distortion and gain fluctuations with signal power result from the short excited state lifetime in SOAs and cause problems particularly when adding and removing WDM channels. The required pigtail coupling losses into waveguide are around 3 dB per facet.

Because, unlike rare earth-doped fibre amplifiers, SOAs are polarisation dependent, they may be most suitable for power and pre-amplifiers. However, one way to compensate for this is to pass the light through a polarising beam-splitter and amplify each beam with orthogonal amplifiers.

SOAs are most promising for use in metro systems in coarse WDM (CWDM), which is a possible solution for transmitting data over shorter distances which uses large wavelength spacings of around 20 nm. These systems are expected to require a SOA for each 4 channels in a 16 channel system [21].

2.5.2 Future amplifier technology

Advances in fabrication techniques continued throughout the 1990s resulting in silica fibres with a minimum loss of less than 0.2 dB/km. In 1998, Lucent Technologies introduced the AllWave fibre which contains less than one part per billion hydroxyl ions. Figure 2.10 shows the reduction

in absorption caused by the removal of hydroxyl in silica fibre. The introduction of this new fibre brings possibilities of increased bandwidth transmission by utilising the E and S-bands (which are shown in Fig. 2.10.

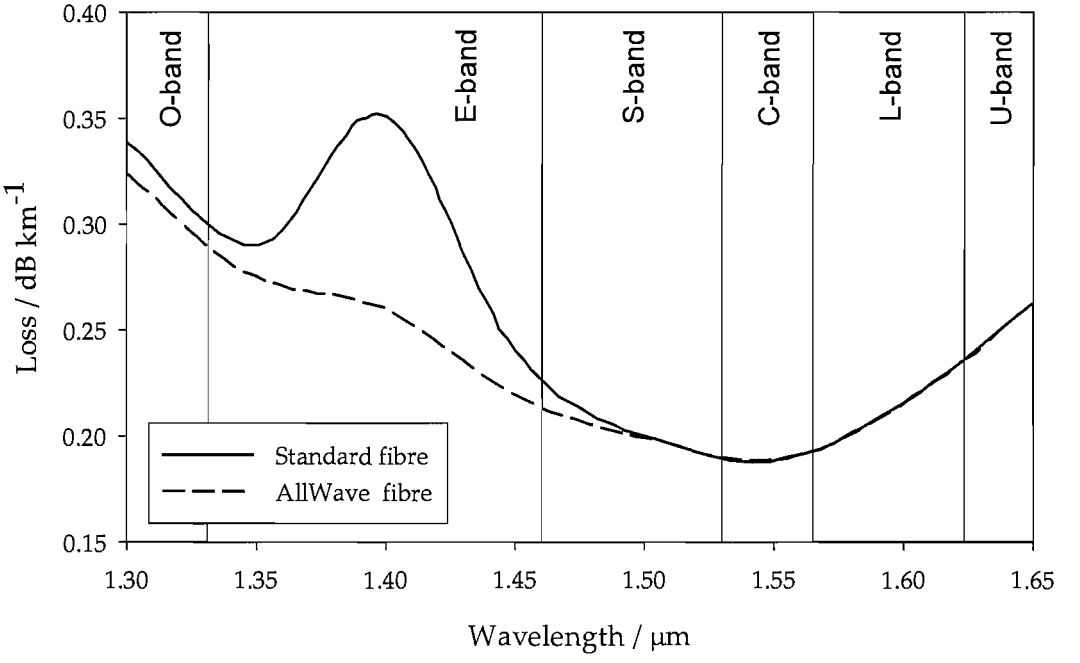

Figure 2.10: Loss of silica fibres over the standard telecoms bands, showing the effect of reduced hydroxyl content in AllWave fibres [15].

The intrinsic transmission loss of silica fibre arises from the infrared absorption tail and losses from Rayleigh, Raman and Brillouin scattering. Raman and Brillouin scattering are both nonlinear processes and so cause problems only at high light intensities. Rayleigh scattering represents the largest loss in silica and shows a dependence on λ^{-4}, this leads to the decrease in loss from shorter wavelengths to 1550 nm. Multiphonon absorption limits transmission beyond this wavelength. There are several candidates for fibres with increased infrared transmission, which have much lower theoretical minimum losses than silica. Chalcogenide glasses such as Ga:La:S and fluoride and tellurite glasses (oxide glass with TeO_2 as the major component) are all low phonon energy glasses, which not only have excellent infrared transmission, but also benefit from useful spectroscopic properties as glass hosts. However, problems associated with making high quality fibres from these glasses have limited their usefulness so far.

In order to utilise the potential bandwidth over all the telecoms bands in long-haul telecommunications, amplifiers are required for these wavelengths. Figure 1.1 shows an overview of the wavelengths over which various amplifiers operate. Though none of the other rare earth-doped amplifiers rivals the efficiency of the EDFA, there are some interesting alternatives to Raman and SOAs outside of the C and L-bands.

2.5.2.1 Attributes of a new amplifier system

There are many requirements to be fulfilled for a new optical amplifier:

- The gain bandwidth of an amplifier should be large so that many WDM channels can be amplified. Materials exhibiting strong homogeneous and inhomogeneous broadening are suitable to fulfil this requirement.
- The gain profile should be as flat as possible. This reduces the requirement for gain equalisation and will increase the overall efficiency of the device. Again this will be satisfied by materials with strong broadening.
- The amplifier should not introduce excessive noise to the system. Amplified spontaneous emission (ASE) introduces noise into rare earth amplifiers.
- Amplifiers should exhibit minimal interchannel crosstalk. The long lifetimes of the excited states in rare earth-doped materials mean that crosstalk in these materials is minimal [22].
- A low loss method of splicing the amplifier to telecoms fibre is required. Silica fibres are usually fusion-spliced which is fast and cheap and results in a strong, low loss connection. Materials with different melting points or thermal expansion coefficients may not be suitable for fusion splicing with silica fibre.
- For an optically pumped amplifier, inexpensive high power pump sources should be commercially viable for the required wavelength. Materials with broad absorption bands may allow more flexibility in the pump source.

- Fabrication techniques should be reliable and reproducible. This includes maintaining consistent glass composition in a fibre and achieving a reproducible splicing technique.
- The amplifier should have sufficient mechanical strength and chemical stability. Fibre amplifiers can be protected from physical and chemical damage by applying suitable coatings, though this is likely to increase the production costs.

The importance of each of these attributes will be weighted according to the type of optical amplifier required. For example the requirement for low noise is more important in pre-amplifiers and in-line amplifiers than for power amplifiers. Mechanical strength and chemical stability may be more important for submarine in-line amplifiers where accessibility is difficult and expensive. High output power is important for both power and in-line amplifiers, but not for pre-amplifiers.

2.5.2.2 Future rare earth amplifiers

Erbium-doped fibre amplifier

Fluoride-based EDFAs have been demonstrated to show flatter gain characteristics than standard aluminosilicate-based EDFAs. The gain bandwidth may also be extended on the long wavelength side by optimisation of the pump wavelength [23]. Fluorozirconate glass has a greater solubility of erbium ions than silica, and emission at 1550 nm has been observed from ZBLAN containing 18% erbium [24]. However, fluoride glasses are fragile and environmentally unstable, showing sensitivity to humidity and temperature. The large difference in melting points between fluorides and silica means that these fibres cannot be fusion spliced to standard telecoms fibre.

More recently, erbium-doped tellurite fibres were studied for their emission at 1550 nm. These fibres show increased rare earth solubility, and a broad, flat gain of 70 nm from 1535-1605 nm [25]. The origin of this increased emission bandwidth has been attributed to both the range and flexibility of dopant sites in the tellurite structure [26]. Tellurite glasses are more stable and resistant to corrosion than fluoride glasses.

Neodymium-doped fibre amplifier

Neodymium-doped silica is well known as an active medium for fibre lasers at 1060 nm. Unfortunately, the 1320 nm emission fromlevels $^4F_{3/2} \rightarrow ^4I_{13/2}$ (shown in Fig. 2.11 i)) is limited by the broad ESA band from the metastable level to $^4G_{9/2}$ and $^4G_{7/2}$ [27]. This means that the 1320 nm emission in neodymium-doped silica cannot be exploited for use in optical telecoms [28]. An investigation into neodymium-doped tellurite glasses also concluded that ESA eliminates gain for this transition [29]. However, gain from 1320-1350 nm has been demonstrated in neodymium-doped fluoride glasses [30], though strong emission from the metastable state at 1060 nm severely limits the quantum efficiency of the amplification transition.

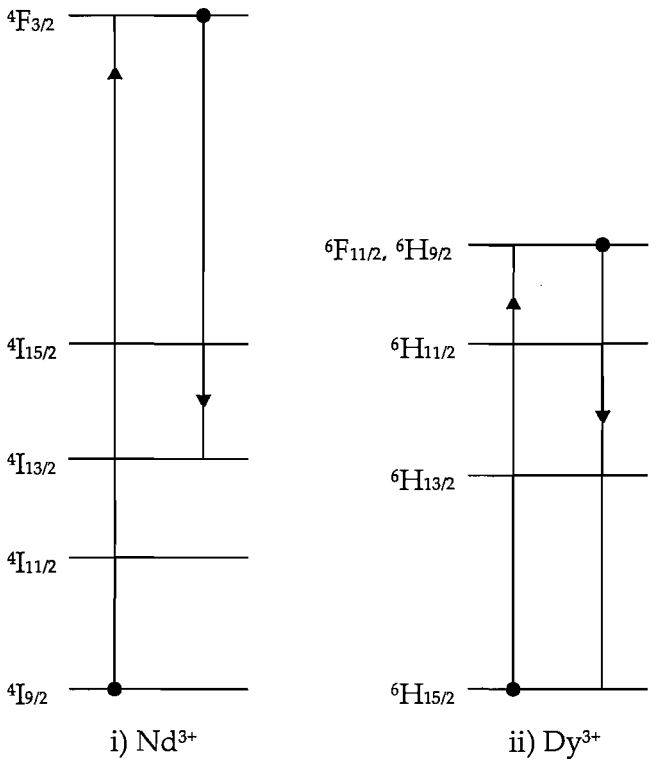

Figure 2.11: Partial energy level diagrams for i) Nd^{3+} ii) Dy^{3+} [4].

Dysprosium-doped fibre amplifier

Several spectroscopic studies of dysprosium-doped chalcogenide glasses have been carried out [31–36]. The near infrared emission from dysprosium relies on the transition shown in Fig. 2.11 ii) from $^6F_{11/2}$,$^6H_{9/2}$ $\rightarrow$$^6H_{15/2}$ and is centred at 1350 nm. Though these glasses have low phonon energies, and have reasonable thermal characteristics for fibre drawing, they also have a high refractive index. This can be a disadvantage in optical devices due to the increased back-reflection at the interface with silica fibres. The main advantage of a dysprosium-based amplifier over a PDFA is the small interaction length required. Dysprosium amplifiers have the potential to be made from just 1 m of fibre.

Thulium-doped fibre amplifier

Thulium is a promising dopant ion for new optical amplifiers in the S-band. There have been many studies of fluoride-based TDFAs which have been reported to exhibit gain from 1450-1490 nm [25, 37–41]. More recently multicomponent silicate fibres doped with thulium have produced gain from

1460-1520 nm [42]. Thulium-doped amplifiers require a low phonon host, because the 1460 nm emission is quenched by multiphonon emission in silica glass. However, it is less sensitive than dysprosium and praseodymium to multiphonon decay. Thulium-doped tellurite glasses have also recently been considered for amplification for telecoms applications [43–45]. It was observed that the emission at 1460 nm broadened by around 30 nm to a FWHM of 105 nm in these glasses. However, the efficiency of these materials is compromised by the presence of hydroxyl impurities, which has an overtone absorption at around 1.4 μm.

The upper level, $^3F_4$, can be pumped by reliable, low-cost AlGaAs laser diodes at around 800 nm. The 1470 nm transition is self-terminating and requires the $^3H_4$ level to be depopulated. This can be done by co-doping with another rare earth ion which has an absorption band coinciding with the lower level (e.g. holmium) to deplete the lower level through energy transfer processes followed by multiphonon decay of the acceptor ion [44]. Another method of achieving population inversion is by simultaneously pumping ions in the $^3H_4$ level to the $^3F_{2,3}$ levels with a 1064 nm source, multiphonon decay from these levels then serves to populate the $^3F_4$ level [46].

However, as with the other non-silica-based amplifier systems, there is a loss associated with the interface between the amplifier fibre and the transmission fibre which introduces extra noise into the system.

An interesting possible solution for broadband amplification was investigated in a parallel amplifier. Here a fluoride-based TDFA was combined in parallel with a tellurite-based EDFA to provide a flat amplification bandwidth of 113 nm [25], although there is a gap of 48 nm between the gain bands.

2.5.2.3 Transition metal doped fibre amplifier

Though transition metal ions are well known for their use as active ions in laser crystals, no transition metal glass laser has been demonstrated to date. The tetravalent form of the chromium ion is particularly interesting for telecoms applications. The emission bandwidth is extremely broad and covers much of the telecoms window. Cr^{4+}-based lasers have been

demonstrated in a number of crystal hosts [47–49]. The optical properties and potential of Cr^{4+} as the active ion in an amplifier are discussed further in the introduction of chapter 4.

2.5.2.4 Glass-ceramics for optical amplifiers

Transparent glass-ceramics are an interesting type of material which has been identified to provide possible new hosts for optical amplifiers and lasers [50–53]. These are glasses which contain nanocrystals with dimensions of the order of 10 nm. These materials have the potential to combine the advantages of a low phonon energy environment for the active ion with the material properties of a glass.

One recently discovered method of obtaining a silica-based glass-ceramic is by processing through the sol-gel route. A review of this technology is given at the start of chapter 5.

2.6 Summary

While demand for bandwidth continues to increase, there is an increasing need for better broadband amplifiers. The EDFA technology is now relatively mature, and it is unlikely that its gain bandwidth will be significantly increased further. While other devices utilising low-phonon glasses can provide gain outside the C-band, challenges remain in solving the mechanical and stability problems associated with these fibres. Raman amplification can also provide gain over a very wide wavelength range, but is an expensive and complicated solution. The work described in this thesis will explore some of the alternative solutions outlined in this chapter, and will assess their potential by comparison with current technologies.

Chapter 3

Spectroscopic techniques

This chapter gives details of the experimental techniques employed throughout this work. While ultraviolet, visible and infrared absorption spectra and Raman spectra can be measured using commercially manufactured equipment, emission and lifetime properties are better obtained through manually constructed setups.

3.1 Optical absorption spectroscopy

Absorption spectra for the chalcogenide samples studied in chapter 4 were measured using a Perkin-Elmer Lambda-9 spectrophotometer. This instrument uses a split beam system, which measures the difference between the beam passing through the sample, and an unobstructed beam. An accuracy of ±0.2 nm can be achieved in the UV and visible ranges, and ±0.8 nm in the near infrared. The Lambda-9 operates over the range 185-3200 nm (3,100-54,000 cm^{-1}). The spectrophotometer is controlled by computer, which also records the spectral data.

A Varian Cary 500 spectrophotometer was used to take the absorption spectra for the samples in chapters 5 and 6. This instrument operates over the range 175-3300 nm with a resolution of ±0.1 nm and ±0.4 nm in the UV-vis and infrared regions respectively.

Data is obtained from the spectrophotometer in units of absorbance A:

$$A = \log \frac{I_0}{I}, \tag{3.1}$$

where I_0 is the incident intensity and I is the transmitted intensity. In order to compare absorption intensities of samples of different thickness, results in this thesis are presented in the unit of absorption coefficient α:

$$\alpha = \frac{A}{d} \ln 10, \tag{3.2}$$

where d is the sample thickness. Absorption measurements are used in this thesis to help determine the valence state of transition metal ions doped into glass. Integrated absorption measurements are used to determine transition strengths in rare earth ion doped glasses for Judd-Ofelt analysis. For this analysis absorption in expressed in terms of the absorption cross section σ:

$$\sigma = \frac{\alpha}{N}, \tag{3.3}$$

where N is the number of absorbing species.

3.1.1 Fourier transform infrared spectroscopy

While UV-vis spectroscopy covers the spectral range of electronic transitions of dopant ions, Fourier transform infrared spectroscopy FTIR spectra cover the region of molecular vibrations. Relative concentrations of hydroxyl can be determined from FTIR spectra, since the fundamental O-H stretching band lies at around 3500 cm^{-1} (2900 nm).

FTIR spectra were measured using a Perkin-Elmer 2000 FTIR spectrometer. An FTIR spectrometer consists primarily of an interferometer and an infrared detector, as shown in Fig. 3.1. To obtain a spectrum the translating mirror is moved at a constant speed so that its position is known at all times. Intensity is measured by the infrared detector through the range of positions of the translating mirror. A background scan must be taken before the data is taken for the sample, this background will depend on the characteristics of the instrument and the amount of water and carbon dioxide in the air. This data is an interferogram and for the initial background scan contains

information about all the frequencies emitted by the source. A computer is used to perform a Fourier transform on the data, which results in a plot of frequency against intensity.

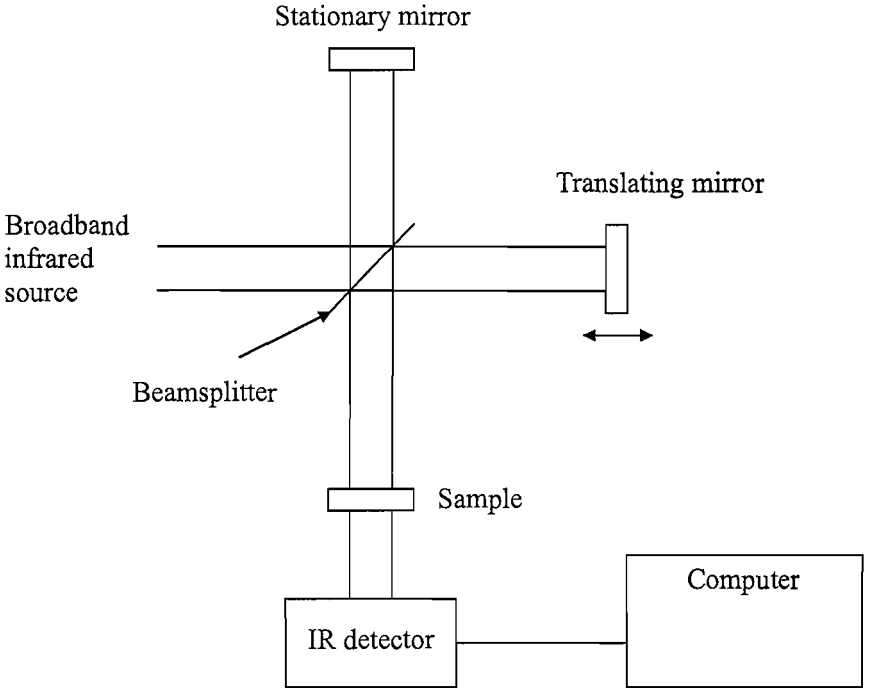

Figure 3.1: Schematic representation of an FTIR spectrometer.

3.2 Raman spectroscopy

Raman spectroscopy is a useful tool for identifying crystals in materials. For active optical materials, Raman spectra can be used to determine the maximum phonon energy.

Raman spectra were measured using a Renishaw Ramascope with a 10 mW 633 nm HeNe laser and a 50× objective lens. Figure 3.2 shows the setup, which incorporates a notch filter which reflects the incoming laser beam into the microscope, and filters out the 633 nm light as the scattered light passes through to the CCD. The beam is focused down onto the sample, and the 180° back-scattered light is collected by the objective lens, and passes through the notch filter to be dispersed by a grating onto the CCD. The grating rotates allowing the measurement of a range of wavelengths, at a resolution of 4 cm^{-1}.

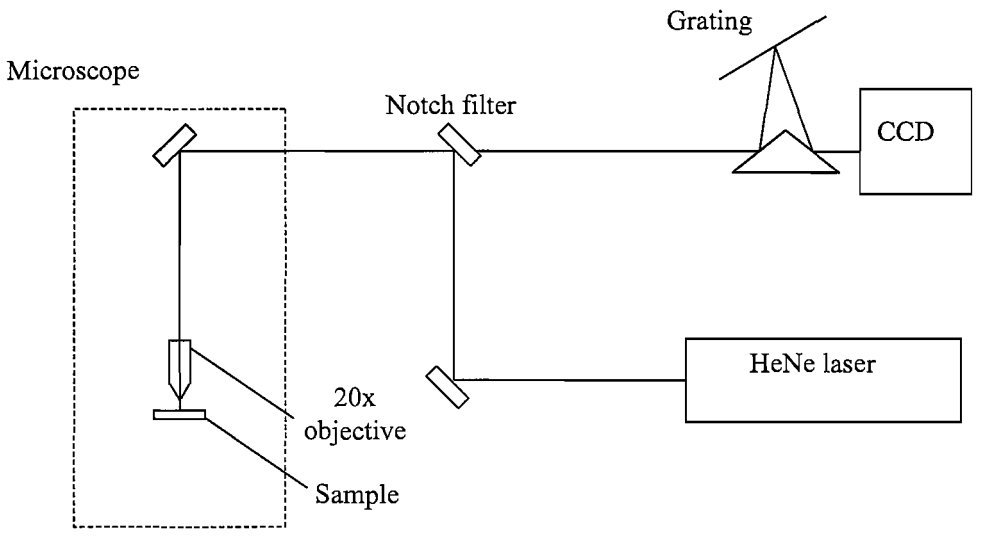

Figure 3.2: Schematic representation of Raman measurement setup.

While vibrational modes in crystals lead to sharp peaks in Raman spectra, the lack of long range order in glasses leads to broadened Raman peaks. This leads to a problem in the definition of the maximum phonon energy. Since it is the highest energy phonons which contribute most to multiphonon decay in rare earth-doped materials, it would seem appropriate to define the maximum phonon energy as the point at which the Raman has decreased to $1/e$ of its maximum intensity. However, reports in literature usually consider the maximum phonon energy to be the peak value of the Raman shift, so this is the convention used here.

3.3 Fluorescence spectroscopy

Fluorescence spectra can be used to give information on the dopant ion's site in the host material. Disorder in the host causes inhomogeneous broadening which produces broad peaks in fluorescence spectra. The position of peaks in fluorescence spectra provides information on the valence states of dopant ions, particularly in the case of transition metals. The full width at half maximum (FWHM) of fluorescence peaks also gives an indication of the possible wavelength range that the material may be useful for in a device.

In order to measure fluorescence spectra from doped materials, the material is excited with a pump laser, the fluorescence is then collected and dispersed

so that the intensity at difference wavelengths can be measured. A Spectra-Physics 2040E argon-ion laser was used to pump a Spectra-Physics 3900S Ti:sapphire laser, as shown in Fig. 3.3. The maximum power output of the argon ion laser is 20 W, and the Ti:sapphire laser has a tuning range of 675-1100 nm. For later experiments on thulium-doped samples, the pump source was replaced by a Milon laser diode which was tunable from 800-813 nm. An Acton SpectraPro 300i monochromator was placed in front of a New Focus 2034 InGaAs photodiode (sensitive from 800-2200 nm). The beam from the Ti:sapphire was raised to the height of the monochromator's entrance and chopped using a Stanford SR540 optical chopper. The triangular configuration of mirrors was required because the beam needed to be raised by just a few millimetres. The beam was then focused into the sample, and the fluorescence was collimated and focused into the monochromator through a filter. The filter was required to attenuate any scattered excitation light which may enter the monochromator. The InGaAs detector was aligned to the exit of the monochromator and was connected to a Stanford SR530 lock-in amplifier with the reference signal from the chopper. The monochromator was controlled by a computer, and the data from the lock-in amplifier was recorded as the monochromator scanned over the required wavelength range.

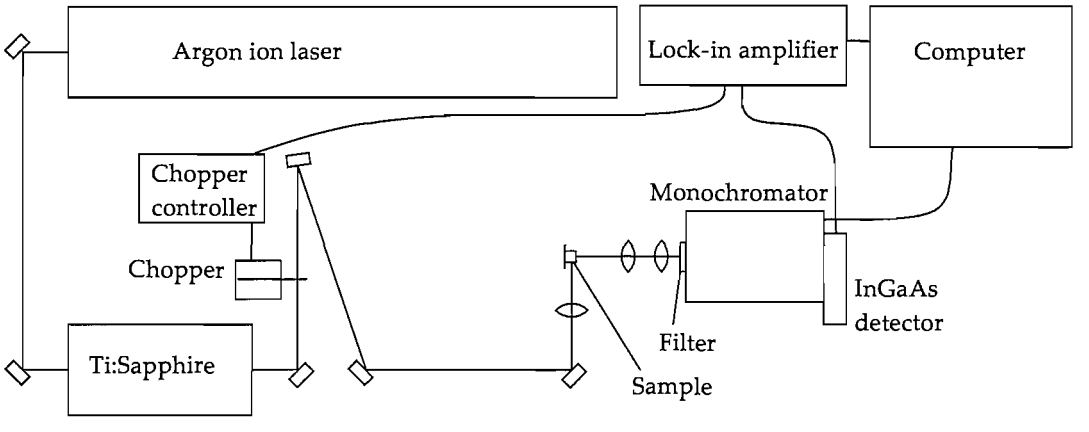

Figure 3.3: Experimental configuration used to obtain fluorescence spectra.

The chopper speed was set according to the approximate fluorescence lifetime of the sample being studied. At very low frequencies $1/f$ noise is increased, and the time taken to obtain spectra becomes prohibitively long.

At higher frequencies, the emission intensity varies little during chopping so a weaker signal is detected.

The laser was focused onto the edge of the sample being studied. This is important, particularly for transition metal-doped samples, to prevent distortion of the fluorescence spectrum caused by reabsorption. An example of the effect of reabsorption of a chromium-doped glass is shown in Fig. 4.5.

In order to correct measured data for the uneven spectral response of the system, a spectrum was taken of a 50 W halogen lamp. Assuming that the halogen lamp acts as a blackbody at 3100 K, the intensity of corrected spectrum is given by:

$$I(\lambda) = \frac{I_{raw}(\lambda)}{I_{halogen}(\lambda)/I_{blackbody}(\lambda)} \tag{3.4}$$

3.3.1 Low temperature fluorescence spectroscopy

Low temperature fluorescence spectra are particularly useful for determining inhomogeneous linewidths for transition metal-doped materials. Changes in fluorescence intensity at low temperature can also give an indication of the significance of nonradiative decay at room temperature.

A similar arrangement to that in Fig. 3.3 was used for low temperature spectroscopy. The sample was placed in a bath cryostat, which consists of a central reservoir surrounded by liquid nitrogen insulating reservoirs, as shown in Fig. 3.4. For emission measurements at 4 K the central reservoir was filled with liquid helium, for measurements at 77 K liquid nitrogen was used instead. The sample was immersed in the liquid, and the beam passed through glass windows in the cryostat. Fluorescence was collected perpendicular to the beam through another window in the cryostat.

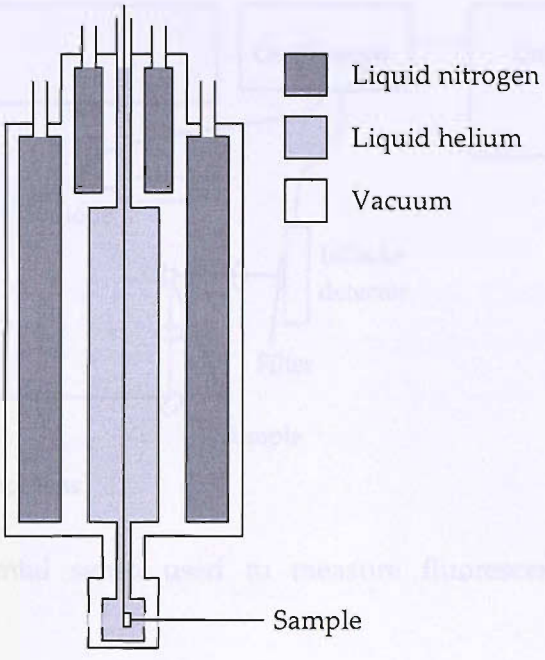

Figure 3.4: Cross section of the liquid helium cryostat. The sample is excited and fluorescence is collected through windows in the base of the cryostat.

3.4 Time-resolved fluorescence spectroscopy

Fluorescence lifetime data can be used to give information about the site of dopant ions in materials. It can also be used to help calculate quantum efficiencies in rare earth-doped materials. Fluorescence lifetime data can also be used to study energy transfer in heavily doped materials.

The setup used to obtain lifetime measurements is shown in Fig. 3.5. The fluorescence was focused onto the InGaAs detector through a filter, which was necessary to cut out the scattered excitation light. A silicon diode (which is sensitive between 350-1100 nm) was positioned to collect excitation light, and was used as the trigger signal for a Tektronix 2232 100 MHz digital storage oscilloscope. The data collected by the oscilloscope was stored by a computer, where many data sets were recorded and averaged.

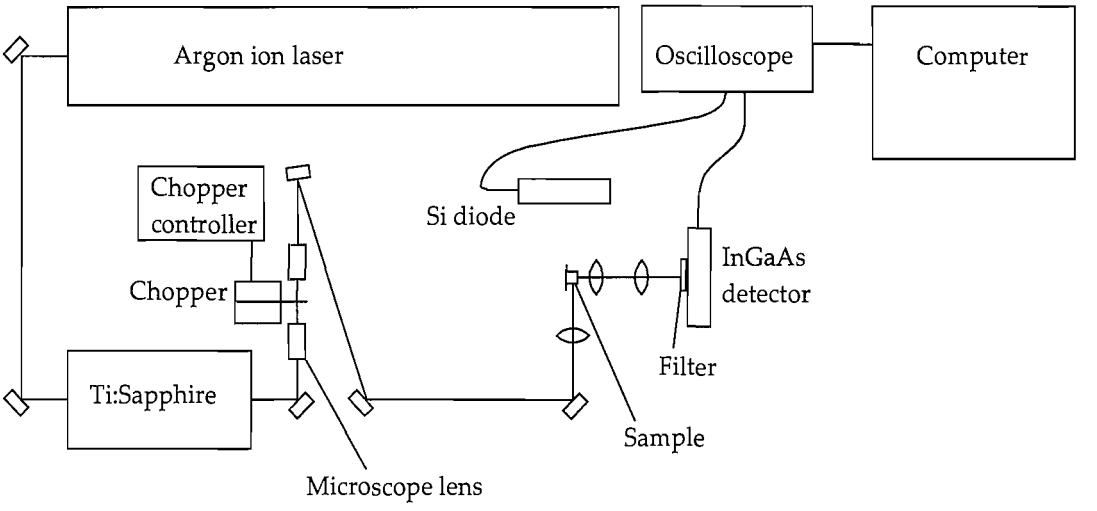

Figure 3.5: Experimental setup used to measure fluorescence lifetimes.

The time response of the system was measured by observing the light scattered from an alumina ceramic tile. In order to increase the time resolution of the system, 10× microscope objective lenses were used to focus the beam onto the chopper blade. For measurements requiring a faster response, the chopper was replaced by an acousto-optic modulator which has a fall-time of 180 ns/mm.

In order to detect fluorescence at visible wavelengths, the InGaAs photodiode was replaced with a Hamamatsu R3236 S1 photocathode photomultiplier tube attached to a monochromator. The monochromator was set to pass fluorescence of the required wavelength. The signal from the photomultiplier was amplified by a Stanford SR445 DC-300 MHz amplifier. A Stanford SR430 Multi-Channel Scaler was then used to collect the data. The resolution of this system is determined by the bin-width defined by the user.

There are a number of reasons that the measured lifetime data deviates from single exponential behaviour. In glasses, the site-to-site variation which causes inhomogeneous broadening of spectral lines also leads to a range of lifetimes in the material. In cases where ions are hosted in two distinctly different types of site, a double exponential decay may be observed. A useful way of describing non-exponential decay is by fitting data to a stretched

exponential:

$$I(t) = I(t_o)e^{-(t/\tau)^p}, \tag{3.5}$$

where $I(t)$ is the fluorescence intensity at time t, t_0 is the time at the start of the decay and p is the stretch factor ($p \leq 1$). The stretch factor is a measure of the deviation from exponential behaviour of the fluorescence decay. The lifetime is given by τ which is the time taken for the emission intensity to decrease to $1/e$ of its initial value. The stretched exponential function was fitted to decay data using Systat Sigmaplot which perfoms least squares fitting using the Levenberg-Marquardt algorithm.

3.5 Fluorescence excitation spectroscopy

Fluorescence excitation spectra can provide useful information about the position of energy levels in transition metal-doped materials. The technique involves scanning the excitation through a range of wavelengths, while monitoring fluorescence intensity at a constant wavelength. Fluorescence excitation spectra only reveals absorption bands which contribute to fluorescence at the observed wavelength.

The experimental setup for this technique is shown in Fig. 3.6. A halogen lamp was used as the excitation source and the light was dispersed using a monochromator. A filter was placed in front of the InGaAs detector to prevent scattered excitation light from being detected. The system was calibrated by measuring the intensity of light passed through the monochromator at different wavelengths with a calibrated Newport optical power meter.

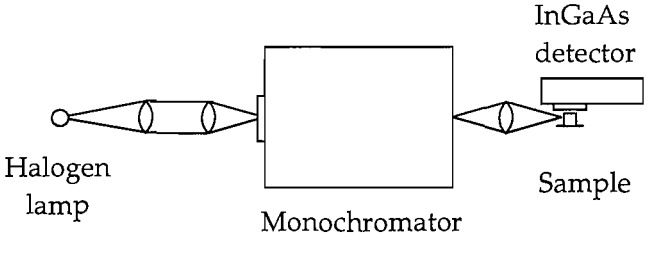

Figure 3.6: Experimental setup used for measuring fluorescence excitation spectra.

In order to test the setup, absorption and fluorescence excitation spectra were measured for a chromium-doped $Y_3Al_5O_{12}$ (YAG) crystal. The results are shown in Fig. 3.7 and show a good correlation between absorption and excitation spectra. The two large peaks at ~650 nm and ~1000 nm are observed in both spectra, as well as smaller features near at the peak at 650 nm and 1100 nm.

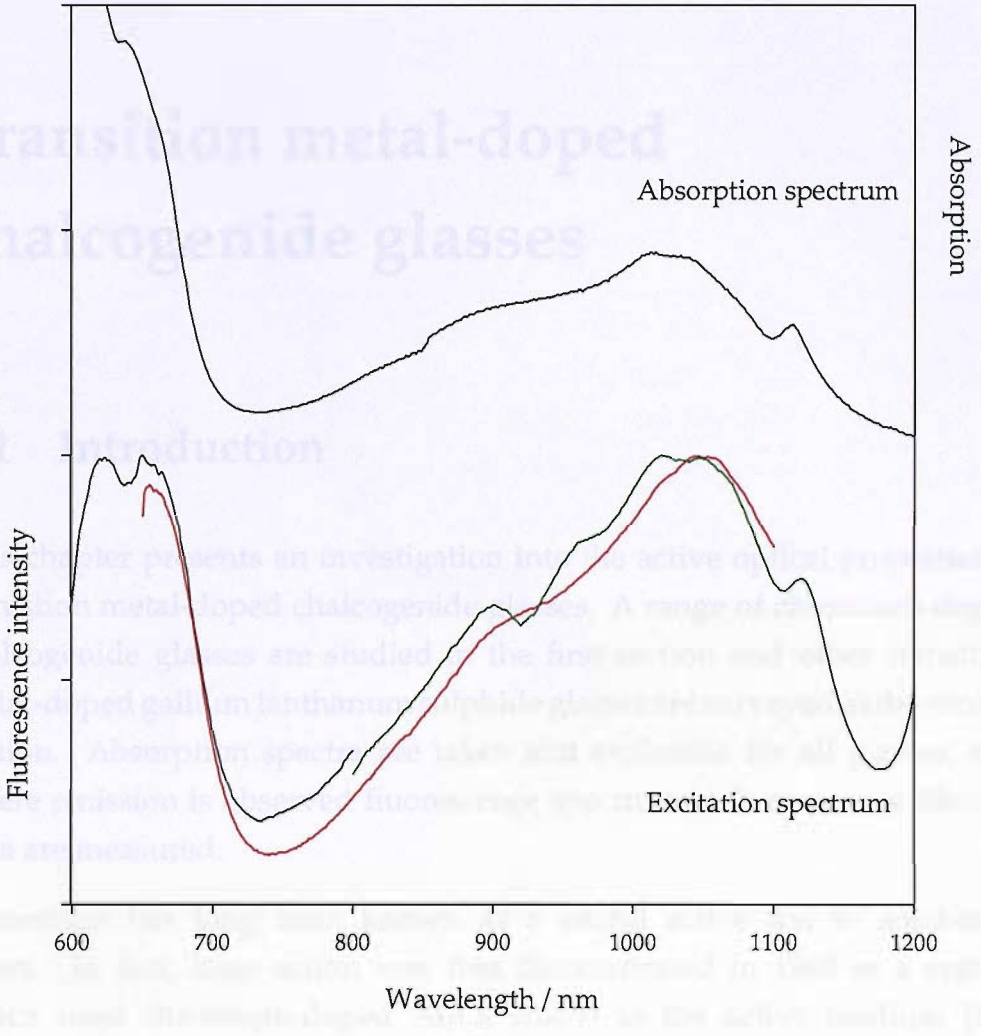

Figure 3.7: Absorption and fluorescence excitation spectra for Cr^{4+}-doped YAG. The peaks in the excitation correspond with peaks in the absorption spectrum.

Chapter 4

Transition metal-doped chalcogenide glasses

4.1 Introduction

This chapter presents an investigation into the active optical properties of transition metal-doped chalcogenide glasses. A range of chromium-doped chalcogenide glasses are studied in the first section and other transition metal-doped gallium lanthanum sulphide glasses are surveyed in the second section. Absorption spectra are taken and evaluated for all glasses, and where emission is observed fluorescence spectra and fluorescence lifetime data are measured.

Chromium has long been known as a useful active ion in solid-state lasers. In fact, laser action was first demonstrated in 1960 in a system which used chromium-doped Al_2O_3 (ruby) as the active medium [54], and the first solid-state tunable laser to operate at room temperature was based on chromium-doped $BeAl_2O_4$ (alexandrite) [55]. These lasers utilise electronic transitions of the Cr^{3+} ion, and operate at wavelengths of around 700-800 nm. In 1988, Cr^{4+} was used for the first time as an active ion in the chromium-doped Mg_2SiO_4 (forsterite) laser which operates in the near infrared [47]. Many Cr^{4+}-doped crystals have since been used as laser media operating around 1400 nm and tunable over wavelength ranges of up to 287 nm [56].

A number of other transition metal ions have also been used in tunable solid-state lasers, the most successful of which has been the titanium-doped Al_2O_3 (sapphire) laser. The Ti:sapphire laser used as the pump source for experiments in this thesis is tunable from 700-1100 nm. Solid-state lasers based on vanadium, manganese, iron, cobalt and nickel have also been demonstrated. An overview of the wavelengths covered by some of these lasers is given in Fig. 4.1.

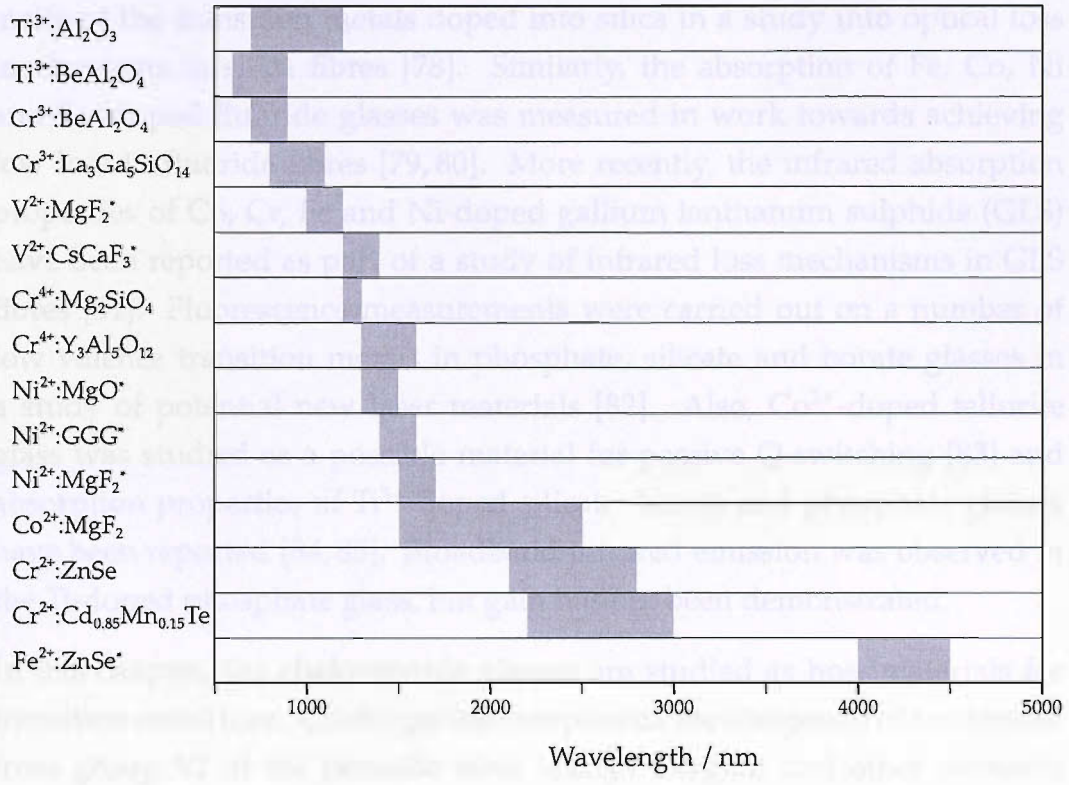

Figure 4.1: Wavelength ranges covered by selected tunable transition metal ion lasers [57–69]. * These lasers operate only at low temperatures.

The broad emission bands often shown by transition metal-doped solids make them particularly interesting for broadly-tunable amplifiers and lasers. Since the emission band of Cr^{4+} can cover the entire telecoms window and the absorption band overlaps with many commercially available lasers, the prospect of a Cr^{4+}-doped amplifier for telecoms applications is extremely attractive.

There have been many spectroscopic studies of chromium-doped glasses, and a number of phosphates and silicates and a borate and zirconate glass

were found to host Cr^{3+} [70]. Broadband infrared fluorescence due to Cr^{4+} has been observed in several aluminate and silicate glasses [71–77]. However, gain has not been reported in any of these materials. This is likely to be due to low room temperature quantum efficiencies and excited state absorption.

There have been relatively few publications reporting the spectroscopy of other transition metal-doped glasses. Absorption measurements were made of the transition metals doped into silica in a study into optical loss mechanisms in silica fibres [78]. Similarly, the absorption of Fe, Co, Ni and Cu-doped fluoride glasses was measured in work towards achieving low loss in fluoride fibres [79,80]. More recently, the infrared absorption properties of Co, Cr, Fe and Ni-doped gallium lanthanum sulphide (GLS) have been reported as part of a study of infrared loss mechanisms in GLS fibres [81]. Fluorescence measurements were carried out on a number of low valence transition metals in phosphate, silicate and borate glasses in a study of potential new laser materials [82]. Also, Co^{2+}-doped tellurite glass was studied as a possible material for passive Q-switching [83] and absorption properties of Ti^{3+}-doped silicate, borate and phosphate glasses have been reported [84,85]. Broadband infrared emission was observed in the Ti-doped phosphate glass, but gain has not been demonstrated.

In this chapter, the chalcogenide glasses are studied as host materials for transition metal ions. Chalcogenide compounds are composed of an element from group VI of the periodic table (except oxygen) and other elements such as arsenic, gallium and germanium. These materials exhibit excellent infrared transparency and have good glass-forming properties. The infrared transparency is a result of a low maximum phonon energy which shifts the multiphonon absorption edge out as far as 10 μm [28]. The good glass-forming ability of these materials has enabled the fabrication of a number of chalcogenide glass fibres, in particular As_2S_3 fibre is commercially available with a loss of 23 dB/km at 2.3 μm [86]. Gallium lanthanum sulphide is another promising chalcogenide glass which has been successfully drawn into fibre with a loss of <3 dB/m at 1.5 μm [87]. Several studies of rare earth-doped chalcogenide glasses have been carried out, and the first chalcogenide fibre laser to be demonstrated was Nd-doped GLS [88]. It is worth noting that although both a rare earth-doped chalcogenide fibre laser and several

transition metal-doped chalcogenide crystal lasers have been reported, no transition metal-doped glass laser has been demonstrated to date.

The chromium-doped chalcogenide samples studied in this work were made by Haythornthwaite, who investigated these materials as potential materials for broadband amplification [89]. This study reported absorption and fluorescence properties and measured radiative quantum efficiencies. The absorption and emission spectra suggested that chromium is hosted as Cr^{4+} in chalcogenide glasses. Broad emission at room temperature was observed from 900-1500 nm, which was seen to shift to longer wavelengths as the temperature was reduced to ~70 K. Room temperature lifetime measurements showed lifetimes of 0.5-1.7 μs and quantum efficiencies were <4%. The investigation is extended here by measuring emission spectra at 77 K and 4 K. Fluorescence excitation measurements are also made, which provide further evidence that chromium is hosted in its tetravalent state in these glasses. The absorption and room temperature emission measurements are also repeated here.

The transition metal-doped GLS samples were prepared by Petrovich who had previously studied the effect of transition metal ion impurities on infrared absorption in GLS [90]. In the previous work by Petrovich, the valence states of dopant ions in GLS and GLSO were assigned by comparison with transition metal-doped ZBLAN and silica glasses and the specific absorptivities of the transition metal ions were estimated. In this work, the fluorescence properties of these glasses are investigated for the first time. Fluorescence spectra, fluorescence excitation spectra and lifetime measurements are obtained for nickel and vanadium-doped GLS glasses. Low temperature fluorescence spectra and lifetime measurements are then made for V-doped GLS. Absorption measurements are repeated here and valence states are assessed with a detailed comparison with transition metal-doped crystals and glasses in octahedral and tetrahedral symmetry. The fluorescence spectra and lifetime measurements of the vanadium and nickel-doped GLS glasses were experiments carried out jointly with Mark Hughes, who also fabricated the vanadium-doped samples for Fig. 4.19.

4.2 Chromium doped into different chalcogenide glasses

In this section, the spectroscopic properties of a range of chromium-doped chalcogenide glasses are studied with a focus on assessing their potential as possible optical amplifier materials.

In order to interpret the spectroscopic data it is important to identify the electronic energy levels of the system. For transition metal-doped solids, this can be done by referring to the Tanabe-Sugano diagram for the site symmetry and number of $3d$ electrons of the system. Tetrahedrally-coordinated Cr^{4+} is the interesting chromium ion for optical telecoms applications, and the Tanabe-Sugano diagram for this system is shown in Fig. 4.2. The broad emission around 1.1-1.6 μm arises from the $^3T_2 \rightarrow {}^3A_2$ transition.

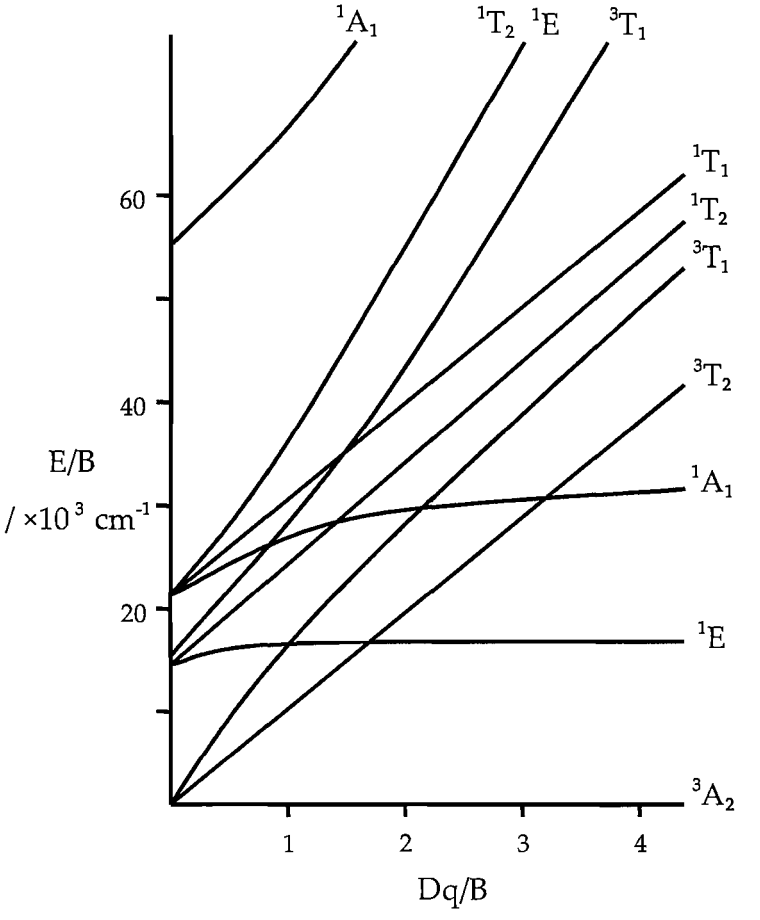

Figure 4.2: The Tanabe-Sugano diagram for Cr^{4+} in tetrahedral symmetry, showing the relevant energy levels [2]. Energies are plotted relative to the lowest level.

The glasses investigated here were chosen for their suitability for fibre-drawing. As_2S_3 is commercially available both in bulk and fibre form and has good transparency from 0.8-6.5 μm [91]. GLS glass with increased oxygen content is referred to as gallium lanthanum sulphide oxide (GLSO) and is more stable against crystallisation than GLS, making fibre drawing easier. However, the higher oxygen content adds a higher phonon energy component to the vibrational spectrum of this glass which can affect the emission properties of dopant ions [35]. Gallium sodium sulphate (GNS) glass has also been made into fibre, and a Pr-doped GNS optical amplifier has been demonstrated [92]. Germanium sulphur iodide (GeSI) is another promising glass for low-loss fibre drawing [93]. This glass is a chalcohalide (due to the presence of iodine) and has been studied as a possible host for Pr and Dy-doped fibre amplifiers for optical telecoms [94].

All samples were melted from high purity (at least 99.99%) powders, except for the As_2S_3 sample where a commercial bulk glass was obtained and remelted with Cr_2S_3. The glasses were cut into cuboids and polished on three surfaces. The nominal dopant concentration for all samples was 200 ppm (5×10^{18} ions/cm^3). Full details of the melting and annealing procedures are described elsewhere [89].

4.2.1 Absorption spectra

Absorption spectra for the chromium-doped samples were measured using the technique described in section 3.1 with a resolution of 1 nm. The spectra are shown in Fig. 4.3 and show absorption edges at ~550 nm and single broad peaks at 700 nm or 850 nm. The absorption edge is due to electronic absorption from the valence to the conduction band in the glass. The spectra can be divided into two groups: group 1 samples (As_2S_3 and GeSI) which have peaks at around 700 nm and group 2 glasses (GLS-based glasses and GNS) which have peaks at 850 nm. This difference in peak position could be due to the glasses hosting Cr in different valence states or could be a result of the different local environment provided by different glasses. This difference is discussed further in section 4.2.2.

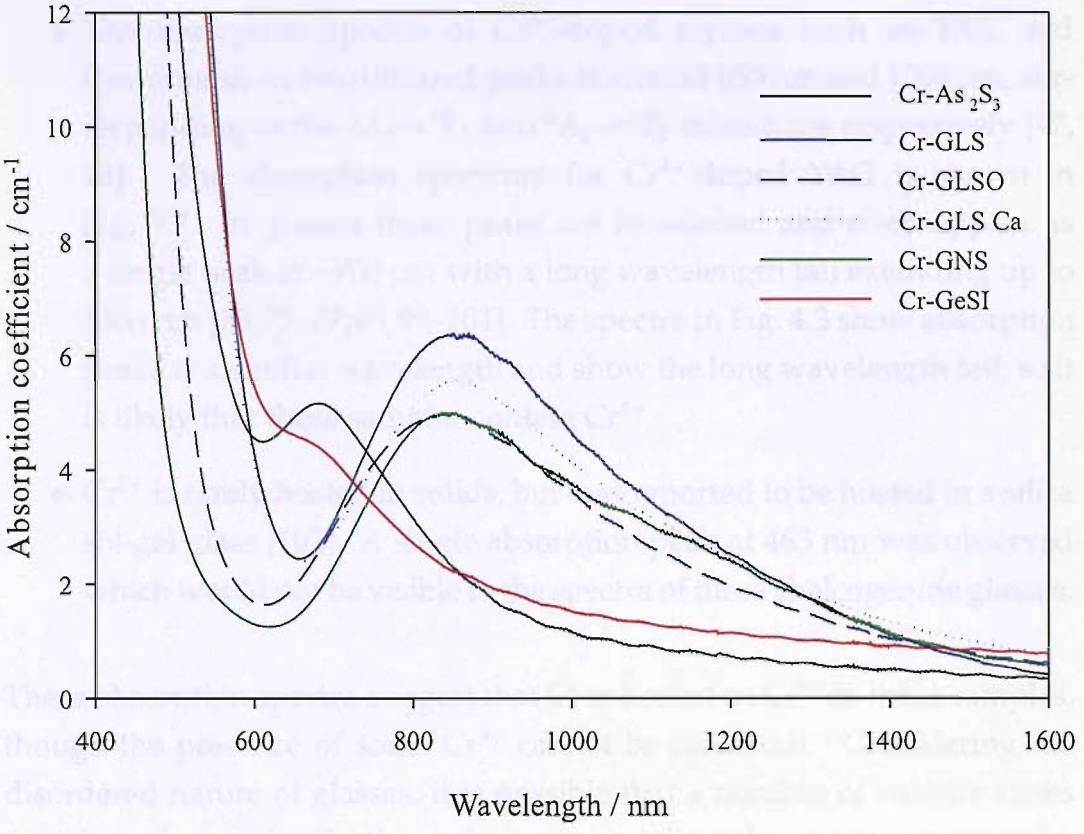

Figure 4.3: Absorption spectra of Cr-doped chalcogenide glasses. Glasses fall into two groups: the Cr absorption peaks at 700 nm in group 1 glasses and at 850 nm in group 2 glasses.

Chromium commonly exists in 2+, 3+, 4+ and 6+ valence states in solids, by comparison with absorption data from such valence states in other materials it is possible to identify which states may exist in these glasses. The long wavelength visible absorption edge precludes the observation of many higher energy absorption bands and restricts our attention to the infrared region. Therefore, since Cr^{6+} absorbs at wavelengths shorter than 400 nm [73, 95], its presence cannot be detected from the spectra in Fig. 4.3.

- The absorption of Cr^{2+} has been observed in several chalcogenide crystals and covers a broad band from ~1400 nm to 2400 nm. Absorption bands at these wavelengths were not present in the spectra of these samples.
- Cr^{3+} exhibits absorption bands at ~400 nm and ~650 nm [95, 96] and though the shorter wavelength band would be obscured, it is possible that the peaks we observe in these spectra are due to Cr^{3+}.

- The absorption spectra of Cr^{4+}-doped crystals such as YAG and forsterite show two infrared peaks at around 650 nm and 1000 nm, corresponding to the $^3A_2 \rightarrow {}^3T_1$ and $^3A_2 \rightarrow {}^3T_2$ transitions respectively [97, 98]. The absorption spectrum for Cr^{4+}-doped YAG is shown in Fig. 3.7. In glasses these peaks are broadened and often appear as a single peak at ~700 nm with a long wavelength tail extending up to 1400 nm [73,75–77,95,99–101]. The spectra in Fig. 4.3 show absorption peaks at a similar wavelength and show the long wavelength tail, so it is likely that these samples contain Cr^{4+}.

- Cr^{5+} is rarely hosted in solids, but was reported to be hosted in a silica sol-gel glass [102]. A single absorption peak at 465 nm was observed which would not be visible in the spectra of these chalcogenide glasses.

These absorption spectra suggest that Cr is hosted as Cr^{4+} in these samples, though the presence of some Cr^{3+} cannot be ruled out. Considering the disordered nature of glasses, it is possible that a number of valence states exist in each sample. Further information on the valence states is given by fluorescence measurements in the next section.

The peak absorption coefficients are ~4-6 cm^{-1}, which corresponds to a cross-section of $\sim 5 \times 10^{-19}$ cm^2. This is similar to the value measured in a Cr^{4+}-doped aluminosilicate [101] and aluminate glasses [100].

The Stokes shift is related to the the Huang-Rhys factor, so it can be used to determine the strength of the electron-lattice coupling of a system. Unfortunately, since the $^3T_2$ level cannot be resolved in the absorption spectra, it is not possible to measure the Stokes shift from the absorption and emission spectra in this work.

4.2.2 Temperature-dependent fluorescence spectra

In order to observe fluorescence from the samples, they were pumped at around the peak of absorption (800 nm) with a Ti:sapphire laser at room temperature, using the setup described in section 3.3. A Schott RG 850 glass filter was placed before the monochromator to prevent the detection of scattered excitation light. A New Focus Model 2034 extended-wavelength

InGaAs detector which was sensitive from 800-2200 nm was used to detect the fluorescence. The spectral resolution of the system was 33 nm and the system response was calibrated with a halogen lamp.

Single broad emission peaks were observed for all the samples, except for the GNS sample, the fluorescence spectra are shown in Fig. 4.4. Emission from the Cr-doped GNS sample was too weak to allow a spectrum to be measured. This broad emission from 900-1500 nm is characteristic of the $^3T_2 \rightarrow {}^3A_2$ transition of Cr^{4+} and further suggests that tetravalent chromium is hosted in these glasses. Emission from Cr^{3+} in glass hosts tends to be centred at 800 nm [70], emission around this wavelength was not observed in these glasses.

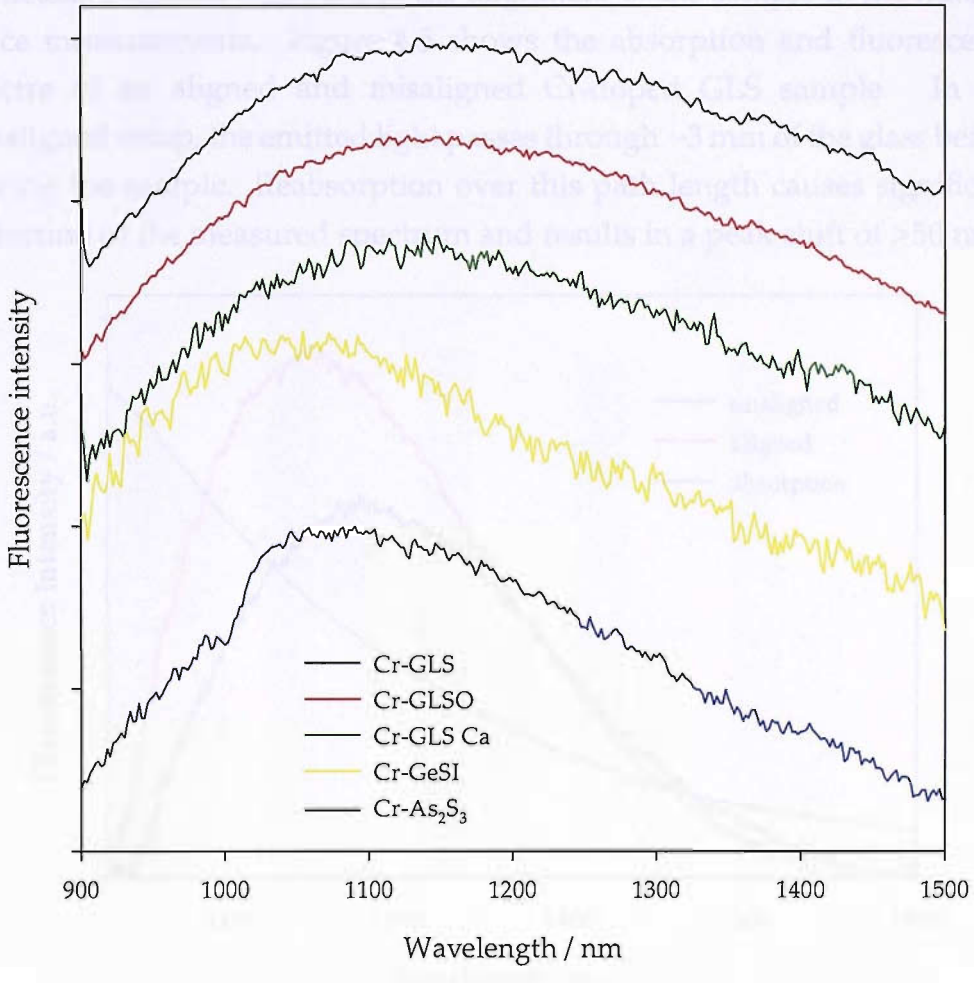

Figure 4.4: Room temperature fluorescence spectra of Cr-doped chalcogenide glasses pumped at 800 nm, showing broad emission bands centred at 1050 nm or 1150 nm. The spectra are normalised and offset vertically for clarity.

Again the samples fall into two groups, with the emission from group 1 glasses peaking at 1050 nm and from group 2 glasses at 1150 nm. The fact that both absorption and emission occur at higher energies in the group 1 samples can be explained in terms of the sites occupied by Cr in the different hosts. Glasses which provide higher crystal field sites for Cr ions would exhibit higher energy absorption and emission transitions. So the shorter wavelength absorption and emission peaks in the group 1 samples can be accounted for by considering Cr to be hosted at higher crystal field sites in these glasses than in group 2. A difference in crystal field strength is likely to affect the emission lifetimes and radiative quantum efficiencies of these groups. These effects are discussed in section 4.2.3.

Particular attention was paid to the alignment of the sample in the fluorescence measurements. Figure 4.5 shows the absorption and fluorescence spectra of an aligned and misaligned Cr-doped GLS sample. In the misaligned setup, the emitted light passes through ~3 mm of the glass before leaving the sample. Reabsorption over this path length causes significant distortion of the measured spectrum and results in a peak shift of >50 nm.

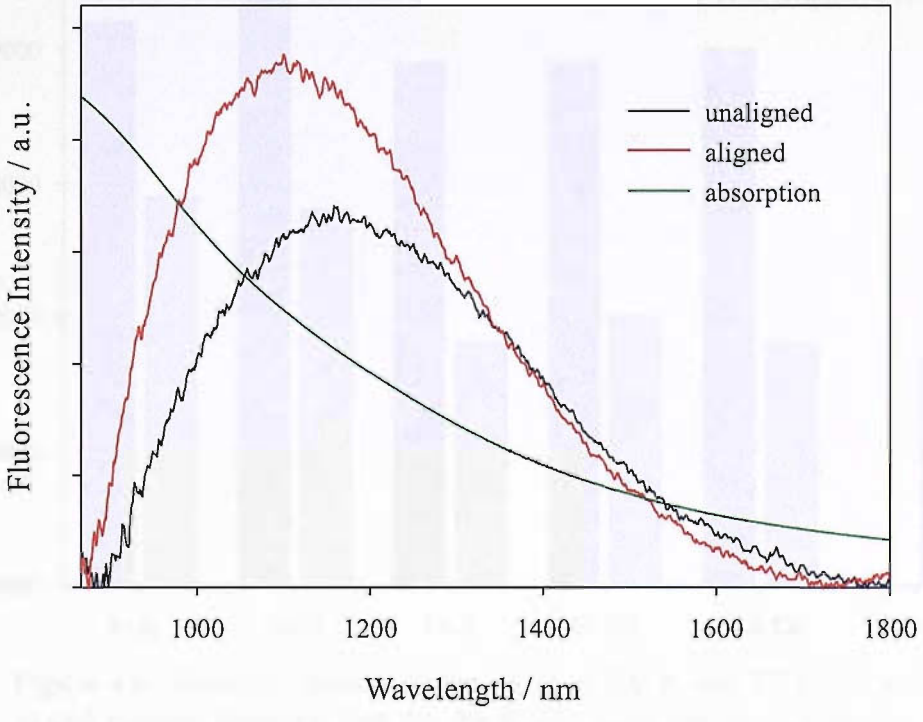

Figure 4.5: Fluorescence spectra of an aligned and unaligned sample, showing the effect of reabsorption on the emission band shape.

Low temperature emission measurements were taken using a bath cryostat filled with liquid nitrogen or helium as described in section 3.3.1. Again, a Ti:sapphire laser tuned to 800 nm was used as the excitation source and an RG 850 glass filter was used to prevent scattered excitation light being detected. Fluorescence spectra were taken for all the samples at 77 K, and the As_2S_3 and GLSO samples were chosen for spectra at 4 K.

At 77 K, the emission peaks of all samples shifted to longer wavelengths and fluorescence intensities were significantly increased. The emission peak energies are shown Fig. 4.6 and show that emission from the As_2S_3 and GeSI samples (group 1) is at higher energy than that from the GLS-based glasses (group 2). Emission from the GNS sample was sufficiently strong at 77 K to enable a spectrum to be recorded. The fluorescence spectrum of Cr-doped GNS was similar to that of the GLS-based glasses (as was the absorption spectrum). A narrowing of emission bands was also observed for all samples at lower temperature.

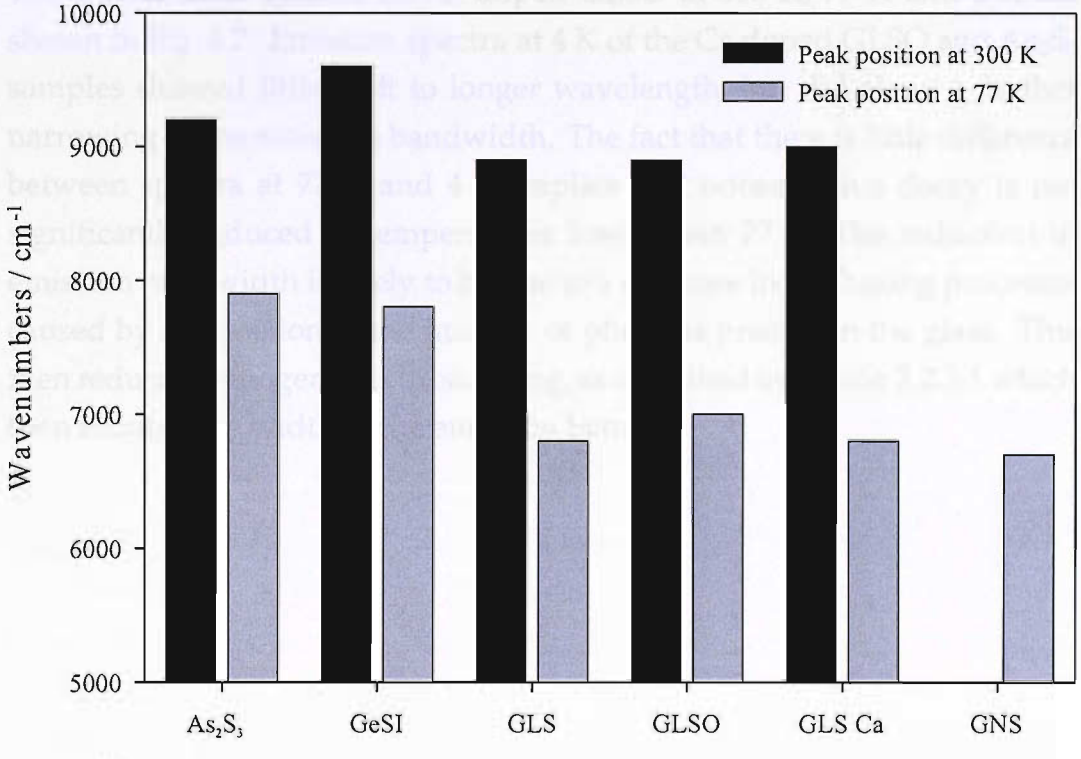

Figure 4.6: Emission peak positions and at 300 K and 77 K of Cr-doped glasses, showing that the As_2S_3 and GeSI (group 1) samples have emission peaks at higher energy than the GLS-based samples (group 2).

The large increase in fluorescence intensity observed at low temperature suggests that there is significant thermally-activated nonradiative decay at room temperature. An increase in absolute intensity of 10-20 times was observed, though quantitative measurements were not made. A similar temperature dependence is commonly observed in Cr-doped glasses and crystals [72, 76, 99, 103] and is an indication that the radiative quantum efficiency is low at room temperature. Nonradiative decay in transition metal-doped systems is site-dependent, and preferentially affects ions hosted at low crystal field sites. This is one of the processes responsible for the temperature-dependence of the emission peak. The other mechanism is the effect of lattice expansion at higher temperatures, causing a reduction of the crystal field strength. This results in smaller gaps between energy levels at high temperatures which shifts the emission to longer wavelengths. The reduction of emission bandwidths at low temperatures is caused by a change in the population of vibrational levels in the ground electronic state.

The fluorescence spectra for Cr-doped GLSO at 300 K, 77 K and 4 K are shown in Fig. 4.7. Emission spectra at 4 K of the Cr-doped GLSO and As_2S_3 samples showed little shift to longer wavelength, but did show a further narrowing of the emission bandwidth. The fact that there is little difference between spectra at 77 K and 4 K implies that nonradiative decay is not significantly reduced at temperatures lower than 77 K. The reduction in emission bandwidth is likely to be due to a decrease in dephasing processes caused by a reduction in the number of phonons present in the glass. This then reduces homogeneous broadening, as described in section 2.2.3.1 which then reduces the width of the emission band.

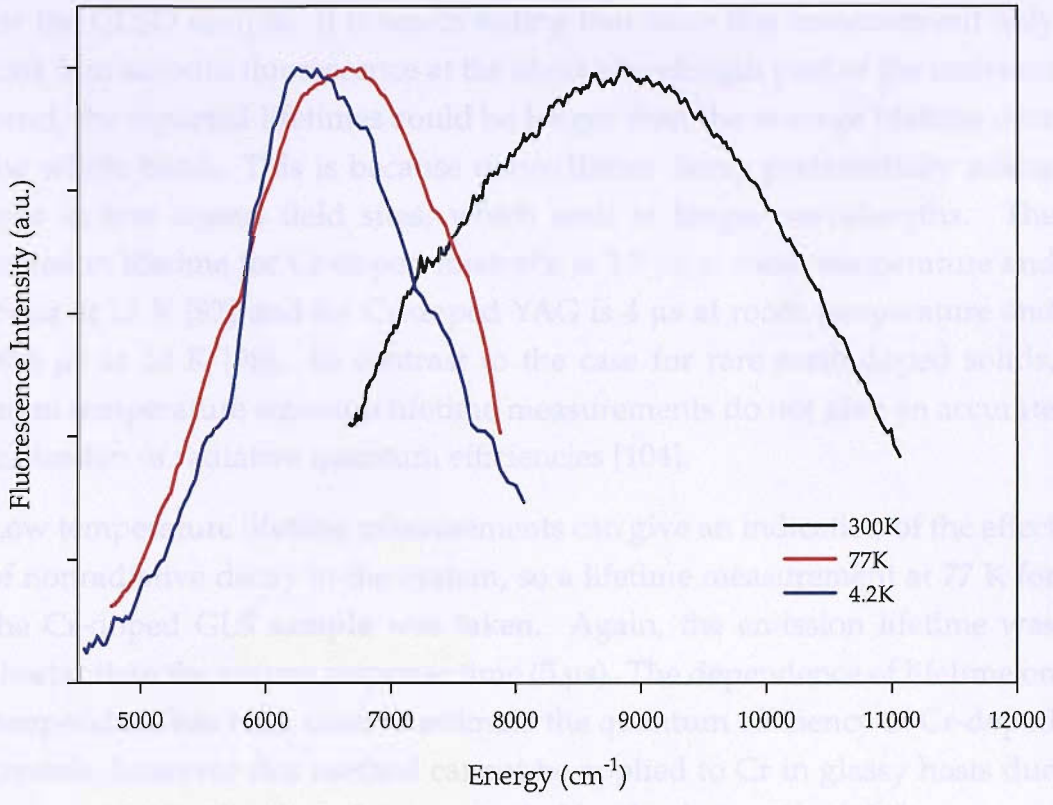

Figure 4.7: Fluorescence spectra of Cr-doped GLSO at 300 K, 77 K and 4 K, showing a reduction in emission bandwidth and a shift to lower energy at low temperatures. The spectra are scaled to the peak of emission.

4.2.3 Fluorescence lifetime and quantum efficiency

Lifetime measurements were made using an InGaAs detector in the setup described in section 3.4. In order to improve the system response time, an acousto-optic modulator with a fall time of 180 ns/mm was used to modulate the pump light. A silicon filter was placed in front of the detector to prevent the detection of scattered pump light, and the removal of the monochromator from the setup allowed the entire emission band to be measured. The measured lifetimes of all the Cr-doped samples were shorter than the system response time, which was measured to be 5 μs. The previous study of these samples includes room temperature lifetime measurements [89]. This was achieved by using a photomultiplier with S1 characteristics which was sensitive up to 1.1 μm. The measured lifetimes were non-exponential and ranged from 0.7 μs for the As_2S_3 sample to 1.7 μs

for the GLSO sample. It is worth noting that since this measurement only took into account fluorescence at the short wavelength part of the emission band, the reported lifetimes could be longer than the average lifetime over the whole band. This is because nonradiative decay preferentially affects ions in low crystal field sites, which emit at longer wavelengths. The emission lifetime for Cr-doped forsterite is 2.7 μs at room temperature and 29 μs at 15 K [97] and for Cr-doped YAG is 4 μs at room temperature and 30.6 μs at 10 K [98]. In contrast to the case for rare earth-doped solids, room temperature emission lifetime measurements do not give an accurate indication of radiative quantum efficiencies [104].

Low temperature lifetime measurements can give an indication of the effect of nonradiative decay in the system, so a lifetime measurement at 77 K for the Cr-doped GLS sample was taken. Again, the emission lifetime was shorter than the system response time (5 μs). The dependence of lifetime on temperature has been used to estimate the quantum efficiency of Cr-doped crystals, however this method cannot be applied to Cr in glassy hosts due to the wide distribution of sites occupied by the dopant ion [104].

Quantum efficiency measurements in transition metal-doped glasses require a more direct measurement than for rare earths. They are rarely reported in Cr^{4+}-doped glasses and are often given with large experimental errors. Room temperature quantum efficiency measurements have previously been made on these samples [89], using the integrating sphere technique with Cr:YAG as a reference sample (which has a quantum efficiency of 11%). Typical quantum efficiency values were ~2% with a systematic error of ±50%. Cr-doped As_2S_3 has the largest quantum efficiency of 3.4%.

4.2.4 Fluorescence excitation measurements

Fluorescence spectra were measured with a Ti:sapphire laser tuned to 850 nm and then an ALC D500 Nd:YAG laser at 1064 nm. The recorded spectra are shown in Fig. 4.8.

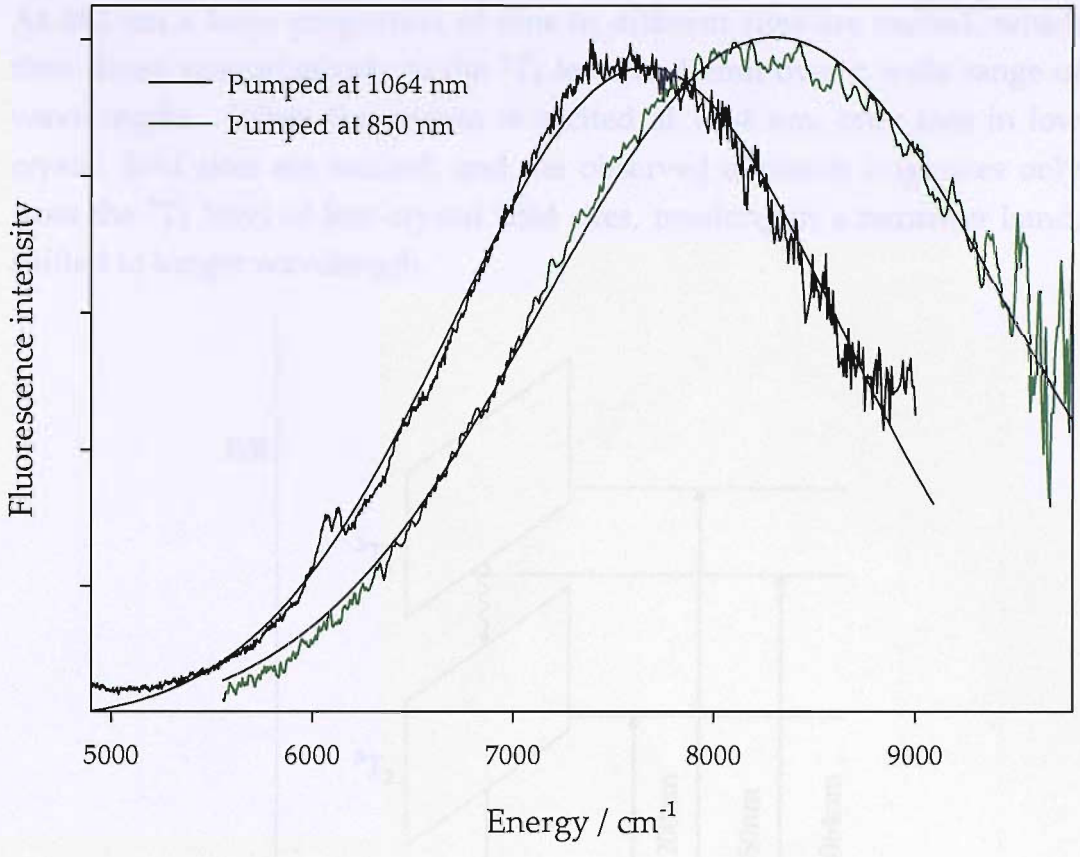

Figure 4.8: Fluorescence spectra of Cr-doped GLS when pumped at 850 nm and 1064 nm normalised to the peak intensity, showing a shift in peak emission to lower energy and a narrowing of the emission band with the lower energy pump source.

The measurements show a shift to lower energy and a narrowing of the emission band when excited by the longer wavelength source. This is consistent with fluorescence line narrowing, which arises when a narrow-band excitation source is used to excite a subset of the inhomogeneous population of ions. If the excitation source used is at the low energy side of the absorption band, then only ions at lower crystal field sites will be excited. For a sufficiently low dopant concentration, the resulting fluorescence spectrum will arise only from these ions, and the emission will shift to long wavelength. Also, because inhomogeneous broadening is effectively reduced, the emission band will be reduced in width. A schematic representation of fluorescence line narrowing is shown in Fig. 4.9. This is a partial Tanabe-Sugano diagram where the inhomogeneous broadening is represented by the range of crystal field strengths on the x-axis and homogeneous broadening gives rise to the range of energies on the y-axis.

At 850 nm a large proportion of ions in different sites are excited, which then decay nonradiatively to the $^3T_2$ level and emit over a wide range of wavelengths. When the system is excited at 1064 nm, only ions in low crystal field sites are excited, and the observed emission originates only from the $^3T_2$ level of low crystal field sites, resulting in a narrower band, shifted to longer wavelength.

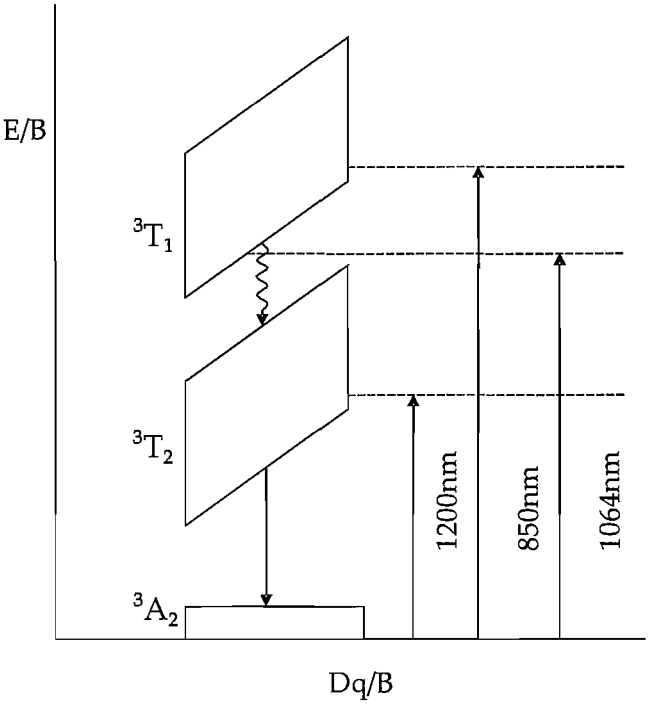

Figure 4.9: Schematic representation of fluorescence line narrowing: a partial Tanabe-Sugano diagram showing that only a subset of the inhomogeneous population of ions are excited at 1064 nm.

Fluorescence line narrowing has been observed in a number of Cr^{3+}-doped glasses [82, 105] and implies a broad site distribution for dopant ions in the host. It is worth noting that Fig. 4.9 is highly schematic and it is quite possible that pumping at 850 nm does not excite ions at all sites in the glass, and that pumping at 1064 nm excites some ions at high crystal field sites directly into the $^3T_2$ level.

Fluorescence excitation spectra were measured for the Cr-doped GLS sample using the method described in section 3.5. The results are shown in Fig. 4.10 and show peaks at 600 nm and 850 nm. Though the 850 nm peak is clearly observed in the absorption spectrum in Fig. 4.3, the 600 nm peak is not seen

from absorption measurements. The positions of these peaks correspond closely to those of the Cr^{4+} ion as discussed in section 4.2.1 and so these results provide further evidence that chromium is hosted as Cr^{4+} in these glasses.

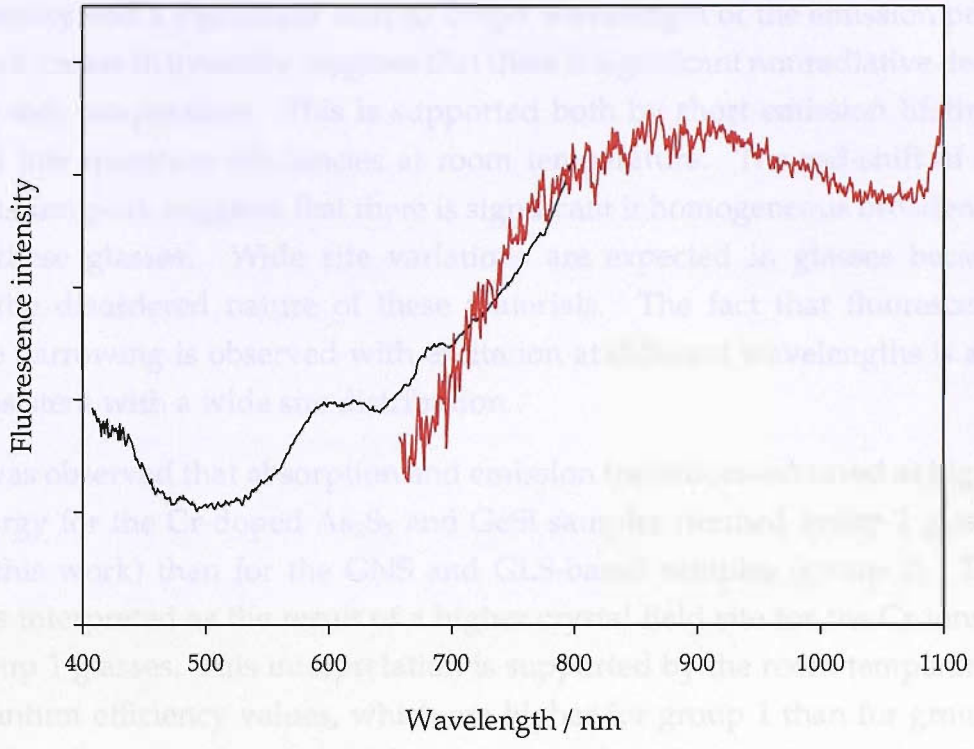

Figure 4.10: Excitation spectrum of Cr-doped GLS, collecting emission from 1100-2200 nm revealing absorption peaks at 600 nm and 850 nm.

4.2.5 Conclusions

Spectroscopic properties of a range of Cr-doped chalcogenide glasses were measured with a focus on determining the valence state and assessing their potential as gain media.

Absorption measurements showed single infrared peaks at the same wavelength as many other Cr^{4+}-doped glasses and crystals. Broad fluorescence centred around 1100 nm was observed under excitation at 800 nm, this is also similar to the emission of Cr^{4+} in other glasses and crystals. The optical transitions observed in these glasses are therefore assigned to Cr^{4+} in tetrahedral symmetry. It is possible that Cr exists in

other valence states, though the presence of other states cannot be detected from the measurements in this work. If other valence states do exist in these samples, they do not appear significantly to affect the spectroscopy.

Low temperature fluorescence spectra revealed a large increase in emission intensity and a significant shift to longer wavelength of the emission peak. The increase in intensity suggests that there is significant nonradiative decay at room temperature. This is supported both by short emission lifetimes and low quantum efficiencies at room temperature. The red-shift of the emission peak suggests that there is significant inhomogeneous broadening in these glasses. Wide site variations are expected in glasses because of the disordered nature of these materials. The fact that fluorescence line narrowing is observed with excitation at different wavelengths is also consistent with a wide site distribution.

It was observed that absorption and emission transitions occurred at higher energy for the Cr-doped As_2S_3 and GeSI samples (termed group 1 glasses in this work) than for the GNS and GLS-based samples (group 2). This was interpreted as the result of a higher crystal field site for the Cr ions in group 1 glasses. This interpretation is supported by the room temperature quantum efficiency values, which are higher for group 1 than for group 2 glasses. Because of the large inhomogeneous broadening observed in these materials, this difference in crystal field strength can be considered as a change in the site distribution rather than a distinct change in a specific site.

The optical spectroscopy presented in this work gives a number of indications as to how useful these Cr-doped chalcogenide glasses would be as gain media. Strong inhomogeneous broadening contributes to the broad absorption band exhibited by these glasses. This strong absorption coincides with several commercially available, high power laser sources. The glasses emit at room temperature, and the broad infrared emission covers much of the telecoms window. However, high nonradiative decay rates at room temperature result in relatively low quantum efficiencies. In their present form, it is unlikely that these glasses would be suitable for active optical devices.

4.3 Vanadium and nickel-doped Ga:La:S glasses

This section contains a spectroscopic study of vanadium, nickel, titanium, iron, cobalt and copper-doped GLS glasses. The aim of this investigation is to determine if any of the other transition metal-doped GLS glasses could be useful in laser or optical amplifier applications.

The glass composition of the samples was 65% Ga_2S_3, 30% La_2S_3, 5% La_2O_3 and ~0.05% dopant. Details of the dopant compounds and concentrations used in the samples are given in table A.1. The batches were melted for 24 hours in a reducing atmosphere. Samples of thickness ~5 mm were cut and polished on parallel sides.

4.3.1 Absorption spectra

The absorption spectrum of each of the glass samples was taken using the method described in section 3.1 with a resolution of 1 nm. The results are presented in Figs. 4.11-4.16 and possible valence states for the dopant ion in each sample are evaluated.

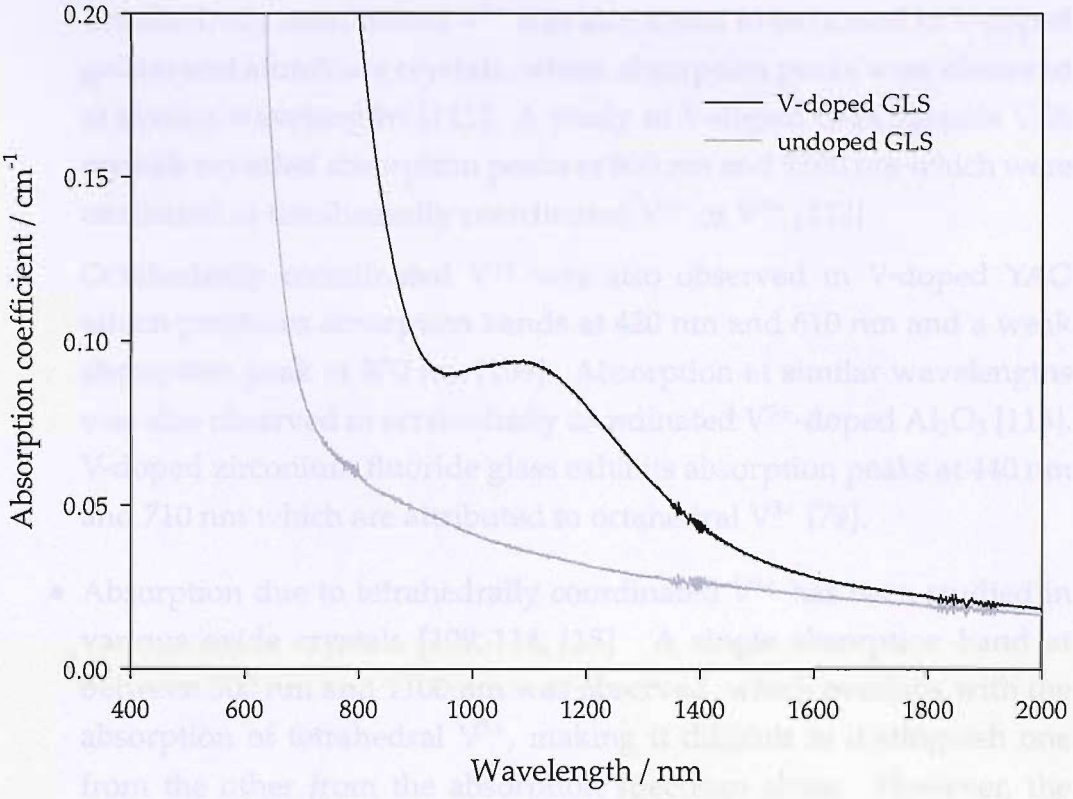

Figure 4.11: Absorption spectra of vanadium-doped GLS and undoped GLS. The V-doped sample shows a single peak at 1100 nm and a strong absorption at ~800 nm.

- V^{2+} is isoelectronic to Cr^{3+} and has been demonstrated as a laser ion in MgF_2 and $CsCaF_3$ crystals operating between 1240 nm and 1330 nm [61, 106]. Absorption due to octahedrally coordinated V^{2+} has been measured in several halide crystals and reveals three distinct peaks in the visible and infrared regions. The longer two peaks were found at 840-1210 nm and 560-770 nm depending on the crystal field strength of the host [107, 108]. These peaks are in the same region as the absorption recorded in the V-doped GLS sample, however the infrared absorption peak shown in Fig. 4.11 extends beyond 1400 nm. Absorption spectra of V^{2+} in the literature do not show such a long wavelength tail.

- Tetrahedral V^{3+} is isoelectronic to Cr^{4+} and therefore has the same energy level structure as the Cr-doped chalcogenide glasses studied in section 4.2. Tetrahedrally coordinated V^{3+} exhibits absorption bands at 800 nm, 1100 nm and 1300 nm in YAG crystals [109, 110].

Tetrahedrally coordinated V^{3+} was also found to be hosted in V-doped gallate and aluminate crystals, where absorption peaks were observed at similar wavelengths [111]. A study of V-doped chalcogenide CdS crystals revealed absorption peaks at 800 nm and 1100 nm which were attributed to tetrahedrally coordinated V^{2+} or V^{3+} [112].

Octahedrally coordinated V^{3+} was also observed in V-doped YAG which produces absorption bands at 420 nm and 610 nm and a weak absorption peak at 970 nm [109]. Absorption at similar wavelengths was also observed in octahedrally coordinated V^{3+}-doped Al_2O_3 [113]. V-doped zirconium fluoride glass exhibits absorption peaks at 440 nm and 710 nm which are attributed to octahedral V^{3+} [79].

- Absorption due to tetrahedrally coordinated V^{4+} has been studied in various oxide crystals [109, 114, 115]. A single absorption band at between 500 nm and 1100 nm was observed, which overlaps with the absorption of tetrahedral V^{3+}, making it difficult to distinguish one from the other from the absorption spectrum alone. However, the fluorescence spectra described in section 4.3.2 suggest that V^{4+} is not the active ion in this glass.

  Octahedrally coordinated V^{4+} has been reported in V-doped Al_2O_3, exhibiting absorption and emission only in the visible spectral region [116].

Comparison of the absorption spectrum of V-doped GLS with those reported in other glasses and crystals suggests that tetrahedrally coordinated V^{3+} is responsible for the single infrared peak observed. The peak at 1100 nm extending out to 1600 nm is therefore assigned to the $^3A_2 \rightarrow {}^1E$ and $^3A_2 \rightarrow {}^3T_2$ transitions of tetrahedral V^{3+} and the strong absorption observed at 800 nm is assigned to the $^3A_2 \rightarrow {}^3T_1$ transition. The similarity in the shapes of the spectra of V-doped GLS and Cr^{4+}-doped GLS further supports this assignment, and further evidence is provided by the fluorescence spectrum which is discussed further in section 4.3.2.

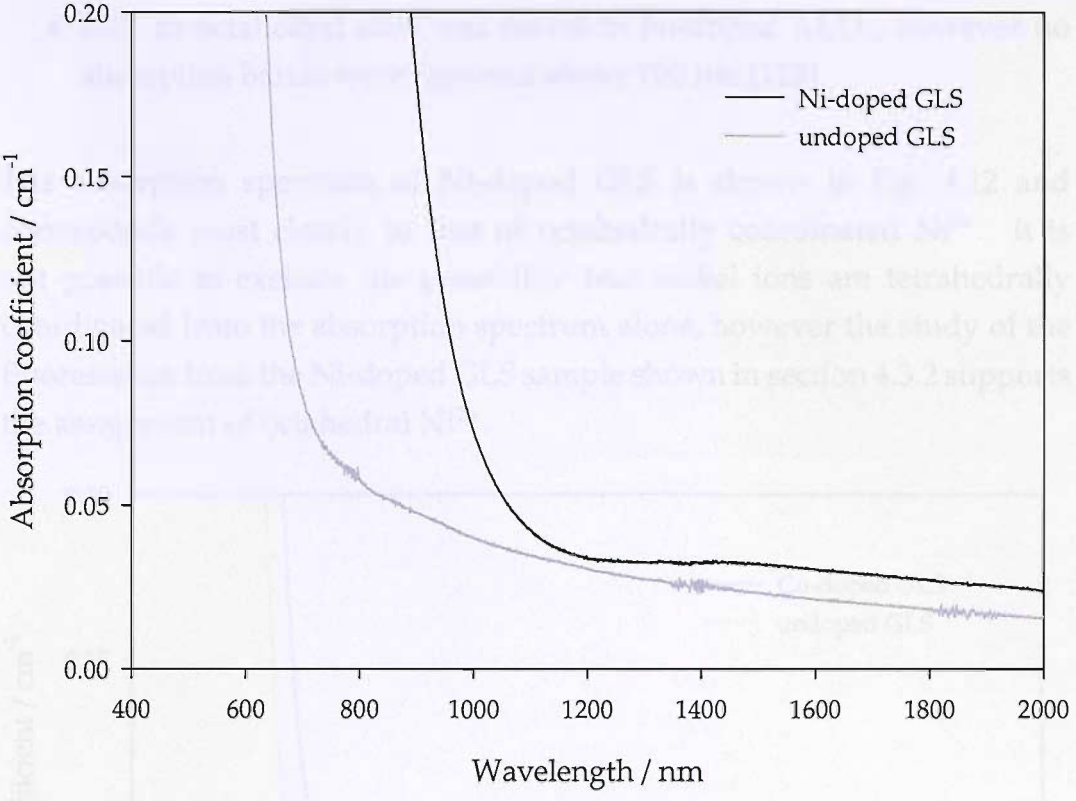

Figure 4.12: Absorption spectra of nickel-doped GLS and undoped GLS. The Ni-doped sample shows a strong absorption at ~900 nm and a broad, weak absorption at ~1600 nm.

- Ni^{2+} has been known as a laser ion since the early 1960s, when lasing from octahedrally coordinated nickel-doped MgF_2 was demonstrated at ~1.6 μm at 77 K [117]. However, despite various spectroscopic investigations into nickel-doped fluoride, chloride, oxide and sulphide crystals, lasing has not been achieved at room temperature [80, 112, 118–120]. Infrared absorption of octahedral Ni^{2+} shows peaks at ~900 nm and ~1500 nm. The long wavelength peak varies considerably from 1100 nm to 1650 nm in crystals with different crystal field strengths [56]. Studies of Ni-doped zirconium fluoride glasses also revealed absorption peaks due to octahedrally coordinated Ni^{2+} at 900 nm and 1500 nm [79, 80].

  Absorption due to tetrahedral Ni^{2+} has been recorded in Ni-doped chalcogenide crystals [121] and in a Ni-doped oxide crystal [56]. Both these crystals showed a strong absorption peak at ~800 nm and weaker peaks at ~1100 nm and ~2000 nm.

- Ni^{3+} in octahedral sites was found in Ni-doped Al_2O_3, however no absorption bands were reported above 700 nm [113].

The absorption spectrum of Ni-doped GLS is shown in Fig. 4.12 and corresponds most closely to that of octahedrally coordinated Ni^{2+}. It is not possible to exclude the possibility that nickel ions are tetrahedrally coordinated from the absorption spectrum alone, however the study of the fluorescence from the Ni-doped GLS sample shown in section 4.3.2 supports the assignment of octahedral Ni^{2+}.

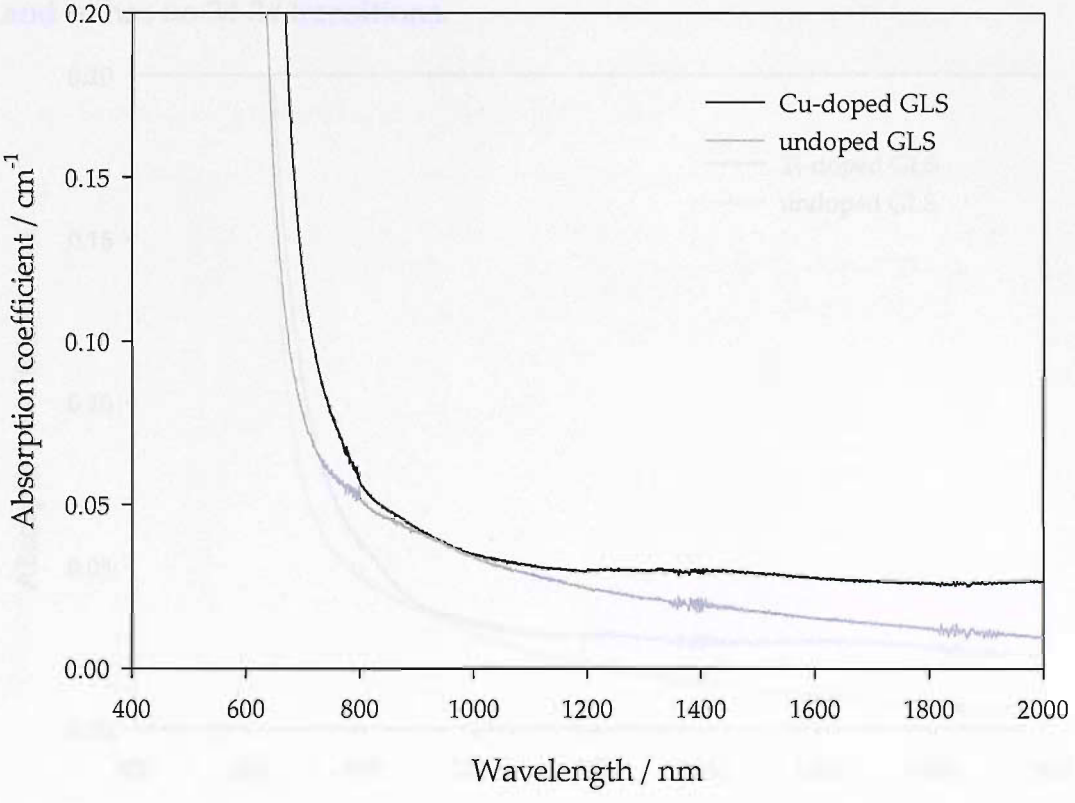

Figure 4.13: Absorption spectra of copper-doped GLS and undoped GLS, showing no clear infrared absorption peaks.

- Cu-doped silica glass has been found to host only Cu^+, which has a full $3d$ shell [78]. Absorption spectra of Cu-doped silica shows an increased UV absorption and no absorption in the infrared.

- Octahedrally coordinated Cu^{2+} was found to be hosted in a zirconium fluoride glass [79]. A broad infrared absorption peak was observed from 950-2000 nm.

Absorption due to tetrahedral Cu^{2+} was reported in crystalline CdS from 1000-2000 nm, peaking at 1300 nm [112].

- Octahedrally coordinated Cu^{3+} was identified in Al_2O_3 where a strong absorption peak was measured at 470 nm and a weaker peak at 590 nm [122].

The absorption spectrum for Cu-doped GLS is shown in Fig. 4.13 and shows no significant increase in absorption coefficient from 700-2000 nm. It is likely that the dopant ion appears as Cu^{+} which has a $3d^{10}$ electronic configuration and so has no $3d$-$3d$ transitions.

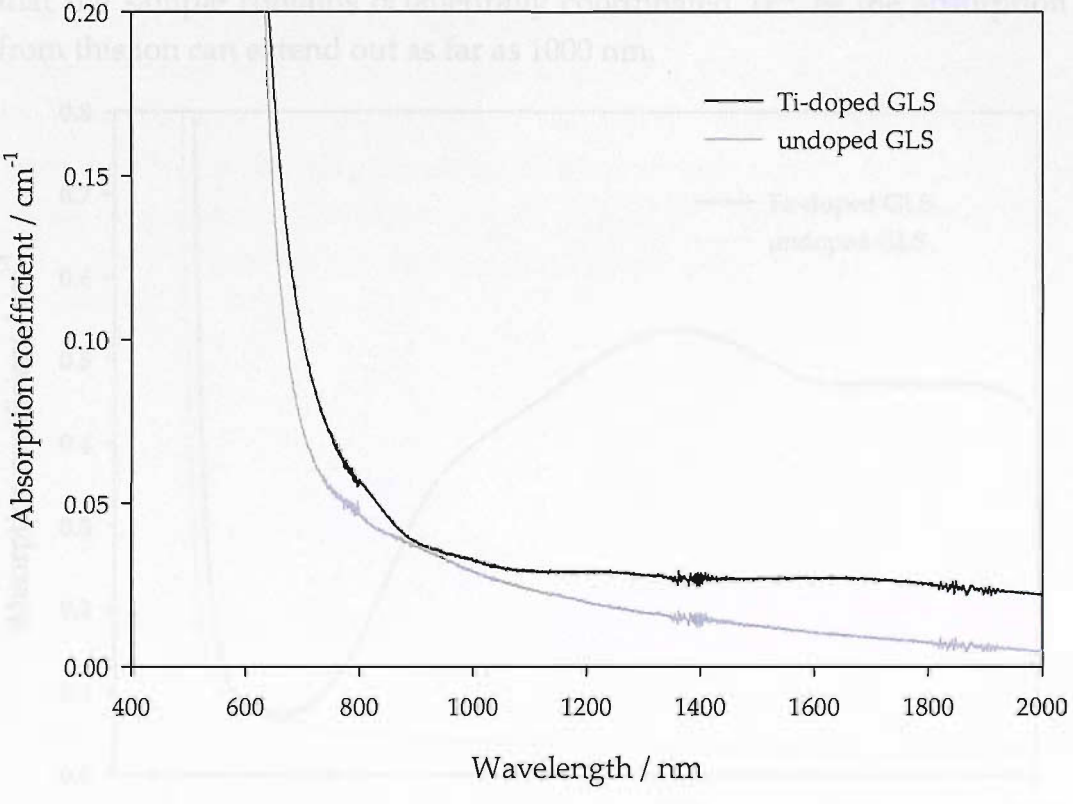

Figure 4.14: Absorption spectra of titanium-doped GLS and undoped GLS, showing no distinct infrared absorption peaks.

- Ti-doped Al_2O_3 has been known as a useful tunable laser material at room temperature since the early 1980s. Octahedrally coordinated Ti^{3+} is the laser ion and has an absorption peak at around 500 nm [123]. Studies of Ti-doped silicate, borate and phosphate glasses all showed a single absorption peak at ~550 nm [85] with a shoulder at ~750 nm

which extends to 1000 nm. This absorption was attributed to octahedrally coordinated Ti^{3+}.

- Ti^{4+} has no $3d$ electrons and therefore cannot be identified by absorption peaks in the visible or infrared. However Ti^{4+} was identified in a Ti-doped fluoride glass by an increase in ultraviolet absorption caused by a charge transfer process [79].

The absorption spectrum for Ti-doped GLS shown in Fig. 4.14 shows little change in absorption from that of undoped GLS. It is therefore not possible to identify the valence of the Ti ions in the GLS sample, though it looks unlikely that the sample contains octahedrally coordinated Ti^{3+} as the absorption from this ion can extend out as far as 1000 nm.

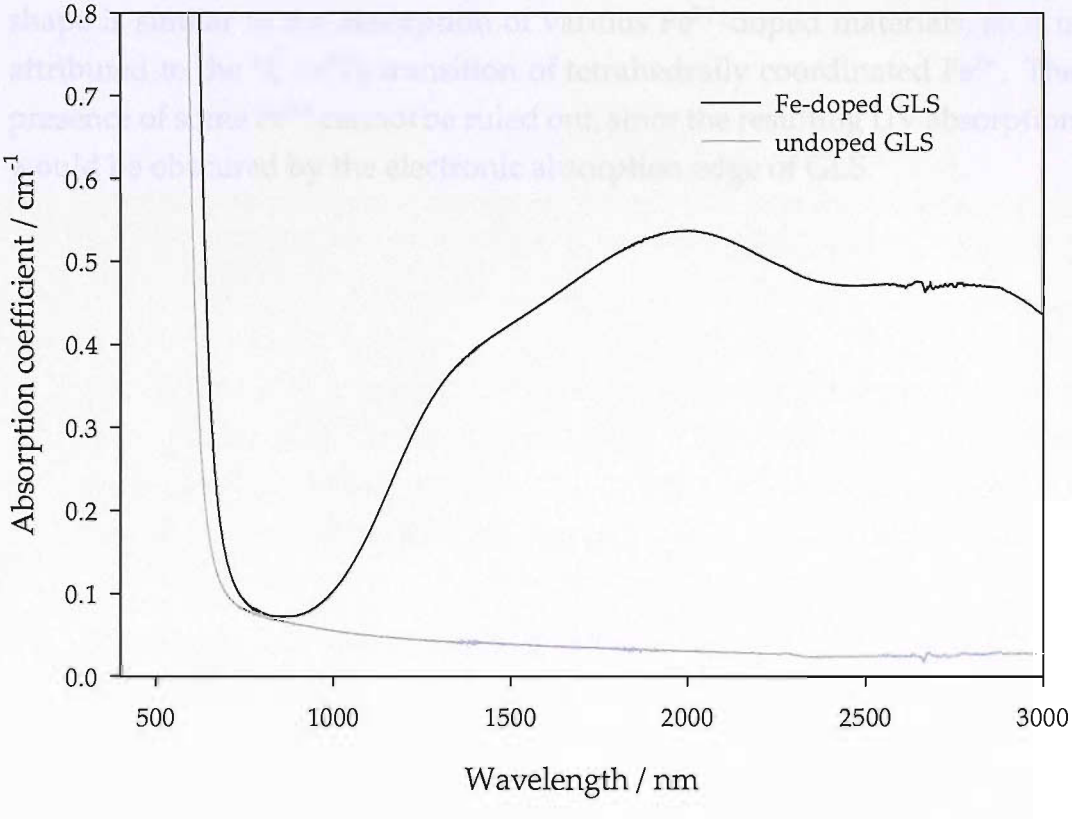

Figure 4.15: Absorption spectra of iron-doped GLS and undoped GLS, showing a broad strong absorption structure from 1000 nm to beyond 3000 nm.

- Tetrahedrally coordinated Fe^{2+} has been demonstrated as a tunable laser ion in Fe-doped ZnSe at 180 K [69]. The infrared absorption

spectrum of this laser crystal shows a broad double-peaked band from 2.5 μm to 4 μm. A similar spectrum was observed in a Fe-doped fluoride glass which spans from 0.9 μm to 3 μm and was also attributed to Fe^{2+} [79].

- Absorption due to tetrahedrally coordinated Fe^{3+} was observed in Fe-doped silica [78]. This causes a strong absorption band in the UV region below 600 nm.
- Tetrahedral Fe^{6+} has been reported to be hosted in a K_2SO_4 crystal. Absorption bands were reported at 500 nm and 770 nm.

The absorption spectrum for Fe-doped GLS is shown in Fig. 4.15 and shows a strong, broad band from 1000 nm to beyond 3000 nm. This distinctive shape is similar to the absorption of various Fe^{2+}-doped materials, so it is attributed to the ${}^5E \rightarrow {}^5T_2$ transition of tetrahedrally coordinated Fe^{2+}. The presence of some Fe^{3+} cannot be ruled out, since the resulting UV absorption would be obscured by the electronic absorption edge of GLS.

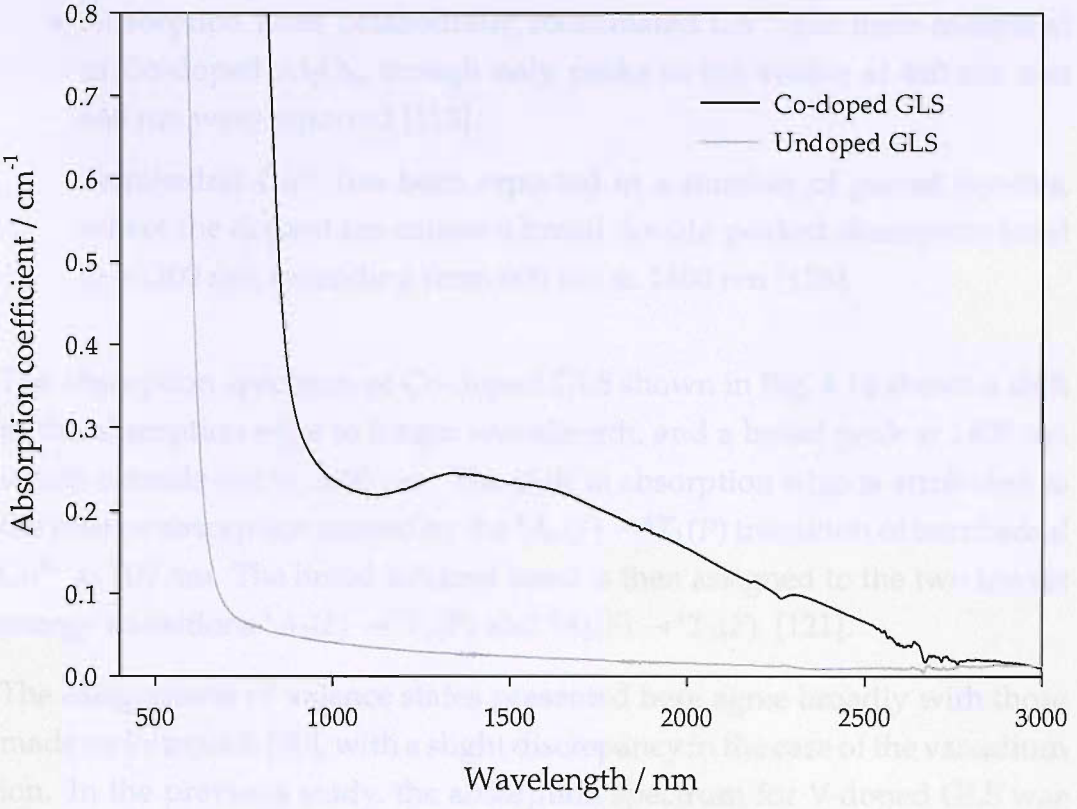

Figure 4.16: Absorption spectra of cobalt-doped GLS and undoped GLS, showing a broad infrared absorption band which extends from 1 μm out to 2.7 μm.

- Octahedrally coordinated Co^{2+} has been demonstrated as a tunable laser ion in MgF_2 at low temperature [124]. Co^{2+} was also found to occupy octahedral sites in Co-doped fluoride glasses, showing strong absorption peaks at 550 nm and 1550 nm and a weaker peak at 880 nm [79, 80].

  Co-doped zinc chalcogenide crystals were found to host Co^{2+} in tetrahedral sites where absorption spectra showed an intense peak at 700 nm and two broader, weaker bands at 1400-2000 nm and 2300-3000 nm [121]. Similar bands at 750 nm and 1700 nm were reported from Co^{2+} in tetrahedral sites in CdS crystals [112, 125]. Co^{2+} was found in Co-doped silica glass, where Co^{2+} was identified in octahedral sites by absorption peaks in the visible and in tetrahedral sites by absorption peaks at 685 nm and 1700 nm [78].

- Absorption from octahedrally coordinated Co^{3+} has been measured in Co-doped Al_2O_3, though only peaks in the visible at 440 nm and 640 nm were reported [113].

  Tetrahedral Co^{3+} has been reported in a number of garnet crystals, where the dopant ion causes a broad double-peaked absorption band at ~1200 nm, extending from 900 nm to 1400 nm [126].

The absorption spectrum of Co-doped GLS shown in Fig. 4.16 shows a shift in the absorption edge to longer wavelength, and a broad peak at 1400 nm which extends out to 2600 nm. The shift in absorption edge is attributed to the intense absorption caused by the $^4A_2(F) \rightarrow ^4T_1(P)$ transition of tetrahedral Co^{2+} at 700 nm. The broad infrared band is then assigned to the two lowest energy transitions $^4A_2(F) \rightarrow ^4T_1(F)$ and $^4A_2(F) \rightarrow ^4T_2(F)$ [121].

The assignments of valence states presented here agree broadly with those made by Petrovich [90], with a slight discrepancy in the case of the vanadium ion. In the previous study, the absorption spectrum for V-doped GLS was assumed to arise from both V^{3+} and V^{4+}, with V^{3+} causing absorption at 700 nm and V^{4+} causing the peak at 1100 nm. However, absorption at 1000-1100 nm has been observed in V^{3+}-doped YAG and CdS crystals, so it is quite possible that vanadium is hosted just as V^{3+} in this glass.

It appears from the absorption spectra that transition metal ions are preferentially hosted in tetrahedral sites. From the analysis of the absorption spectra V, Fe and Co all appear to be in tetrahedral sites and Ni may be in tetrahedral or octahedral sites. The absorption spectra of Cu and Ti-doped GLS provide no evidence of the site symmetry. This contrasts with transition metal-doped ZBLA glasses, which are known to host dopant ions in octahedral symmetry [80].

4.3.2 Temperature-dependent fluorescence spectra

In order to observe fluorescence from the transition metal-doped samples, each was pumped at both 800 nm and 1064 nm by Ti:sapphire and Nd:YAG lasers respectively. The experiment was setup as described in section 3.3, using a New Focus extended InGaAs detector (sensitive from 800-2200 nm)

and a Graseby Infrared liquid nitrogen-cooled InSb detector (sensitive from 2000-5000 nm).

Emission was not observed at either pump wavelength from the Fe, Cu, Ti and Co-doped GLS samples over the range 800-5000 nm. The Ti-doped GLS sample was also pumped directly with the Ar^+ laser, but again no fluorescence was observed in the near infrared.

Emission appears to be centred around 1200 nm was observed from the Ni-GLS sample when pumping at 800 nm. Similar emission was also observed on pumping with 900 nm, but with much lower intensity, pumping at 1064 nm did not produce any measurable emission. The emission spectrum on pumping with the 800 nm laser is shown in Fig. 4.17.

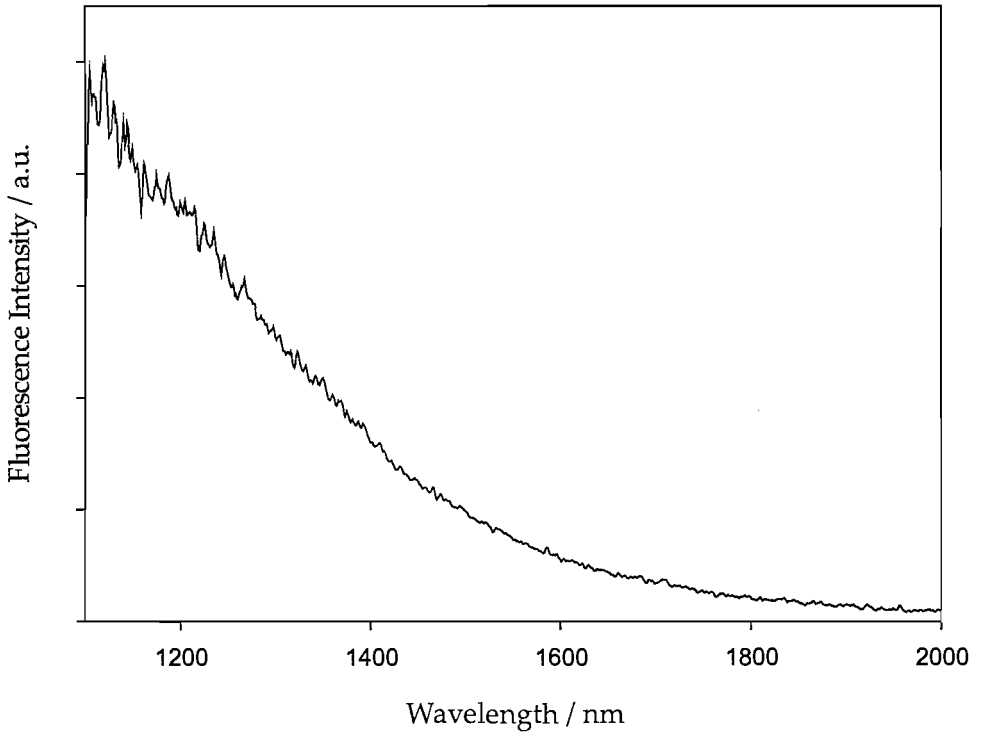

Figure 4.17: Emission spectrum of nickel-doped GLS pumped at 800 nm.

Emission was also observed from the V-doped GLS when pumping both at 800 nm and 1064 nm. The emission intensity was stronger when pumping at 1064 nm than at 800 nm, though quantitative measurements were not made. Figure 4.18 shows the spectrum measured by pumping at 1064 nm.

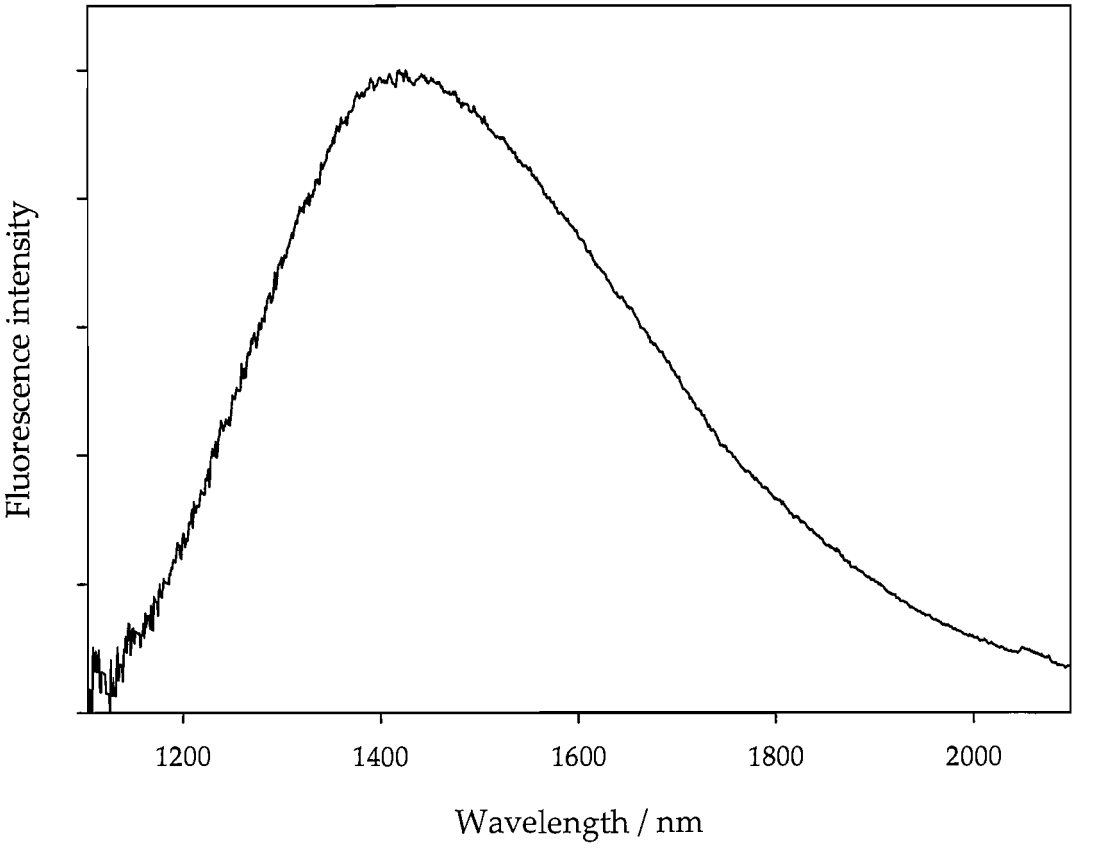

Figure 4.18: Emission spectrum of V-doped GLS pumped at 1064 nm, showing a broad emission with a FWHM of 450 nm.

The emission from V-doped GLS has a FWHM of 450 nm and spans the region from 1200 nm to 2100 nm, peaking at 1420 nm. This is similar to emission spectra recorded from V-doped $LiGaO_2$ and $LiAlO_2$ crystals which span from 1400 nm to 2000 nm, peaking at 1650 nm and 1730 nm respectively [115]. This wavelength range covers all the telecoms bands and makes this glass very interesting as a potential amplifier material.

A further emission spectrum was then taken at 77 K using the setup described in section 3.3.1. The 1064 nm pump was used for this measurement, with the extended InGaAs detector. The resulting spectrum is shown in Fig. 4.19 with the room temperature spectrum for reference.

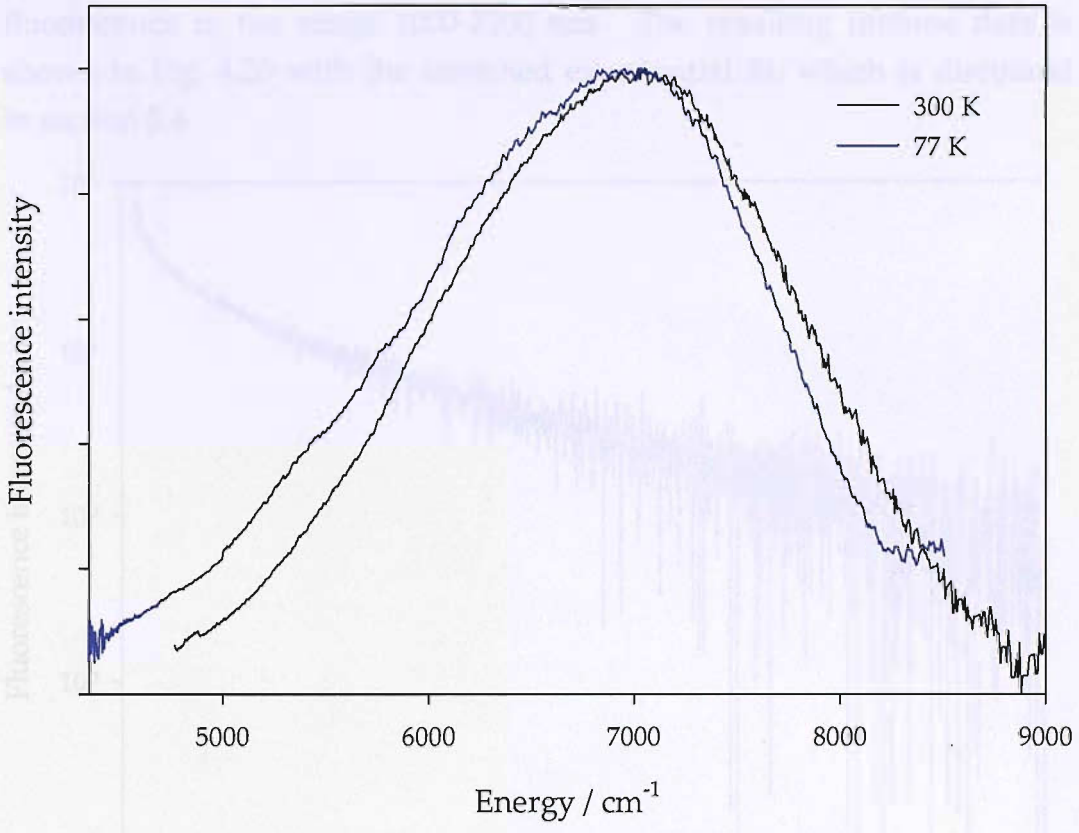

Figure 4.19: Emission spectra of V-doped GLS pumped at 1064 nm at 77 K and 300 K, showing a shift of the emission band to lower energy. The spectra are normalised to peak intensity.

The fluorescence intensity increased at lower temperature and the emission spectrum was shifted to lower energy. These changes were also observed for the Cr-doped samples in section 4.2.2, though both the increase in intensity and shift in energy of the V-doped GLS sample were much less dramatic than for the Cr-doped chalcogenide glasses. The emission peak in V-doped GLS shifted by 100 cm^{-1} at 77 K compared to ~2500 cm^{-1} in the Cr-doped samples.

4.3.3 Temperature-dependent lifetime measurements

Lifetime measurements were made for both the V and Ni-doped GLS samples using the setup described in section 3.4. For the lifetime measurement for Ni-GLS, a silicon filter was placed before an extended InGaAs detector in order to cut out excitation light and measure all

fluorescence in the range 1000-2200 nm. The resulting lifetime data is shown in Fig. 4.20 with the stretched exponential fit, which is discussed in section 3.4.

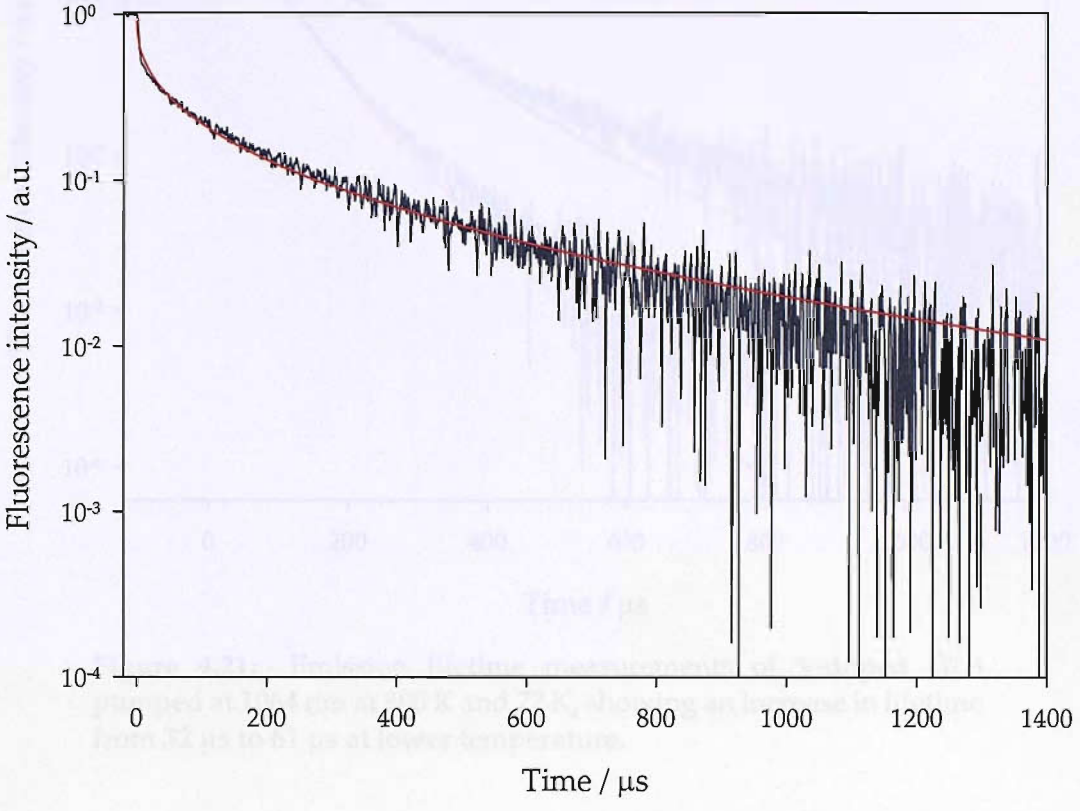

Figure 4.20: Emission lifetime measurements of Ni-doped GLS pumped at 800 nm at room temperature, showing a stretched exponential lifetime of 40 μs.

The stretched exponential lifetime for Ni-doped GLS is 40 μs at room temperature. This is 20 times greater than the lifetime of the Cr-doped chalcogenide glasses. However, the decay is highly non-exponential, with a stretch factor of 0.42.

Lifetime data for the V-doped GLS sample was obtained using the same setup as used for the Ni-doped sample, except a Nd:YAG laser was used as the pump. A semiconductor filter with a bandgap at 1200 nm was placed in front of the detector so that emission over the range 1200-2200 nm was collected. The same measurement was repeated with the V-doped GLS sample in a cryostat at 77 K . The data obtained is shown in Fig. 4.21 with stretched exponential fits.

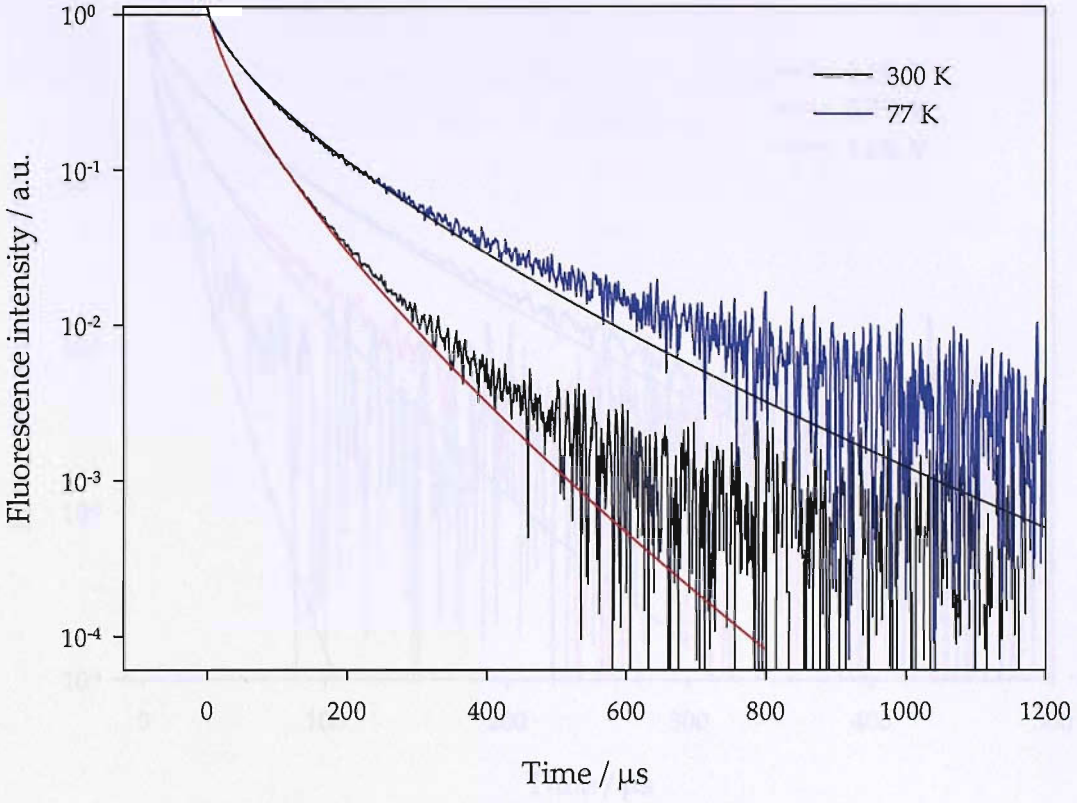

Figure 4.21: Emission lifetime measurements of V-doped GLS pumped at 1064 nm at 300 K and 77 K, showing an increase in lifetime from 32 μs to 61 μs at lower temperature.

The lifetimes measured for V-doped GLS were 32 μs at 300 K and 61 μs at 77 K, with stretch factors of 0.70 and 0.69 respectively. This room temperature lifetime is longer than the lifetime of V-doped $LiGaO_2$ and $LiAlO_2$ which showed room temperature lifetimes of 11 μs and 0.5 μs respectively.

In order to investigate the concentration dependence of the emission lifetime in V-doped GLS, three more GLS samples were obtained with V concentrations of 0.1%, 0.5% and 1.0%. Lifetime data for these glasses is shown in Fig. 4.22.

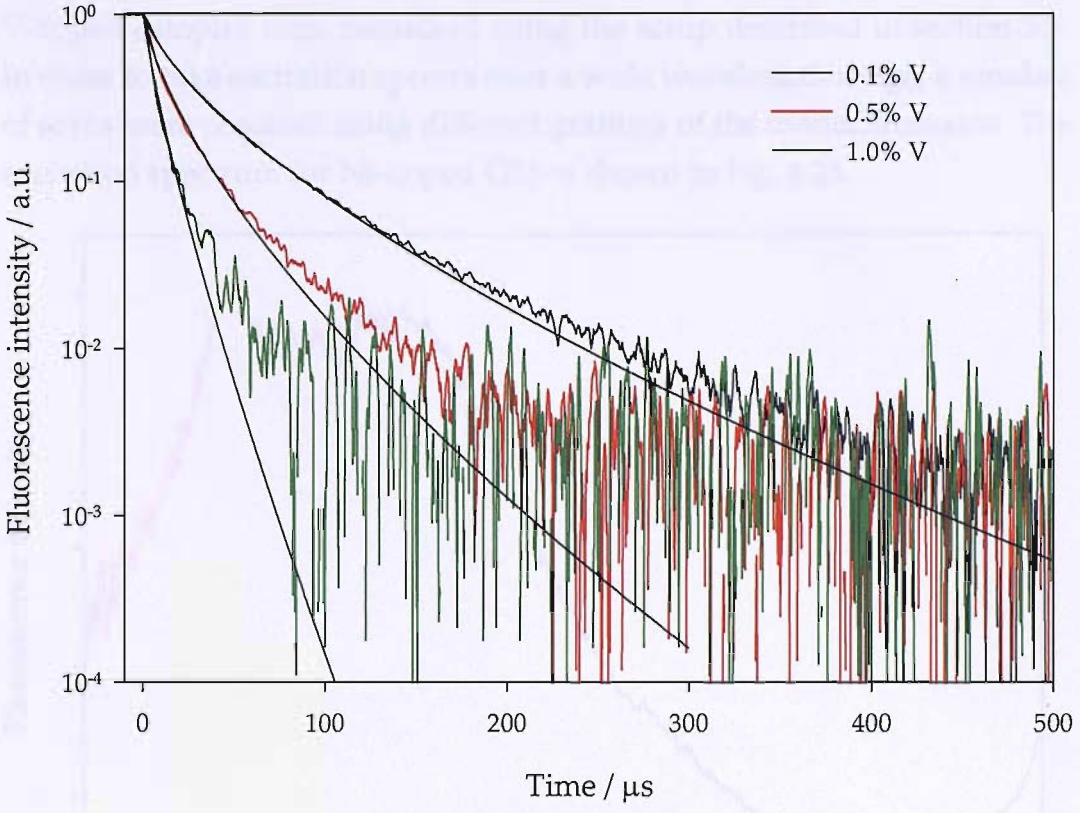

Figure 4.22: Emission lifetime measurements of V-doped GLS with V concentrations of 0.1%, 0.5% and 1.0%, showing stretched exponential lifetime fits of 24 μs, 12 μs and 7 μs respectively.

The GLS samples with 0.1%, 0.5% and 1.0% vanadium showed lifetimes of 24 μs, 12 μs and 7 μs, with stretch factors of 0.68, 0.70 and 0.82 respectively. The increase in the stretch factor is likely in this case to be a result of the decreasing quality of the data as the vanadium concentration is increased, which was a result of a decreased fluorescence intensity. The fact that the lifetime of the 0.1% V-doped sample is less than that observed in the original sample (32 μs, shown in Fig. 4.21), shows that concentration quenching is occurring even in the 0.1% V-doped GLS sample.

4.3.4 Fluorescence excitation spectra

Fluorescence excitation measurements can provide useful additional information on the positions of energy levels in doped solids. The information provided by absorption spectra in GLS glasses is particularly limited by the position of the electronic absorption edge. Excitation spectra of the Ni and

V-doped samples were measured using the setup described in section 3.5. In order to take excitation spectra over a wide wavelength range, a number of scans were required using different gratings of the monochromator. The excitation spectrum for Ni-doped GLS is shown in Fig. 4.23.

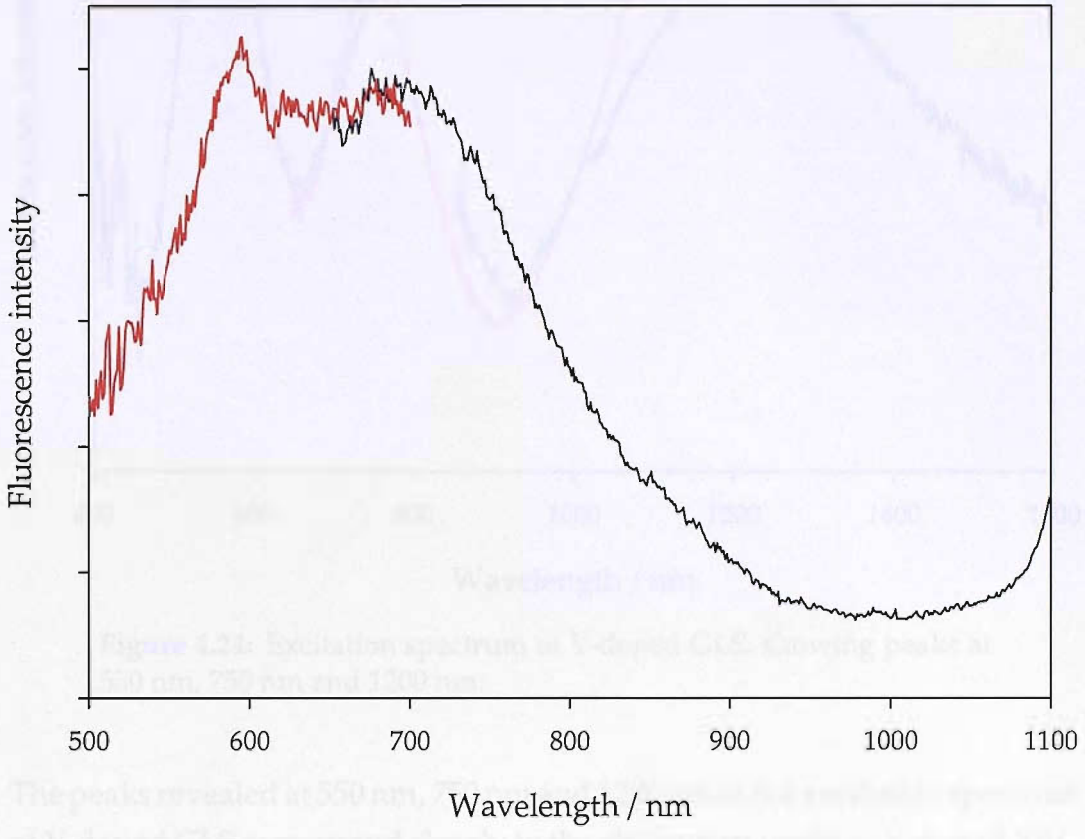

Figure 4.23: Excitation spectrum of Ni-doped GLS, collecting emission from 1000-2200 nm showing a single band centred around 650 nm.

The excitation spectrum for Ni-doped GLS appears to have a peak between 600-700 nm which extends out to 950 nm. This follows the absorption spectrum shown in Fig. 4.12, however as the excitation wavelength approaches the bandgap absorption of GLS (~650 nm) absorption of the glass host will deform the measured spectrum.

The excitation spectrum for V-doped GLS is shown in Fig. 4.24. This excitation spectrum reveals more detail than is shown in the absorption spectrum of V-doped GLS (Fig. 4.11). Three distinct peaks are observed at 550 nm, 750 nm and 1200 nm.

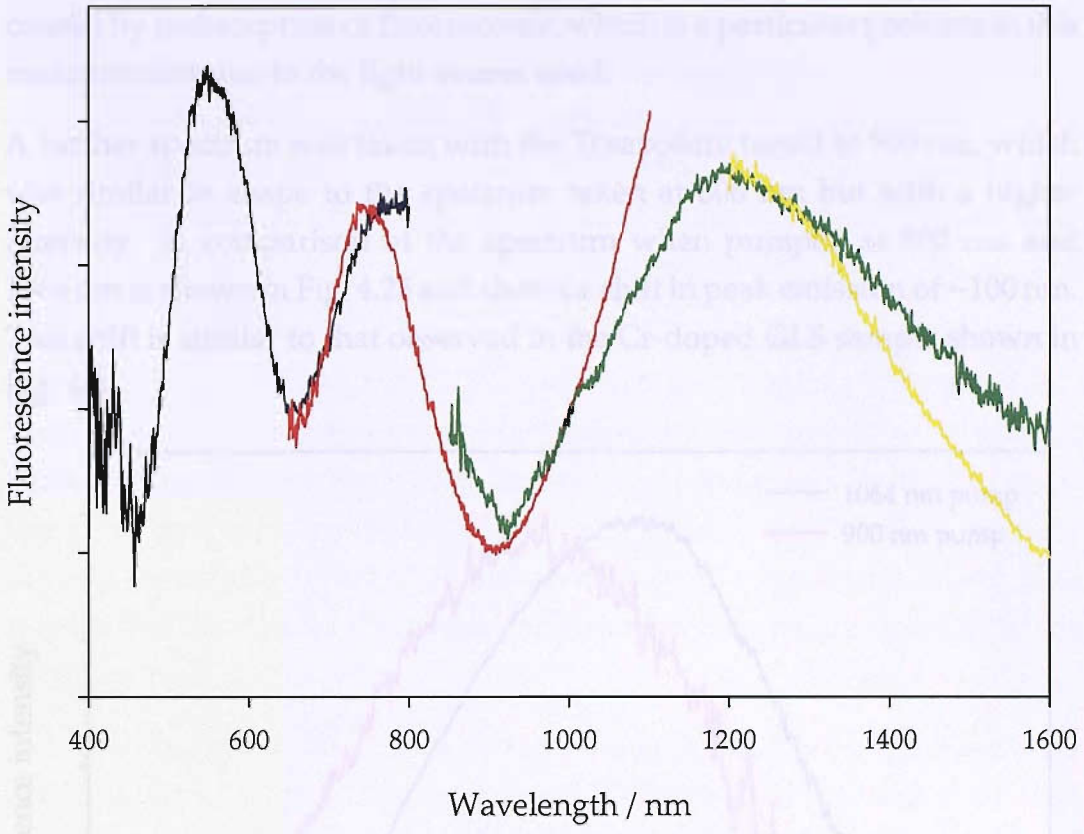

Figure 4.24: Excitation spectrum of V-doped GLS, showing peaks at 550 nm, 750 nm and 1200 nm.

The peaks revealed at 550 nm, 750 nm and 1200 nm in the excitation spectrum of V-doped GLS correspond closely to the absorption peaks of V-doped YAG which were measured at 590 nm, 800 nm and 1250 nm [110]. A comparison with the absorption spectrum of V-doped GLS (Fig. 4.11) shows a difference in the longest wavelength peak which is centred at 1100 nm in the absorption spectrum and 1200 nm in the excitation spectrum. It is important here to distinguish between the set of ions which contribute to the absorption spectrum and those which contribute to the excitation spectrum. Ions in all sites in the material will absorb incoming light of certain wavelengths and contribute to the absorption spectrum. However, in fluorescence excitation measurements, only ions which lead to fluorescence contribute to the spectrum. Considering the fact that nonradiative decay preferentially affects ions in low crystal field sites, it is expected that excitation spectra may be shifted to higher energy with respect to absorption spectra. However, the opposite is true in the spectra of V-doped GLS. This shift could be

caused by reabsorption of fluorescence, which is a particular problem in this measurement due to the light source used.

A further spectrum was taken with the Ti:sapphire tuned to 900 nm, which was similar in shape to the spectrum taken at 800 nm but with a higher intensity. A comparison of the spectrum when pumped at 900 nm and 1064 nm is shown in Fig. 4.25 and shows a shift in peak emission of ~100 nm. This shift is similar to that observed in the Cr-doped GLS sample shown in Fig. 4.8.

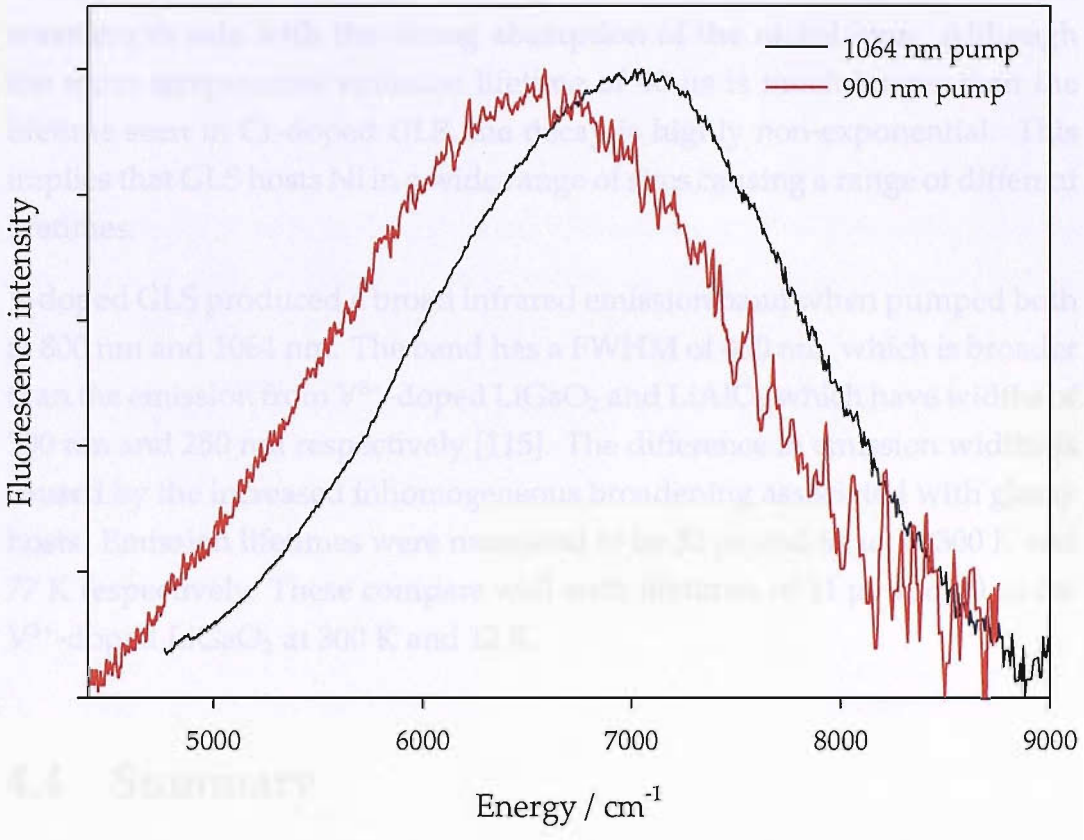

Figure 4.25: Emission spectra of V-doped GLS pumped at 1064 nm and 900 nm, showing a shift in emission peak of ~500 cm^{-1} (~100 nm).

4.3.5 Conclusions

A spectroscopic survey of a range of transition metal-doped GLS glasses was carried out. Absorption spectra revealed possible valence states of the dopant ions and emission was observed for two of the samples.

The valence states of the dopant ions were identified and are presented in table 4.1. The absorption bands observed in these materials are generally broader than corresponding bands in crystals, and absorption peaks are at lower energy than seen in crystals. The broader bands are caused by the wider distribution of crystal field strengths at different sites in the glass. The peaks are shifted to lower energy because molecules in a glass host are less tightly packed than those of a crystal host.

Emission was observed from Ni-doped GLS on pumping with a 800 nm laser. The emission band appears very broad, but also overlaps at the short wavelength side with the strong absorption of the nickel ions. Although the room temperature emission lifetime of 40 μs is much longer than the lifetime seen in Cr-doped GLS, the decay is highly non-exponential. This implies that GLS hosts Ni in a wide range of sites causing a range of different lifetimes.

V-doped GLS produced a broad infrared emission band when pumped both at 800 nm and 1064 nm. The band has a FWHM of 450 nm, which is broader than the emission from V^{3+}-doped $LiGaO_2$ and $LiAlO_2$ which have widths of 300 nm and 250 nm respectively [115]. The difference in emission widths is caused by the increased inhomogeneous broadening associated with glassy hosts. Emission lifetimes were measured to be 32 μs and 61 μs at 300 K and 77 K respectively. These compare well with lifetimes of 11 μs and 80 μs for V^{3+}-doped $LiGaO_2$ at 300 K and 12 K.

4.4 Summary

A range of transition metal-doped chalcogenide glasses were studied as possible new active optical materials. The study of different Cr-doped chalcogenide glasses provides more evidence that chromium is hosted in its tetravalent state in these materials. The survey of other transition metal-doped GLS glasses revealed, for the first time, emission from Ni and V-doped chalcogenide glasses.

Low temperature fluorescence measurements of the Cr-doped chalcogenide glasses suggest that nonradiative decay would be a problem in using these

materials as efficient infrared devices. The higher quantum efficiency of the Cr-doped As_2S_3 sample suggests that this may be a good choice for further study. However, the emission from the As_2S_3 sample was shifted away from the telecoms window and the fact that this glass is toxic makes this glass far from ideal.

Absorption and emission spectra measured for the other transition metal-doped samples were used to assess possible valence states and site symmetries of dopant ions. A qualitative approach was used because the absorption edge at ~700 nm obscures higher energy absorption peaks. The valence states and site symmetries assigned to each ion in this chapter are summarised in table 4.1. The assignments agree broadly with those made by Petrovich in a previous study of these materials [90], though it was shown in this work that V^{3+} alone may account for features in the absorption spectrum, not V^{3+} and V^{4+} as previously stated. However, it is unlikely that dopant ions appear only in these valence states, but these are the valence states which cause the main spectral features.

Dopant	Electronic structure	Likely valence state in GLS glass	Likely symmetry in GLS glass
Cr	[Ar]$3d^2$	Cr^{4+}	Tetrahedral
V	[Ar]$3d^2$	V^{3+}	Tetrahedral
Ni	[Ar]$3d^8$	Ni^{2+}	Octahedral
Ti	[Ar]$3d^0$	Ti^{4+}	*
Fe	[Ar]$3d^6$	Fe^{2+}	Tetrahedral
Co	[Ar]$3d^7$	Co^{2+}	Tetrahedral
Cu	[Ar]$3d^{10}$	Cu^{+}	*

Table 4.1: Electronic structure and likely valence state and site symmetry of transition metal dopant ions in GLS glass. * There was no evidence for the site symmetry for these ions.

Emission was not observed from the Co, Cu, Fe and Ti-doped samples and so these materials appear not to be useful for active optical applications. The broad infrared absorption bands seen in both Fe and Co-doped GLS mean that these glasses are unlikely to be useful in the near infrared. The Cu and Ti-doped glasses are also unlikely to make useful active materials due to the lack of absorption bands in the transparent range of GLS.

Emission was measured for the first time from Ni-doped GLS glass. Pumping at 800 nm produced emission centred around 1200 nm extending out as far as 1800 nm. The shorter wavelength side of the emission overlaps with the strong absorption peak at ~900 nm. This strong absorption band also presents a difficulty in evaluating the fluorescence excitation spectrum where a single broad peak was observed at ~650 nm.

Emission was also observed for the first time in V-doped GLS glass. The emission had a FWHM of 450 nm and peaks at 1420 nm. Low temperature fluorescence spectra suggest that nonradiative decay does not affect this material to the same extent as in the Cr-doped glasses. This material is an interesting candidate for a new active optical material.

4.5 Further work

There is much scope for expanding on the current results presented in this chapter. It would be interesting to produce both V and Ni-doped As_2S_3 samples to see this glass also hosts these ions at higher crystal field sites. Because the Ga:Na:S glass has better visible transmission than GLS, Ga:Na:S could be used as a host for a Ni-doped sample in order to reveal more of the absorption structure at shorter wavelengths.

Useful further work concerning the use of these materials in practical devices would include studies of excited state absorption (ESA). It is vital that a wavelength region exists where stimulated emission exceeds ESA if a material is going to be used as a gain medium.

Chapter 5

Rare earth-doped tin silicate glass-ceramics

5.1 Introduction

In this chapter, erbium- and thulium-doped tin silicate glasses are studied as potential new active materials in the near infrared. Raman spectra and infrared and ultraviolet absorption spectra were measured to characterise the host material, then fluorescence and fluorescence lifetime measurements were carried out to study the properties of dopant ions. The samples studied were produced by the sol-gel method and contain different concentrations of rare earth, hydroxyl and tin.

The main advantage of producing silica by the sol-gel method over more conventional methods (MCVD, melt casting) is that a wide range of dopants can be incorporated at relatively high concentration without devitrification. The sol-gel method can be used to produce high purity, homogeneous films or bulk glasses at low temperatures and at potentially low cost [127]. These properties make sol-gel-produced silica glasses potentially useful materials for active optical devices.

The fabrication of glass by the sol-gel method starts with the formation of a gel from a solution of the glass components. The gel is then dried and sintered to form glass. The sol-gel process for tin silicate glasses is outlined in Fig. 5.1 and starts with solutions of organic precursors of the glass

components. The glass composition can be altered by changing the ratio of the reactants and dopants can be incorporated by adding an appropriate organic precursor. These solutions are mixed with water and gelation occurs by hydrolysis. The gel is then dried to form a porous, low density solid material called a xerogel, which contains the glass components, organic reagents and often some residual water. Xerogels are more than 50% air, so in order to form the consolidated glass, the xerogel is subjected to a heat treatment at a temperature above the glass transition. Further details of the procedure used to make the tin silicates studied in this chapter are given elsewhere [128].

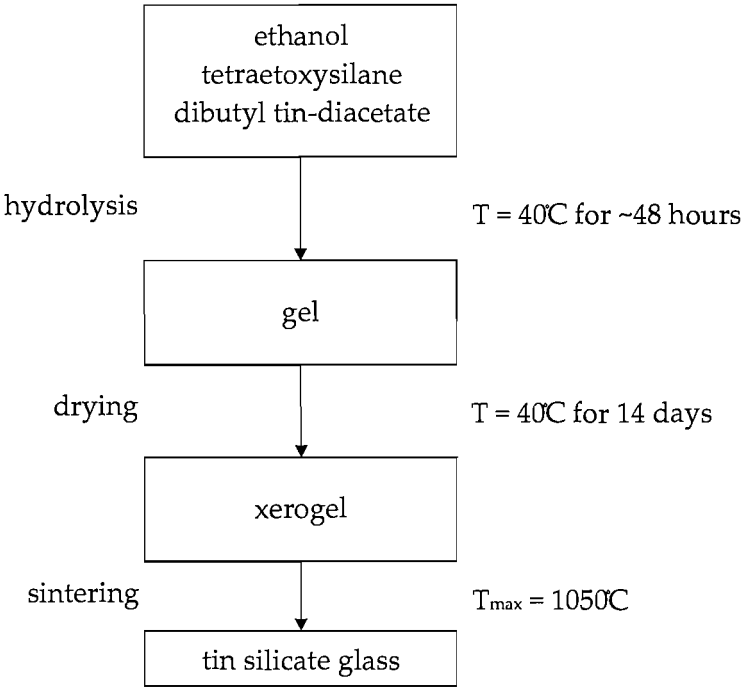

Figure 5.1: An overview of the sol-gel method for fabricating tin silicate glass.

There have been studies on several sol-gel-produced erbium-doped silica glasses in the search for suitable materials for erbium-doped waveguide amplifiers (EDWA). The first report of net gain from a sol-gel EDWA used SiO_2-P_2O_5 as the host [129]. Various silica-based host compositions have been studied including pure SiO_2 [130], SiO_2-TiO_2 [131], SiO_2-Al_2O_3 [132], SiO_2-TiO_2-Al_2O_3 [133] and SiO_2-GeO_2 [134]. Doping with TiO_2 allows good control of the refractive index of the glass and adding Al_2O_3 to silica inhibits clustering of Er^{3+} ions. GeO_2 has a lower maximum phonon energy than

SiO_2 and so may allow for more efficient optical transitions; it is also photosensitive and therefore allows UV-writing of permanent refractive index changes.

Photosensitive germanosilicate glass fibre was first reported in 1978 and has since proved an important material for optical telecoms applications [135]. More recently, tin-codoped germanosilicate and tin-doped silica optical fibres have been fabricated which show photo-induced refractive index changes three times larger than that shown in germanosilicate fibers. These glasses show good thermal stability of the refractive index change and tin-doping does not affect transmission at telecoms wavelengths [136]. Photosensitivity in materials for planar devices is desirable so that direct writing of waveguide structures and Bragg gratings within these waveguides can be achieved.

There have been several studies of tin silicate glasses prepared by the sol-gel method [128, 137] including investigations into the mechanisms responsible for the photosensitivity [138] and the effect of SnO_2-doping on the Raman spectrum [139]. A study of erbium-doped tin silicate glass confirmed that this composition retains the photosensitivity of only tin-doped silica and that the fluorescence properties of erbium were not affected by the tin doping [140]. It was reported in one of the early publications on sol-gel-produced tin silicate glass that nanocrystals of SnO_2 were formed in compositions with higher tin concentrations [128]. There have since been several studies of this glass-ceramic material [141–143], which reported UV absorption, Raman and transmission electron microscope analysis. An investigation into the photosensitivity of tin silicate glass-ceramics reported a UV-induced negative refractive index change of the same strength as that shown by tin-doped silica glass [144, 145].

One study of erbium-doped tin silicate glass-ceramics fabricated by the sol-gel method reported that erbium ions are embedded in low phonon energy SnO_2 nanoclusters in these materials [142]. However, this was not confirmed by another study of these materials in which it was shown that erbium ions are not hosted in SnO_2 crystals [146].

In this chapter, a range of thulium- and erbium-doped tin silicate glass-ceramics containing different concentrations of rare earth, tin oxide and

hydroxyl are characterised using Raman, absorption and emission spectroscopy. This is the first reported study of thulium-doped tin silicate glass-ceramics. The samples were fabricated by the sol-gel method by Norberto Chiodini and Alberto Paleari from the Universitá di Milano-Bicocca. The samples were produced in the form of 1 mm thick discs with a 10 mm diameter.

5.2 Raman spectra

The vibrational structure of each of the samples was examined through Raman spectroscopy, using the procedure described in section 3.2. The Raman spectrum of the 15% SnO_2, 1000 ppm wt. Tm^{3+}-doped sample is shown in Fig. 5.2. The Raman spectra of the other samples differed only in the magnitude of the SnO_2 peak, which scales approximately with SnO_2 concentration.

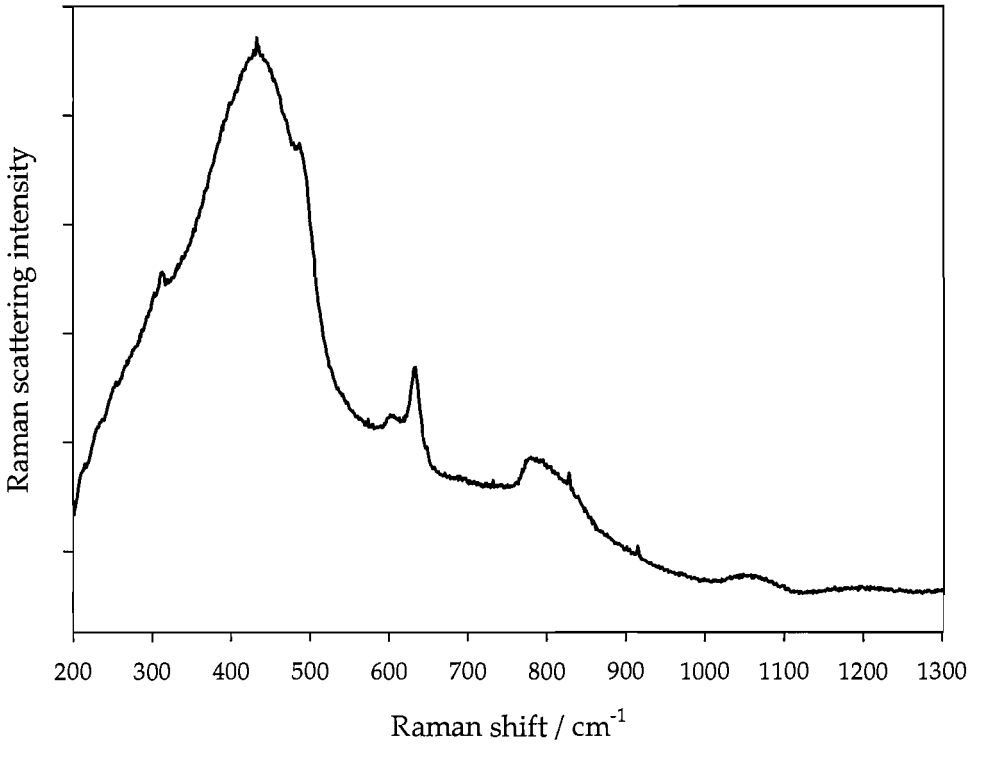

Figure 5.2: Raman spectrum of the 15% SnO_2 1000 ppm Tm^{3+}-doped sample, showing the characteristic vibrational modes of amorphous silica with the crystalline SnO_2 peak at 630 cm^{-1}.

The general form of the vibrational structure is that of amorphous silica [147, 148] with the addition of a sharp peak at 630 cm^{-1}, which is caused by the presence of crystalline SnO_2 [149]. This peak scales approximately with SnO_2 concentration, and confirms that all the samples studied contain the crystalline phase of SnO_2 and are therefore glass-ceramics. This SnO_2 peak has been observed previously in tin silicates produced by the sol-gel method and was found to exist only in samples with >0.8% SnO_2 [141].

Previous studies of the Raman spectra of nanometer-sized SnO_2 crystals reported two peaks which are not present in single-crystal or polycrystalline SnO_2 [149]. These surface-related modes appear at 358 cm^{-1} and 572 cm^{-1}. When the crystal size is less than 5 nm the peak at 630 cm^{-1} will be of similar strength to the 572 cm^{-1} peak [149, 150]. The 358 cm^{-1} peak will not be observed unless the crystalline size is <13 nm. Since neither peak is observed here, it could be inferred that the average size of the crystals is >13 nm. However, previous studies of tin silicate glass-ceramics produced by the sol-gel method have shown through transmission electron microscopy that these materials contain crystals of dimensions <10 nm [144, 145]. This suggests that these surface modes are not preserved when SnO_2 nanocrystals are incorporated into glasses. Crystal size and distribution are important properties for transparent glass-ceramics. It has been shown that in order to obtain low loss glass-ceramics in the order of tens of dB/km, the particle size should be <15 nm, the particle size distribution should be small and the interparticle spacing should be comparable to the particle size [50]. It has been shown that crystallisation in tin silicate glass-ceramics can be controlled both by altering the composition and by changing the thermal treatment [141].

5.3 Infrared absorption of hydroxyl groups

A high concentration of hydroxyl groups is undesirable for photonics applications because they have an absorption peak in the telecoms window and because they act as quenching sites during energy migration in an active material. Glasses produced by the sol-gel method often contain high concentrations of hydroxyl due to the central role of water in the fabrication

process. The hydroxyl absorption which coincides with part of the telecoms window is centred at ~1400 nm and the strength of this absorption band can be used to determine the hydroxyl concentration. However, this absorption arises from the first OH-stretching overtone and is much weaker than the absorption of the fundamental vibration [151]. Since the tin silicate samples were just 1 mm thick, it was more appropriate to measure the intensity of the fundamental OH-stretching mode which occurs further in the infrared at ~2700 nm. The fundamental hydroxyl absorption of each of the tin silicate samples was measured by Fourier transform infrared spectroscopy (FTIR). Experimental details are given in section 3.1.1 and the results for the Er-doped samples are shown in Fig. 5.3. The background absorption slope was subtracted from each spectrum so that the intensity of the hydroxyl band could be more easily measured.

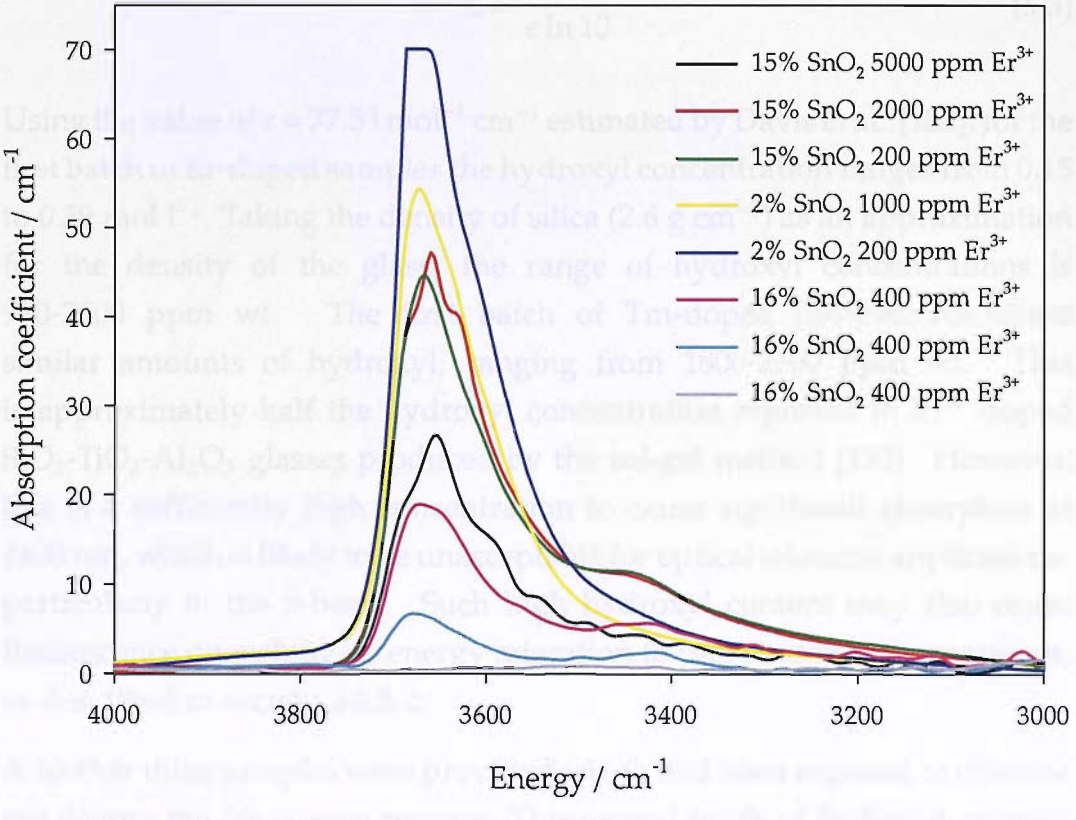

Figure 5.3: FTIR spectra of Er-doped tin silicate glass-ceramics, showing the range of strengths of the fundamental OH-stretching absorption. The background absorption slope has been subtracted from each spectrum.

The Beer-Lambert law can be used to calculate the hydroxyl concentration in the samples:

$$C = \frac{A}{\epsilon L}, \tag{5.1}$$

where C is the concentration of the absorbing species, A is the maximum height of the absorption band ($A = \log[I_{in}/I_{out}]$), ϵ is the extinction coefficient of the absorbing species (in this case it is the molar absorptivity of the OH stretching band) and L is the path length through the sample. All absorption measurements in this thesis are given as absorption coefficients α:

$$\alpha = \frac{A}{L} \ln 10, \tag{5.2}$$

so the concentration of hydroxyl groups is given by:

$$C = \frac{\alpha}{\epsilon \ln 10} \tag{5.3}$$

Using the value of $\epsilon = 77.5\,\mathrm{l\,mol^{-1}\,cm^{-1}}$ estimated by Davis et al. [152], for the first batch of Er-doped samples the hydroxyl concentration ranges from 0.15 to 0.39 mol $\mathrm{l^{-1}}$. Taking the density of silica (2.6 g $\mathrm{cm^{-3}}$) as an approximation for the density of the glass, the range of hydroxyl concentrations is 980-2600 ppm wt. The first batch of Tm-doped samples contained similar amounts of hydroxyl, ranging from 1800-2300 ppm wt. This is approximately half the hydroxyl concentration reported in Er^{3+}-doped SiO_2-TiO_2-Al_2O_3 glasses produced by the sol-gel method [133]. However, this is a sufficiently high concentration to cause significant absorption at 1400 nm, which is likely to be unacceptable for optical telecoms applications, particularly in the S-band. Such high hydroxyl content may also cause fluorescence quenching by energy migration to trap sites in these materials, as described in section 2.2.5.2.

A further three samples were provided which had been exposed to chlorine gas during the fabrication process. This second batch of Er-doped samples contain 700 ppm wt. 250 ppm wt. and ~0 ppm wt. hydroxyl and the second batch of Tm-doped samples all contain ~100 ppm wt. hydroxyl. The second batch of Er-doped samples will be used to assess the effect of hydroxyl concentration on the emission properties in sections 5.5.2 and 5.5.3.

5.4 Ultraviolet absorption edge

Ultraviolet and visible absorption measurements were made for all the samples using the Varian Cary 500 spectrophotometer as described in section 3.1. The measurements were made with a resolution of 1 nm.

The UV absorption spectra of all the samples are shown in Fig. 5.4, with absorption coefficient plotted against energy in eV. The spectra show absorption edges at ~3.5 eV which arise from the onset of the electronic bandgap absorption of SnO_2 [153]. The position of the UV edge shifts with the average crystal size and so gives an indication of the mean size of the nanocrystals in the glass-ceramic [154]. These spectra show that samples with higher SnO_2 concentrations have UV edges that are shifted to lower energy; this indicates larger SnO_2 crystals. The 16% SnO_2 samples show greater absorption towards lower energy. These samples were produced in a separate batch, and may contain different amounts of impurities.

The 15% SnO_2 5000 ppm Er^{3+} sample, which is marked on the figure by an asterisk, appears from the UV spectra to contain more than 15% SnO_2 because it is shifted further to lower energy than the other 15% and 16% SnO_2 samples.

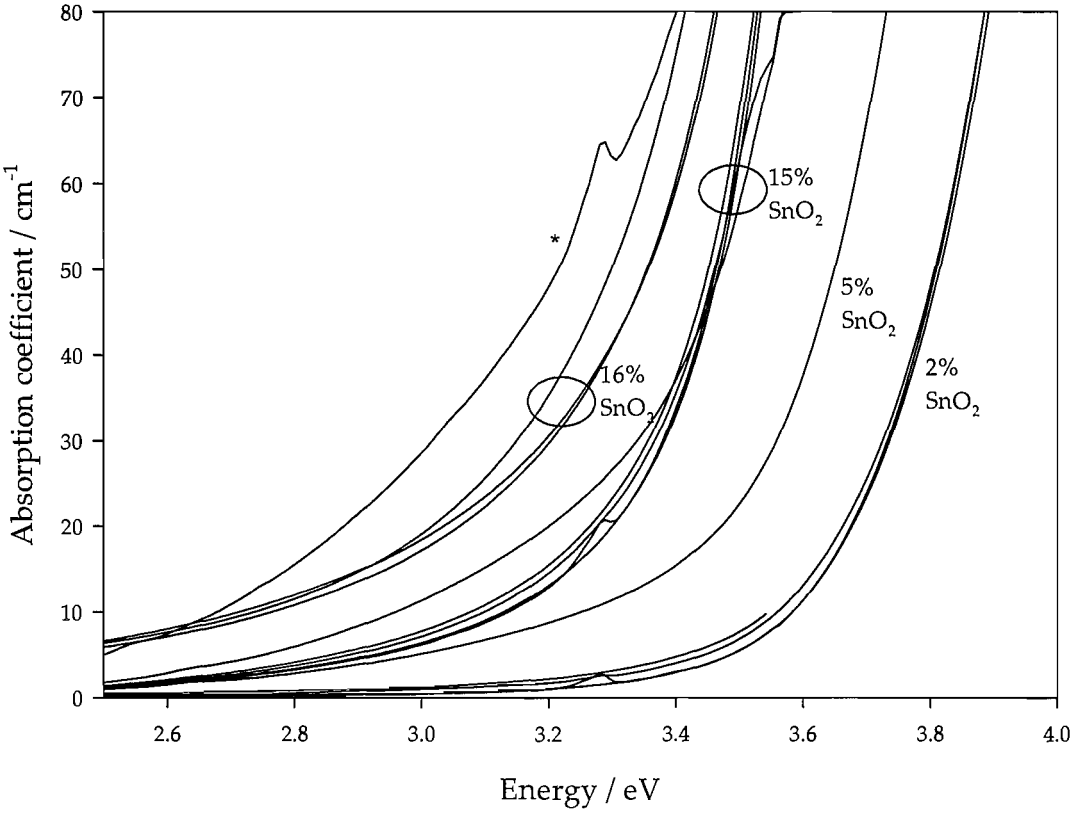

Figure 5.4: UV absorption edges of all tin silicate samples. *The UV edge of this 15% SnO_2 5000 ppm Er^{3+} sample suggests that it may actually contain more than 15% SnO_2.

5.5 Erbium-doped tin silicate glass-ceramics

Figure 5.5 shows a partial energy level diagram for Er^{3+} with the relevant transitions. The important emission for telecoms applications is at 1550 nm from the $^4I_{13/2}$ energy level, which can be excited in-band at ~1480 nm or indirectly at shorter wavelengths.

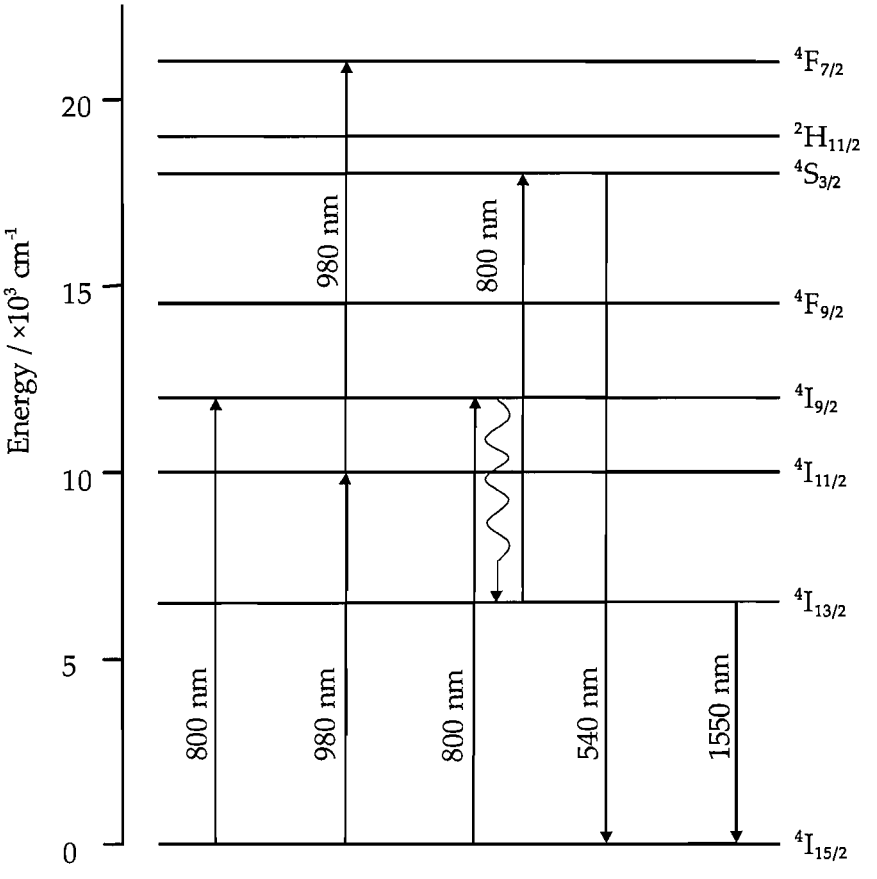

Figure 5.5: A partial energy level diagram for Er^{3+}, showing the relevant transitions.

Excitation to the $^4F_{7/2}$ can occur through ESA or upconversion, and is only efficient in low-phonon hosts. This is followed by nonradiative relaxation to the $^4S_{3/2}$ level and radiative emission to the ground state produces green fluorescence at 540 nm.

Table 5.1 lists the concentrations of Er^{3+} and SnO_2 in the samples studied in this work. The second batch of samples with reduced hydroxyl content were doped with 16% SnO_2 and 400 ppm Er^{3+}.

SnO_2 content	Er^{3+} concentration / ppm wt.
2%	200
2%	1000
15%	200
15%	2000
15%	5000

Table 5.1: Concentrations of Er^{3+} and SnO_2 in the samples studied in this work. SnO_2 content is given in molar percent.

5.5.1 Absorption spectra

Absorption spectra for the Er-doped samples are shown in Fig. 5.6. The absorption spectra show the characteristic absorption peaks of Er^{3+}, which are labelled with the corresponding energy levels shown in Fig. 5.5. The discontinuity at 800 nm is a feature of the spectrophotometer. The peak at ~1400 nm is the absorption due to the first stretching overtone of OH^- [151].

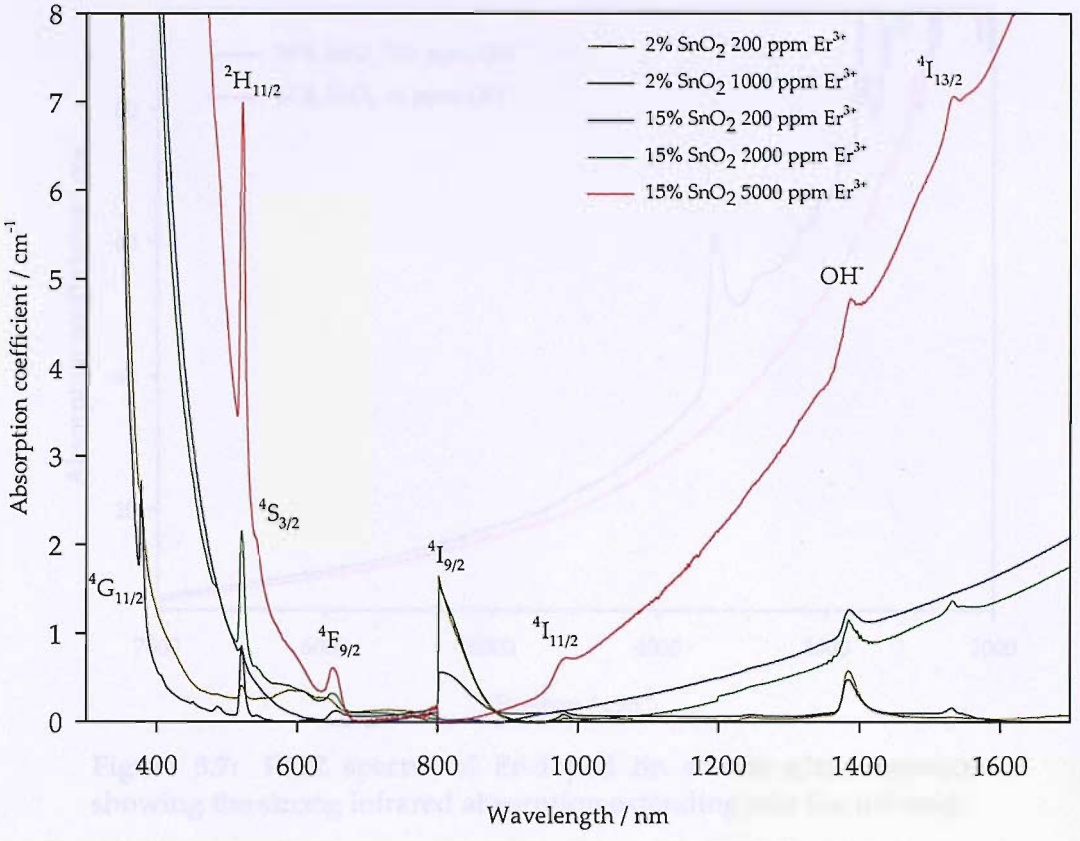

Figure 5.6: Absorption spectra for the Er^{3+}-doped tin silicate glass-ceramics, showing the electronic transitions of Er^{3+}, a hydroxyl absorption peak at 1400 nm and increased infrared absorption for samples with >15% SnO_2.

The strong infrared absorption edge for samples with 15% SnO_2 has not been reported in previous studies of tin silicate glasses or glass-ceramics.

The broad infrared absorption observed in the spectra of the 15% SnO_2 samples was investigated further using FTIR spectroscopy. FTIR absorption measurements were made as described in section 3.1.1 and the spectra of the samples with 200 ppm Er^{3+} are shown in Fig. 5.7. These spectra show the that infrared absorption tail continues into the mid infrared. The peak at 3600 cm^{-1} is due to the fundamental hydroxyl stretching band [155].

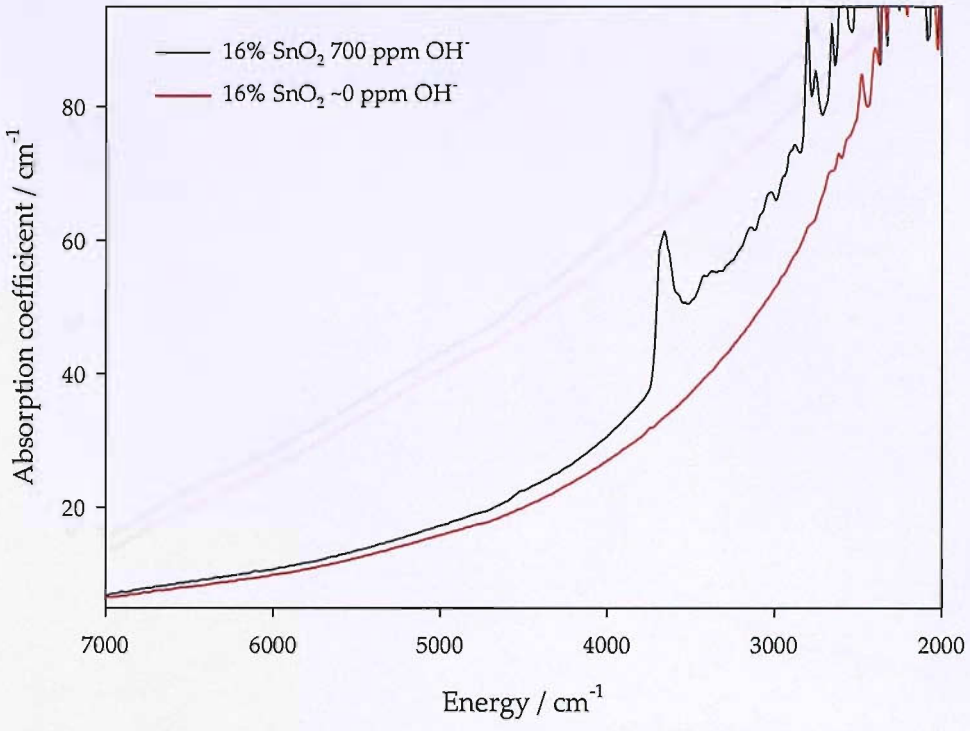

Figure 5.7: FTIR spectra of Er-doped tin silicate glass-ceramics, showing the strong infrared absorption extending into the infrared.

This increase in infrared absorption cannot be explained simply by a shift in the multiphonon absorption edge due to the addition of crystalline SnO_2, because SnO_2 does not have a higher maximum phonon energy than silica. The contribution to the absorption coefficient of multiphonon absorption is given empirically by:

$$\alpha_{mp} = C \exp(-D\nu), \tag{5.4}$$

where C and D are material-dependent constants [81]. When the natural logarithm of the absorption is plotted against wavenumber (which is directly proportional to ν) as in Fig. 5.8, a near linear dependence is shown. This may suggest that the increase in infrared absorption is caused by multiphonon absorption, though it is not clear which vibrations are responsible.

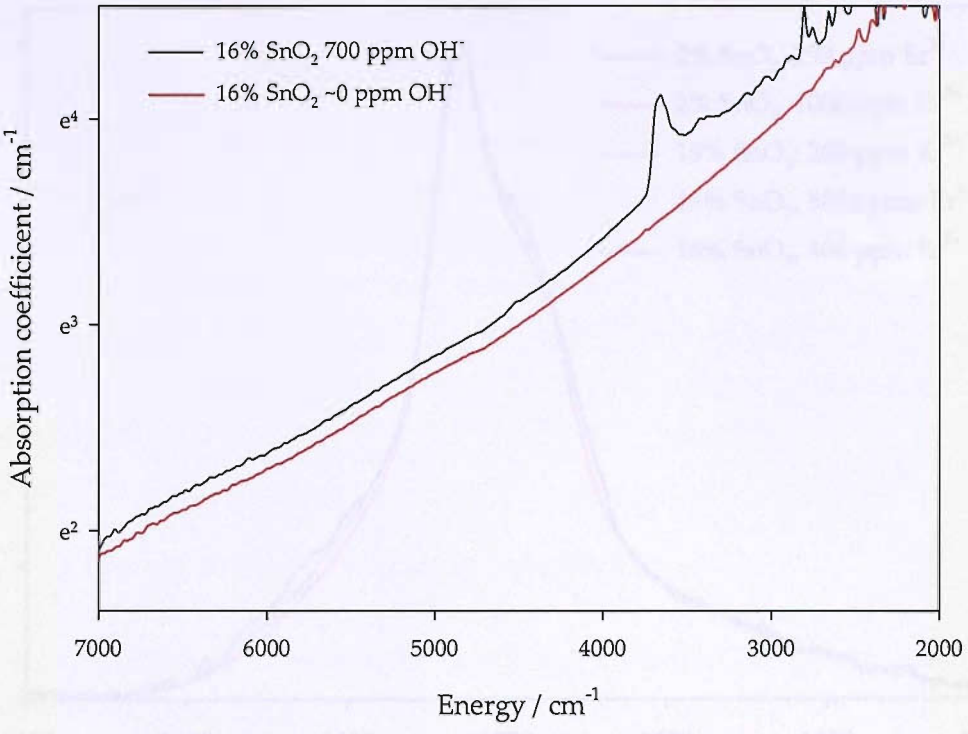

Figure 5.8: Logarithmic plot of the FTIR spectra of Er-doped tin silicate glass-ceramics, showing a near linear dependence of the natural log of the absorption coefficient on the energy.

Though the infrared absorption edge appears to arise from the addition of >2% SnO_2 to the silica glass, the origin of this absorption is not known.

It is interesting to note that the 15% SnO_2 5000 ppm Er^{3+} sample which appears to have >15% SnO_2 from the UV absorption measurements in section 5.4 also shows a larger infrared absorption than the other 15% SnO_2 samples.

5.5.2 Fluorescence spectra

Room temperature emission spectra were taken for all the Er^{3+}-doped glass-ceramics using the technique described in section 3.3 with the Ti:sapphire laser tuned to 800 nm. A silicon filter was placed in front of the monochromator to prevent scattered excitation light from entering the detection system. A representative selection of the emission spectra is shown in Fig. 5.9. The resolution is 11 nm and the spectra are corrected for the spectral response of the system.

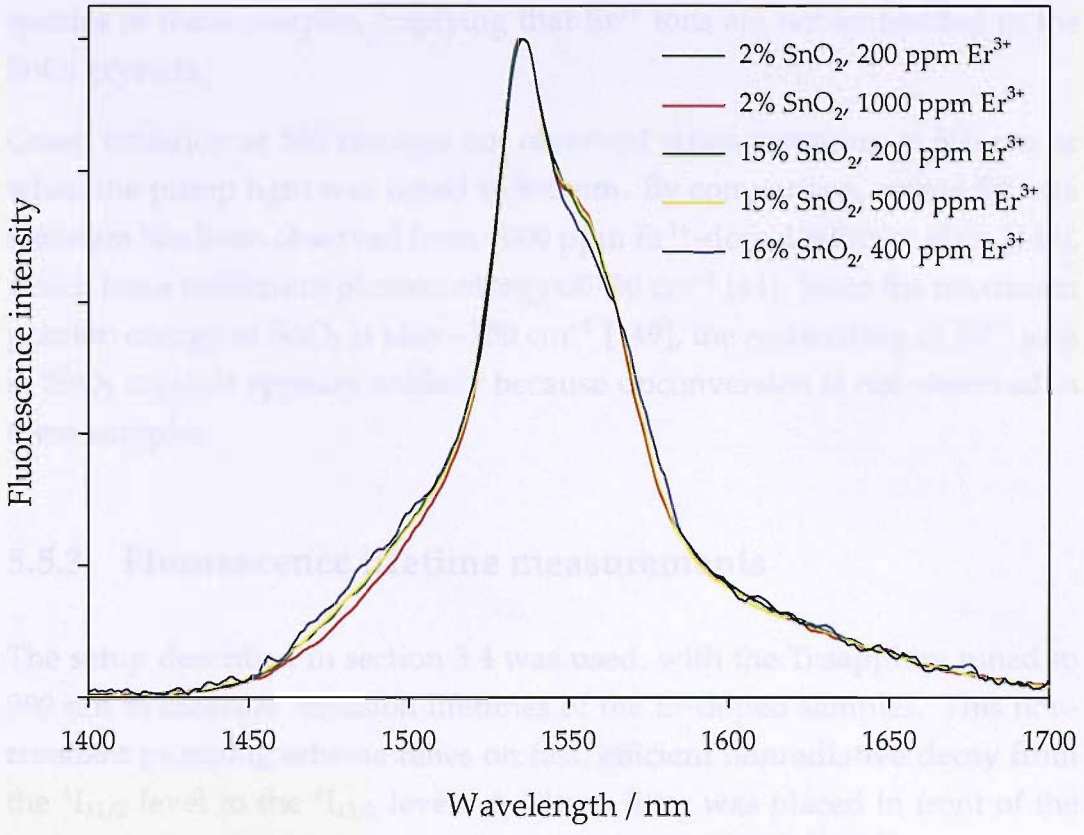

Figure 5.9: Emission spectra from the $^4I_{13/2}$ level in Er^{3+}-doped tin silicate glass-ceramics, showing similar band shapes for samples with different SnO_2 and Er^{3+} concentrations. The 16% SnO_2 sample contains ~0 ppm hydroxyl. The spectra are normalised to peak intensity.

All of the emission spectra showed peaks at 1535 nm and had FWHMs of ~48 nm. This is broader than the emission observed from both sol-gel-produced Er-doped SiO_2 [130] and Er-doped SiO_2-GeO_2 [134] which have FWHMs of 37 nm and 39 nm respectively. This emission is nearly as broad as that measured from Er-doped SiO_2-Al_2O_3 which has a FWHM of 50 nm [130]. This broad emission is a desirable property for amplifiers used in WDM systems and suggests that Er^{3+} ions are hosted is a wide range of sites in these materials.

Samples with different Er^{3+}, SnO_2 and hydroxyl concentrations did not show any differences in the shape of the emission. The incorporation of dopant ions into the crystals would result in some sharper lines in absorption and emission spectra, due to the reduction of inhomogeneous broadening of ions in the crystalline phase. No such sharp features were observed in the

spectra of these samples, implying that Er^{3+} ions are not embedded in the SnO_2 crystals.

Green emission at 540 nm was not observed when pumping at 800 nm or when the pump light was tuned to 980 nm. By comparison, strong 540 nm emission has been observed from 1000 ppm Er^{3+}-doped tellurite glass [146], which has a maximum phonon energy of 750 cm^{-1} [44]. Since the maximum phonon energy of SnO_2 is also ~750 cm^{-1} [149], the embedding of Er^{3+} ions in SnO_2 crystals appears unlikely because upconversion is not observed in these samples.

5.5.3 Fluorescence lifetime measurements

The setup described in section 3.4 was used, with the Ti:sapphire tuned to 980 nm to measure emission lifetimes of the Er-doped samples. This non-resonant pumping scheme relies on fast, efficient nonradiative decay from the $^4I_{11/2}$ level to the $^4I_{13/2}$ level. A silicon filter was placed in front of the detector to prevent measurement of both scattered pump light and emission at 980 nm from the $^4I_{11/2}$ level. The pump beam was focused through an acousto-optic modulator (AOM) using 10× microscope objectives. The resolution of the system was measured to be 5 μs.

The time-dependent emission data with fitted curves are shown in Fig. 5.10 and the lifetime data is summarised in Fig. 5.11. The curves were fitted using the stretched exponential function which is described in section 3.4.

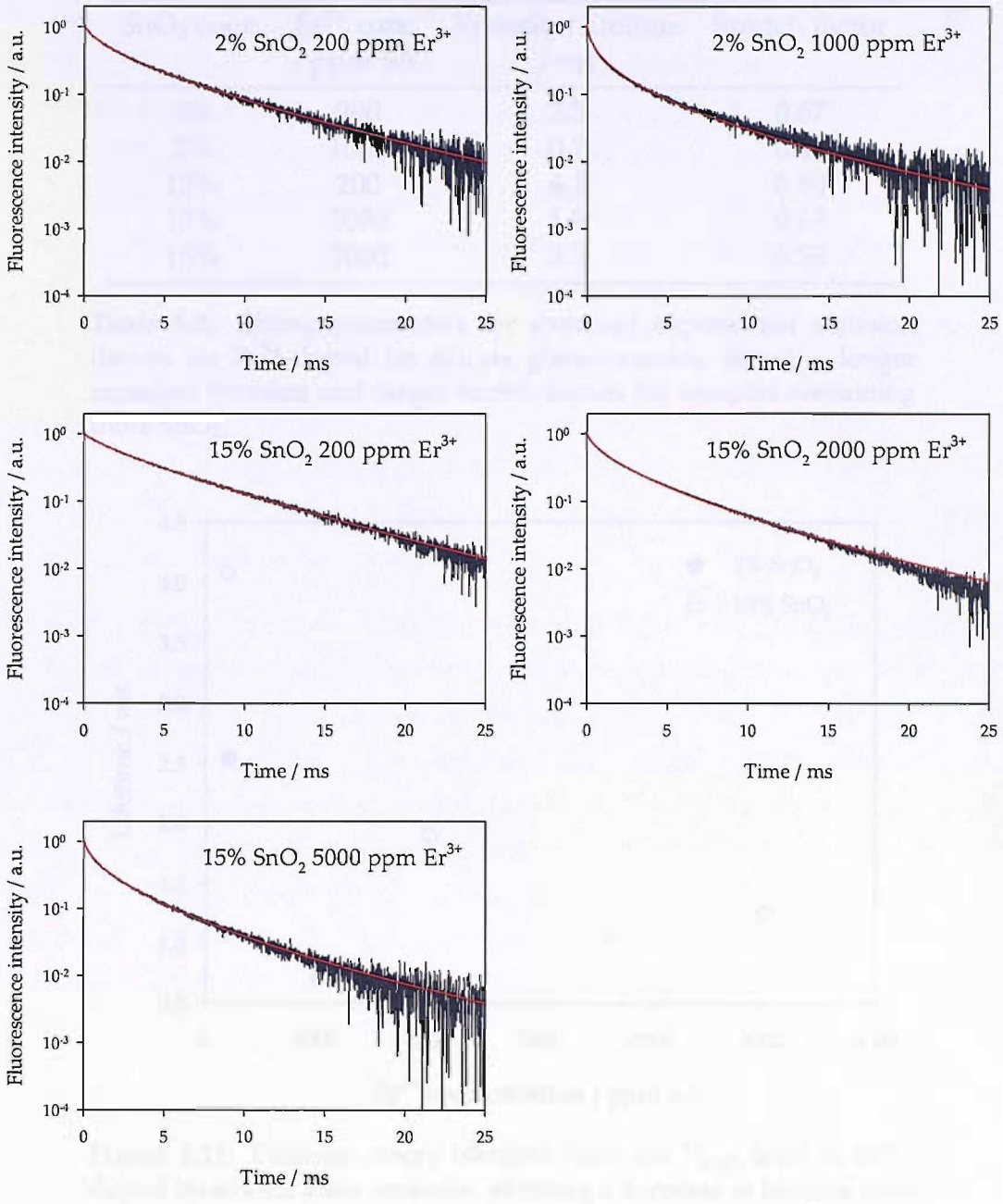

Figure 5.10: Emission decay data from the $^4I_{13/2}$ level in Er^{3+}-doped tin silicate glass-ceramics, showing longer and more exponential decays for samples with higher SnO_2 content.

It is worth noting that although the decay curves are all non-exponential, the lifetime data does not appear as a double exponential decay. A double exponential decay would suggest that the Er^{3+} are hosted in two distinctly different sites in the material, which would be the case if some of the ions were embedded in the SnO_2 nanocrystals.

SnO_2 conc.	Er^{3+} conc. / ppm wt.	Emission lifetime / ms	Stretch factor
2%	200	2.5	0.67
2%	1000	0.7	0.48
15%	200	4.1	0.80
15%	2000	1.9	0.63
15%	5000	1.3	0.58

Table 5.2: Fitting parameters for stretched exponential emission decays for Er^{3+}-doped tin silicate glass-ceramics, showing longer emission lifetimes and larger stretch factors for samples containing more SnO_2.

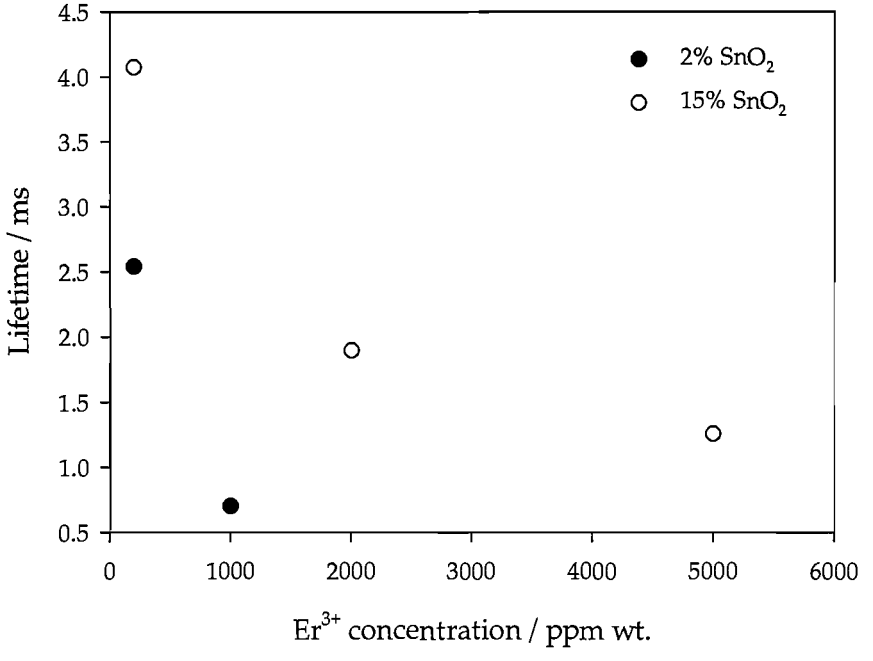

Figure 5.11: Emission decay lifetimes from the $^4I_{13/2}$ level in Er^{3+}-doped tin silicate glass-ceramics, showing a decrease in lifetime with higher Er concentration and with lower SnO_2 content.

Shorter emission lifetimes are observed in samples with higher Er^{3+} concentrations and the 15% SnO_2 samples show longer emission lifetimes than the 2% SnO_2 samples for similar Er^{3+} concentrations. This is in contrast to the case for Er^{3+}-doped tin silicate glasses, for which the tin doping did not affect the fluorescence properties [140]. Samples with higher SnO_2 concentrations also produced decay curves which were closer to exponential behaviour. This can be seen in Fig. 5.10 and is also reflected in the stretch

factors listed in table 5.2. This suggests that interionic interactions causing energy migration to fluorescence traps are reduced in these samples which may be a result of increased disruption of the tightly-packed silica network by the SnO_2 crystals. Another factor which will alter decay rates between 2% and 15% SnO_2 samples is the difference in refractive index. The spontaneous emission rate is dependent on the refractive index of the host material with a n^3! dependance, as shown in equation 2.9. Since the refractive index of SnO_2 (~2.0) is higher than that of silica (~1.4), samples containing more SnO_2 would be expected to have a higher refractive index. This would increase the decay rate and therefore reduce the lifetime, so this does not account for the observed change. It is therefore likely that the lifetimes are increased by the reduction of energy migration caused by the disruption of the silica network by the tin oxide crystals.

The maximum emission lifetime measured in these Er-doped samples (4.1 ms) is greater than that measured in sol-gel-produced Er-doped TiO_2-SiO_2 (1.8 ms [131] and only slightly shorter than that of Er-doped GeO_2-SiO_2 (6.5 ms [134]). The lifetime data is similar to that observed in an Er-doped tin silicate glass-ceramic by Jander [146], which was fabricated using the same process as the samples studied in this work. This shows that while increasing the SnO_2 content increases the emission lifetime within the range of samples studied in this work, tin silicate glass-ceramics show no significant improvement over tin silicate glasses in terms of emission lifetimes.

Lifetime measurements were also carried out on the second batch of Er-doped samples which had reduced hydroxyl content. The stretched exponential fitting parameters are shown in table 5.3. As the emission lifetimes and stretch factors are similar for all these samples, it appears that the hydroxyl content may not have been reduced sufficiently to reduce quenching by energy migration to trap sites.

SnO_2 conc.	Er^{3+} conc. / ppm wt.	OH^- conc. / ppm wt.	Emission lifetime / ms	Stretch factor
16%	400	~0	3.0	0.59
16%	400	250	3.4	0.67
16%	400	700	3.4	0.69

Table 5.3: Fitting parameters for stretched exponential emission decays for the reduced hydroxyl content Er^{3+}-doped tin silicate glass-ceramics.

5.6 Thulium-doped tin silicate glass-ceramics

Figure 5.12 shows a partial energy level diagram for Tm^{3+} with relevant transitions. The $^3F_4$ and $^3H_4$ levels are superpositions of wavefunctions with $^3F_4$ and $^3H_4$ characteristics, and are labelled here according to the major contribution.

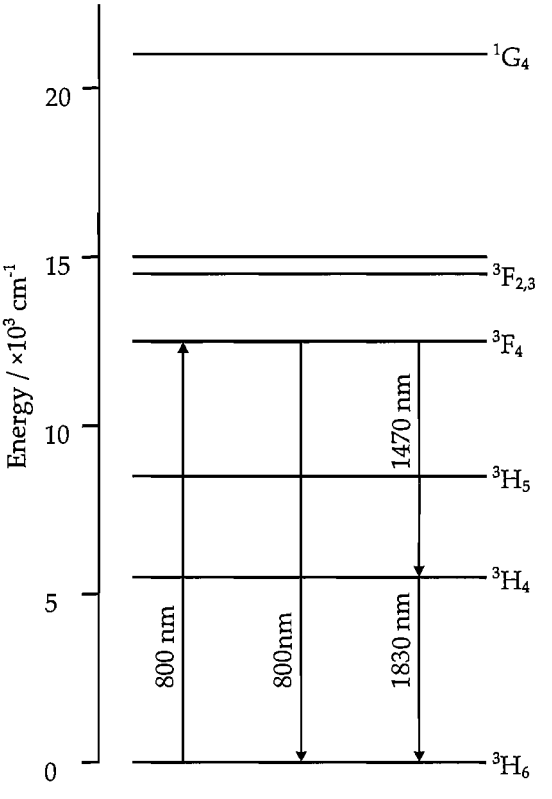

Figure 5.12: A partial energy level diagram for Tm^{3+}, showing the transitions relevant to this study.

The interesting transition for telecoms applications in Tm^{3+} is the $^3F_4 \rightarrow ^3H_4$ transition which is centred at ~1.47 μm. Because the energy gap between the $^3F_4$ and $^3H_5$ levels is relatively small (~4000 cm^{-1}), efficient emission at 1.47 μm requires a low phonon energy host.

The Tm^{3+} and SnO_2 concentrations of the samples studied in this work are listed in table 5.4.

SnO_2 conc.	Tm^{3+} conc. / ppm wt.
2%	200
2%	1000
5%	5000
15%	200
15%	1000
15%	10000

Table 5.4: Concentrations of Tm^{3+} and SnO_2 in the samples studied in this work. SnO_2 content is given in molar percent.

5.6.1 Absorption spectra

The absorption spectra for the Tm-doped samples are shown in Fig. 5.13. The absorption peaks scale approximately with dopant concentration and are labelled according to the Tm^{3+} energy levels in Fig. 5.12. The increased infrared absorption tail is again present for samples with >2% SnO_2. The peak at 2200 nm is due to the O-H stretching-SiO_2 bending mode [147] and was also observed in the Er^{3+}-doped samples.

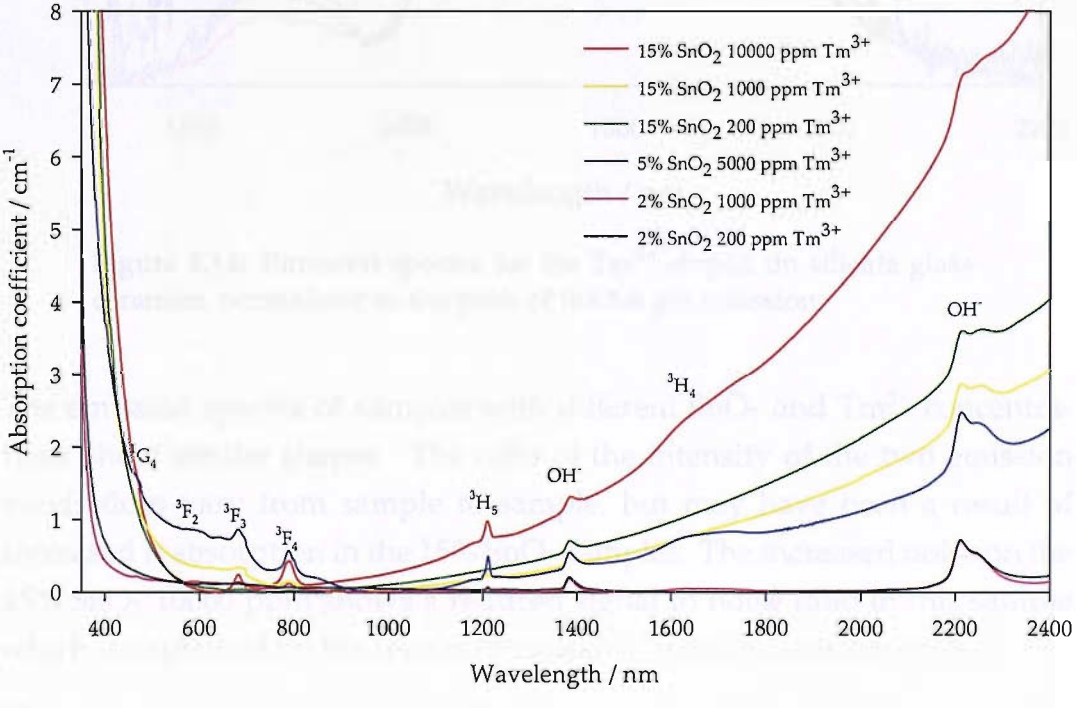

Figure 5.13: Absorption spectra for the Tm^{3+}-doped tin silicate glass-ceramics, showing Tm^{3+} electronic absorption peaks, hydroxyl vibrational peaks and a broad SnO_2-dependent infrared absorption.

5.6.2 Fluorescence spectra

The experimental setup described in section 3.3 was used for measuring emission spectra, with the Ti:sapphire laser tuned to the peak of the $^3F_4$ level absorption (795 nm). The emission spectra for the Tm^{3+}-doped samples are shown in Fig. 5.14.

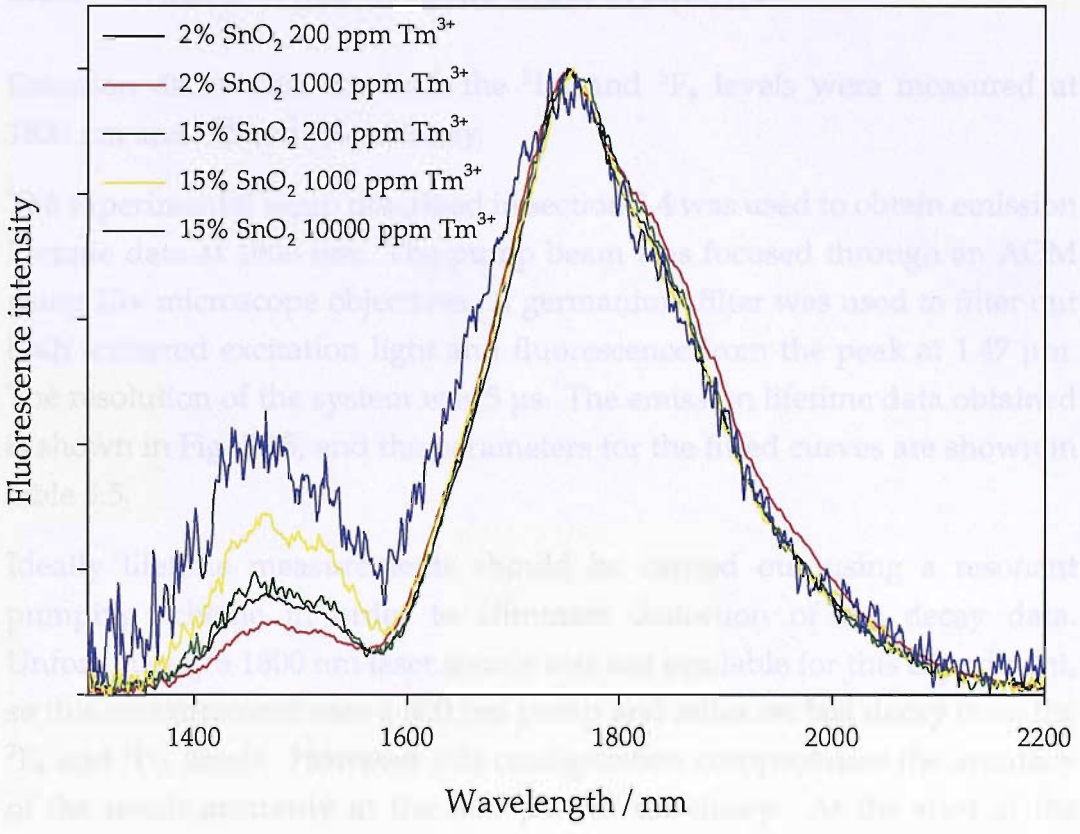

Figure 5.14: Emission spectra for the Tm^{3+}-doped tin silicate glass-ceramics, normalised to the peak of the 1.8 μm emission.

The emission spectra of samples with different SnO_2 and Tm^{3+} concentrations show similar shapes. The ratio of the intensity of the two emission bands does vary from sample to sample, but may have been a result of increased reabsorption in the 15% SnO_2 samples. The increased noise on the 15% SnO_2 10000 ppm shows a reduced signal to noise ratio in this sample which is explained by the results of emission lifetime measurements.

The emission bandwidth at 1.47 μm was estimated by subtracting the short wavelength tail of the 1.8 μm emission. A FWHM of 120 nm was measured, which is broader than the width of the same band in pure

silica glass (~80 nm [156]), fluoride glass (76 nm [43]) and tellurite glass (105-115 nm [43,44]). This broad emission is a good property for broadband amplification, and suggests that Tm^{3+} is hosted in a wide range of sites in these materials.

5.6.3 Fluorescence lifetime measurements

Emission decay data for both the $^3H_4$ and $^3F_4$ levels were measured at 1800 nm and 795 nm respectively.

The experimental setup described in section 3.4 was used to obtain emission lifetime data at 1800 nm. The pump beam was focused through an AOM using 10× microscope objectives. A germanium filter was used to filter out both scattered excitation light and fluorescence from the peak at 1.47 μm. The resolution of the system was 5 μs. The emission lifetime data obtained is shown in Fig. 5.15, and the parameters for the fitted curves are shown in table 5.5.

Ideally lifetime measurements should be carried out using a resonant pumping scheme in order to eliminate distortion of the decay data. Unfortunately a 1800 nm laser source was not available for this experiment, so this measurement uses a 800 nm pump and relies on fast decay from the $^3F_4$ and $^3H_5$ levels. However this configuration compromises the accuracy of the result primarily in the first part of the decay. At the start of the decay, when the pump source is switched off, the $^3H_4$ level will continue to be populated by decay from the $^3F_4$ and $^3H_5$ levels. To accommodate for this distortion in this measurement, the first 50 μs of the decay data has been discarded. It should be noted that as fluorescence decays in rare-earth-doped glasses are usually non-exponential, fitting curves to decay data in this way is likely to produce artificially long lifetimes. However, such data can still be used to compare lifetimes within a group of similar samples.

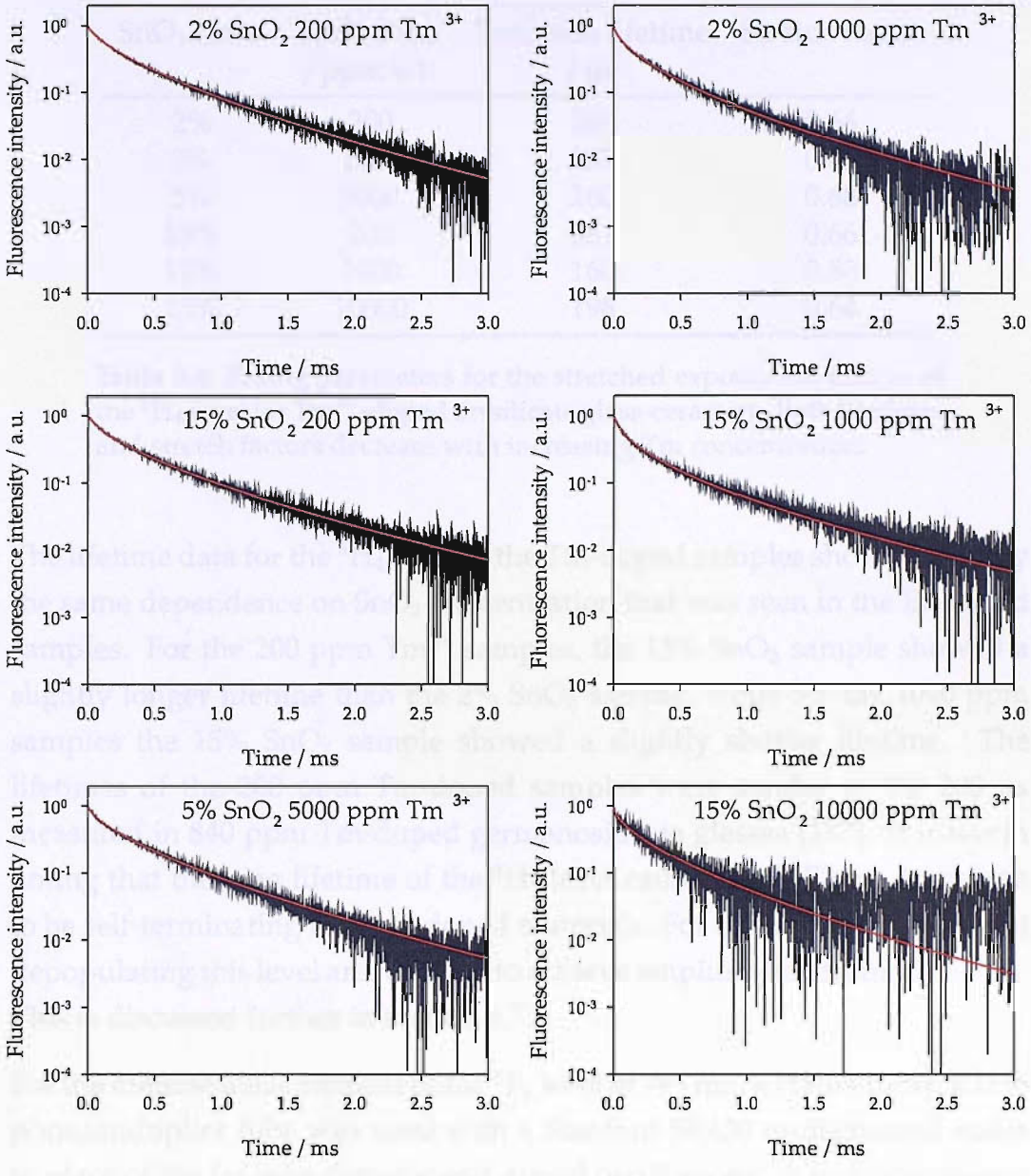

Figure 5.15: Lifetime measurements for the $^3H_4$ level in Tm^{3+}-doped tin silicate glass-ceramics. The initial 50 μs has been removed from each decay curve to minimise distortion due to the non-resonant pumping scheme.

SnO_2 conc.	Tm^{3+} conc. / ppm wt.	Emission lifetime / μs	Stretch factor
2%	200	246	0.66
2%	1000	167	0.60
5%	5000	260	0.68
15%	200	261	0.66
15%	1000	160	0.58
15%	10000	198	0.64

Table 5.5: Fitting parameters for the stretched exponential decays of the $^3H_4$ level for Tm^{3+}-doped tin silicate glass-ceramics. Both lifetimes and stretch factors decrease with increasing Tm concentration.

The lifetime data for the $^3H_4$ level of the Tm-doped samples showed broadly the same dependence on SnO_2 concentration that was seen in the Er-doped samples. For the 200 ppm Tm^{3+} samples, the 15% SnO_2 sample showed a slightly longer lifetime than the 2% SnO_2 sample, while for the 1000 ppm samples the 15% SnO_2 sample showed a slightly shorter lifetime. The lifetimes of the 200 ppm Tm-doped samples were similar to the 200 μs measured in 840 ppm Tm-doped germanosilicate glasses [157]. It is worth noting that the long lifetime of the $^3H_4$ level causes the 1470 nm transition to be self-terminating in Tm^{3+}-doped materials. For this reason, methods of depopulating this level are required to achieve amplification from $^3F_4 \rightarrow ^3H_4$. This is discussed further in section 6.7.5.

For the lifetime measurement of the $^3F_4$ level at 795 nm, a Hamamatsu R3236 photomultiplier tube was used with a Stanford SR430 multichannel scaler in place of the InGaAs detector and digital oscilloscope. A monochromator with a resolution of 5 nm was used to pass only the fluorescence at 795 nm to the detector. The Ti:sapphire laser was tuned to 785 nm, and a 785 nm notch filter was used to filter out scattered excitation light. The decay data obtained is shown in Fig. 5.16 with the fitted stretched exponential curves.

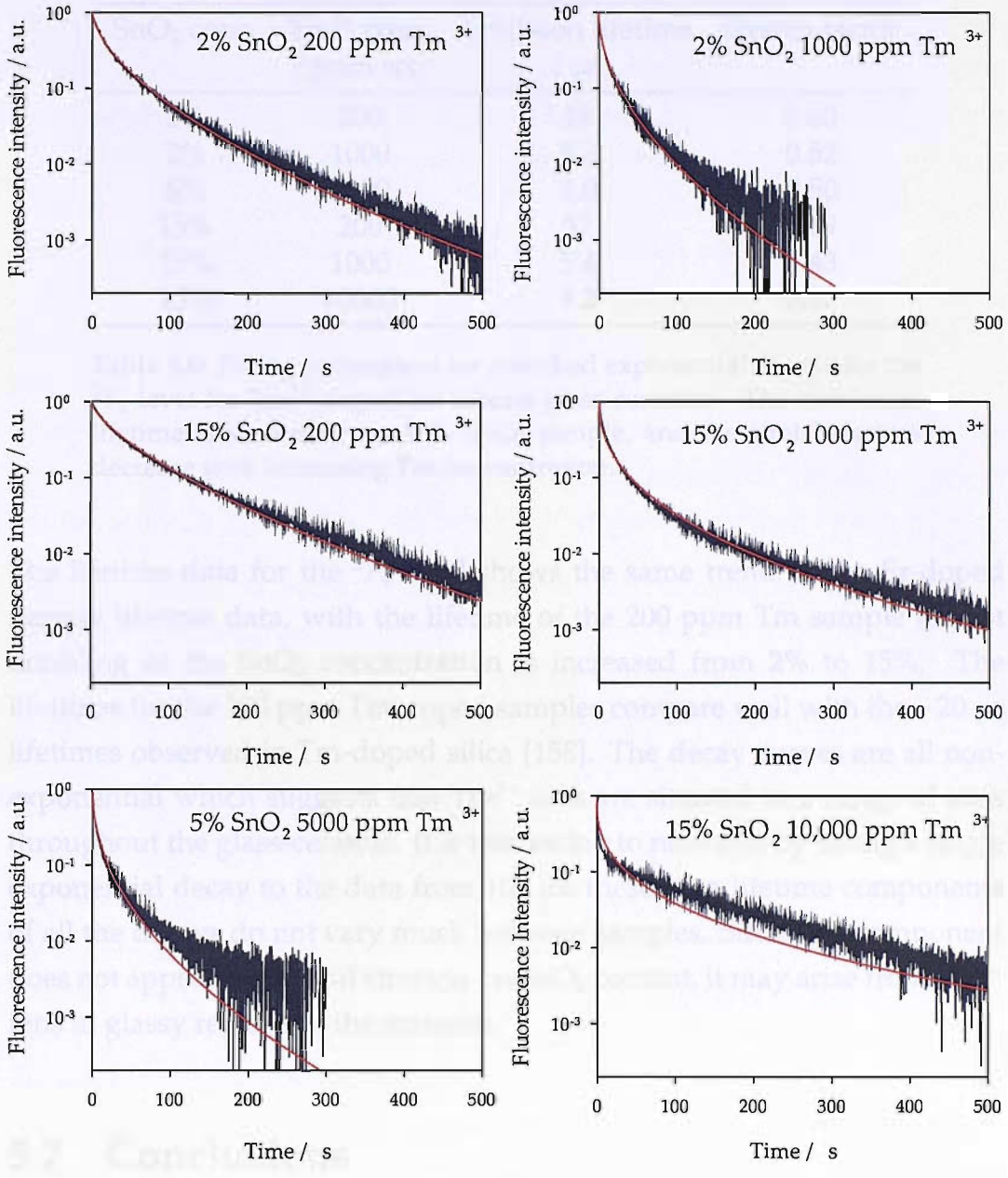

Figure 5.16: Lifetime measurements for the $^3F_4$ level in Tm^{3+}-doped tin silicate glass-ceramics.

The stretched exponential fitting parameters are shown in table 5.6. The stretched exponential for the 10000 ppm Tm^{3+} sample showed a particularly poor fit.

SnO_2 conc.	Tm^{3+} conc. / ppm wt.	Emission lifetime / μs	Stretch factor
2%	200	18	0.60
2%	1000	5.2	0.52
5%	5000	4.0	0.50
15%	200	37	0.69
15%	1000	5.4	0.43
15%	10000	4.2	0.37

Table 5.6: Fitting parameters for stretched exponential decays for the $^3F_4$ level for Tm^{3+}-doped tin silicate glass-ceramics. The maximum lifetime is shown by the 15% SnO_2 sample, and the stretch factors decrease with increasing Tm concentration.

The lifetime data for the $^3F_4$ level shows the same trend as the Er-doped sample lifetime data, with the lifetime of the 200 ppm Tm sample almost doubling as the SnO_2 concentration is increased from 2% to 15%. The lifetimes for the 200 ppm Tm-doped samples compare well with the ~20 μs lifetimes observed in Tm-doped silica [158]. The decay curves are all non-exponential which suggests that Tm^{3+} ions are situated in a range of sites throughout the glass-ceramic. It is interesting to note that by fitting a single exponential decay to the data from 100 μs, these long lifetime components of all the decays do not vary much between samples. Since this component does not appear to depend strongly on SnO_2 content, it may arise from Tm^{3+} ions in glassy regions of the material.

5.7 Conclusions

A spectroscopic investigation was carried out into erbium and thulium-doped tin silicate glass-ceramics. The lifetime data for the Er-doped samples show that emission lifetimes are increased in samples with higher tin oxide concentrations. This is not the case for Er^{3+}-doped tin silicate glasses, where the addition of tin has been shown not to affect the emission properties of Er^{3+} [140]. Since absorption, fluorescence and fluorescence lifetime measurements show no evidence that erbium ions are embedded into the tin oxide crystals, it seems likely that erbium ions are hosted at interfaces between the glass and nanocrystals.

The FWHM of the 1550 nm emission in the Er-doped samples is 48 nm, which is broader than that of Er-doped silica produced by the sol-gel method [130]. Fluorescence lifetime measurements of the $^4I_{13/2}$ level revealed a maximum lifetime of 4.1 ms which is comparable to other Er-doped silica glasses produced by the sol-gel method. The hydroxyl content of these glass-ceramics was estimated to be between 1000-2500 ppm wt. though this is sufficiently high to cause a significant absorption at 1400 nm, it does not appear to have a strong affect on lifetimes. Unfortunately, samples containing 5% or more tin oxide showed a large infrared absorption which would preclude their use as amplifier materials. With regard to the spectroscopy, these Er^{3+}-doped tin silicate glass-ceramics therefore appear not to have any advantage over other Er^{3+}-doped silica-based glasses.

Thulium-doped tin silicate glass-ceramics were studied for the first time. The emission observed from the $^3F_4$ to $^3H_4$ levels at 1470 nm showed a particularly broad FWHM of 120 nm. This was not significantly altered in samples with different compositions and is broader than that observed in thulium-doped silica, tellurite and fluoride glasses. Again, the fluorescence lifetimes were influenced by the SnO_2 concentration. The lifetime of the $^3F_4$ level increased in samples with higher SnO_2 concentration and the longest lifetime measured was 37 μs. Though this is much shorter than the lifetimes shown in Tm-doped tellurite and fluoride glasses, it is almost double the lifetime observed in Tm-doped silica. Since the lifetime of the $^3F_4$ level is particularly sensitive to changes in the maximum phonon energy of the host material, this suggests that Tm^{3+} ions occupy sites with reduced phonon energy in these glasses, compared to pure silica. Again, the strong infrared absorption affects samples with higher SnO_2 concentrations, which would be a major obstacle to the use of these materials in a device. However, the broad emission shown in these glasses is an attractive property for achieving broadband amplification.

5.8 Further work

In their present state, tin silicate glass-ceramics appear to offer no advantage over tin silicate glasses as hosts for active ions. However, if glass-

ceramics could be fabricated which showed the active ions embedded in the nanocrystals, then the emission properties would be drastically changed. It would be interesting to determine how different heat treatments both during and after fabrication affect the spectroscopy of the dopant ions.

If these materials are to be considered further for telecoms applications, it is important to determine the origin of the increase in infrared absorption. This could involve fabricating samples with a range of SnO_2 concentrations in order to establish if there is a threshold for this absorption edge increase. Also, absorption measurements should be made on samples at different stages of the fabrication process.

Chapter 6

Thulium-doped yttrium aluminosilicate glass

6.1 Introduction

The first part of this chapter contains an investigation into the effect of glass composition on the optical properties of thulium-doped yttrium aluminosilicate glasses. The second part describes the fabrication and characterisation of a thulium-doped yttrium aluminosilicate optical fibre.

In order to obtain efficient emission from certain energy levels in rare earth-doped materials, a low phonon energy host is required. This is because multiphonon decay becomes comparable to radiative decay when the gap between the upper and lower energy levels can be spanned by five phonons. Details of this relationship are given in section 2.2.5.1. Multiphonon emission is a problem for useful transitions at telecoms wavelengths in praseodymium, dysprosium and thulium-doped silica glasses. This is the reason that PDFAs and TDFAs traditionally utilise a fluoride glass host which has a maximum phonon energy of 590 cm^{-1} [159]. More recently TDFAs using a tellurite glass host have been investigated [43,44,160]. Tellurite glass has a maximum phonon energy of 750 cm^{-1} and offers improved thermal and chemical stability and broader emission over thulium-doped ZBLAN glass [43,44]. However, there are a number of problems associated with these so-called soft glasses. Low phonon energy glasses tend to contain heavy and

weakly-bound atoms which leads to low melting temperatures and poor mechanical strength. This can cause fibres to be fragile and precludes the possibility of fusion-splicing to silica fibre.

There have been several recent studies investigating silica-based glasses doped with thulium for telecoms applications. A patent application was made in 2001 for thulium-doped glasses containing ≥70% SiO_2 with gallium or yttrium as a modifier for use as optical amplifier materials for telecoms applications [158, 161]. Another patent application was made in 2002 for S-band amplification using thulium-doped glasses containing ≥65% SiO_2, ≤30% of ZnO, BaO, SrO or PbO and ≤15% SnO_2 or TiO_2, additionally between 3-30% of the oxygen is replaced with fluorine [162]. Amplification has also been reported in thulium-doped antimony-silicate glasses [42, 163], though these fibres were not fusion spliced to silica fibres. A thulium-doped bismuth oxide-based glass has also been considered for S-band amplification and, though this is not a silicate glass, it has been possible to fusion-splice bismuth oxide glass fibres to silica fibres [164].

In 2003, a thulium-doped Y_2O_3-Al_2O_3-SiO_2 (YAS) glass composition was reported which had a maximum phonon energy of 950 cm^{-1} [165]. The emission bandwidth at 1470 nm was 125 nm, which is broader than that observed in silica, ZBLAN and tellurite glasses. The upper level lifetime was measured to be 100 μs, which is several times longer than that in pure silica [166]. The same study also reported an erbium-doped YAS glass containing 0.78 mol% (26000 ppm wt.) Er^{3+} which showed no sign of concentration quenching. Differential thermal analysis showed that the difference between the crystallisation and glass transition temperatures ($T_x - T_g$) was 242°C, which makes YAS glass potentially suitable for fibre drawing [146].

Though there have been a number of studies of the properties of rare earth aluminosilicate glasses, there have been no investigations involving the spectroscopy of dopant ions in YAS glasses other the one mentioned above. Studies of rare earth aluminosilicate systems include investigations into glass-forming regions [167, 168], refractive index measurements [168, 169] and Raman and FTIR measurements [170, 171].

In this chapter it is shown that the vibrational properties of YAS glass can be altered through changes in glass composition. This leads to a change in excited state lifetime of 20% in the range studied. Despite problems identified with glass quality, an unclad YAS glass was successfully pulled from a preform which was drilled out of bulk cast glass. YAS glass fibre appears to be physically robust and retains the good spectroscopic properties of the bulk glass.

The first part of this study is an investigation into the effects of glass composition on the optical properties of thulium-doped YAS glass. This includes Raman, FTIR, absorption, fluorescence and fluorescence lifetime measurements of different YAS compositions. The second part of the study reports on a first attempt to fabricate a thulium-doped YAS fibre. The fabrication technique is described and fibre loss, fluorescence and fluorescence lifetime measurements are reported.

6.2 Sample preparation

A number of YAS samples of different composition were prepared for this investigation. Samples were produced by melting high purity powders in a platinum crucible in an electric furnace and casting into a brass mould before annealing. Great care was taken both to prevent contamination and to maintain consistency between glass melts.

Powders of at least 99.99% purity were batched in a dry nitrogen-purged glovebox and were weighed out in 30 g batches to an accuracy of ±0.02 g. The powders were mixed thoroughly in a sealed polyethylene bottle, using a mechanical rotating mixer for 30 mins. The batch was then transferred to a platinum crucible which was placed uncovered in an electric furnace at 1600°C. The batch was held at 1600°C in flowing oxygen gas for 1-2 hours before being removed and cast into a brass mould which was preheated on a hot plate to ~300°C. The glass was then immediately removed from the mould and transferred to an annealing furnace at 900°C, which is just below T_g for these glasses [169]. After being held at 900°C for 1 hour, the temperature was reduced to room temperature at a rate of 30°/hour. The

samples were cut into slabs of ~5 mm thickness which were then polished on two parallel faces and on one perpendicular side.

As some glass remained in the platinum crucible after casting, crucibles were cleaned in HF solution for at least 5 hours, then rinsed with deionised water and placed in a drying cabinet for at least 1 hour.

The initial selection of compositions was made to cover a wide area of the glass-forming region. The glass-forming region was investigated by Shelby and covers the approximate ranges: 10-30% Y_2O_3, 15-45% Al_2O_3 and 35-80% SiO_2 [168]. The position of all the chosen compositions in the Y_2O_3-Al_2O_3-SiO_2 system is shown in Fig. 6.1. Further compositions were chosen either with different dopant concentrations or with a modified preparation procedure in order to improve sample quality. Various problems were encountered in the quality of the samples, these are outlined inthe appendix in tables B.1 and B.2 and are discussed further in section 6.7.

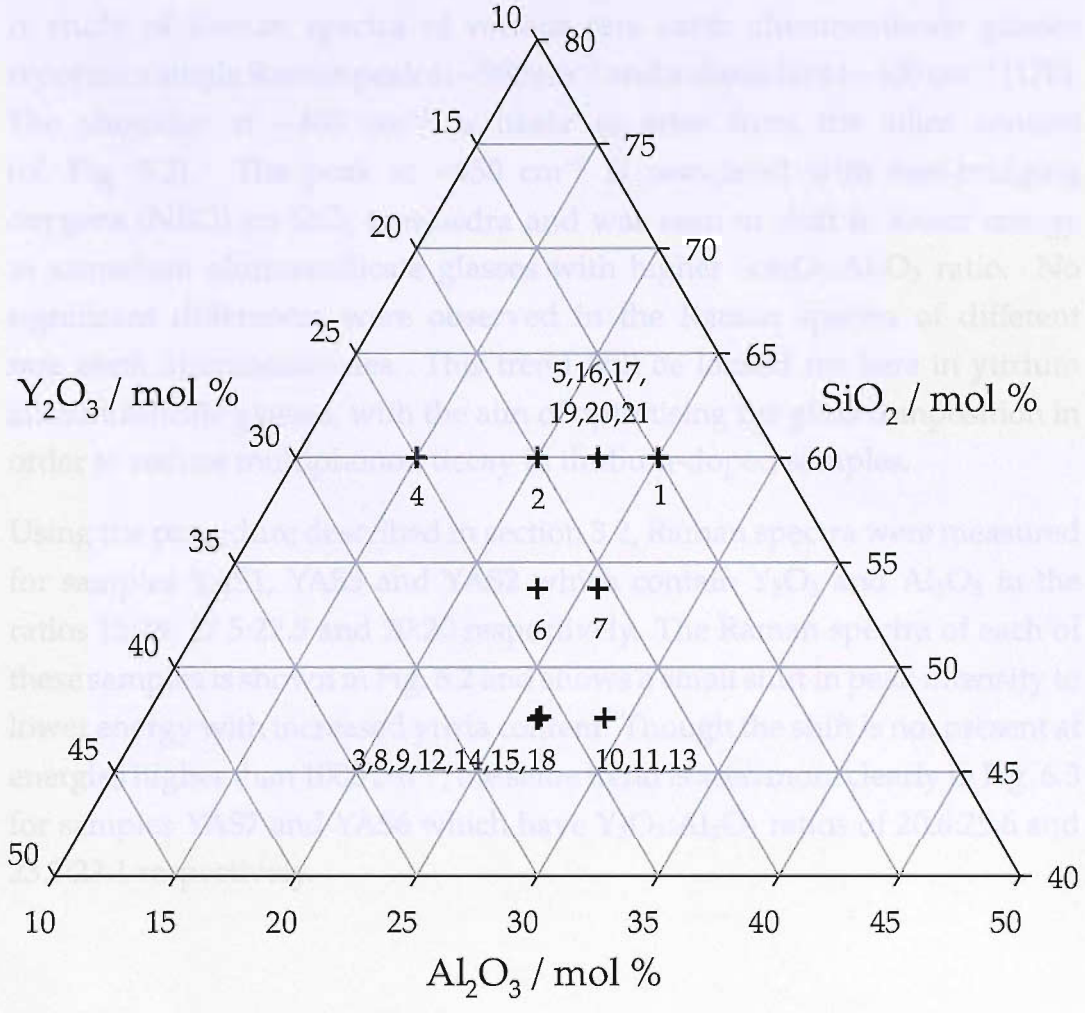

Figure 6.1: YAS glass compositions melted in this work. The numbers by each crosshair are the sample numbers of each composition.

6.3 Raman spectra

The maximum phonon energy of a silicate host for thulium is an important parameter affecting the radiative efficiency of the 1470 nm transition. This is because the maximum phonon energy for silica is 1150 cm^{-1} and the energy gap between the $^3F_4$ and $^3H_5$ levels is ~4400 cm^{-1} and so around four phonons are required to bridge the gap. As described in section 2.2.5.1, the multiphonon decay rate depends exponentially on the number of phonons required to bridge the gap and at 5-6 phonons radiative and multiphonon rates will be comparable.

A study of Raman spectra of various rare earth aluminosilicate glasses reported a single Raman peak at ~950 cm^{-1} and a shoulder at ~400 cm^{-1} [170]. The shoulder at ~400 cm^{-1} is likely to arise from the silica content (cf. Fig. 5.2). The peak at ~950 cm^{-1} is associated with non-bridging oxygens (NBO) on SiO_4 tetrahedra and was seen to shift to lower energy in samarium aluminosilicate glasses with higher Sm_2O_3:Al_2O_3 ratio. No significant differences were observed in the Raman spectra of different rare earth aluminosilicates. This trend will be looked for here in yttrium aluminosilicate glasses, with the aim of optimising the glass composition in order to reduce multiphonon decay in thulium-doped samples.

Using the procedure described in section 3.2, Raman spectra were measured for samples YAS1, YAS5 and YAS2 which contain Y_2O_3 and Al_2O_3 in the ratios 15:25, 17.5:22.5 and 20:20 respectively. The Raman spectra of each of these samples is shown in Fig. 6.2 and shows a small shift in peak intensity to lower energy with increased yttria content. Though the shift is not present at energies higher than 1000 cm^{-1}, the same trend is seen more clearly in Fig. 6.3 for samples YAS7 and YAS6 which have Y_2O_3:Al_2O_3 ratios of 20.6:25.6 and 23.1:23.1 respectively.

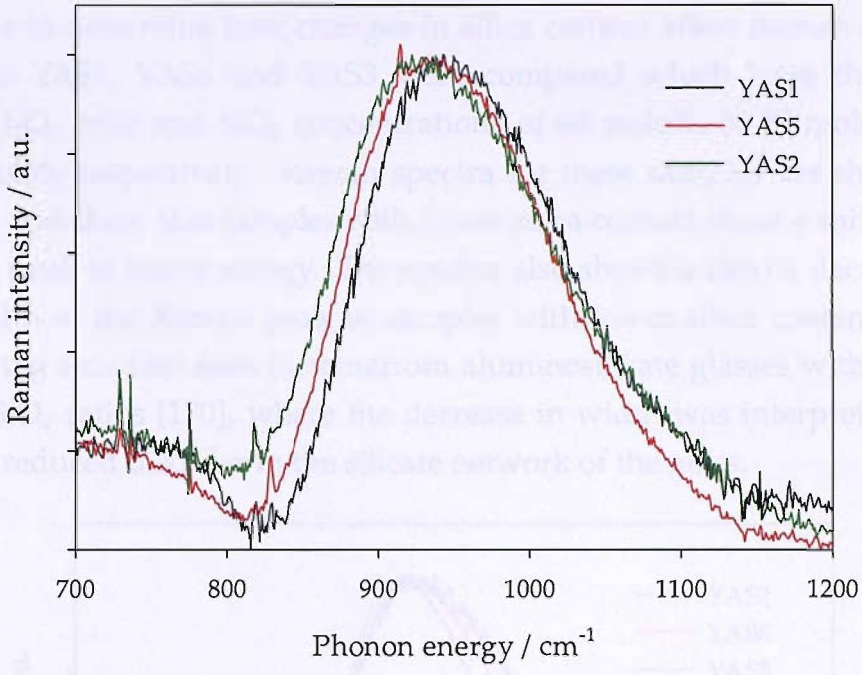

Figure 6.2: Raman spectra of samples YAS1, YAS5 and YAS2 in order of increasing Y_2O_3:Al_2O_3 ratio, showing a decrease in the phonon energy in samples with high yttria content. The spectra are normalised to peak intensity.

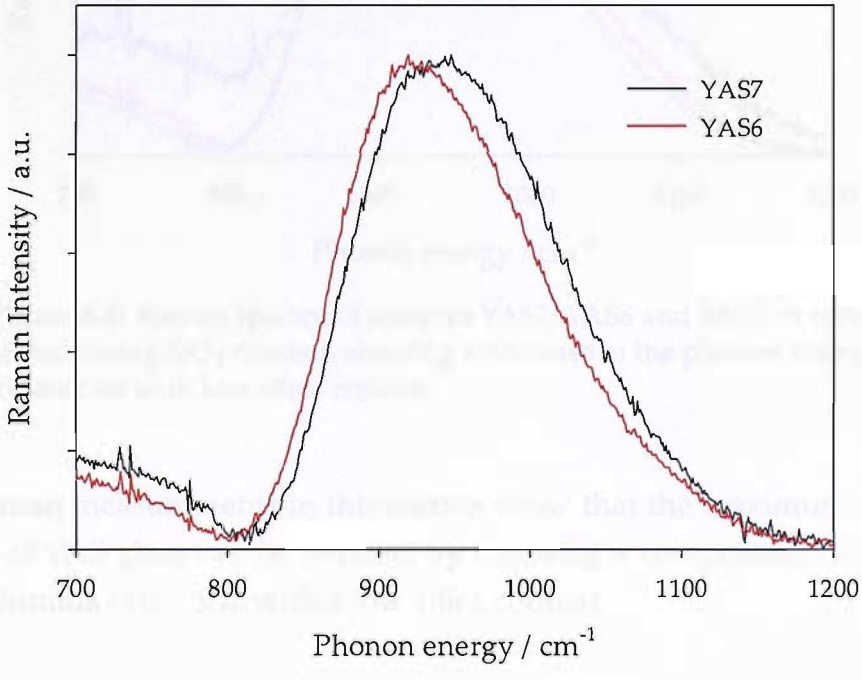

Figure 6.3: Raman spectra of samples YAS7 and YAS6 in order of increasing Y_2O_3:Al_2O_3 ratio, showing a decrease in the phonon energy in samples with high yttria content.

In order to determine how changes in silica content affect Raman spectra, samples YAS2, YAS6 and YAS3 were compared which have the same Y_2O_3:Al_2O_3 ratio and SiO_2 concentrations of 60 mole%, 53.75 mole% and 47.5 mole% respectively. Raman spectra for these samples are shown in Fig. 6.4 and show that samples with lower silica content show a shift of the Raman peak to lower energy. The spectra also shows a clear a decrease in the width of the Raman peak in samples with lower silica content. This narrowing was also seen in samarium aluminosilicate glasses with higher Al_2O_3:SiO_2 ratios [170], where the decrease in width was interpreted as a sign of reduced disorder in the silicate network of the glass.

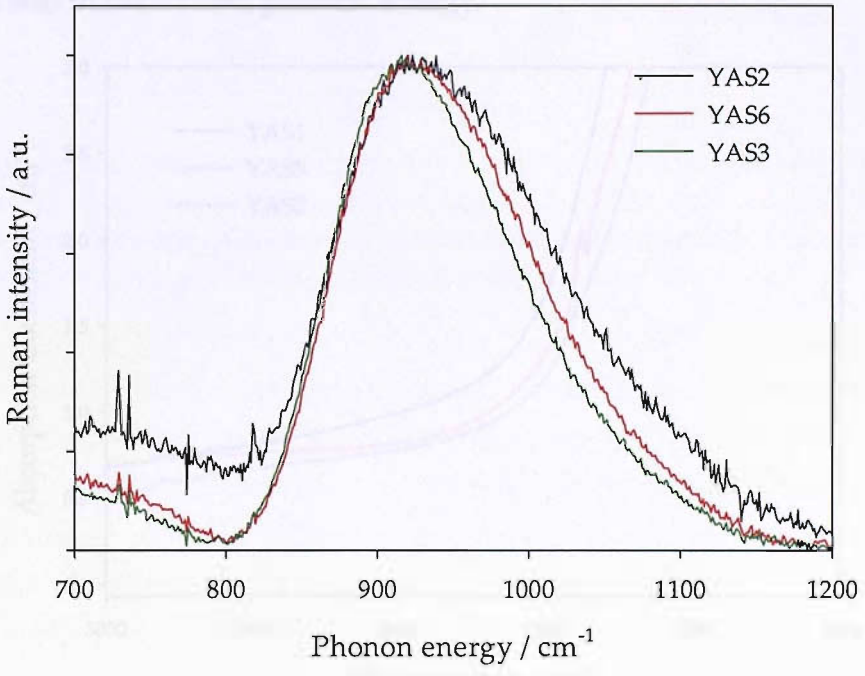

Figure 6.4: Raman spectra of samples YAS2, YAS6 and YAS3 in order of decreasing SiO_2 content, showing a decrease in the phonon energy in samples with low silica content.

The Raman measurements in this section show that the maximum phonon energy of YAS glass can be reduced by choosing a composition with high yttria:alumina ratio, and with a low silica content.

6.4 Absorption spectra

FTIR spectra were measured for all the samples for which Raman spectra were taken, using the procedure described in section 3.1.1. The infrared absorption edges for the samples containing different Y_2O_3:Al_2O_3 ratios are shown in Fig. 6.5 and show a shift to lower energy for samples with high yttria content. This is consistent with the Raman spectra in section 6.3. Similarly, spectra were taken for the samples containing various SiO_2 concentrations and are shown in Fig. 6.6. The absorption edges of the samples with lower silica content were shifted to lower energy, confirming a reduction in maximum phonon energy.

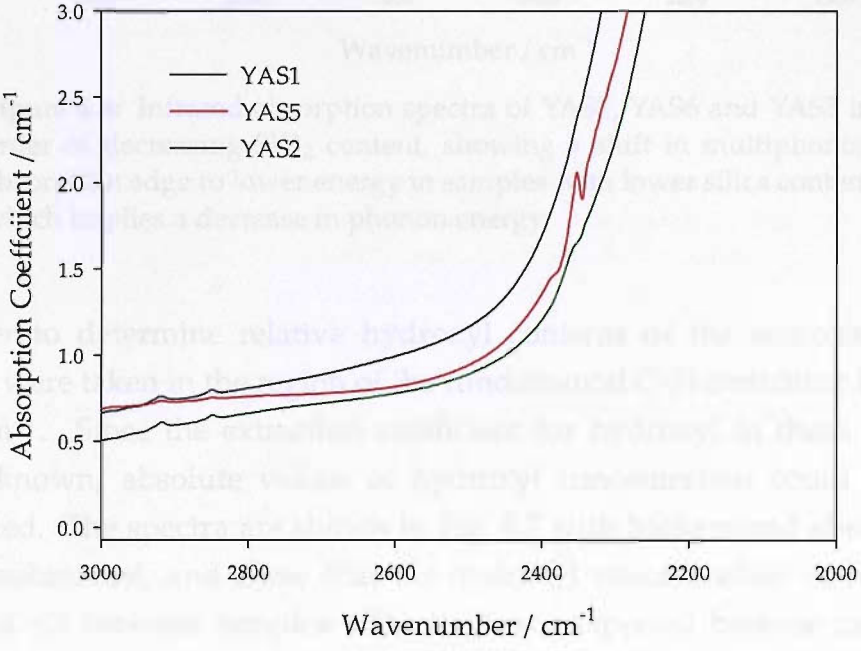

Figure 6.5: Infrared absorption spectra of YAS1, YAS5 and YAS2 in order of increasing Y_2O_3:Al_2O_3 ratio, showing a shift in multiphonon absorption edge to lower energy in samples with higher yttria content which implies a decrease in phonon energy.

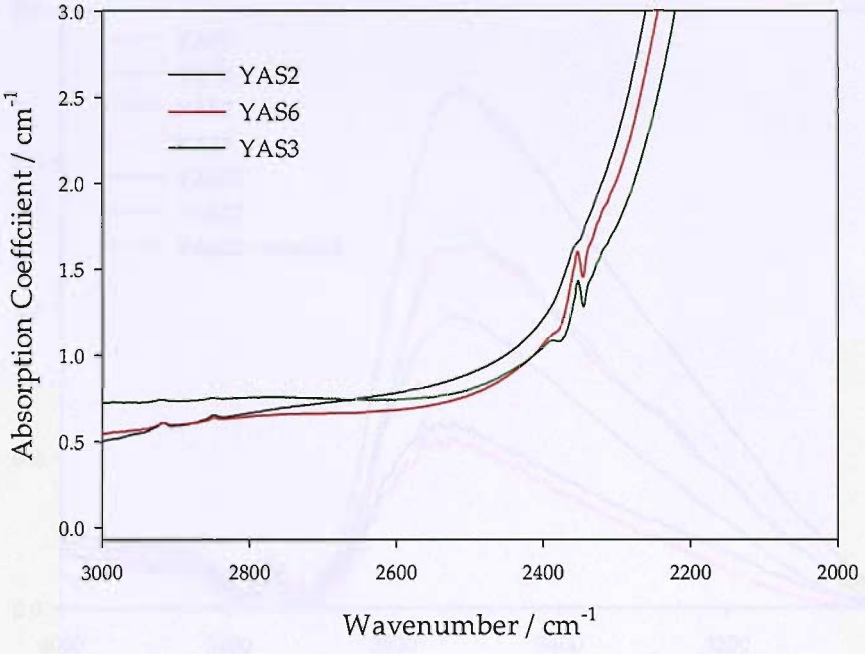

Figure 6.6: Infrared absorption spectra of YAS2, YAS6 and YAS3 in order of decreasing SiO_2 content, showing a shift in multiphonon absorption edge to lower energy in samples with lower silica content which implies a decrease in phonon energy.

In order to determine relative hydroxyl contents of the samples, FTIR spectra were taken in the region of the fundamental O-H stretching band at 3500 cm^{-1}. Since the extinction coefficient for hydroxyl in these glasses is not known, absolute values of hydroxyl concentration could not be calculated. The spectra are shown in Fig. 6.7 with background absorption slopes subtracted, and show that the hydroxyl concentration varies by a factor of ~3 between samples. This was not expected because care was taken to maintain consistency between glass melts. The reason for this difference is not clear, though since the hydroxyl content of YAS12 was not altered after remelting it is not likely to be introduced during melting.

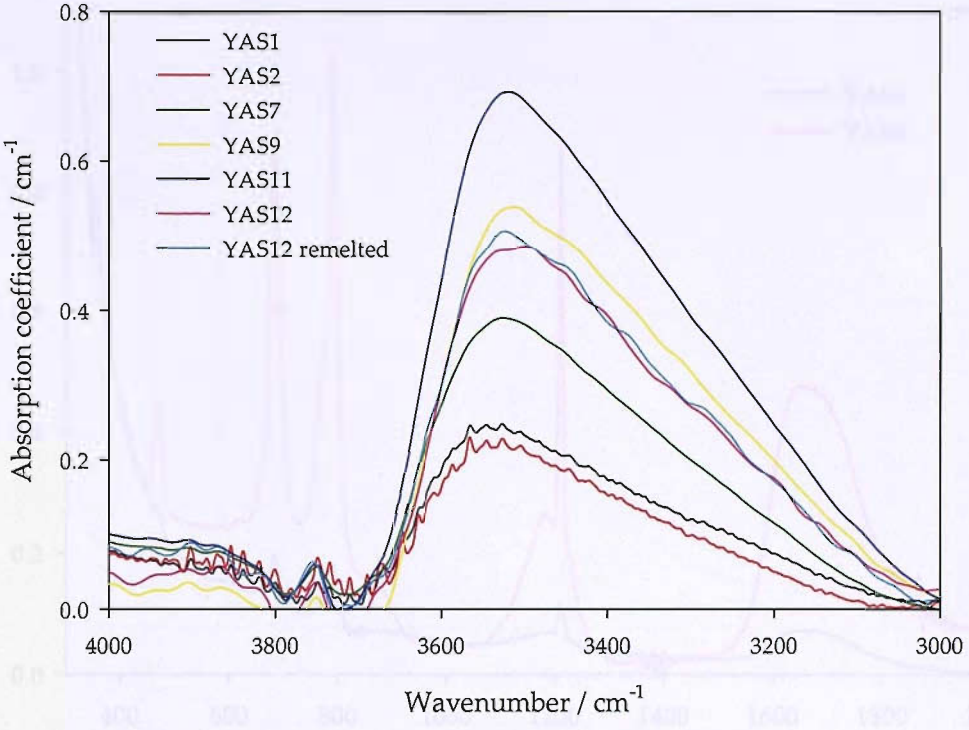

Figure 6.7: Infrared absorption spectra of YAS samples showing the fundamental hydroxyl stretching band. The range of intensities reflects the range of hydroxyl concentrations in the samples. The background slope was subtracted from each curve.

Absorption spectra of the YAS samples were measured over the visible and near infrared range using the procedure described in section 3.1. Figure 6.8 shows the absorption spectra of YAS samples containing 440 ppm and 3911 ppm Tm^{3+}. The absorption spectrum for the YAS8 sample shows increased absorption below 900 nm. This was also observed in the previous study of Tm-doped YAS [166] and is likely to be caused by transition metal ion impurities. This was not present in many of the other spectra, including YAS1 which is also shown in Fig. 6.8. In contrast to the absorption spectra for the tin silicate glass-ceramics shown in Figs. 5.6 and 5.13, there is no strong absorption peak at 1400 nm arising from hydroxyl groups. This is particularly important for optical materials operating in the S-band, as the OH^- absorption band overlaps with this region of the telecoms window.

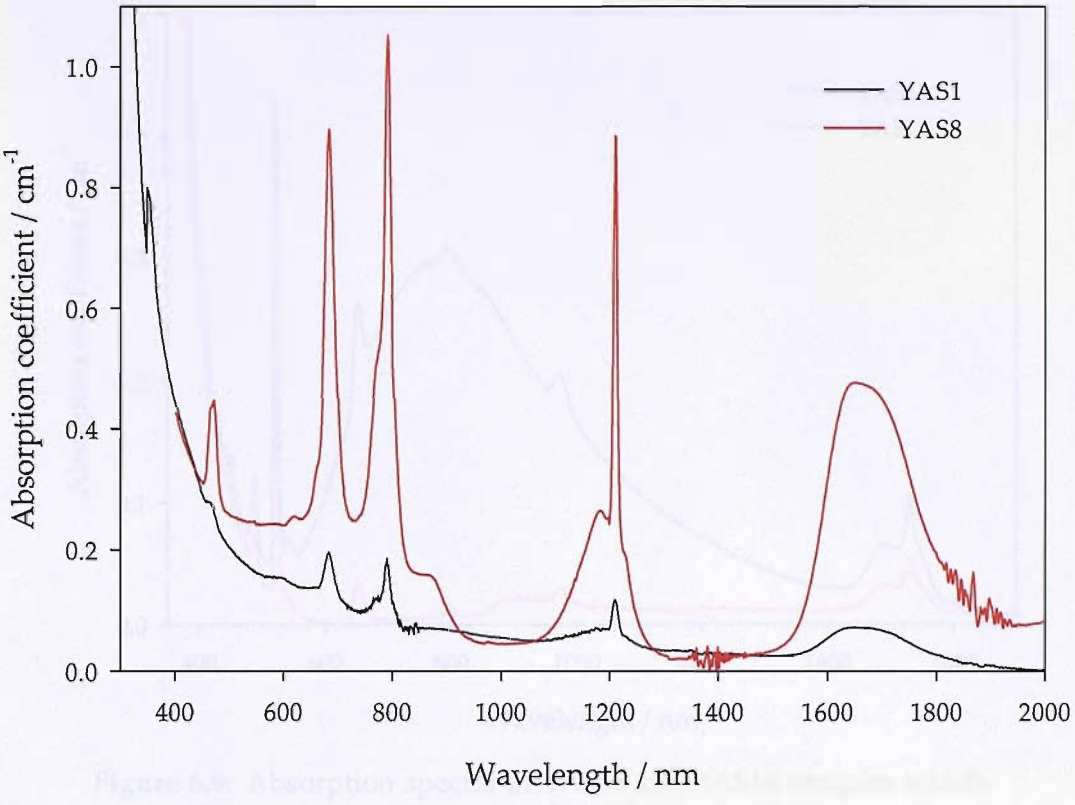

Figure 6.8: Absorption spectra of YAS1 and YAS8 samples which contain 440 ppm and 3911 ppm Tm^{3+} respectively. The spectra show the characteristic absorption peaks from electronic transitions in the Tm^{3+} ion. There is an increased UV absorption in the YAS8 sample, which may be due to transition metal impurities.

Figure 6.9 shows absorption spectra of two samples which were doped with erbium. The large absorption peak centred at 800 nm found in the spectrum of YAS13 is likely a result of copper contamination, as the glass was crushed with brass blocks before remelting. Copper appears to be hosted in YAS glass as Cu^{2+} and it is interesting to note that copper is incorporated almost entirely as Cu^{+} in pure silica produced by flame hydrolysis [78]. However, contamination by other transition metals cannot be ruled out, particularly because the shape of the absorption band is similar to that of Cr^{4+}-doped glasses, as discussed in section 4.2.1.

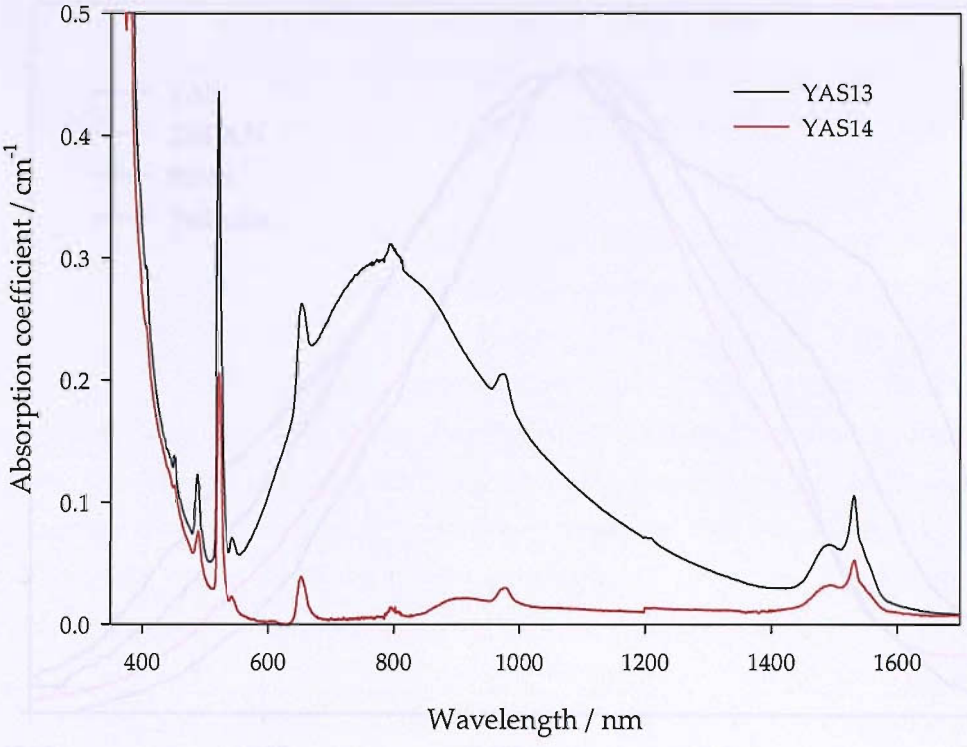

Figure 6.9: Absorption spectra of YAS13 and YAS14 samples which contain 500 ppm and 200 ppm Er^{3+} respectively, showing a broad strong absorption peak centred at 800 nm which is due to Cu impurity.

6.5 Fluorescence spectra

Fluorescence spectra were measured using the technique described in section 3.3, using a Milon laser diode at 800 nm as the excitation source. The emission from the $^3F_4 \rightarrow ^3H_4$ transition in the YAS2 sample is shown in Fig. 6.10 with a resolution of 5 nm and corrected for the spectral response of the system. The emission bandwidth is remarkably broad and flat and has a FWHM of 129 nm, which is similar to that measured in Tm-doped YAS glass by Jander [165]. This is much broader than the same transition measured in ZBLAN [43], tellurite [44] and pure silica [156] as illustrated in the figure, which suggests that YAS glasses exhibit a higher degree of disorder.

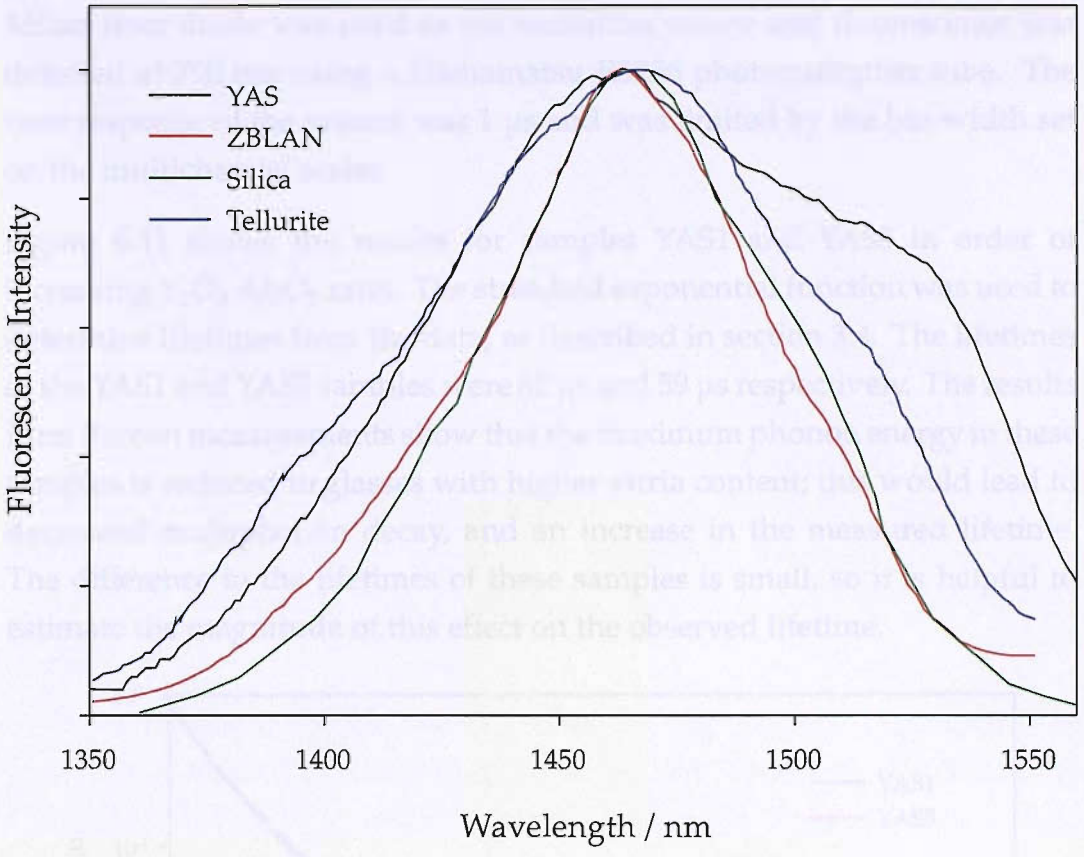

Figure 6.10: Emission spectrum of the thulium-doped YAS2 sample, with data from thulium-doped ZBLAN, tellurite and silica [43, 156]. The emission from the YAS glass is much broader than from the other glass hosts. The spectra are normalised to peak intensity.

Emission spectra measured from samples with different compositions showed no significant differences in bandwidth or shape, even though Raman spectra indicate samples with low SiO_2 content are less disordered. A broad emission at 1470 nm would be a key requirement for a broadband amplifier for WDM telecoms systems. Another advantage of the emission shown by Tm-doped YAS is that the spectrum has a relatively flat top, which may reduce the need for gain equalisation in an amplifier.

6.6 Fluorescence lifetime measurements

Fluorescence lifetime measurements for the $^3F_4 \rightarrow ^3H_6$ transition were made using the method described in section 3.4. A directly-modulated 800 nm

Milon laser diode was used as the excitation source and fluorescence was detected at 790 nm using a Hamamatsu R3236 photomultiplier tube. The time response of the system was 1 μs and was limited by the bin-width set on the multichannel scaler.

Figure 6.11 shows the results for samples YAS1 and YAS5 in order of increasing Y_2O_3:Al_2O_3 ratio. The stretched exponential function was used to determine lifetimes from the data, as described in section 3.4. The lifetimes of the YAS1 and YAS5 samples were 60 μs and 59 μs respectively. The results from Raman measurements show that the maximum phonon energy in these samples is reduced in glasses with higher yttria content; this would lead to decreased multiphonon decay, and an increase in the measured lifetime. The difference in the lifetimes of these samples is small, so it is helpful to estimate the magnitude of this effect on the observed lifetime.

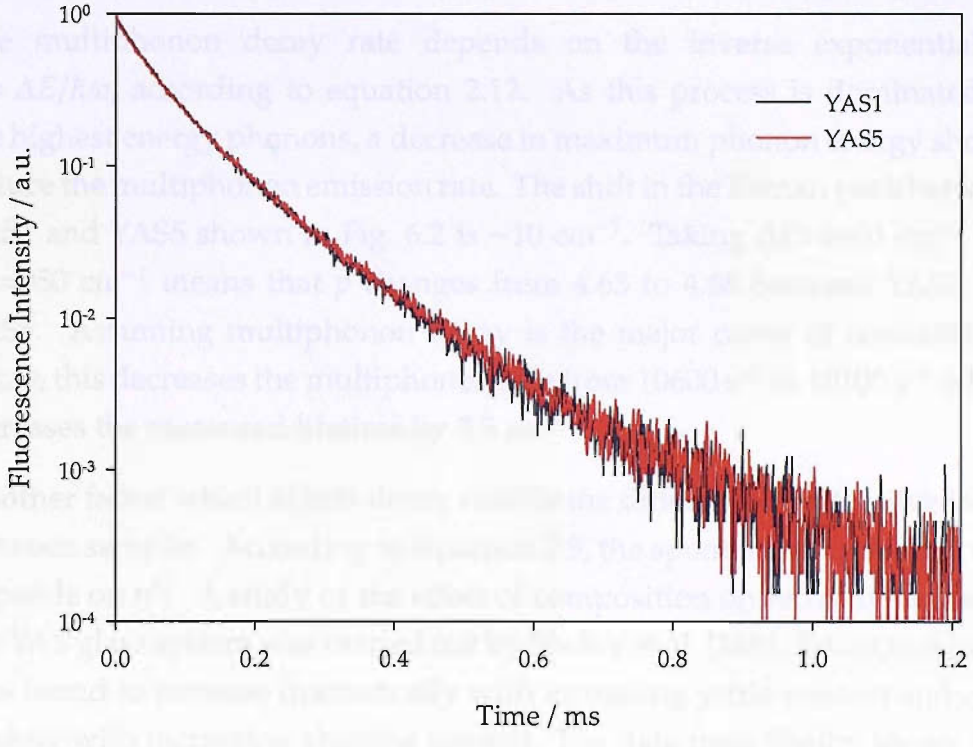

Figure 6.11: Fluorescence lifetime measurements of the $^3F_4$ level of thulium-doped samples YAS1 and YAS5, showing lifetimes of 58 μs and 59 μs respectively.

The increase in fluorescence lifetime caused by a decrease in the maximum phonon energy of the host can be estimated with knowledge of the multiphonon decay rate and equation 2.12. Since the measured lifetime has

contributions from both radiative and nonradiative processes, the quantum efficiency is required to calculate the nonradiative decay rate from the measured lifetime:

$$W_{nr} = \frac{1 - QE}{\tau} \tag{6.1}$$

In the previous investigation into thulium-doped YAS glass, Jander used Judd-Ofelt analysis to calculate the quantum efficiency to be ~20% [166]. Since this calculation was made using data from a YAS glass with the same composition as sample YAS3 and YAS8, quantum efficiencies of these samples were calculated and compared to the value determined by Jander. This analysis is described in section 6.6.1 and shows that the quantum efficiency of these samples is ~14%. Using 14% as the quantum efficiency gives a radiative rate of 1730 s^{-1} and a nonradiative rate of 10600 s^{-1} for the YAS1 sample.

The multiphonon decay rate depends on the inverse exponential of $p = \Delta E/\hbar\omega$, according to equation 2.12. As this process is dominated by the highest energy phonons, a decrease in maximum phonon energy should reduce the multiphonon emission rate. The shift in the Raman peak between YAS1 and YAS5 shown in Fig. 6.2 is ~10 cm^{-1}. Taking ΔE=4400 cm^{-1} and $\hbar\omega$=950 cm^{-1} means that p changes from 4.63 to 4.68 between YAS1 and YAS5. Assuming multiphonon decay is the major cause of nonradiative decay, this decreases the multiphonon rate from 10600 s^{-1} to 10100 s^{-1} which increases the measured lifetime by 3.5 μs.

Another factor which affects decay rates is the difference in refractive index between samples. According to equation 2.9, the spontaneous emission rate depends on n^3!. A study of the effect of composition on refractive index in the YAS glass system was carried out by Shelby et al. [168]. Refractive index was found to increase dramatically with increasing yttria content and only slightly with increasing alumina content. The data from Shelby shows that an increase in yttria content from 15% to 17.5% will cause an increase in refractive index of 1.2%. The YAS5 sample contains 2.5% more yttria than YAS1, so according to equation 2.9 the radiative rate from the same level will be increased by from 1730 s^{-1} to 1800 s^{-1}. This corresponds to a decrease in lifetime of 0.5 μs when changing composition from YAS1 to YAS5.

These approximate calculations show that the change in maximum phonon energy between YAS1 and YAS5 will increase the lifetime by 3.5 μs and the change in refractive index will decrease the lifetime by 0.5 μs. This shows that by increasing the yttria content from 15% to 17.5%, while keeping the silica content constant, the measured lifetime will be increased by 3 μs. This is larger than the 1 μs increase measured from the YAS1 sample to the YAS5 sample, however this may be due to some inhomogeneity in the YAS1 sample which was not mixed mechanically.

Fluorescence lifetime data for the $^3F_4$ level of thulium-doped samples YAS7 and YAS6 are shown in Fig. 6.12 and also shows an increase in lifetime with higher yttria content. The increase in lifetime appears more clearly in the data, and this is reflected in the larger increase in the lifetime from 63 μs to 67 μs. This is to be expected from the larger shift between the samples shown in the Raman spectra in Fig. 6.3. The difference measured between the lifetimes of YAS7 and YAS6 is 4 μs, which in reasonable agreement with the estimated value of 3 μs.

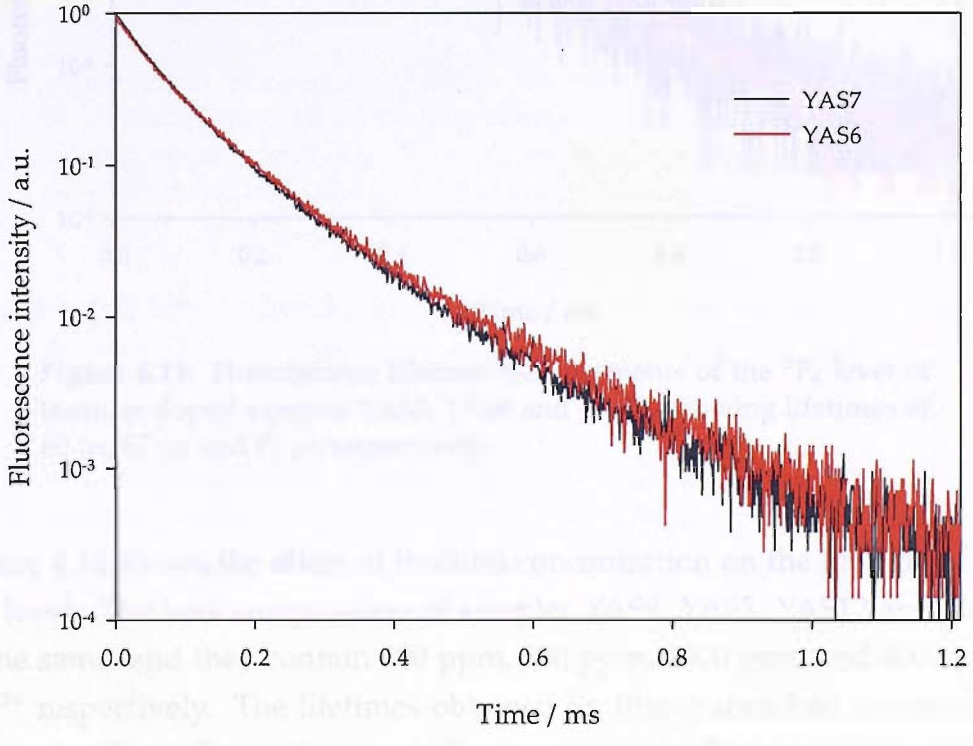

Figure 6.12: Fluorescence lifetime measurements of the $^3F_4$ level of thulium doped samples YAS7 and YAS6, showing lifetimes of 63 μs and 67 μs respectively.

Fluorescence lifetime data for the $^3F_4$ level of thulium doped samples YAS2, YAS6 and YAS3 which contain decreasing amounts of silica are shown in Fig. 6.13. These samples all contain the same Y_2O_3:Al_2O_3 ratio and the lifetimes of 60 μs, 67 μs and 71 μs show that decreasing the silica content of this glass increases the $^3F_4$ lifetime, as expected from Raman measurements. The difference measured between the lifetimes of YAS6 and YAS3 is 4 μs and that between YAS2 and YAS6 is 7 μs; these are both in reasonable agreement with the estimated value of 3 μs.

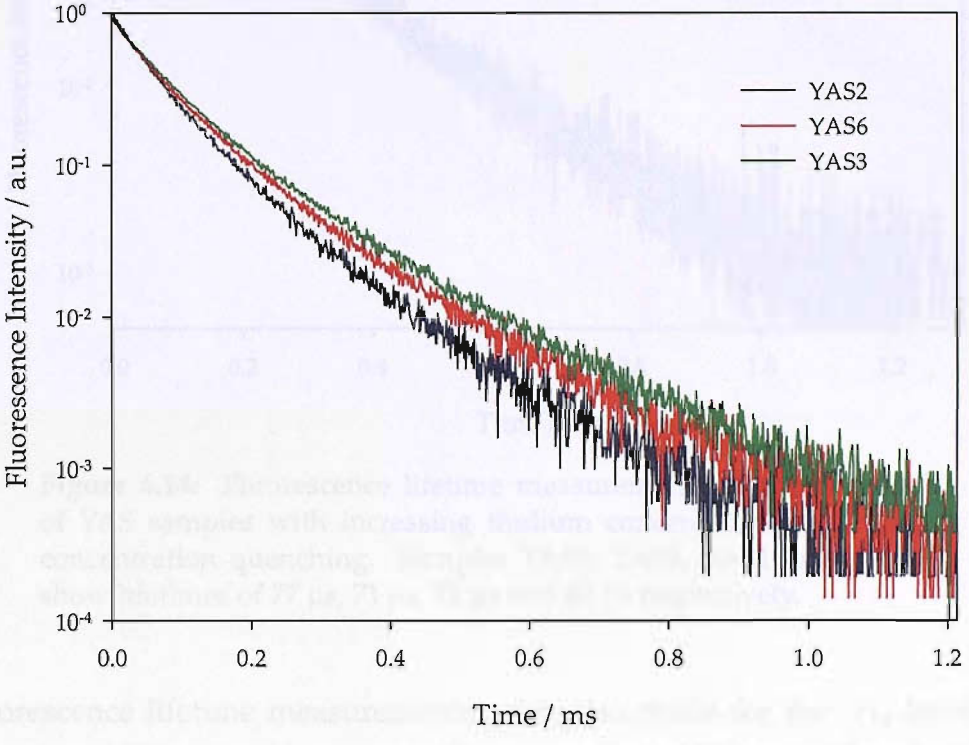

Figure 6.13: Fluorescence lifetime measurements of the $^3F_4$ level of thulium doped samples YAS2, YAS6 and YAS3, showing lifetimes of 60 μs, 67 μs and 71 μs respectively.

Figure 6.14 shows the effect of thulium concentration on the lifetime of the $^3F_4$ level. The host composition of samples YAS9, YAS3, YAS12 and YAS8 is the same, and they contain 200 ppm, 500 ppm, 1000 ppm and 4000 ppm Tm^{3+} respectively. The lifetimes obtained by fitting stretched exponential curves are 77 μs, 71 μs, 71 μs and 62 μs respectively. The decay data for the 500 ppm and 1000 ppm samples are almost within the noise of the 200 ppm sample, the lifetime for the 4000 ppm is clearly shorter than that of lower

doped samples. This indicates that concentration quenching does occur in the 4000 ppm sample.

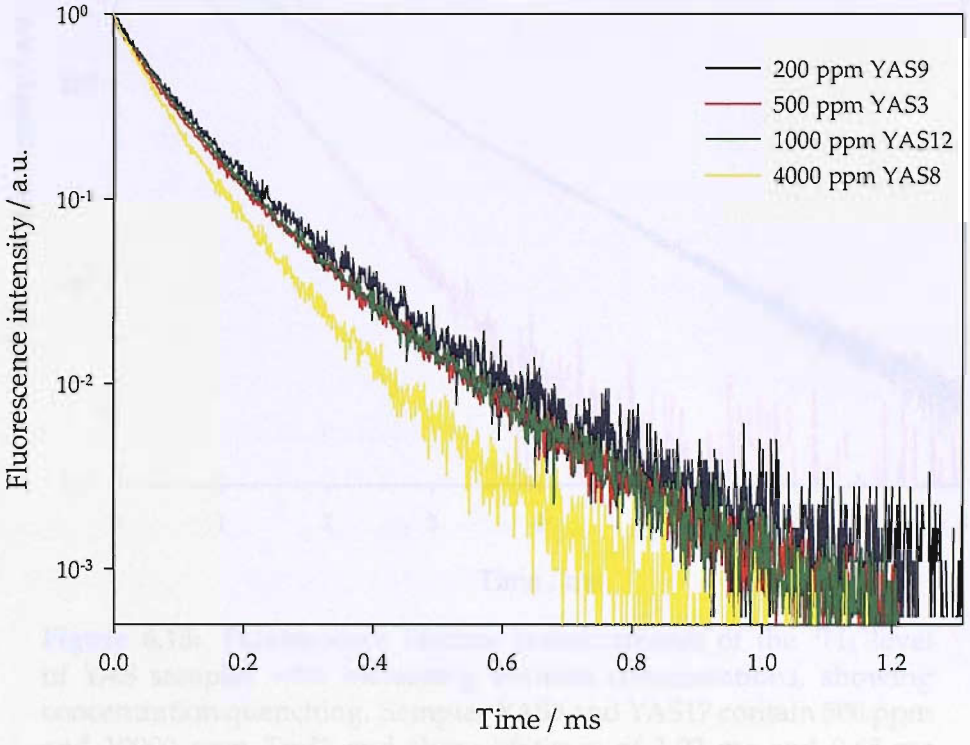

Figure 6.14: Fluorescence lifetime measurements of the $^3F_4$ level of YAS samples with increasing thulium concentrations, showing concentration quenching. Samples YAS9, YAS3, YAS12 and YAS8 show lifetimes of 77 μs, 71 μs, 71 μs and 62 μs respectively.

Fluorescence lifetime measurements were also made for the $^3H_4$ level by pumping at 800 nm and measuring fluorescence at >1700 nm with an InGaAs detector.

It should be noted that this measurement relies on decay from the $^3F_4$ and $^3H_5$ levels to populate the $^3H_4$ level; this will cause a distortion to the first part of the decay data as the $^3H_4$ level continues to be populated for a short time after the excitation light has been removed. Samples YAS5 and YAS17 have the same host composition and Tm^{3+} concentrations of 500 ppm and 10000 ppm respectively. The lifetime data is shown in Fig. 6.15 and shows concentration quenching at Tm^{3+} concentrations of >500 ppm. This is not consistent with lifetime data from Er-doped YAS, which showed no concentration quenching at a dopant concentration 26000 ppm wt. (10000 ppm ions).

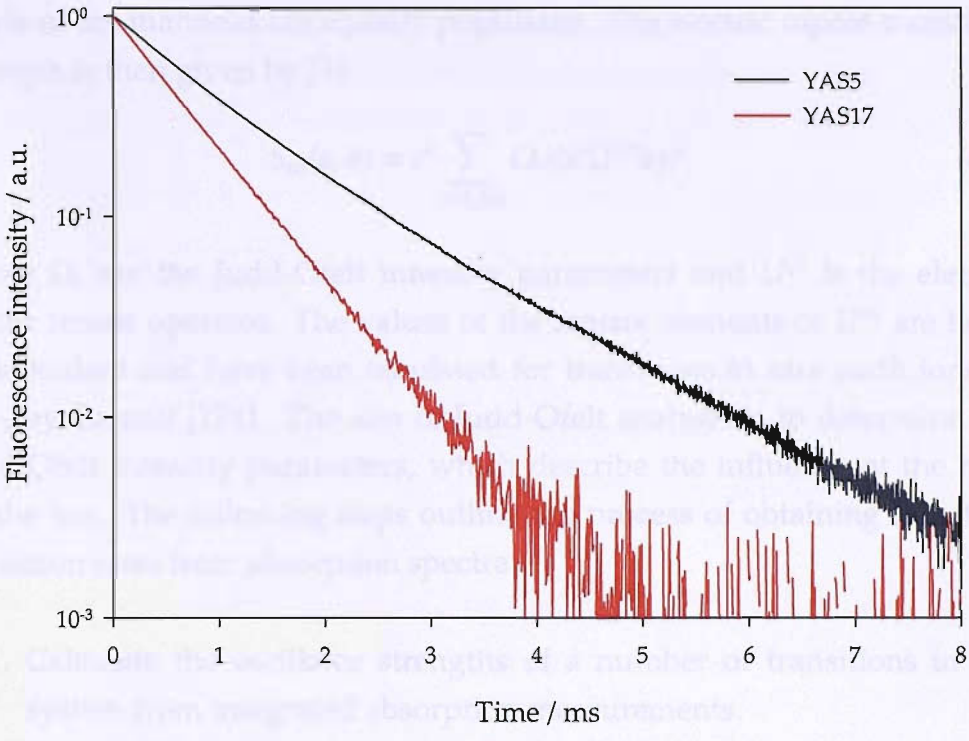

Figure 6.15: Fluorescence lifetime measurements of the $^3H_4$ level of YAS samples with increasing thulium concentrations, showing concentration quenching. Samples YAS5 and YAS17 contain 500 ppm and 10000 ppm Tm^{3+} and show lifetimes of 1.02 ms and 0.65 ms respectively.

6.6.1 Judd-Ofelt analysis

In 1962, Judd [172] and Ofelt [173], working independently, published a system of parameters which allows radiative transition rates to be calculated from absorption measurements. This allows the calculation of radiative rates between any two levels in rare earth-doped materials and, for levels with fluorescence lifetime data, can be used to determine quantum efficiencies.

Electric dipole transitions between $4f$ states are parity forbidden in a free ion, as stated in section 2.2.4. However, the crystal field of the host material mixes $5d$ states with opposite parity into the $4f$ configuration. This then allows $4f$-$4f$ transitions to occur. Judd and Ofelt used a number of assumptions in order to obtain an expression for the electric dipole transition strength. The assumptions are that the excited $5d$ states are degenerate, the energy differences between the $5d$ levels and the $4f$ levels are equal and all the stark

levels of the manifold are equally populated. The electric dipole transition strength is then given by [3]:

$$S_{ed}(a,b) = e^2 \sum_{t=2,4,6} \Omega_t |\langle a|U^{(t)}|b\rangle|^2, \tag{6.2}$$

where Ω_t are the Judd-Ofelt intensity parameters and $U^{(t)}$ is the electric dipole tensor operator. The values of the matrix elements of $U^{(t)}$ are host-independent and have been tabulated for transitions in rare earth ions in LaF_3 by Carnall [174]. The aim of Judd-Ofelt analysis is to determine the Judd-Ofelt intensity parameters, which describe the influence of the host on the ion. The following steps outline the process of obtaining radiative transition rates from absorption spectra:

1. Calculate the oscillator strengths of a number of transitions in the system from integrated absorption measurements.

2. Determine the transition strengths, S, from the calculated oscillator strength using equation 6.3.

3. Calculate the magnetic dipole contribution to the transition strengths and subtract from the measured transition strengths. This gives the electric dipole contribution to the transition strengths, neglecting multipolar interactions.

4. Determine Ω_t by least-squares fitting the electric dipole transition strengths to equation 6.2.

5. The Ω_t parameters can then be used in equation 6.2 to determine the electric dipole contribution to the transition strength. Combining this with the magnetic dipole contribution allows the calculation of transition rates between any two levels in the system. The sum of the transition rates to all lower levels gives the total radiative rate.

Transition strengths can be calculated by rearranging equation 2.8:

$$S(a,b) = \frac{3g_a h\epsilon_0 c}{2\pi^2 \nu \chi} \int \sigma(\nu) d\nu \tag{6.3}$$

The magnetic dipole contribution was calculated from tabulated data published by Carnall [174]. Of the transitions considered here, only the $^3H_6 \leftrightarrow {}^3H_5$ transition is significantly affected by the magnetic dipole process.

The quality of the fit is given by the root-mean-square (RMS) error of the measured and calculated transition strengths. Generally more than three absorption peaks should be used in the analysis to reduce the RMS error. While Judd-Ofelt analysis is a useful technique for evaluating radiative decay rates, the errors involved can be as high as 10-20% and three of the transitions used in this analysis are hypersensitive. This means that the technique may not be appropriate for evaluating small compositional changes in host materials [175].

Judd-Ofelt analysis was carried out on the YAS3 and YAS8 samples which both contain 26.25% Y_2O_3, 26.25% Al_2O_3 and 47.5% SiO_2 and contain 500 ppm and 4000 ppm Tm^{3+} respectively. The results are shown in table 6.1 with the results of an analysis of a 1300 ppm Tm^{3+}-doped YAS glass sample of the same composition which were calculated by Jander [146]. In order to reduce the RMS errors in these calculations, the $^3F_2$ and $^3F_3$ levels were merged in the measurement of the integrated absorption spectra and the $^1D_2$ was not included because of difficulty in subtracting the background absorption.

Sample	Ω_2	Ω_4 /$\times 10^{-24}$m^2	Ω_6	RMS error	τ_r ($^3F_4$) / μs	QE ($^3F_4$)
YAS3	3.8±1.4	1.6±1.2	1.0±0.3	11%	740	14%
YAS8	5.1±0.7	0.6±0.6	1.4±0.2	5.4%	600	14%
YAS15J*	7.0±0.7	0.2±0.5	1.6±0.2	4.1%	470	20%

Table 6.1: Judd-Ofelt parameters and radiative transition rates for thulium-doped YAS samples with the same host composition. *The results for YAS15J were provided by Jander [146].

For calculations of quantum efficiency, single exponential fits were used to obtain the measured lifetimes. These were 101 μs for YAS3 and 83 μs for YAS8. The quantum efficiency of the YAS8 sample is expected to be lower than that of YAS3 because of the concentration quenching, however the large errors in τ_r mean that a comparison of quantum efficiencies between these samples is not appropriate. The results do show that the quantum efficiency of 14% calculated for these samples appears to be lower than of the

YAS sample melted by Jander [166], using an identical sample preparation technique. The reason for this is not clear, but considering the relatively large errors in the Judd-Ofelt analysis, the results are in reasonable agreement.

6.7 Thulium-doped YAS fibre

The intention in this investigation was to optimise the YAS glass composition with respect to the spectroscopy and then attempt to fabricate a fibre using the optimised glass composition. However, a number of problems were encountered during sample preparation which limited the choice of glass composition:

- Several compositions with lower silica content cracked during annealing. This may be due to an increased thermal expansion coefficient which has been reported in YAS compositions with low silica content [168].
- Many of the samples with <60% silica contained small bubbles distributed throughout the glass. These bubbles were removed after remelting in the YAS13 sample, however as the sample was being broken up before remelting it was contaminated with brass, causing the large infrared peak shown in Fig. 6.9. YAS15 was broken up using a pestle and mortar and remelted without significant transition metal contamination, however the resulting glass was not completely clear.
- For the YAS4 composition, the batch did not melt at 1600°C and higher temperatures were not attainable with available furnaces.
- Compositions containing 60% SiO_2 were consistently free of bubbles and particles, though they often showed cloudy regions of bubbles on the top surface.

Several attempts were made to improve sample quality with regard to the problems listed above. For the YAS11 sample, the crucible was put into the furnace at 750°C and the furnace was ramped up to 1600°C for 3 h. This extended melting process did not improve sample quality. YAS12

was prepared with particular attention to reducing exposure of the batch to moisture in the atmosphere. The batch was prepared and placed in the crucible in the glovebox and then placed in a sealed polyethylene bag, which was opened immediately before the crucible was put into the furnace. The FTIR spectrum of this sample, shown in Fig. 6.7, shows that this procedure did not significantly reduce hydroxyl content. The batch for the YAS13 sample was compressed in the crucible in order to remove air pockets in the powder, however the sample still contained bubbles. The powders for the YAS14 were mixed using a pestle and mortar in order to break up small clusters in the powder and improve homogeneity, though no improvement in the sample quality was observed. YAS17 was prepared from new powders, but still showed cloudiness on the surface. Sample YAS18 was prepared without any active dopant, this sample still contained bubbles and cracked during annealing.

Since compositions with 17.5% Y_2O_3, 22.5% Al_2O_3 and 60% SiO_2 were consistently clear in the bulk of the glass, this was the host composition chosen for the attempt at fibre-drawing. A summary of the physical properties and characteristic temperatures of this glass is given in table 6.2.

Expansion coefficient	50×10^{-7} K^{-1}
Density	3.4 g/cm^3
Refractive Index	1.65
T_m	1350°C
T_g	895°C
T_x	1150°C
Softening temperature	935°C

Table 6.2: Summary of physical properties and characteristic temperatures of the YAS glass used for fibre fabrication.

6.7.1 Fibre fabrication

Since this was a first attempt at pulling a YAS fibre, it was decided to try to pull a single rod of YAS glass into an unclad fibre.

6.7.1.1 Preform fabrication

For the production of the YAS preform rod, a 120 g batch of the chosen composition was melted and cast into a brass mould using the procedure described in section 6.2. On the first attempt at casting, the glass cracked before it was placed in the annealing furnace. The glass was remelted and the procedure was repeated, but this time with the mould temperature increased from ~300°C to ~550°C to reduce the thermal shock experienced by the glass. The glass was annealed without cracking, and the resulting 100 × 15 × 10 mm glass bar is shown in Fig. 6.16. The glass was clear apart from surface bubbles at one end which were folded into the glass as it was cast.

Figure 6.16: 10 cm long YAS glass bar used for the preform for the unclad fibre.

In order to cut out the rod from the glass bar, the bar was mounted onto an L-shaped piece of aluminium using wax and was then mounted onto an

ultrasonic drill. A drill bit with an internal diameter of 8 mm was used to cut out a rod from the glass bar at a speed of 1 mm/min. The rod was drilled out without cracking and is shown in Fig. 6.17. As the drilling progressed, the outer part of the glass bar cracked showing that future attempts at this process should be carried out at a slower rate.

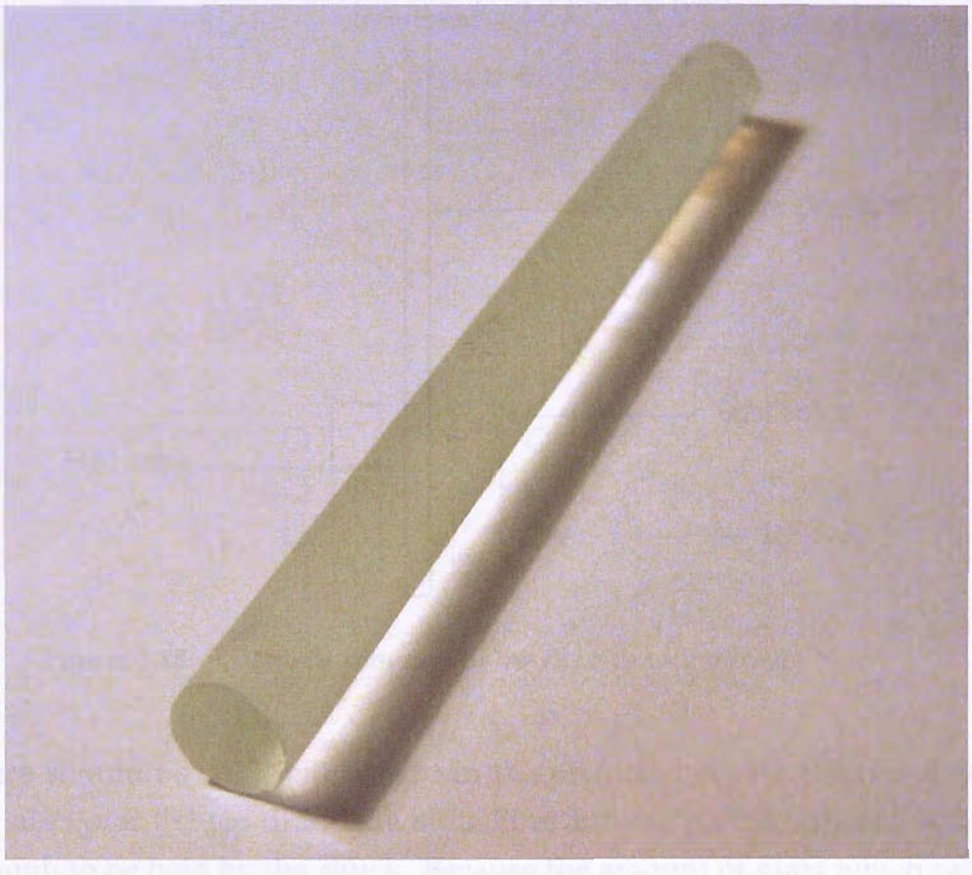

Figure 6.17: Thulium-doped YAS fibre preform.

6.7.1.2 Fibre fabrication

A schematic diagram of the fibre-drawing apparatus is shown in Fig. 6.18. The fibre tower essentially consists of an RF furnace with a cylindrical hole through the middle where the preform is placed. The temperature of the furnace is increased until necking starts to occur in the preform. The fibre 'drop' is allowed to move out of the furnace and the attached fibre is then wound round a drum at the base of the tower. The drum is rotated to apply tension to the fibre as it is drawn. Since the preform will begin necking at the hottest part of the inside of the susceptor, the weight of preform below this

point will help draw down the fibre as the fibre-drawing starts. As material is removed from the preform during fibre-drawing, the preform feed control lowers more of the preform into the hotzone.

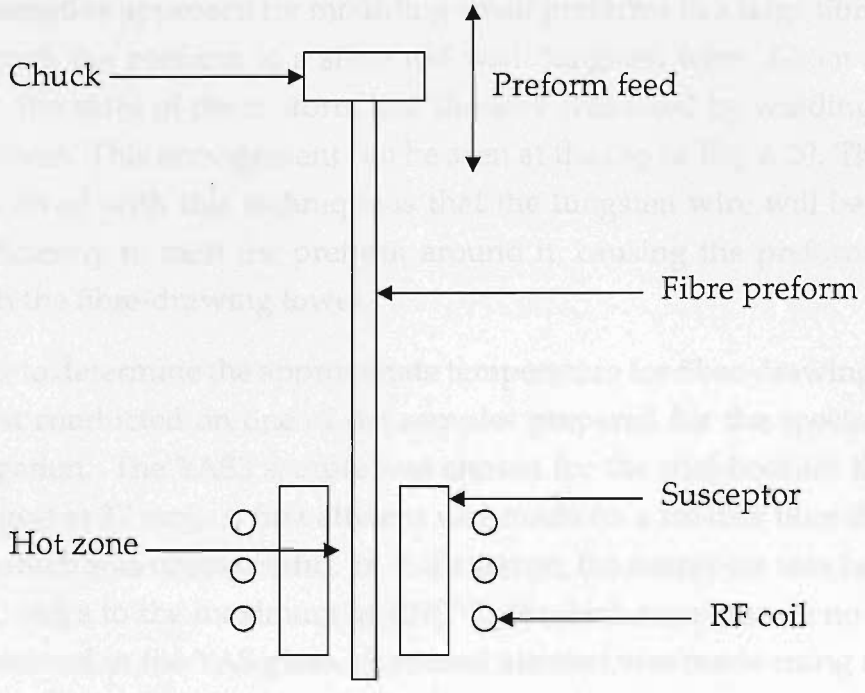

Figure 6.18: Schematic diagram of the fibre-drawing tower.

There should be sufficient weight in the preform beneath the hot-zone in the susceptor to help draw down the fibre and the preform should be long enough to be held by the chuck. Because the amount of glass which can be formed into a rod by casting was limited by the volume of the crucible, it was not possible to produce a sufficiently long preform. One possible solution to this problem is to weld the end of the YAS preform to a longer silica rod.

Several attempts were made to join YAS glass samples to silica glass. On the first attempt both the silica rod and YAS glass here heated with a hydrogen-oxygen torch. While heating the YAS glass, many small bubbles were produced, forming a white foam. These bubbles at the interface between materials made the join too weak for practical use. A number of other YAS compositions were heated in the same way with similar results. In order to discount that the torch was introducing the bubbles, a sample of YAS glass was heated with a 40 W Synrad CO_2 laser. The foam was still produced on heating with the CO_2 laser. When a YAS sample was melted inside a

silica tube, the sample melted without producing foam. It appears that the foaming is only created by vigorous heating, though the origin of the foaming is not known.

The alternative approach for mounting small preforms in a large fibre tower is to attach the preform to a silica rod with tungsten wire. Grooves were cut into the sides of the preform and the wire was fixed by winding round the preform. This arrangement can be seen at the top of Fig. 6.20. The main risk involved with this technique is that the tungsten wire will be heated up sufficiently to melt the preform around it, causing the preform to fall through the fibre-drawing tower.

In order to determine the approximate temperature for fibre-drawing, a trial was first conducted on one of the samples prepared for the spectroscopic investigation. The YAS3 sample was chosen for the trial because this was the longest at 37 mm. A first attempt was made on a smaller fibre-drawing tower which was unsuccessful. In this attempt, the susceptor was heated in 20-30°C steps to the maximum at 1070°C, at which temperature no change was observed in the YAS glass. A second attempt was made using a larger drawing tower which was capable of reaching higher temperatures. This attempt was successful, and movement of the sample was observed at 1160°C. The result of this trial is shown in Fig. 6.19, which shows that the glass was heavily crystallised during heating. This was to be expected at this temperature as Jander reported the crystallisation temperature of this composition to be 1142°C [146]. However, as the YAS composition used for the preform was nearer the centre of the glass-forming region and so would be less prone to crystallisation.

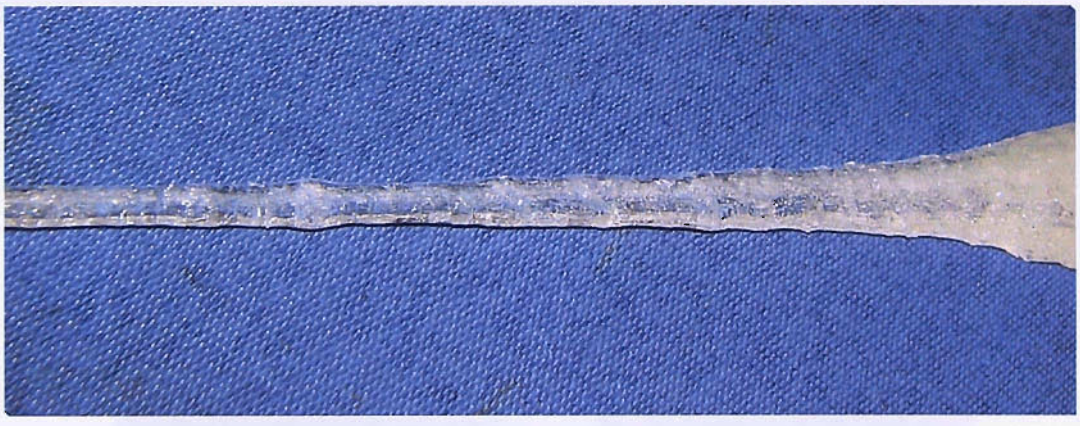

Figure 6.19: The result of a trial attempt at pulling a fibre from the YAS3 sample. The glass is heavily devitrified.

For the attempt at fibre-drawing using the YAS preform, a weight of 100 g was attached to the bottom of the preform using tungsten wire. This weight provides an additional tension force on the preform for the start of the fibre-draw which helps the fibre-drawing to proceed at lower temperature and therefore reduces the risk of devitrification. The temperature was ramped up to 1050°C and the weight started dropping slowly. The temperature was increased in steps of 10°C to 1150°C in order to increase the drawing rate. The fibre was attached to a drum below the drawing tower and 7.5 m of fibre was drawn onto the drum. Unfortunately, a malfunction in the mechanism which rotates the drum caused the fibre to break in the furnace before the fibre diameter was stabilised. Figure 6.20 shows the YAS preform after fibre-drawing and shows that the fibre is fire-polished as it is pulled from the preform. An attempt was made at drawing more fibre from the remaining preform, however there was insufficient material on the preform to attach a weight so the furnace was heated to a temperature of 1235°C. At this temperature the preform became detached from the supporting tungsten wire and the so the attempt was aborted.

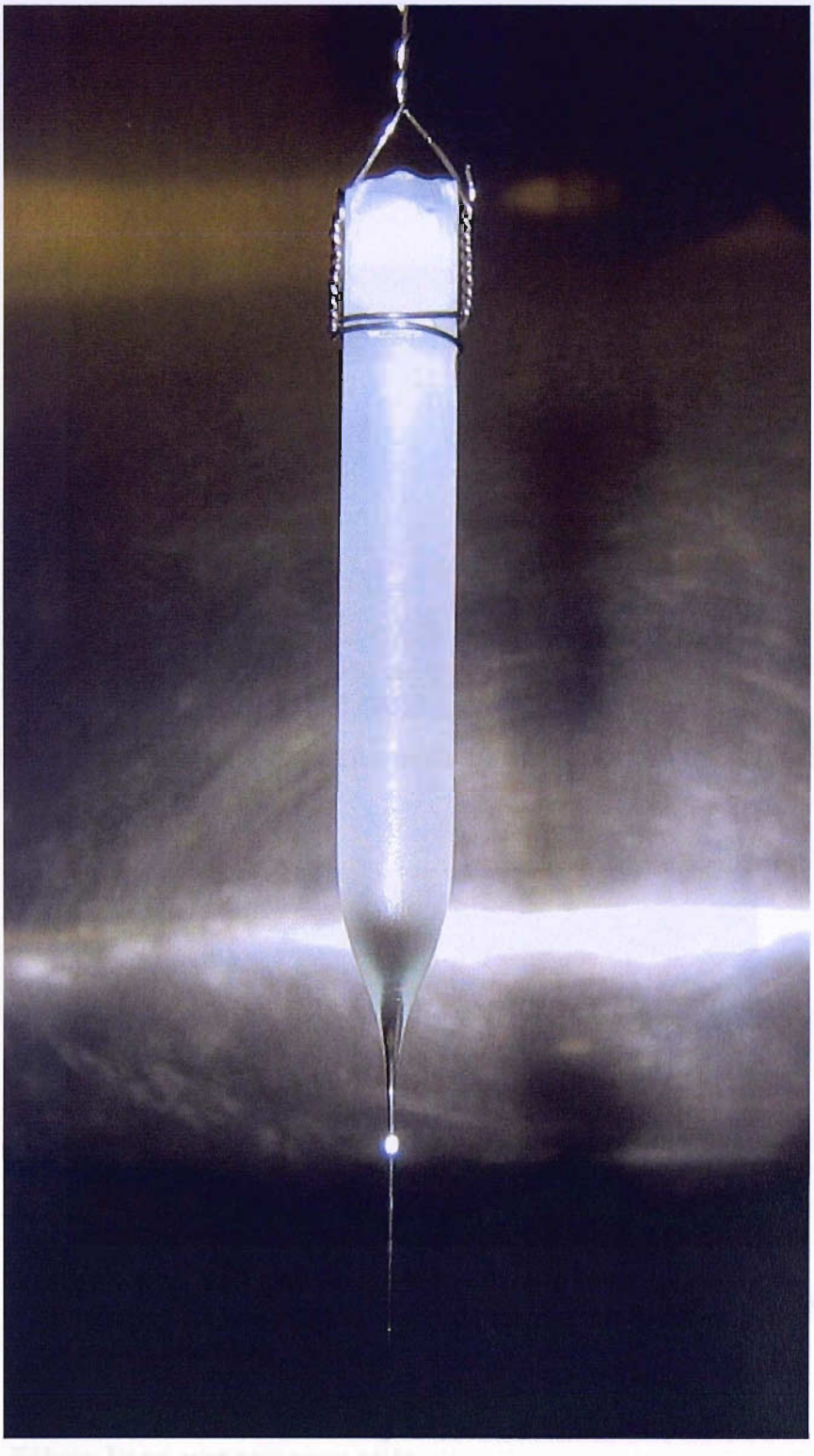

Figure 6.20: YAS fibre preform after fibre-drawing, showing how the tungsten wire was attached and that the preform is fire-polished as it is pulled into fibre.

The diameter of the fibre ranged from 150 μm to 350 μm along the length. The fibre was easily cleaved; Fig. 6.21 shows the end of a section of the fibre with diameter of 210 μm and Fig. 6.22 shows a side view of the same piece of fibre. The fibre was strong enough to be handled throughout experiments without being broken accidentally.

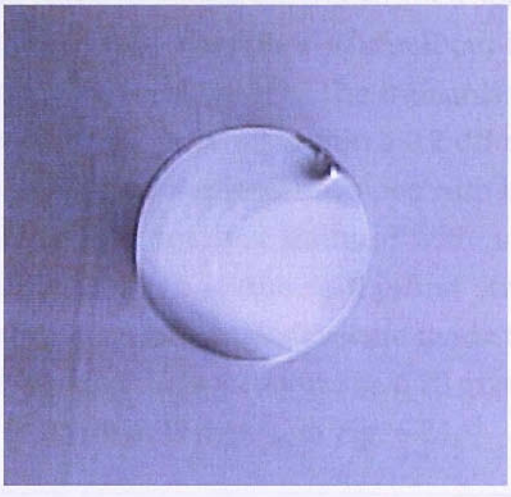

Figure 6.21: Top view of a 210 μm diameter cleaved section of YAS fibre.

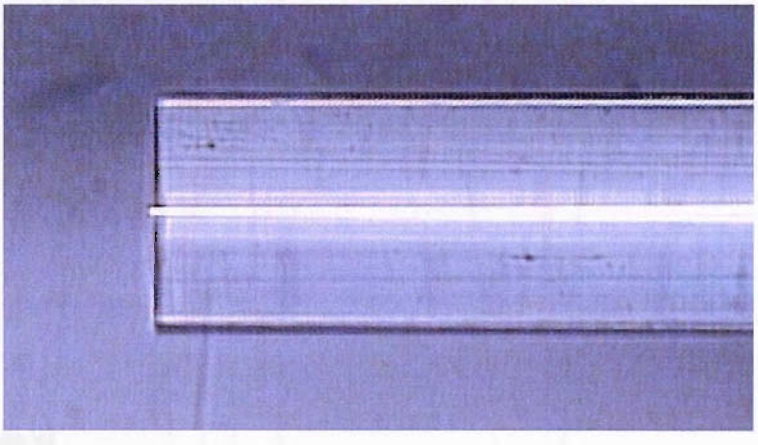

Figure 6.22: Side view of a 210 μm diameter cleaved section of YAS fibre.

6.7.2 Fibre loss measurements

Loss measurements for the YAS fibre were made using the cutback method. This method involves focusing a broadband light source into one end of the fibre and measuring the transmitted spectrum at the other end of the fibre

using an optical spectrum analyser (OSA). The fibre is then cut back without disturbing the end where the light is coupled in. The transmitted spectrum is measured from the cutback fibre, and the difference between the spectra gives the loss of the fibre. For this experiment, a 50 W halogen lamp was used as the broadband source and the light from fibre was coupled into an Ando OSA which was used to record the transmitted spectra. An initial fibre length of 1.7 m was used and a number of small cut-backs were made to ensure the fibre cleaves were consistent. The transmission spectra through the first four 26 mm cutbacks were all within a 0.2 dB range. The fibre was then cut back by 1656 mm and the resulting spectrum is shown in Fig. 6.23, which shows the absorption peaks of thulium with an additional peak at 1400 nm. This additional peak is due to the first stretching overtone of OH^- [151]. Again, several 26 mm cutbacks were made to ensure the cleaves were consistent. Subtracting the spectra in Fig. 6.23 gives the minimum loss of 3.6 dB/m at 1360 nm, which is shown in Fig. 6.24.

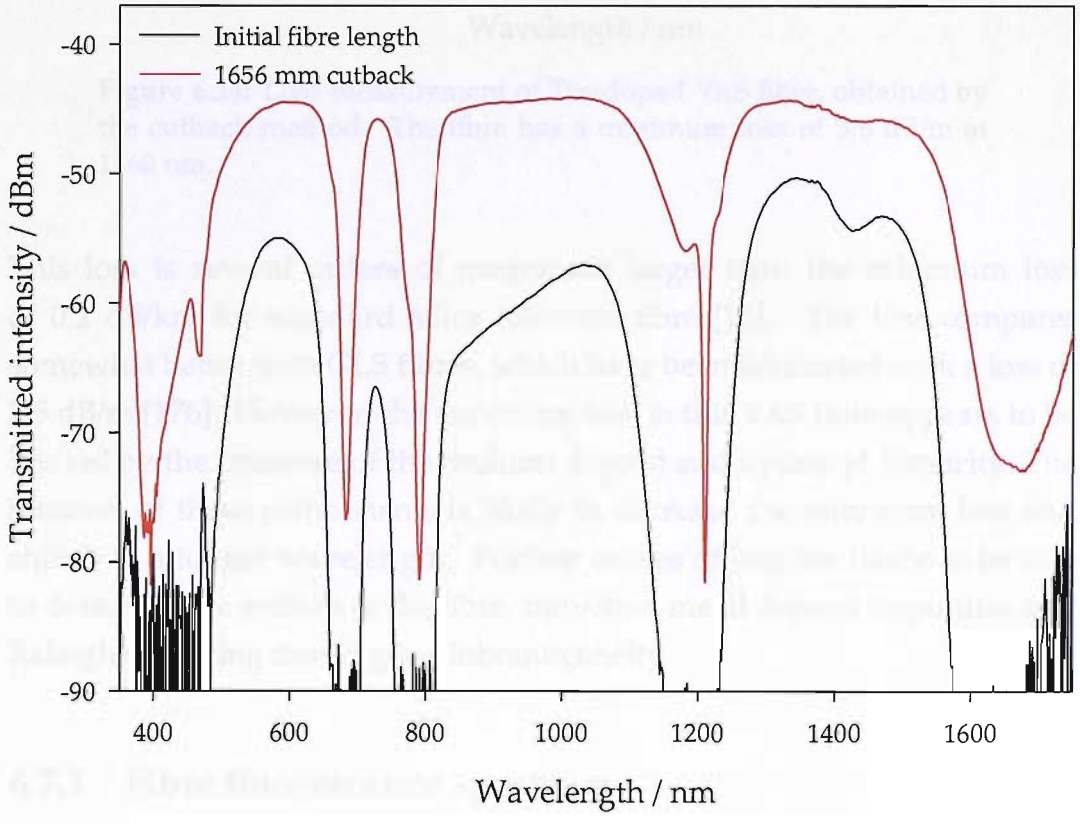

Figure 6.23: Spectra recorded for YAS fibre loss measurements, showing the absorption peaks of thulium and an extra peak due to hydroxyl at 1400 nm.

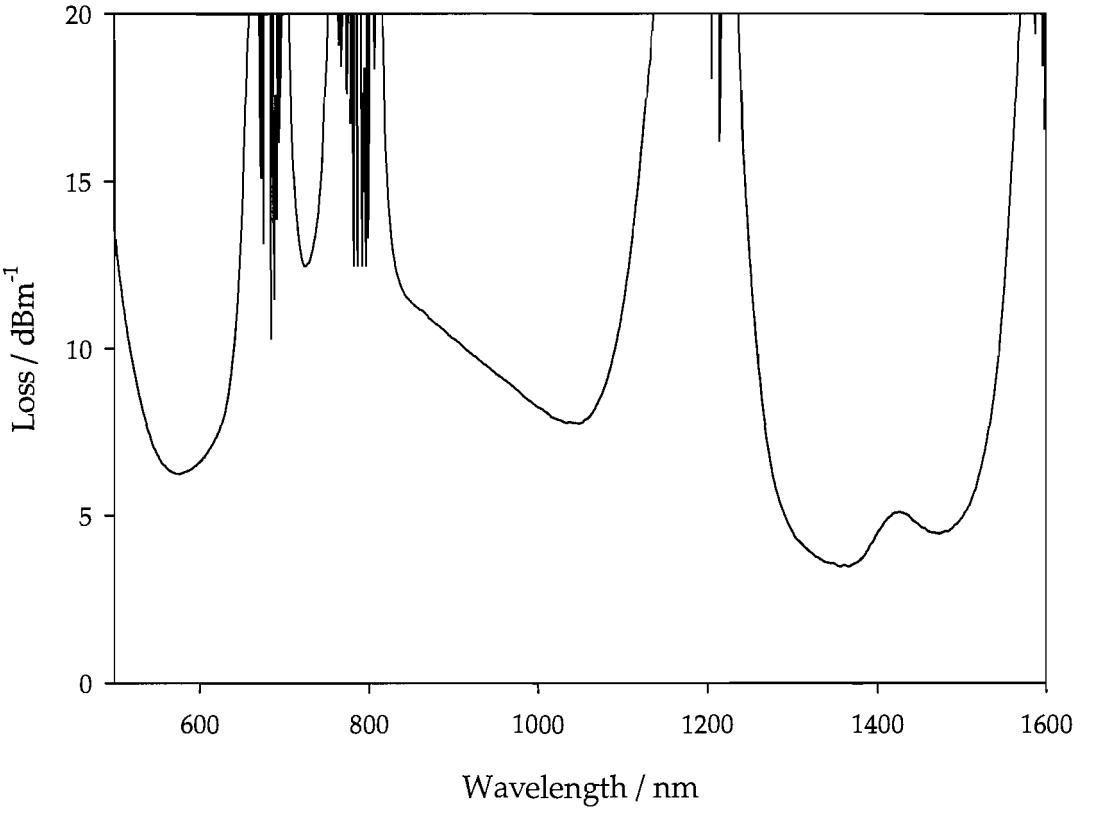

Figure 6.24: Loss measurement of Tm-doped YAS fibre, obtained by the cutback method. The fibre has a minimum loss of 3.6 dB/m at 1360 nm.

This loss is several orders of magnitude larger than the minimum loss of 0.2 dB/km for standard silica telecoms fibre [15]. The loss compares somewhat better with GLS fibres, which have been fabricated with a loss of 2.5 dB/m [176]. However, the minimum loss in this YAS fibre appears to be limited by the presence of the thulium dopant and hydroxyl impurity. The removal of these components is likely to decrease the minimum loss and shift it to a longer wavelength. Further causes of loss are likely to be due to defects in the surface of the fibre, transition metal dopant impurities and Raleigh scattering due to glass inhomogeneity.

6.7.3 Fibre fluorescence spectrum

In order to measure fluorescence from the thulium-doped YAS fibre, 800 nm light from a laser diode was coupled into one end of the fibre. Fluorescence was collected from the same end using a 50 μm core multimode silica fibre,

the light from which was focused into a monochromator. A Stanford lock-in amplifier with an InGaAs photodiode was used to measure the light passed through the monochromator in a similar arrangement to that described in section 3.3.

The emission at 1470 nm is shown in Fig. 6.25 and is corrected for the spectral response of the system. The emission FWHM is 137 nm in the fibre, which is broader than the 129 nm FWHM observed in the bulk glass. This may be due in part to the lower resolution of the YAS fibre spectrum (11 nm instead of 5 nm), although there does appear to be broadening of the short wavelength tail of the 1800 nm emission. This could be a result of increased inhomogeneous broadening caused by the either the extra heat treatment, or by the fibre drawing, in which case it further increases the material's potential as a broadband S-band amplifier.

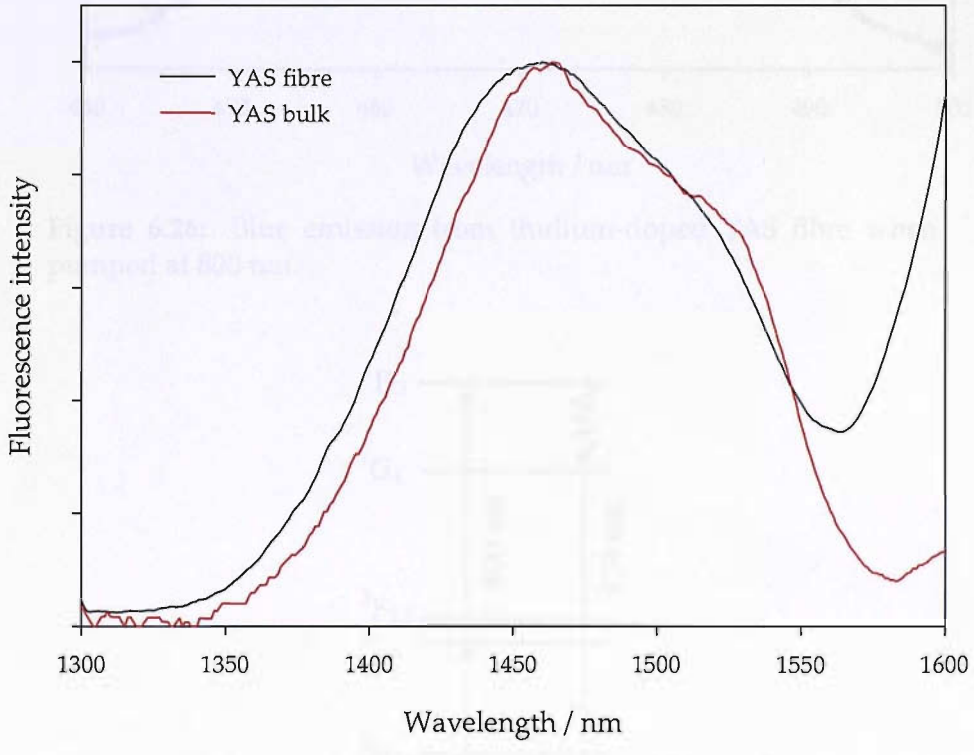

Figure 6.25: Emission from thulium-doped YAS fibre when pumped at 800 nm. The spectral resolution is 11 nm.

While pumping at 800 nm to measure the emission at 1470 nm, blue emission could be seen from the fibre at pump powers of >1 W. A spectrum was recorded of this blue emission using an OSA and is shown in Fig. 6.26.

This blue emission is evidence of upconversion in the fibre and a possible mechanism is shown in Fig. 6.27

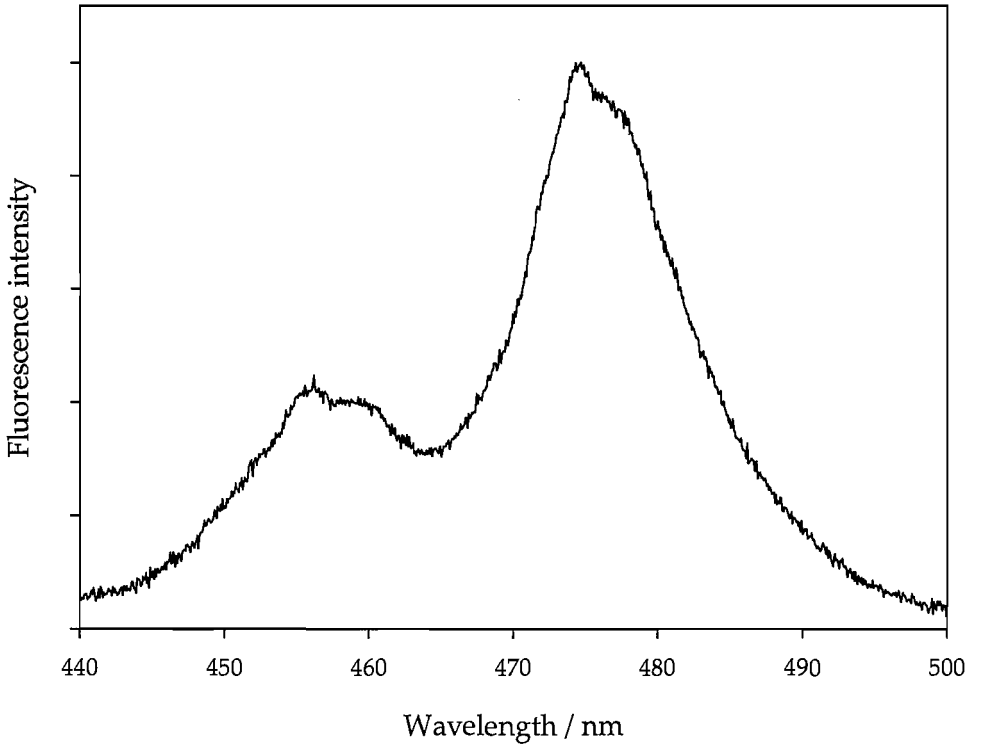

Figure 6.26: Blue emission from thulium-doped YAS fibre when pumped at 800 nm.

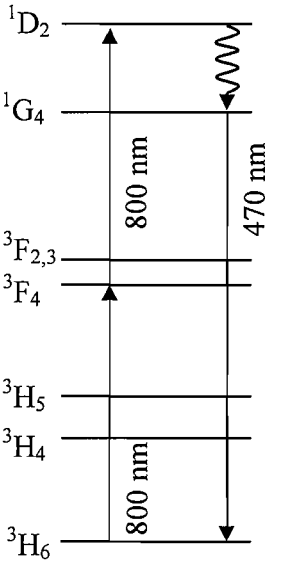

Figure 6.27: Possible upconversion pumping scheme for the blue emission centred at 470 nm, showing the absorption of two 800 nm photons and multiphonon emission from $^1D_2$ to $^1G_4$.

6.7.4 Fluorescence lifetime measurements

Fluorescence lifetime measurements of the $^3F_4$ level of the thulium-doped YAS fibre were made by pumping with an 800 nm laser diode and collecting fluorescence perpendicular to the fibre axis using a 1 mm multimode silica fibre. The fluorescence from the silica fibre was focused into a monochromator and a Hamamatsu R3236 photomultiplier tube was used as the detector. For this measurement the monochromator was set to pass fluorescence at 790 nm and a Stanford SR430 multichannel scaler was used to record the decay data. The resulting lifetime data is shown in Fig. 6.28 with the stretched exponential fit. The $^3F_4$ level in the YAS fibre showed a lifetime of 51 μs. This is shorter than the 60 μs lifetime of the YAS2 sample which has the same Tm^{3+} concentration. It is possible that this is caused by a redistribution of Tm^{3+} ions during fibre-drawing.

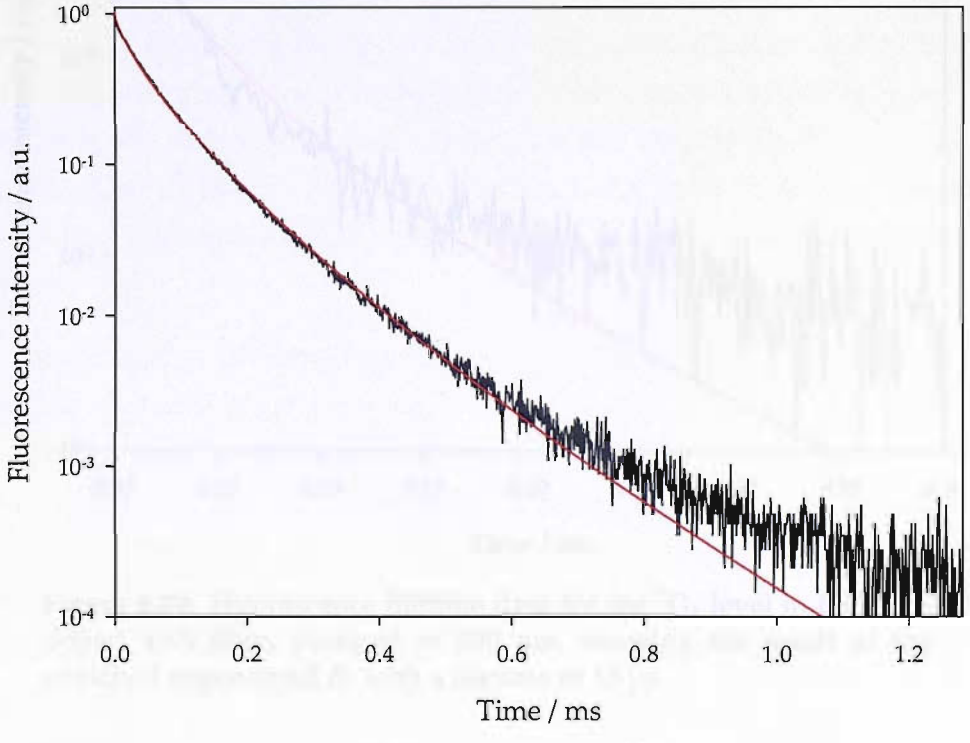

Figure 6.28: Fluorescence lifetime data for the $^3F_4$ level in the thulium-doped YAS fibre, pumped at 800 nm, showing the result of the stretched exponential fit with a lifetime of 51 μs.

By setting the monochromator to pass light at 470 nm, lifetime data was obtained for the $^1G_4$ level. The results are shown in Fig. 6.29 with the fitted

stretched exponential producing a lifetime of 13 μs. This is much shorter than that measured in various fluoride and silica glasses. The $^1G_4$ level lifetime was measured to be ~550 μs in Tm-doped fluorozirconate glasses [177,178] and 200 μs and 300 μs in Tm-doped germanosilicate and aluminosilicate glass fibres respectively [179]. It is unlikely that differences in multiphonon decay rates could be responsible, because the energy difference between the $^1G_4$ and $^3F_2$ levels is approximately 6500 cm^{-1} (almost 7 times the host phonon energy). It is likely that the lifetime measurement is distorted to some extent due to the indirect pumping scheme used to populate the upper level. Further experiments utilising different pump schemes would be useful to confirm this measurement.

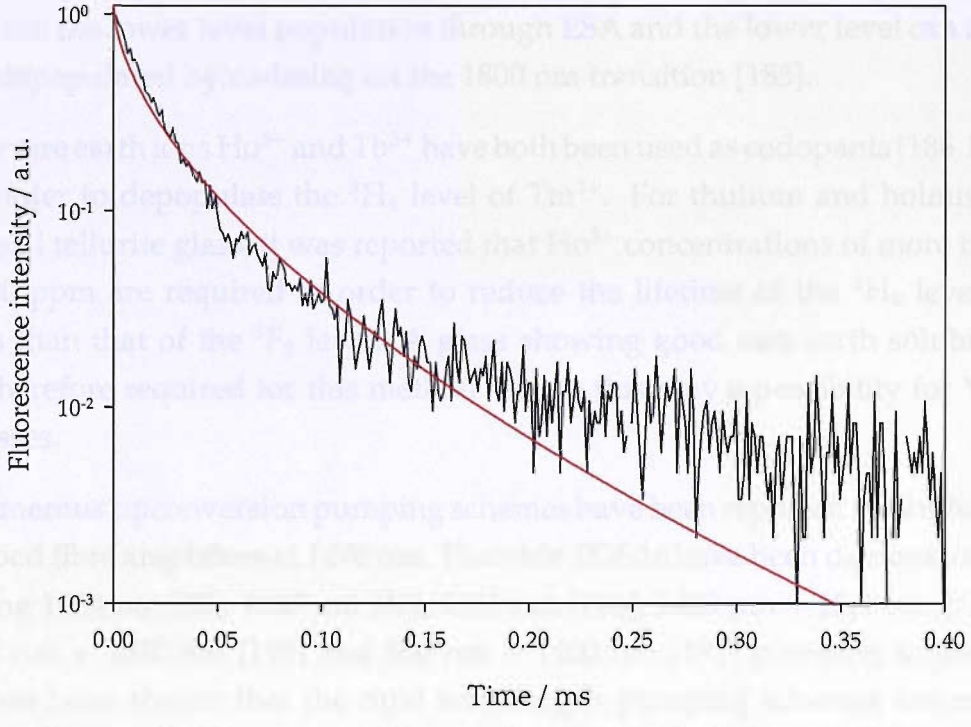

Figure 6.29: Fluorescence lifetime data for the $^1G_4$ level in thulium-doped YAS fibre, pumped at 800 nm, showing the result of the stretched exponential fit with a lifetime of 13 μs.

There has been considerable interest in visible upconversion lasers, particularly in thulium-doped glass fibre lasers [180–182]. However, the use of these fibres has been limited by the effect of photodarkening, which occurs on the timescale of hours in Tm^{3+}-doped ZBLAN [183] and in seconds in Tm^{3+}-doped silica [184]. No reduction in the intensity of the 470 nm emission

from the Tm^{3+}-doped YAS fibre was observed on a timescale of several minutes.

6.7.5 Discussion of amplification in Tm-doped YAS

Since the lifetime of the lower level of the 1470 nm transition is longer than that of the upper level, this is termed a self-terminating transition and the lower level should be depopulated in order to achieve a population inversion between the levels. There are three main ways to achieve this: the lower level can be depopulated by codoping with a species which has a fast decay rate, upconversion or dual pumping schemes can be employed which reduce the lower level population through ESA and the lower level can also be depopulated by co-lasing on the 1800 nm transition [185].

The rare earth ions Ho^{3+} and Tb^{3+} have both been used as codopants [186,187] in order to depopulate the $^3H_4$ level of Tm^{3+}. For thulium and holmium-doped tellurite glass, it was reported that Ho^{3+} concentrations of more than 5000 ppm are required in order to reduce the lifetime of the $^3H_4$ level to less than that of the $^3F_4$ level. A glass showing good rare earth solubility is therefore required for this method and so this may a possibility for YAS glasses.

Numerous upconversion pumping schemes have been reported for thulium-doped fibre amplifiers at 1470 nm. Fluoride TDFAs have been demonstrated using 1064 nm [37], 1047 nm [40], 1410 nm [188], 1400 nm + 1560 nm [189], 800 nm + 1050 nm [190] and 800 nm + 1400 nm [191] pumping schemes. It has been shown that the dual wavelength pumping schemes are more efficient [189, 192]; this is because dual-wavelength pumping schemes generally do not rely on multiphonon decay and wavelengths can be selected to reduce upconversion to levels above the $^3F_4$ level.

The chosen pumping scheme has a strong effect on the length of fibre required for an amplifier. As shown in the absorption spectra in Fig. 6.8, the absorption coefficient at 800 nm is many times stronger than that at 1064 nm, 1410 nm and 1560 nm.

The major obstacle to achieving gain in the Tm-doped YAS fibre fabricated in this work is the large core size. For example, Minelly et al. reported 20 dB gain at 1490 nm in a thulium-doped antimony silicate fibre with a 4 μm core diameter. This was achieved by pumping at 1405 nm with a power of 1 W [42]. In order to achieve the same excitation intensity in a fibre with a 150 μm core, the pump power would need to be increased by a factor of 6000. Since for low powers the gain is linearly dependent upon the pump power, using the same power to pump a fibre with a 150 μm core would result in a gain of <0.01 dB. An attempt at measuring gain in the Tm-doped YAS fibre was made with a 3 W 1405 nm pump, but it was clear that measuring gain below 1 dB would be difficult. This is largely due to the poor overlap between signal and pump beams in the fibre.

Though it may be possible to demonstrate gain in a bulk sample of Tm-doped YAS glass, for gain to be demonstrated in a Tm-doped YAS fibre a core-cladding structure should be devised. It is possible that a suitable cladding glass would be another YAS composition with reduced refractive index, for example a composition with lower yttria content. A YAS fibre with a cladding would allow a small core size so that sufficient pump intensity and pump-signal overlap can be achieved.

6.8 Summary

A range of thulium-doped compositions in the Y_2O_3-Al_2O_3-SiO_2 system were melted and analysed using various spectroscopic techniques. Raman spectra revealed the maximum phonon energy of 950 cm^{-1} which arises from the high concentration of nonbridging oxygens. Raman and FTIR spectra show a decrease in maximum phonon energy with an increase in yttria:alumina ration and a decrease in silica content. Fluorescence lifetime measurements for the $^3F_4$ level show that by altering these parameters, lifetimes vary from 60 μs to 71 μs within the range studied. Judd-Ofelt analysis shows that the $^3F_4$ level has a quantum efficiency of ~14%. The FWHM of the emission at 1470 nm was measured to be 129 nm and this was unaffected by the host composition.

Concentration quenching was observed for both the $^3F_4$ and $^3H_4$ levels. For the $^3H_4$ level, a lifetime of 1.02 ms was measured for a sample doped with 500 ppm Tm^{3+}; this was reduced to 0.65 ms in a sample doped with 10000 ppm Tm^{3+}. This is a much smaller reduction than was seen in Tm-doped tin silicate glass-ceramics (see section 5.6.3). However, it is not consistent with the behaviour of erbium-doped YAS reported by Jander, where no concentration quenching was observed in a YAS glass with 10000 ppm Er^{3+} [166]. Further investigation into highly doped glasses is necessary to determine the reason for this difference.

A number of problems with the YAS glass quality were identified while preparing samples for this work. Many samples contained small bubbles distributed throughout the bulk of the glass and some of these cracked during annealing. Some other samples were clear in the bulk, but contained regions of small bubbles on the surface. These problems appear to be dependent on the composition.

An unclad thulium-doped YAS glass fibre was drawn from a 10 cm long preform rod. A continuous length of 7.5 m was produced, with a diameter of 150-350 μm. To the author's knowledge, this is the first report of a YAS glass fibre. The preform started necking at 1050°C and continuous fibre-drawing was achieved at 1150°C. Fibre loss measurements show that the YAS fibre has a minimum loss of 3.6 dB/m at 1360 nm.

The Tm-doped YAS fibre exhibited emission with a FWHM of 137 nm at 1470 nm, which is broader than that observed in the bulk glass. The emission lifetime of the $^3F_4$ level in the fibre is decreased compared to that of the bulk glass. These changes in fluorescence behaviour suggests that the fibre-drawing process alters the distribution of Tm^{3+} ions in the glass. Emission was also identified at 470 nm when the fibre was pumped with >1 W pump power at 800 nm; an upconversion scheme for this emission was proposed.

6.9 Further work

Further work should involve finding a suitable cladding glass for a YAS fibre. The fabrication of a clad YAS fibre would then allow an attempt at

demonstrating S-band amplification. In order to investigate the problem of concentration quenching, a range of erbium-doped YAS glasses should be prepared and lifetime measurements compared with those reported by Jander [166]. Photodarkening should also be investigated to establish if YAS glass may be useful for upconversion fibre lasers.

Chapter 7

Conclusions

7.1 Transition metal-doped chalcogenide glasses

Chromium, vanadium and nickel-doped chalcogenide glasses present an attractive proposition for new amplifier materials. Both absorption and emission bands from these glasses are extremely broad compared to rare earth-doped glasses, and fibre fabrication techniques for GLS are well established. The work in this thesis explored some of the fundamental spectroscopic properties of these materials and identified emission transitions from vanadium and nickel-doped GLS which have not previously been reported.

A number of chromium-doped chalcogenide glasses were studied as possible active materials for optical amplification. Fluorescence excitation measurements provide further evidence that chromium is hosted primarily as Cr^{4+} in these glasses. Fluorescence spectra taken at 300 K and 77 K show a shift to longer wavelength in peak emission and an increase in fluorescence intensity at lower temperature. A further decrease in temperature to 4 K leads to a narrowing of the emission band due to a reduction of homogeneous broadening processes.

A survey of the optical properties of transition metal-doped GLS glasses was carried out. Likely valence states were determined through a comprehensive comparison with the literature reporting absorption and emission spectra of transition metals of different valence states and site

symmetries doped into crystals and glasses. Fluorescence was identified for the first time in nickel-doped GLS and vanadium-doped GLS. Emission from the Ni-doped GLS sample is centred at ~1200 nm and shows a non-exponential lifetime of 40 μs. Emission from V-doped GLS is centred at 1420 nm and has a FWHM of 450 nm, making this glass particularly interesting for telecoms applications. Temperature-dependent fluorescence and fluorescence lifetime measurements of V-doped GLS suggest that this material is not affected by nonradiative decay to the same extent as Cr-doped GLS.

For further progress in determining how useful these materials may be as optical amplifiers, both quantum efficiency and ESA measurements should be made. To understand further the nature of the transition metal sites in chalcogenide glasses, electron spin resonance measurements would help to establish which valence states are hosted in these materials.

7.2 Rare earth-doped tin silicate glass-ceramics

Glasses produced by the sol-gel method are attractive for active devices because of the ability to incorporate a wide variety of dopants. The photosensitivity resulting from the addition of tin oxide to silica, makes these materials potentially useful for direct writing of waveguide structures and Bragg gratings. If efficient emission from rare earth ions can be obtained from these glasses, then they would make promising candidates for rare earth-doped waveguide amplifiers.

An investigation into the optical properties of erbium and thulium-doped tin silicate glass-ceramics was carried out on samples containing a range of tin oxide and rare earth dopant concentrations. For the Er-doped samples, fluorescence lifetime data at 1550 nm shows that increased tin oxide content increase lifetimes even at low Er concentrations. It is proposed that erbium occupies sites at the interface between the glass and nanocrystals in these materials. Samples containing 5% or more tin oxide showed a large infrared absorption, the origin of which is not understood.

Thulium-doped tin silicate glass-ceramics were investigated for the first time. Fluorescence at 1470 nm with a FWHM 120 nm, this is broader than that observed in thulium-doped silica. Emission lifetimes were generally increased in samples with higher tin oxide concentration.

The priority for further work should be to identify the origin of the large infrared absorption seen in sample with high tin content. The effect of further heat treatment should also be assessed with the aim of reducing concentration quenching.

7.3 Thulium-doped yttrium aluminosilicate glass

Rare earth-doped yttrium aluminosilicate glasses have a number of useful properties which makes them attractive materials for active optical devices. The glass-forming region for YAS glasses is large and extends up to 30% yttria, allowing high rare earth dopant concentrations with minimal quenching effects. Emission from thulium and erbium-doped YAS is particularly broad and the low maximum phonon energy of YAS (950 cm^{-1}) allows more efficient transitions compared to a silica host.

A number of YAS glass composition were prepared and analysed through Raman, optical absorption, fluorescence and fluorescence lifetime measurements. Raman and FTIR absorption measurements show that compositions with high yttria:alumina ratio and a low silica content exhibit a reduced maximum phonon energy. Fluorescence spectra at 1470 nm from all Tm-doped samples were similar in shape and had an extremely broad FWHM of 129 nm. Fluorescence lifetime measurements show that the reduced maximum phonon energy shown by high yttria:alumina and low silica glasses results in an increased lifetime of up to 20% over the range studied. Unlike a previous study of Er-doped YAS, concentration quenching was observed in lifetime data from both the $^3F_4$ and the $^3H_4$ levels.

A thulium-doped unclad YAS fibre was successfully drawn from a 10 cm preform rod with the composition 17.4% Y_2O_3, 22.5% Al_2O_3 and 60% SiO_2. 7.5 m of continuous fibre with a diameter of 150-350 μm was pulled. The fibre was easily cleaved and had sufficient mechanical strength to be handled

without being broken accidentally. The fibre had a minimum loss of 3.6 dB/m at 1360 nm, which should be improved upon by reducing the hydroxyl content and by fabricating a fibre with a core-cladding structure.

Future work should be focused on finding a suitable cladding glass for a YAS fibre. The fabrication of a Tm-doped YAS fibre with a sufficiently small core would then allow an attempt at S-band amplification. Improvements in the glass quality by removing transition metal and hydroxyl impurities should result in a lower fibre loss. The 470 nm emission observed from the Tm-doped fibre in this work makes this glass a potentially interesting material for an upconversion laser. Experiments to determine if the glass is affected by photodarkening should be carried out. Finally, concentration quenching effects should be investigated further in these materials, since materials which can incorporate rare earth dopants in high concentrations are potentially useful as short fibre of planar waveguide amplifiers.

Appendix A

Transition metal-doped Ga:La:S sample details

Dopant	Concentration (ppm wt.)	Concentration (ions cm^{-3})
V_2S_3	28	6×10^{17}
NiS	36	9×10^{17}
CuS	43	1.0×10^{18}
TiS_2	21	4×10^{17}
FeS	64	1.6×10^{18}
CoS_2	36	7×10^{17}

Table A.1: Details of dopant compounds and concentrations for the transition metal-doped GLS glasses. Concentrations are nominal and errors of ±20% are expected.

Appendix B

Yttrium aluminosilicate glass melt details

Sample	Y_2O_3	Al_2O_3	SiO_2	Dopant	Mass / g	Melting	Comments
YAS1	14.97	25.00	60.00	440 ppm Tm	30	1 h 1500°C	not melted at 1500°C
						1 h 1600°C	viscous, cloudy surface
YAS2	19.97	20.00	60.00	500 ppm Tm	30	1 h 1600°C	heavily cracked & cloudy
YAS2b	19.97	20.00	60.00	1070 ppm Tm	30	1 h 1600°C	mixed for 30 mins using machine
							cloudy on surface,viscous
YAS3	26.21	26.25	47.50	555 ppm Tm	30	1 h 1600°C	cloudy surface, contains small bubbles
YAS4	24.97	15.00	60.00	500 ppm Tm	30	1 h 1600°C	did not melt
YAS5	17.47	22.50	60.00	504 ppm Tm	30	1 h 1600°C	cloudy on surface
YAS6	23.09	23.13	53.75	451 ppm Tm	30	1 h 1600°C	contains small bubbles
YAS7	20.59	25.63	53.75	490 ppm Tm	30	1 h 1600°C	contains small bubbles
YAS8	25.95	26.25	47.50	3911 ppm Tm	30	1 h 1600°C	cracked and contains bubbles
YAS9	26.24	26.25	47.50	195 ppm Tm	30	1.5 h 1600°C	cracked and contains bubbles
YAS10	23.37	29.01	47.50	429 ppm Tm	30	1 h 1600°C	cracked and contains bubbles
YAS11	23.40	29.01	47.50	178 ppm Er	30	ramp up to	cracked and contains bubbles
						3h 1600°C	
YAS12	26.17	26.25	47.50	869 ppm Tm	30	1 h 1600°C	small cracks
							some powder in crucible and glass
YAS13	23.40	29.01	47.50	513 ppm Er	30	1 h 1600°C	cracked and contains bubbles
							removed after remelting
YAS14	26.24	26.25	47.50	198 ppm Er	30	1 h 1600°C	mixed powder with pestle and mortar,
							contains bubbles and some powder
							Remelted: homogeneous but contaminated

Table B.1: Details of YAS glass melts.

Sample	Y_2O_3	Al_2O_3	SiO_2	Dopant	Mass / g	Melting	Comments
YAS15	26.21	26.25	47.50	511 ppm Er	30	1 h 1600°C	contains bubbles and some powder slightly cloudy on remelting
YAS16	17.47	22.50	60.00	505 ppm Tm	30	1.5 h 1600°C	cloudy on surface, viscous
YAS17	16.80	22.50	60.00	9941 ppm Tm	30	1 h 1600°C	new powder: viscous, cloudy surface
YAS18	26.25	26.25	47.50	-	30	1 h 1600°C	old powder: low viscosity, cracked, bubbles
YAS19	17.50	22.50	60.00	-	30	1 h 1600°C	new powder: slightly cloudy on surface
YAS20	17.40	22.50	60.00	1101 ppm Tm	120	2 h 1600°C	cracked in mould
YAS21	17.40	22.50	60.00	1101 ppm Tm	120	2 h 1600°C	mould heated to 550°C, no cracks

Table B.2: Details of YAS glass melts (cont.).

Appendix C

Conference publications

Aronson, J. E., N. Chiodini, A. Paleari and W. S. Brocklesby, "Optical spectroscopy of erbium- and thulium-doped SnO_2:SiO_2 glass-ceramics." *American Ceramic Society: Glass & Optical Materials Division Fall 2003 Meeting*, Corning, USA.

Hughes, M., J. E. Aronson, W. S. Brocklesby, D. P. Shepherd, D. W. Hewak and R. J. Curry, "Transition metal-doped chalcogenide glasses for broadband near-infrared sources." *SPIE: Solid State Laser Technologies and Femtosecond Phenomena 2004*, London, UK.

Curry, R. J., M. A. Hughes, J. E. Aronson, W. S. Brocklesby and D. W. Hewak, "Vanadium doped chalcogenide glasses for broadband near-infrared sources." *American Ceramic Society: Glass & Optical Materials Division Fall 2004 Meeting*, Florida, USA.

Aronson, J. E., C. R. Haythornthwaite, D. W. Hewak and W. S. Brocklesby, "Optical spectroscopy of Cr^{4+}-doped chalcogenide glasses." *PREP 2004*, Hertfordshire, UK.

References

[1] Dieke, G. H., *Spectra and energy levels of rare earth ions in crystals* (Interscience Publishers, New York, 1968).

[2] Tanabe, Y. and S.Sugano, "On the absorption spectra of complex ions II." *Journal of the Physical Society of Japan*, 9(5):766–779, 1954.

[3] Imbusch, G. F. and R. Kopelman, "Optical spectroscopy of electronic centers in solids." In W. M. Yen and P. M. Selzer (eds.), *Laser Spectroscopy of Solids* (Springer, New York, 1981).

[4] Henderson, B. and G. F. Imbusch, *Optical Spectroscopy of Inorganic Solids* (Oxford University Press, New York, 1989).

[5] Layne, C. B., W. H. Lowdermilk and M. J. Weber, "Multiphonon relaxation of rare-earth ions in oxide glasses." *Physical Review B*, 16(1):10–20, 1977.

[6] Förster, T., "Transfer mechanisms of electronic excitation." *Discuss. Faraday Soc.*, 27(7):7–17, 1959.

[7] Dexter, D. L., "A theory of sensitized luminescence in solids." *Journal of Chemical Physics*, 21(5):836–850, 1953.

[8] Silfvast, W. T., *Laser Fundamentals* (Cambridge University Press, 2004), 2nd edn.

[9] Nagel, S. R., J. B. Macchesney and K. L. Walker, "An overview of the modified chemical vapor deposition (MCVD) process and performance." *IEEE Journal of Quantum Electronics*, 18(4):459–476, 1982.

[10] Desurvire, E., *Erbium-Doped Fiber Amplifiers: Device and System Developments* (Wiley Interscience, 2002).

[11] Miniscalco, W. J., "Erbium-doped glasses for fiber amplifiers at 1500 nm." *Journal of Lightwave Technology*, 9(2):234–250, 1991.

[12] Ohishi, Y., T. Kanamori, T. Kitagawa, S. Takahashi, E. Snitzer and G. H. Sigel, "Pr^{3+}-doped fluoride fiber amplifier operating at 1.31 μm." *Optics Letters*, 16(22):1747–1749, 1991.

[13] Shimizu, M., T. Kanamori, J. Temmyo, M. Wada, M. Yamada, Y. Terunuma, Y. Ohishi and S. Sudo, "28.3 dB gain 1.3 μm-band Pr-doped fluoride fiber amplifier module pumped by 1.017 μm InGaAs-LD's." *IEEE Photonics Technology Letters*, 5(6):654–657, 1993.

[14] Nishida, Y., M. Yamada, T. Kanamori, K. Kobayashi, J. Temmyo, S. Sudo and Y. Ohishi, "Development of an efficient praseodymium-doped fiber amplifier." *IEEE Journal of Quantum Electronics*, 34(8):1332–1339, 1998.

[15] Islam, M. N., "Raman amplifiers for telecommunications." *IEEE Journal of Selected Topics in Quantum Electronics*, 8(3):548–559, 2002.

[16] Namiki, S. and Y. Emori, "Broadband amplifiers for WDM transmission." *Optics and Photonics News*, 13(7):52–56, 2002.

[17] Emori, Y., S. Kado and S. Namiki, "Broadband flat-gain and low-noise raman amplifiers pumped by wavelength-multiplexed high-power laser diodes." *Optical Fiber Technology*, 8(2):107–122, 2002.

[18] Islam, M. and M. Nietubyc, "Raman amplification opens the S-band window." *WDM Solutions*, (pp. 53–62), 2001.

[19] Wan, P. and J. Conradi, "Impact of double Rayleigh backscatter noise on digital and analog fiber systems." *Journal of Lightwave Technology*, 14(3):288–297, 1996.

[20] Mecozzi, A. and J. M. Wiesenfeld, "The roles of semiconductor optical amplifiers in optical networks." *Optics and Photonics News*, 12(3):36–42, 2001.

[21] Kincade, K., "CWDM breathes life into metro, access, and enterprise applications." *Laser Focus World*, 39(3):97–100, 2003.

[22] Laming, R. I., L. Reekie, P. R. Morkel and D. N. Payne, "Multichannel crosstalk and pump noise characterization of Er^{3+}-doped fiber amplifier pumped at 980 nm." *Electronics Letters*, 25(7):455–456, 1989.

[23] Massicott, J. F., J. R. Armitage, R. Wyatt, B. J. Ainslie and S. P. Craigryan, "High-gain, broadband, 1.6 μm Er^{3+} doped silica fiber amplifier." *Electronics Letters*, 26(20):1645–1646, 1990.

[24] Bogdanov, V. K., W. E. K. Gibbs, D. J. Booth, J. S. Javorniczky, P. J. Newman and D. R. MacFarlane, "Energy exchange processes in Er^{3+}-doped fluorozirconate glasses." *Journal of Non-Crystalline Solids*, 256-257:288–293, 1999.

[25] Yamada, M., A. Mori, K. Kobayashi, P. Ono, T. Kanamori, K. Oikawa, Y. Nishida and Y. Ohishi, "Gain-flattened tellurite-based EDFA with a flat amplification bandwidth of 76 nm." *IEEE Photonics Technology Letters*, 10(9):1244–1246, 1998.

[26] Jha, A., S. Shen and M. Naftaly, "Structural origin of spectral broadening of 1.5 μm emission in Er^{3+}-doped tellurite glasses." *Physical Review B*, 62(10):6215–6227, 2000.

[27] Morkel, P. R., M. C. Farries and S. B. Poole, "Spectral variation of excited state absorption in neodymium doped fibre lasers." *Optics Communications*, 67(5):349–352, 1988.

[28] Hewak, D. (ed.), *Properties, Processing and Applications of Glass and Rare Earth-Doped Glasses for Optical Fibres*. EMIS Datareviews series No. 22 (INSPEC, 1998).

[29] Wang, J. S., E. M. Vogel, E. Snitzer, J. L. Jackel, V. L. da Silva and Y. Silberberg, "1.3 μm emission of neodymium and praseodymium in tellurite-based glasses." *Journal of Non-Crystalline Solids*, 178:109–113, 1994.

[30] Brierley, M., S. Carter, P. France and J. E. Pedersen, "Amplification in the 1300 nm telecommunications window in a Nd- doped fluoride fiber." *Electronics Letters*, 26(5):329–330, 1990.

[31] Wei, K., D. P. Machewirth, J. Wenzel, E. Snitzer and G. H. Sigel, "Spectroscopy of Dy^{3+} in Ge-Ga-S glass and its suitability for 1.3 μm

fiber-optical amplifier applications." *Optics Letters*, 19(12):904–906, 1994.

[32] Hewak, D. W., B. N. Samson, J. A. M. Neto, R. I. Laming and D. N. Payne, "Emission at 1.3 μm from dysprosium-doped Ga:La:S glass." *Electronics Letters*, 30(12):968–970, 1994.

[33] Samson, B. N., T. Schweizer, D. W. Hewak and R. I. Laming, "Properties of dysprosium-doped gallium lanthanum sulfide fiber amplifiers operating at 1.3 μm." *Optics Letters*, 22(10):703–705, 1997.

[34] Guimond, Y., J. L. Adam, A. M. Jurdyc, J. Mugnier, B. Jacquier and X. H. Zhang, "Dy^{3+}-doped stabilized GeGaS glasses for 1.3 μm optical fiber amplifiers." *Optical Materials*, 12(4):467–471, 1999.

[35] Schweizer, T., R. Goutaland, E. Martins, D. W. Hewak and W. S. Brocklesby, "Site-selective spectroscopy in dysprosium-doped chalcogenide glasses for 1.3 μm optical-fiber amplifiers." *Journal of the Optical Society of America B-Optical Physics*, 18(10):1436–1442, 2001.

[36] Heo, J., "1.3 μm-emission properties and local structure of Dy^{3+} in chalcohalide glasses." *Comptes Rendus Chimie*, 5(11):739–749, 2002.

[37] Percival, R. M. and J. R. Williams, "Highly efficient 1.064 μm up-conversion pumped 1.47 μm thulium-doped fluoride fiber amplifier." *Electronics Letters*, 30(20):1684–1685, 1994.

[38] Sakamoto, T., M. Shimizu, M. Yamada, T. Kanamori, Y. Ohishi, Y. Terunuma and S. Sudo, "35 dB gain Tm-doped ZBLYAN fiber amplifier operating at 1.65 μm." *IEEE Photonics Technology Letters*, 8(3):349–351, 1996.

[39] Kani, J., T. Sakamato, M. Jinno, T. Kanamori, M. Yamada and K. Oguchi, "1470 nm band wavelength division multiplexing transmission." *Electronics Letters*, 34(11):1118–1119, 1998.

[40] Aozasa, S., T. Sakamoto, T. Kanamori, K. Hoshino, K. Kobayashi and M. Shimizu, "Tm-doped fiber amplifiers for 1470-nm-band WDM signals." *IEEE Photonics Technology Letters*, 12(10):1331–1333, 2000.

[41] Kasamatsu, T., Y. Yano and T. Ono, "1.49 μm-band gain-shifted thulium-doped fiber amplifier for WDM transmission systems." *Journal of Lightwave Technology*, 20(10):1826–1838, 2002.

[42] Minelly, J. and A. Ellison, "Applications of antimony-silicate glasses for fiber optic amplifiers." *Optical Fiber Technology*, 8(2):123–138, 2002.

[43] Naftaly, M., S. X. Shen and A. Jha, "Tm^{3+}-doped tellurite glass for a broadband amplifier at 1.47 μm." *Applied Optics*, 39(27):4979–4984, 2000.

[44] Taylor, E. R., L. N. Ng, N. P. Sessions and H. Buerger, "Spectroscopy of Tm^{3+}-doped tellurite glasses for 1470 nm fiber amplifier." *Journal of Applied Physics*, 92(1):112–117, 2002.

[45] Shen, S., A. Jha, E. Zhang and S. J. Wilson, "Compositional effects and spectroscopy of rare earths (Er^{3+}, Tm^{3+}, and Nd^{3+}) in tellurite glasses." *Comptes Rendus Chimie*, 5(12):921–938, 2002.

[46] Komukai, T., T. Yamamoto, T. Sugawa and Y. Miyajima, "Upconversion pumped thulium-doped fluoride fiber amplifier and laser operating at 1.47 μm." *IEEE Journal of Quantum Electronics*, 31(11):1880–1889, 1995.

[47] Petricevic, V., S. K. Gayen, R. R. Alfano, K. Yamagishi, H. Anzai and Y. Yamaguchi, "Laser action in chromium-doped forsterite." *Applied Physics Letters*, 52(13):1040–1042, 1988.

[48] Moncorge, R., H. Manaa and G. Boulon, "Cr^{4+} and Mn^{5+} active centers for new solid state laser materials." *Optical Materials*, 4(1):139–151, 1994.

[49] Alcock, A. J., P. Scorah and K. Hnatovsky, "Broadly tunable continuous-wave diode-pumped Cr^{4+}:YAG laser." *Optics Communications*, 215(1-3):153–157, 2003.

[50] Tick, P. A., "Are low-loss glass-ceramic optical waveguides possible?" *Optics Letters*, 23(24):1904–1905, 1998.

[51] Quimby, R. S., P. A. Tick, N. F. Borrelli and L. K. Cornelius, "Quantum efficiency of Pr^{3+}-doped transparent glass ceramics." *Journal of Applied Physics*, 83(3):1649–1653, 1998.

[52] Mortier, M. and F. Auzel, "Rare-earth doped transparent glass-ceramics with high cross-sections." *Journal of Non-Crystalline Solids*, 257:361–365, 1999.

[53] Goncalves, A. C., L. F. Santos and R. M. Almeida, "Rare-earth-doped transparent glass ceramics." *Comptes Rendus Chimie*, 5(12):845–854, 2002.

[54] Maiman, T. H., "Stimulated optical radiation in ruby." *Nature*, 187:493–494, 1960.

[55] Walling, J. C., H. Jenssen, R. C. Morris, W. W. O'Dell and O. G. Peterson, "Tunable-laser performance in $BeAl_2O_4$:Cr^{3+}." *Optics Letters*, 4(6):182–183, 1979.

[56] Kuck, S., "Laser-related spectroscopy of ion-doped crystals for tunable solid-state lasers." *Applied Physics B-Lasers and Optics*, 72(5):515–562, 2001.

[57] Moulton, P. F., "Spectroscopic and laser characteristics of Ti:Al_2O_3." *Journal of the Optical Society of America B-Optical Physics*, 3(1):125–133, 1986.

[58] Walling, J. C., O. G. Peterson, H. P. Jenssen, R. C. Morris and E. W. Odell, "Tunable alexandrite lasers." *IEEE Journal of Quantum Electronics*, 16(12):1302–1315, 1980.

[59] Lai, S. T., B. H. T. Chai, M. Long and M. D. Shinn, "Room-temperature near-infrared tunable Cr:$La_3Ga_5SiO_{14}$ laser." *IEEE Journal of Quantum Electronics*, 24(9):1922–1926, 1988.

[60] Emmett, J. L., W. F. Krupke and J. B. Trenholme, "Volume 4, The future development of high-power solid state laser systems." Tech. rep., Lawrence Livermore National Laboratory, 1982.

[61] Brauch, U. and U. Durr, "Vibronic laser action of V^{2+}:$CsCaF_3$." *Optics Communications*, 55(1):35–40, 1985.

[62] Seas, A., V. Petricevic and R. R. Alfano, "Continuous-wave mode-locked operation of a chromium-doped forsterite laser." *Optics Letters*, 16(21):1668–1670, 1991.

[63] French, P. M. W., N. H. Rizvi, J. R. Taylor and A. V. Shestakov, "Continuous-wave mode-locked Cr^{4+}:YAG laser." *Optics Letters*, 18(1):39–41, 1993.

[64] Weber, M. J., *Handbook of Lasers* (CRC Press, 2001).

[65] Johnson, L. F., H. J. Guggenheim and R. A. Thomas, "Phonon-terminated optical masers." *Physical Review B*, 149(1):179–185, 1966.

[66] Moulton, P. F., "An investigation of the Co-MgF_2 laser system." *IEEE Journal of Quantum Electronics*, 21(10):1582–1595, 1985.

[67] Page, R. H., K. I. Schaffers, L. D. DeLoach, G. D. Wilke, F. D. Patel, J. B. Tassano, S. A. Payne, W. F. Krupke, K. T. Chen and A. Burger, "Cr^{2+}-doped zinc chalcogenides as efficient, widely tunable mid- infrared lasers." *IEEE Journal of Quantum Electronics*, 33(4):609–619, 1997.

[68] Seo, J. T., U. Hommerich, H. Zong, S. B. Trivedi, S. W. Kutcher, C. C. Wang and R. J. Chen, "Mid-infrared lasing from a novel optical material: Chromium-doped $Cd_{0.55}Mn_{0.45}Te$." *Physica Status Solidi A-Applied Research*, 175(1):R3–R4, 1999.

[69] Adams, J. J., C. Bibeau, R. H. Page, D. M. Krol, L. H. Furu and S. A. Payne, "4.0-4.5 μm lasing of Fe:ZnSe below 180 K, a new mid-infrared laser material." *Optics Letters*, 24(23):1720–1722, 1999.

[70] Andrews, L. J., A. Lempicki and B. C. McCollum, "Spectroscopy and photokinetics of chromium (III) in glass." *Journal of Chemical Physics*, 74(10):5526–5538, 1981.

[71] Wu, X., H. Yuan, W. M. Yen and B. G. Aitken, "Compositional dependence of the luminescence from Cr^{4+}-doped calcium aluminate glass." *Journal of Luminescence*, 66,67:285–289, 1996.

[72] Tanabe, S. and X. Feng, "Temperature variation of near-infrared emission from Cr^{4+} in aluminate glass for broadband telecommunication." *Applied Physics Letters*, 77(6):818–820, 2000.

[73] Choi, Y. G., K. H. Kim, Y. S. Han and J. Heo, "Oxidation state and local coordination of chromium dopant in soda-lime-silicate and calcium-aluminate glasses." *Chemical Physics Letters*, 329(5-6):370–376, 2000.

[74] Felice, V., B. Dussardier, J. K. Jones, G. Monnom and D. B. Ostrowsky, "Cr^{4+}-doped silica optical fibres: absorption and fluorescence properties." *European Physical Journal-Applied Physics*, 11(2):107–110, 2000.

[75] Felice, V., B. Dussardier, J. K. Jones, G. Monnom and D. B. Ostrowsky, "Chromium-doped silica optical fibres: Influence of the core composition on the Cr oxidation states and crystal field." *Optical Materials*, 16:269–277, 2001.

[76] Feng, X. and S. Tanabe, "Spectroscopy and crystal-field analysis for Cr(IV) in alumino-silicate glasses." *Optical Materials*, 20(1):63–72, 2002.

[77] Dvoyrin, V. V., V. M. Mashinsky, V. B. Neustruev, E. M. Dianov, A. N. Guryanov and A. A. Umnikov, "Effective room-temperature luminescence in annealed chromium-doped silicate optical fibers." *Journal of the Optical Society of America B-Optical Physics*, 20(2):280–283, 2003.

[78] Schultz, P. C., "Optical absorption of the transition elements in vitreous silica." *Journal of the American Ceramic Society*, 57(7):309–313, 1974.

[79] Ohishi, Y., S. Mitachi, T. Kanamori and T. Manabe, "Optical absorption of 3d transition metal and rare earth elements in zirconium fluoride glasses." *Physics and Chemistry of Glasses*, 24(5):135–140, 1983.

[80] Suzuki, Y., W. A. Sibley, O. H. Elbayoumi, T. M. Roberts and B. Bendow, "Optical-properties of transition-metal ions in zirconium-based metal fluoride glasses and MgF_2 crystals." *Physical Review B*, 35(9):4472–4482, 1987.

[81] Brady, D. J., T. Schweizer, J. Wang and D. W. Hewak, "Minimum loss predictions and measurements in gallium lanthanum sulphide based glasses and fibre." *Journal of Non-Crystalline Solids*, 242(2-3):92–98, 1998.

[82] Fuxi, G. and L. Huimin, "Spectroscopy of transition metal ions in inorganic glasses." *Journal of Non-Crystalline Solids*, 80(1-3):20–33, 1986.

[83] Wu, E., H. Chen, Z. R. Sun and H. P. Zeng, "Broadband saturable absorber with cobalt-doped tellurite glasses." *Optics Letters*, 28(18):1692–1694, 2003.

[84] Bausa, L. E., F. Jaque, J. G. Sole and A. Duran, "Photoluminescence of Ti^{3+} in P_2O_5-Na_2O-Al_2O_3 glass." *Journal of Materials Science*, 23(6):1921–1922, 1988.

[85] Morinaga, K., H. Yoshida and H. Takebe, "Compositional dependence of absorption-spectra of Ti^{3+} in silicate, borate, and phosphate-glasses." *Journal of the American Ceramic Society*, 77(12):3113–3118, 1994.

[86] Devyatykh, G. G., M. F. Churbanov, I. V. Scripachev, G. E. Snopatin, E. M. Dianov and V. G. Plotnichenko, "Recent developments in As-S glass fibres." *Journal of Non-Crystalline Solids*, 257:318–322, 1999.

[87] West, Y. D., T. Schweizer, D. J. Brady and D. W. Hewak, "Gallium lanthanum sulphide fibers for infrared transmission." *Fiber and Integrated Optics*, 19(3):229–250, 2000.

[88] Schweizer, T., B. N. Samson, R. C. Moore, D. W. Hewak and D. N. Payne, "Rare-earth doped chalcogenide glass fibre laser." *Electronics Letters*, 33(5):414–416, 1997.

[89] Haythornthwaite, C. R., "Spectroscopy of chromium doped glass for amplifiers and lasers." PhD, University of Southampton, 1999.

[90] Petrovich, M., "Gallium lanthanum sulphide glasses for near-infrared photonic applications." PhD, University of Southampton, 2003.

[91] Sanghera, J. S. and I. D. Aggarwal, "Active and passive chalcogenide glass optical fibers for IR applications: a review." *Journal of Non-Crystalline Solids*, 256-257:6–16, 1999.

[92] Itoh, K., H. Yanagita, H. Tawarayama, K. Yamanaka, E. Ishikawa, K. Okada, H. Aoki, Y. Matsumoto, A. Shirakawa, Y. Matsuoka and H. Toratani, "Pr^{3+} doped InF_3/GaF_3 based fluoride glass fibers and

Ga-Na-S glass fibers for light amplification around 1.3 μm." *Journal of Non-Crystalline Solids*, 256-257:1–5, 1999.

[93] Heo, J., J. S. Sanghera and J. D. Mackenzie, "Chalcohalide glasses for infrared fiber optics." *Optical Engineering*, 30(4):470–479, 1991.

[94] Machewirth, D. P., K. Wei, V. Krasteva, R. Datta, E. Snitzer and G. H. Sigel, "Optical characterization of Pr^{3+} and Dy^{3+} doped chalcogenide glasses." *Journal of Non-Crystalline Solids*, 213:295–303, 1997.

[95] Murata, T., M. Torisaka, H. Takebe and K. Morinaga, "Compositional dependence of the valence state of Cr ions in oxide glass." *Journal of Non-Crystalline Solids*, 220:139–146, 1997.

[96] Rasheed, F., K. P. Odonnell, B. Henderson and D. B. Hollis, "Disorder and the optical spectroscopy of Cr^{3+}-doped glasses: I. Silicate glasses." *Journal of Physics-Condensed Matter*, 3(12):1915–1930, 1991.

[97] Moncorge, R., G. Cormier, D. J. Simkin and J. A. Capobianco, "Fluorescence analysis of chromium-doped forsterite (Mg_2SiO_4)." *IEEE Journal of Quantum Electronics*, 27(1):114–120, 1991.

[98] Eilers, H., U. Hommerich, S. M. Jacobsen, W. M. Yen, K. R. Hoffman and W. Jia, "Spectroscopy and dynamics of Cr^{4+}:$Y_3Al_5O_{12}$." *Physical Review B*, 49(22):15505–15513, 1994.

[99] Wu, X., S. Huang, W. M. Yen, B. G. Aitken and M. A. Newhouse, "The temperature and excitation wavelength dependence of the luminescence from Cr^{4+} in MgCaBa aluminate glass." *Journal of Non-Crystalline Solids*, 203:120–126, 1996.

[100] Munin, E., A. Balbin Villaverde, M. Bass and K. Cerqua-Richardson, "Optical absorption, absorption saturation and a useful figure of merit for chromium doped glasses." *Journal of Physics and Chemistry of Solids*, 58(1):51–57, 1997.

[101] Hommerich, U., H. Eilers, W. M. Yen, J. S. Hayden and M. K. Aston, "Near infrared emission at 1.35 μm in Cr doped glass." *Journal of Luminescence*, 60-61:119–122, 1994.

[102] Koepke, C., K. Wisniewski and M. Grinberg, "Excited state spectroscopy of chromium ions in various valence states in glasses." *Journal of Alloys and Compounds*, 341(1-2):19–27, 2002.

[103] Merkle, L. D., T. H. Allik and B. H. T. Chai, "Crystal growth and spectroscopic properties of Cr^{4+} in $Ca_2Al_2SiO_7$ and $Ca_2Ga_2SiO_7$." *Optical Materials*, 1(2):91–100, 1992.

[104] Fernandez, J., R. Balda, M. A. Illarramendi and G. F. Imbusch, "The relationship between quantum efficiency and average lifetime of Cr^{3+} ions in glass." *Journal of Luminescence*, 58(1-6):294–297, 1994.

[105] Balda, R., J. Fernandez, M. A. Illarramendi, M. A. Arriandiaga, J. L. Adam and J. Lucas, "Luminescence thermal quenching of Cr^{3+} in zirconium-barium-based fluoride glasses investigated by time-resolved laser spectroscopy." *Physical Review B*, 44(10):4759–4770, 1991.

[106] Johnson, L. F. and H. J. Guggenheim, "Phonon-terminated coherent emission from V^{2+} ions in MgF_2." *Journal of Applied Physics*, 38(12):4837–4839, 1967.

[107] Sturge, M. D., F. R. Merritt, L. F. Johnson, H. J. Guggenheim and J. P. Van der Ziel, "Optical and microwave studies of divalent vanadium in octahedral fluoride coordination." *Journal of Chemical Physics*, 54(1):405–413, 1971.

[108] Knierim, W., A. Honold, U. Brauch and U. Durr, "Optical and lasing properties of V^{2+}-doped halide crystals." *Journal of the Optical Society of America B-Optical Physics*, 3(1):119–124, 1986.

[109] Weber, M. J. and L. A. Riseberg, "Optical spectra of vanadium ions in yttrium aluminium garnet." *Journal of Chemical Physics*, 55(5):2032–2038, 1971.

[110] Mikhailov, V. P., N. V. Kuleshov, N. I. Zhavoronkov, P. V. Prohohsin and K. V. Yumashev, "Optical absorption and nonlinear transmission of tetrahedral V^{3+} (d^2) in yttrium aluminium garnet." *Optical Materials*, 2:267–272, 1993.

[111] Kuck, S. and P. Jander, "Luminescence from V^{3+} in tetrahedral oxo-coordination." *Chemical Physics Letters*, 300(1-2):189–194, 1999.

[112] Pappalardo, R. and R. E. Dietz, "Absorption spectra of transition ions in CdS crystals." *Physical Review*, 123(4):1188–1203, 1961.

[113] McClure, D. S., "Optical spectra of transition-metal ions in corundum." *Journal of Chemical Physics*, 36(10):2757–2779, 1962.

[114] Brunold, T. C., H. U. Gudel and A. A. Kaminskii, "Optical spectroscopy of V^{4+} doped crystals of Mg_2SiO_4 and Ca_2GeO_4." *Chemical Physics Letters*, 271(4-6):327–334, 1997.

[115] Kuck, S. and P. Jander, "Spectroscopic properties of the tetrahedrally coordinated V^{3+} ion in oxide crystals." *Optical Materials*, 13(3):299–310, 1999.

[116] Meyn, J. P., T. Danger, K. Petermann and G. Huber, "Spectroscopic characterization of V^{4+}-doped Al_2O_3 and $YAlO_3$." *Journal of Luminescence*, 55(2):55–62, 1993.

[117] Johnson, L. F., R. E. Dietz and H. J. Guggenheim, "Optical maser oscillation from Ni^{2+} in MgF_2 involving simultaneous emission of phonons." *Physical Review Letters*, 1963.

[118] May, P. S. and H. U. Gudel, "Infrared luminescence properties of Ni^{2+} in various chloride lattices - $CsCdCl_3$, $CsMgCl_3$, $CdCl_2$, and $MgCl_2$." *Journal of Luminescence*, 46(5):277–290, 1990.

[119] Koetke, J., K. Petermann and G. Huber, "Infrared excited-state absorption of Ni^{2+} doped crystals." *Journal of Luminescence*, 60-1:197–200, 1994.

[120] Walker, G., B. Kamaluddin, T. J. Glynn and R. Sherlock, "Luminescence of Ni^{2+} centers in forsterite (Mg_2SiO_4)." *Journal of Luminescence*, 60-1:123–126, 1994.

[121] Deloach, L. D., R. H. Page, G. D. Wilke, S. A. Payne and W. F. Krupke, "Transition metal-doped zinc chalcogenides: Spectroscopy and laser demonstration of a new class of gain media." *IEEE Journal of Quantum Electronics*, 32(6):885–895, 1996.

[122] Blumberg, W. E., J. Eisinger and S. Geschwind, "Cu^{3+} ion in corundum." *Physical Review*, 130(3):900–909, 1963.

[123] Sanchez, A., A. J. Strauss, R. L. Aggarwal and R. E. Fahey, "Crystal-growth, spectroscopy, and laser characteristics of Ti-Al_2O_3." *IEEE Journal Of Quantum Electronics*, 24(6):995–1002, 1988.

[124] Moulton, P. F. and A. Mooradian, "Broadly tunable cw operation of Ni:MgF_2 and Co:MgF_2 lasers." *Applied Physics Letters*, 35(11):838–840, 1979.

[125] Tsai, T. Y. and M. Birnbaum, "Characteristics of Co^{2+}:ZnS saturable absorber Q-switched neodymium lasers at 1.3 μm." *Journal of Applied Physics*, 89(4):2006–2012, 2001.

[126] Wood, D. L. and J. P. Remeika, "Optical absorption of tetrahedral Co^{3+} and Co^{2+} in garnets." *The Journal of Chemical Physics*, 46(9):3595–3602, 1967.

[127] Zhou, Y., Y. L. Lam, S. S. Wang, H. L. Liu, C. H. Kam and Y. C. Chan, "Fluorescence enhancement of Er^{3+}-doped sol-gel glass by aluminum codoping." *Applied Physics Letters*, 71(5):587–589, 1997.

[128] Chiodini, N., F. Morazzoni, A. Paleari, R. Scotti and G. Spinolo, "Sol-gel synthesis of monolithic tin-doped silica glass." *Journal of Materials Chemistry*, 9(10):2653–2658, 1999.

[129] Huang, W., R. R. A. Syms, E. M. Yeatman, M. M. Ahmad, T. V. Clapp and S. M. Ojha, "Fiber-device-fiber gain from a sol-gel erbium-doped waveguide amplifier." *IEEE Photonics Technology Letters*, 14(7):959–961, 2002.

[130] Stone, B. T. and K. L. Bray, "Fluorescence properties of Er^{3+}-doped sol-gel glasses." *Journal of Non-Crystalline Solids*, 197(2-3):136–144, 1996.

[131] Orignac, X., D. Barbier, X. M. Du and R. M. Almeida, "Fabrication and characterization of sol-gel planar waveguides doped with rare-earth ions." *Applied Physics Letters*, 69(7):895–897, 1996.

[132] Armelao, L., S. Gross, G. Obetti and E. Tondello, "Er^{3+}-doped SiO_2-Al_2O_3 thin films prepared by the sol-gel route." *Surface & Coatings Technology*, 190(2-3):218–222, 2005.

[133] Orignac, X., D. Barbier, X. M. Du, R. M. Almeida, O. McCarthy and E. Yeatman, "Sol-gel silica/titania-on-silicon Er/Yb-doped waveguides for optical amplification at 1.5 μm." *Optical Materials*, 12(1):1–18, 1999.

[134] Benatsou, M. and M. Bouazaoui, "Fluorescence properties of sol-gel derived Er^{3+}:SiO_2-GeO_2 planar waveguides." *Optics Communications*, 137(1-3):143–150, 1997.

[135] Hill, K. O., "Photosensitivity in optical fiber waveguides: From discovery to commercialization." *IEEE Journal Of Selected Topics In Quantum Electronics*, 6(6):1186–1189, 2000.

[136] Dong, L., J. L. Cruz, L. Reekie, M. G. Xu and D. N. Payne, "Enhanced photosensitivity in tin-codoped germanosilicate optical fibers." *IEEE Photonics Technology Letters*, 7(9):1048–1050, 1995.

[137] Canevali, C., N. Chiodini, F. Morazzoni, J. Padovani, A. Paleari, R. Scotti and G. Spinolo, "Substitutional tin-doped silica glasses: an infrared study of the sol-gel transition." *Journal Of Non-Crystalline Solids*, 293:32–38, 2001.

[138] Chiodini, N., S. Ghidini and A. Paleari, "Mechanisms responsible for the ultraviolet photosensitivity of SnO_2-doped silica." *Physical Review B*, 6407(7):Art. No. 073102, 2001.

[139] Chiodini, N., F. Meinardi, F. Morazzoni, A. Paleari, R. Scotti and G. Spinolo, "Tin doped silica by sol-gel method: doping effects on the SiO_2 Raman spectrum." *Solid State Communications*, 109(3):145–150, 1999.

[140] Chiodini, N., A. Paleari, G. Spinolo, A. Chiasera, M. Ferrari, G. Brambilla and E. R. Taylor, "Photosensitive erbium doped tin-silicate glass." *Journal of Non-Crystalline Solids*, 311(3):217–222, 2002.

[141] Chiodini, N., F. Meinardi, F. Morazzoni, J. Padovani, A. Paleari, R. Scotti and G. Spinolo, "Thermally induced segregation of SnO_2 nanoclusters in Sn-doped silica glasses from oversaturated Sn-doped silica xerogels." *Journal of Materials Chemistry*, 11(3):926–929, 2001.

[142] Chiodini, N., A. Paleari, G. Brambilla and E. R. Taylor, "Erbium doped nanostructured tin-silicate glass-ceramic composites." *Applied Physics Letters*, 80(23):4449–4451, 2002.

[143] Chiodini, N., A. Paleari, D. DiMartino and G. Spinolo, "SnO_2 nanocrystals in SiO_2: A wide-band-gap quantum-dot system." *Applied Physics Letters*, 81(9):1702–1704, 2002.

[144] Chiodini, N., A. Paleari, G. Spinolo and P. Crespi, "Photorefractivity in SiO_2:SnO_2 glass-ceramics by visible light." *Journal of Non-Crystalline Solids*, 322(1-3):266–271, 2003.

[145] Chiodini, N., A. Paleari and G. Spinolo, "Photorefractivity in nanostructured tin-silicate glass ceramics: A radiation-induced nanocluster size effect." *Physical Review Letters*, 90(5):Art. No. 055507, 2003.

[146] Jander, P., "An investigation of novel materials for active optical devices." PhD, University of Southampton, 2003.

[147] Stolen, R. H. and G. E. Walrafen, "Water and its relation to broken bond defects in fused silica." *Journal of Chemical Physics*, 64(6):2623–2631, 1976.

[148] Galeener, F. L., "Band limits and the vibrational spectra of tetrahedral glasses." *Physical Review B*, 19(8):4292–4297, 1979.

[149] Zuo, J., C. Y. Xu, X. M. Liu, C. S. Wang, C. Y. Wang, Y. Hu and Y. T. Qian, "Study of the raman spectrum of nanometer SnO_2." *Journal of Applied Physics*, 75(3):1835–1836, 1994.

[150] Abello, L., B. Bochu, A. Gaskov, S. Koudryavtseva, G. Lucazeau and M. Roumyantseva, "Structural characterization of nanocrystalline SnO_2 by X-ray and raman spectroscopy." *Journal of Solid State Chemistry*, 135(1):78–85, 1998.

[151] Stone, J. and G. E. Walrafen, "Overtone vibrations of OH groups in fused silica optical fibers." *Journal of Chemical Physics*, 76(4):1712–1722, 1982.

[152] Davis, K. M., A. Agarwal, M. Tomozawa and K. Hirao, "Quantitative infrared spectroscopic measurement of hydroxyl concentrations in silica glass." *Journal of Non-Crystalline Solids*, 203:27–36, 1996.

[153] Robertson, J., "Electronic structure of SnO_2, GeO_2, PbO_2, TeO_2 and MgF_2." *Journal of Physics C-Solid State Physics*, 12:4767–4776, 1979.

[154] Nogami, M., T. Enomoto and T. Hayakawa, "Enhanced fluorescence of Eu^{3+} induced by energy transfer from nanosized SnO_2 crystals in glass." *Journal of Luminescence*, 97(3-4):147–152, 2002.

[155] Walrafen, G. E., "Raman spectra from SiOH groups in solid optical fibers." *Journal of Chemical Physics*, 62(1):297–298, 1975.

[156] Peterka, P., B. Faure, W. Blanc, M. Karasek and B. Dussardier, "Theoretical modelling of S-band thulium-doped silica fibre amplifiers." *Optical and Quantum Electronics*, 36(1-3):201–212, 2004.

[157] Hanna, D. C., I. R. Perry, J. R. Lincoln and J. E. Townsend, "A 1-Watt thulium-doped cw fiber laser operating at 2 μm." *Optics Communications*, 80(1):52–56, 1990.

[158] Cole, B. and M. L. Dennis, "S-band amplification in a thulium doped silicate fiber." In *Optical fiber communication conference and exhibit* (Anaheim, 2001), paper TuQ3.

[159] Bendow, B., P. K. Banerjee, M. G. Drexhage, J. Goltman, S. S. Mitra and C. T. Moynihan, "Comparative-study of vibrational characteristics of fluorozirconate and fluorohafnate glasses." *Journal Of The American Ceramic Society*, 65(1):C8–C9, 1982.

[160] Taylor, E. R. M., L. N. Ng, J. Nilsson, R. Caponi, A. Pagano, M. Potenza and B. Sordo, "Thulium-doped tellurite fiber amplifier." *IEEE Photonics Technology Letters*, 16(3):777–779, 2004.

[161] Cole, B. J. and M. L. Dennis, "Heavy metal modified silica glass fibers doped with thulium, holmium, and thulium-sensitized-holmium high quantum efficiencies." US Patent Appl. No. 09/967942, 2003.

[162] Cho, D. H., Y. G. Choi, H. S. Seo and B. J. Park, "Tm^{3+}-doped silicate glass and the use thereof." US Patent Appl. No. 10/331353, 2002.

[163] Ellison, A. J., "Structure and properties of antimony oxide-based glasses." In *Glass & Optical Materials Division Fall Meeting* (Corning, New York, 2003).

[164] Ohara, "Bi_2O_3-based glass for S-band amplification." In *Rare-Earth-Doped Materials and Devices VI*, vol. 4645, (pp. 8–15) (2002).

[165] Jander, P. and W. S. Brocklesby, "Spectroscopy of Tm^{3+}-doped yttrium-aluminosilicate glass." In *CLEO/Europe EQEC* (Munich, 2003).

[166] Jander, P. and W. S. Brocklesby, "Spectroscopy of yttria-alumina-silica glass doped with thulium and erbium." *IEEE Journal Of Quantum Electronics*, 40(5):509–512, 2004.

[167] Kohli, J. T. and J. E. Shelby, "Formation and properties of rare-earth aluminosilicate glasses." *Physics And Chemistry Of Glasses*, 32(2):67–71, 1991.

[168] Shelby, J. E., S. M. Minton, C. E. Lord and M. R. Tuzzolo, "Formation and properties of yttrium aluminosilicate glasses." *Physics And Chemistry Of Glasses*, 33(3):93–98, 1992.

[169] Hyatt, M. J. and D. E. Day, "Glass properties in the yttria-alumina-silica system." *Journal Of The American Ceramic Society*, 70(10):C283–C287, 1987.

[170] Kohli, J. T., R. A. Condrate and J. E. Shelby, "Raman and infrared spectra of rare earth aluminosilicate glasses." *Physics and Chemistry of Glasses*, 34(3):81–87, 1993.

[171] Aronne, A., S. Esposito and P. Pernice, "FTIR and DTA study of lanthanum aluminosilicate glasses." *Materials Chemistry And Physics*, 51(2):163–168, 1997.

[172] Judd, B. R., "Optical absorption intensities of rare-earth ions." *Physical Review*, 127(3):750, 1962.

[173] Ofelt, G. S., "Intensities of crystal spectra of rare-earth ions." *Journal of Chemical Physics*, 37(3):511, 1962.

[174] Carnall, W. T., P. R. Fields and K. Rajnak, "Electronic energy levels of the trivalent lanthanide aquo ions." *Journal of Chemical Physics*, 49(10):4424–4442, 1968.

[175] Binnemans, K. and C. Gorller-Walrand, "Are the Judd-Ofelt intensity parameters sensitive enough to reflect small compositional changes in lanthanide-doped glasses?" *Journal Of Physics-Condensed Matter*, 10(10):L167–L170, 1998.

[176] Mairaj, A. K., "Optical waveguides and lasers in improved gallium lanthanum sulphide glass." PhD, University of Southampton, 2003.

[177] Sanz, J., R. Cases and R. Alcalá, "Optical properties of Tm^{3+} in fluorozirconate glass." *Journal of Non-Crystalline Solids*, 93:377–386, 1987.

[178] Oomen, E., "Up-conversion of red-light into blue-light in thulium doped fluorozirconate glasses." *Journal of Luminescence*, 50(6):317–332, 1992.

[179] Lincoln, J. R., W. S. Brocklesby, F. Cusso, J. E. Townsend, A. C. Tropper and A. Pearson, "Time resolved and site selective spectroscopy of thulium doped into germano- and alumino-silicate optical fibers and preforms." *Journal of Luminescence*, 50:297–308, 1991.

[180] Tohmon, G., J. Ohya, H. Sato and T. Uno, "Increased efficiency and decreased threshold in Tm-ZBLAN blue fiber laser co-pumped by 1.1-μm and 0.68-μm light." *IEEE Photonics Technology Letters*, 7(7):742–744, 1995.

[181] Sanders, S., R. G. Waarts, D. G. Mehuys and D. F. Welch, "Laser-diode-pumped 106 mw blue up-conversion fiber laser." *Applied Physics Letters*, 67(13):1815–1817, 1995.

[182] Booth, I. J., C. J. Mackechnie and B. F. Ventrudo, "Operation of diode laser pumped Tm^{3+} ZBLAN upconversion fiber laser at 482 nm." *IEEE Journal Of Quantum Electronics*, 32(1):118–123, 1996.

[183] Booth, I. J., J. L. Archambault and B. F. Ventrudo, "Photodegradation of near-infrared-pumped Tm^{3+}-doped ZBLAN fiber upconversion lasers." *Optics Letters*, 21(5):348–350, 1996.

[184] Broer, M. M., D. M. Krol and D. J. Digiovanni, "Highly nonlinear near-resonant photodarkening in a thulium-doped aluminosilicate glass-fiber." *Optics Letters*, 18(10):799–801, 1993.

[185] Allen, R., L. Esterowitz and I. Aggarwal, "An efficient 1.46 μm thulium fiber laser via a cascade process." *IEEE Journal Of Quantum Electronics*, 29(2):303–306, 1993.

[186] Stoneman, R. C. and L. Esterowitz, "Continuous-wave 1.50 μm thulium cascade laser." *Optics Letters*, 16(4):232–234, 1991.

[187] Percival, R. M., D. Szebesta and S. T. Davey, "Thulium-doped terbium sensitized cw fluoride fiber laser operating on the 1.47 μm transition." *Electronics Letters*, 29(12):1054–1056, 1993.

[188] Floridia, C., M. T. Carvalho, S. R. Luthi and A. S. L. Gomes, "Modeling the distributed gain of single (1050 or 1410 nm) and dual-wavelength (800+1050 nm or 800+1410 nm) pumped thulium-doped fiber amplifiers." *Optics Letters*, 29(17):1983–1985, 2004.

[189] Kasamatsu, T., Y. Yano and T. Ono, "Laser-diode pumping (1.4 and 1.56 μm) of gain-shifted thulium-doped fibre amplifier." *Electronics Letters*, 36(19):1607–1609, 2000.

[190] Gomes, A. S. L., M. T. Carvalho, M. L. Sundheimer, C. J. A. Bastos, J. F. Martins, J. P. Von der Weid and W. Margulis, "Low-pump-power, short-fiber copropagating dual-pumped (800 and 1050 nm) thulium-doped fiber amplifier." *Optics Letters*, 28(5):334–336, 2003.

[191] Gomes, A. S. L., M. T. Carvalho and M. L. Sundheimer, "Comparison of distributed gain in two dual-wavelength pumping schemes for thulium-doped fibre amplifiers." *Electronics Letters*, 39(8):647–648, 2003.

[192] Kasamatsu, T., Y. Yano and T. Ono, "Laser-diode-pumped highly efficient gain-shifted thulium-doped fiber amplifier operating in the 1480-1510 nm band." *IEEE Photonics Technology Letters*, 13(5):433–435, 2001.